



HAL
open science

Exploration of ionic conductors and Li-rich sulfides for all-solid-state batteries

Sujoy Saha

► **To cite this version:**

Sujoy Saha. Exploration of ionic conductors and Li-rich sulfides for all-solid-state batteries. Material chemistry. Sorbonne Université, 2020. English. NNT : 2020SORUS041 . tel-03153280

HAL Id: tel-03153280

<https://theses.hal.science/tel-03153280>

Submitted on 26 Feb 2021

HAL is a multi-disciplinary open access archive for the deposit and dissemination of scientific research documents, whether they are published or not. The documents may come from teaching and research institutions in France or abroad, or from public or private research centers.

L'archive ouverte pluridisciplinaire **HAL**, est destinée au dépôt et à la diffusion de documents scientifiques de niveau recherche, publiés ou non, émanant des établissements d'enseignement et de recherche français ou étrangers, des laboratoires publics ou privés.

Sorbonne Université

Ecole Doctorale – ED 397 · Physique et Chimie des Matériaux

Collège de France

Laboratoire – Chaire de Chimie du Solide et de l'Energie

Exploration of ionic conductors and Li-rich sulfides for all-solid-state batteries

Sujoy Saha

Doctoral thesis in Materials Science / Chemistry

Directed by Jean-Marie Tarascon and Gwenaëlle Rousse

Presented and defended in public on January 6th 2020 in front of the jury,

Dr. Valérie Pralong	Directrice de Recherche, CRISMAT, Caen	Referee
Prof. Silke Biermann	Professor, Ecole Polytechnique	Referee
Prof. Christel Laberty-Robert	Professor, Sorbonne Université	Examiner
Prof. Philippe Barboux	Professor, Chimie ParisTech	Examiner
Prof. Artem Abakumov	Professor, Skolkovo Institute of Science and Technology, Russia	Examiner
Dr. Gwenaëlle Rousse	Associate Professor, Sorbonne Université	Director
Prof. Jean-Marie Tarascon	Professor, Collège de France	Director



Except where otherwise noted, this work is licensed under
<http://creativecommons.org/licenses/by-nc-nd/3.0/>

Acknowledgements

Time flies. Three years have passed, since I started my PhD at College de France. Now, I take immense pleasure for the chance to thank the people whom I am indebted for their help and enriching my experience during this time.

First and foremost, I would like to thank Prof. Jean-Marie Tarascon. He not only introduced me to the fascinating world of batteries, but also has helped me with his invaluable guidance and fascinating encouragement. He is a person of immense enthusiasm and wisdom. His dedication and push for research and questioning towards fundamental science is invaluable and rewarding. Looking back, it was a rich and wonderful experience to work under his guidance, which will motivate me for the rest of my life. I feel very fortunate to be a part of this lab.

I would like to thank Dr. Gwenaëlle Rousse also, for her constant help and guidance. Especially, because of her guidance I could learn and carry out the crystallography works, which has been an indispensable part of this thesis. Thanks a lot for your help during the whole PhD.

I would like to thank Dr. Ignacio Blazquez Alcover also, for working with me during my initial time in the lab and helping me to settle in the lab. In this chance I would like to thank Dr. Daniel Alves Dalla Corte also who helped me (with his friendliness) during these years.

I would like to express my sincere thanks to Gaurav Assat also for his help during my work on anionic redox. He not only took time to show me tips and tricks to make batteries, but also constantly filled me with his ideas and suggestions. Without your help this thesis wouldn't be the same.

At this moment, I would like to thank Dr. Florencia Marchini for our work together in solid state batteries. It was a rich experience and also motivating for me sometime.

I would like to extend my gratitude to the RS2E network for funding my PhD. Thanks to its academic and industrial members for managing such an excellent collaborative network.

I must thank my collaborators- Prof Artem M. Abakumov, Dr Dominique Foix, Dr Moulay Tahar Sougrati, Haifeng Li, Prof Jordi Cabana, Dr Yang Ha, Dr Wanli Yang, Dr François Fauth, Dr Vladimir Pomjakushin, Jean Vergnet, and so on. Because of their expertise, this thesis work found completeness and thanks a lot for their contributions and help to extend my scientific knowledge.

It was indeed a cheerful experience to work around such dynamic and intelligent people in the lab. My sincere thanks to Paul Pearce, Nicolas Dubouis, Pierre Lemaire, Benjamin Campech, Sathiya Mariappan, Jean, Florencia, Marc Duchardt, Thomas Marchandier, Qing Wang, Wei Yin, Laura Albero-Blanquer, Fanny Betermier, Soma Turi, Alexis Grimaud, Marie Francine Lagadec, Claudio Cometto, Biao Li, Chunzhen Yang, Antonella Iadecola, Jiwei Ma, Vanessa Perreira Pimenta, Iban Azcarrate, Jiaqiang Huang, Lukas Lutz, Jessica Duvosin and others for helping me in various ways and contributing

to cheerful mood. Thanks to the other lab members also. With such an international and collaborative working environment, science and research becomes very smooth and enjoyable.

I would also like to thank Prof Silke Biermann and Dr Valérie Pralong for their time to review this thesis, and also to Prof Christel Laberty-Robert, Prof Philippe Barboux, and Prof Artem Abakumov for being part of the jury.

Finally, on more personal note, I would like to thank Frédéric Lavaud, Sumit Sarkar, and all my friends here, and also to Maison de L'Inde. Thanks also to my old teachers, supervisors and friends. Finally and most importantly, I would like to dedicate this work and effort to my Family for everything they have done for me. Without their silent love, encouragement and support, I could not go forward with science and research.

Table of Contents

Acknowledgements	i
Table of Contents	iii
Broader context and thesis overview	1
○ Thesis Outline	2
Chapter I. Brief introduction to the battery technologies	5
I.1 Brief overview of Li-battery technology	6
I.1.1 Early Li-metal batteries with sulfide cathodes.....	6
I.1.2 Li-ion batteries with oxide cathodes for higher voltage	7
I.1.3 Anionic redox to push capacity limits	9
I.2 From LIBs to all-solid-state batteries (ASSBs)	14
I.2.1 Why all-solid-state batteries	14
I.2.2 Battery technologies using solid electrolytes (SEs)	15
I.2.3 Requirements for ASSBs	15
I.3 Evolution of solid electrolytes (SEs)	17
I.3.1 Journey towards conductivity surpassing liquid electrolytes.....	17
I.3.2 State of the art.....	19
I.3.3 Design principle of superionic conductors	22
I.3.4 Choosing the electrolyte: Oxides or Sulfides ?.....	27
I.4 Progress in full ASSBs	30
I.5 Chapter Conclusions	31
Chapter II. Searching Ionic Conductors in the Li(Na)-Zn-P-O phase diagram	33
II.1 Chapter Introduction	34
II.2 $\text{Li}_6\text{Zn}(\text{P}_2\text{O}_7)_2$	35
II.2.1 Probing the polymorphism with temperature	35
II.2.2 Structural solution of ordered α -phase.....	37
II.2.3 Structural solution of disordered ζ -phase.....	38

II.2.4	Influence of disorder on ionic conductivity	41
II.2.5	Mechanism of Li-conduction from BVEL calculations	43
II.3	Li₄Zn(PO₄)₂	44
II.3.1	Crystal structure of Li ₄ Zn(PO ₄) ₂	45
II.3.2	Order-disorder transition with temperature	46
II.3.3	Structural solution of the β -polymorph	47
II.3.4	Stabilization of β -phase by ball-milling	49
II.3.5	Stabilization of β -phase by aliovalent substitution	50
II.3.6	Structural solution of the Ga-substituted phases	51
II.3.7	Transition in Ionic Conductivity	54
II.3.8	Higher conductivity in RT-stabilized phases	56
II.3.9	Conduction mechanism	58
II.4	Na₄Zn(PO₄)₂	61
II.4.1	Polymorphism in Na ₄ Zn(PO ₄) ₂	61
II.4.2	Structural solutions	63
II.4.3	Stabilization of the β -polymorph.	66
II.4.4	Ionic Conductivity transition in pristine Na ₄ Zn(PO ₄) ₂	69
II.4.5	Higher conductivity in Ga/Al-substituted β -phases	70
II.5	Chapter Conclusions.	72
 Chapter III. Sulfide-based cathode materials: Anionic redox in Li-rich sulfides.....		75
III.1	Chapter Introduction	76
III.2	Pseudo-layered TiS₃.....	77
III.2.1	Synthesis of TiS ₃	78
III.2.2	Structural characterizations: a different variant of TiS ₃	79
III.2.3	Electrochemistry of TiS ₃	82
III.2.4	Evolution of crystal structure during discharge-charge	83
III.2.5	Tracking oxidation states during Li (de)intercalation.....	87
III.2.6	Practicability of the anionic redox	90
III.3	Li-rich layered sulfides	92
III.3.1	Li ₂ TiS ₃	92
III.3.1.1	Structural Characterizations	92
III.3.1.2	Electrochemical activity	93
III.3.2	Fe ²⁺ -substituted Li ₂ TiS ₃	94
III.3.2.1	Structural Characterizations	94

III.3.2.2	Electrochemical Properties.....	97
III.3.2.3	Cycling behaviour over larger voltage range	100
III.3.2.4	Structural integrity during charge-discharge.....	101
III.3.2.5	Crystal structures of charged-discharged phases.....	103
III.3.2.6	Charge compensation mechanism.....	106
III.3.2.6.1	Cationic redox process.....	106
III.3.2.6.2	Anionic redox process	110
III.3.3	Discussions.....	113
III.4	Expanding the S-redox chemistry	115
III.4.1	Ti ³⁺ -substituted Li ₂ TiS ₃	115
III.4.2	Co ²⁺ -substituted Li ₂ TiS ₃	116
III.4.3	Na ₂ TiS ₃	117
III.5	Chapter Conclusions	118
Chapter IV. Practicability of Anionic redox in Li-rich sulfides		119
IV.1	Chapter Introduction	120
IV.1.1	Voltage hysteresis	120
IV.1.2	Electrochemical Kinetics.....	125
IV.1.3	Voltage fade	128
IV.1.4	Na ₂ TiS ₃	130
IV.2	Chapter Conclusions	132
Chapter V. Application of Sulfide-based Cathode materials in All-Solid-State Batteries		135
V.1	Chapter Introduction.....	136
V.2	Designing a cell for ASSB assembly.....	137
V.3	Protocol to fabricate ASSB in the setup	138
V.4	Solid electrolytes used for ASSB	138
V.5	Cycling results of ASSBs.....	141
V.5.1	Cycling with glassy LPS SE.....	142
V.5.2	ASSB with β -Li ₃ PS ₄ SE.....	143
V.5.3	EIS study of the ASSB.....	144
V.6	Chapter Conclusions.....	145

Chapter VI. General Conclusions	147
Appendix.....	A-1
A1 Supporting Information for Chapter II.....	A-2
A1.1 Methods.....	A-2
A1.2 Supporting Figures	A-7
A1.3 Supporting Tables	A-13
A2 Supporting information for Chapter III	A-19
A2.1 Methods.....	A-19
A2.2 Supporting Figures.....	A-22
A2.3 Supporting Tables	A-34
A3 Supporting Information for Chapter IV	A-40
A3.1 Methods.....	A-40
A3.2 Supporting Figures	A-40
A4 Supporting Information for Chapter V.....	A-43
A4.1 Supporting Figures	A-43
List of Figures.....	F-i
List of Tables	T-i
List of Publications	P-i
References.....	R-i

Broader context and thesis overview

The global energy demand is rising every year and projected to increase by ~56% between 2010 and 2040 (Figure 1a).¹ To meet this energy demand, consumption of all fuels is accelerated, with fossil fuels meeting ~70% of the growth. As a result, global energy-related CO₂ emissions is soaring at an alarming rate (by 1.7% in 2018). In efforts to limit the climate change, ‘clean’ electricity is being projected as the “fuel” of the future, and utilization of renewable energies is growing fast to meet the increase in demand for electricity (Figure 1b).

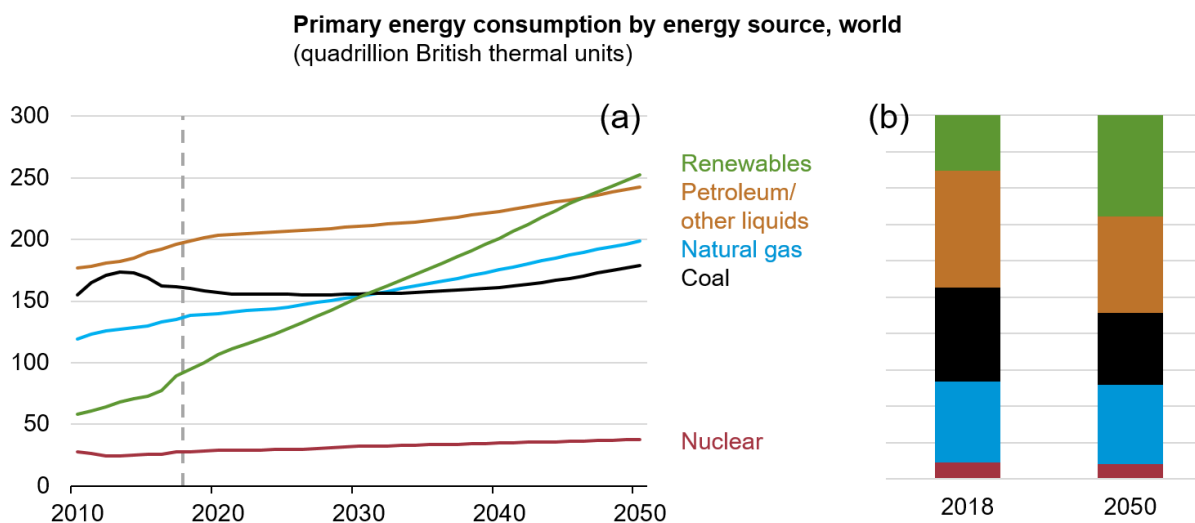


Figure 1. Worldwide energy consumption from various sources. (a) The projection by year, and (b) their share (in percentage) of energy sources. Figure adapted from *International Energy Outlook 2019*.¹

Energy storage systems (ESS) are the basis for this future transformation, as they ensure energy availability when the wind is not blowing and the sun is not shining. Various ESS, such as, batteries, flywheel, pumped water storage, compressed air energy storage, etc., have been developed in the past.² Amongst them, batteries, specifically rechargeable Li-ion batteries (LIBs) outperform other systems, thanks to its high specific energy (250 - 300 Wh·kg⁻¹), while also providing a high specific power.³ Historically, portable electronics have been the primary driving force for the LIB market, however, today the demand comes from electric vehicles (EVs) also. Furthermore, to enable large-scale energy storage for grids, etc., not only increasing the energy density, but also the safety (more important for EVs) of the LIBs, have become important. This thesis aims to contribute towards the cathode materials of LIBs, and all-solid-state Li-batteries which will be outlined below.

○ Thesis Outline

This work is divided into six Chapters, they consist, which are detailed below:

Chapter I briefly introduces the current Li-ion battery (LIB) and future ‘all-solid-state battery’ (ASSB) technology. The new phenomena ‘anionic redox’ will be explained and its associated ‘limitations’ will be identified. It is followed by a discussion on requirements for ASSBs, which

highlights the importance to act on solid electrolytes (SEs) and the ‘interface’ of SE-cathode material in ASSBs.

Chapter II focuses on designing new oxide-based SEs, more specifically by stabilization of disordered high-temperature phases (HTPs) at room temperature (RT) within the Li-Zn-P-O phase diagram. The phases $\text{Li}_6\text{Zn}(\text{P}_2\text{O}_7)_2$, $\text{Li}_4\text{Zn}(\text{PO}_4)_2$ and $\text{Na}_4\text{Zn}(\text{PO}_4)_2$ were chosen for this study. Their structural transition accompanied by the increase of ionic conductivity has been characterized. Then the stabilization of their HTPs by means of chemical substitution and mechanochemical treatment (ball-milling) has been shown.

Chapter III deals with designing sulfide-based cathode materials that involves anionic sulfur-redox to increase energy density of the LIBs. First we revisited TiS_3 for its structural aspects and practicability as an anionic redox compound. Next, we designed a new family of Li-rich layered sulfides $\text{Li}_{1.33-2y/3}\text{Ti}^{4+}_{0.67-y/3}\text{Fe}^{2+}_y\text{S}_2$ (i.e., Fe^{2+} substituted $\text{Li}_2\text{Ti}^{4+}\text{S}_3$) and unveiled the benefits of sulfur redox. Furthermore, we extended our studies to other Li/Na-rich sulfides.

Chapter IV presents practical assessment of anionic redox in Li-rich sulfides. We systematically benchmarked the performance of the Li-rich sulfides against Li-rich NMC oxide via detailed electrochemical analysis.

Chapter V shows application of the Li-rich sulfide $\text{Li}_{1.13}\text{Ti}_{0.57}\text{Fe}_{0.3}\text{S}_2$ ($y = 0.3$ composition) as cathode material in ASSB.

To conclude, Chapter VI summarizes the findings of this thesis together with its impact with respect to application.

Furthermore, an Appendix section can be found at the end, that includes the experimental methods and additional figures and tables.

Chapter I

Brief introduction to the battery technologies

I.1 Brief overview of Li-battery technology

Development of portable devices and electronics has been accelerated in last few decades. In addition, growing need for green mobility has led to emergence of electric vehicles (EVs). EVs, in combination with renewable energies, are important to tackle the global mobility needs. Batteries are a key enabler to limit the CO₂-emission, and recent market developments of batteries strongly reflect this. The competitive market of electronics and EVs present a strong motivation to work on the development of ‘better’ batteries with increased energy and power density, with more safety, at a lower cost. Among a wide range of energy storage systems, rechargeable lithium-ion batteries (LIBs), are currently the dominant technology for powering portable devices, mostly due to their capability of delivering electrical energy with high power and energy densities.^{4,5} A battery is a system consisting in a positive and a negative electrode, separated by an ionically conducting electrolyte. The external circuit allows for the flow of electrons, while the internal electrolyte solution allows for the flow of ions. Simultaneous electrochemical reactions at the two electrodes lead to energy storage or release (charge or discharge), depending on the direction of flow of electrons. In the next section we will introduce the Li-battery technology followed by its transition to ‘next-generation’ all-solid-state batteries.

I.1.1 Early Li-metal batteries with sulfide cathodes

Sulfide based electrodes played a crucial role to pave the way for today’s Li-battery technology. The oil crisis in early 1970s had prompted serious investigations on renewable solar, wind, and domestic fossil fuels as alternative power source.⁶ However, the intermittency of these power sources, together with the emergence of portable electronic products, sparked worldwide research for energy storage system, especially for rechargeable batteries.^{7,8} In 1975, transition-metal (TM) chalcogenide TiS₂ was first reported by Whittingham, as Li insertion host (Figure I.1a) for Li-metal batteries.⁹ The Li/TiS₂ system shows excellent reversibility of Li-intercalation for Li_xTiS₂ with 0 < x < 1, according to the reaction scheme,



Furthermore, other Li-free 3d/4d TM-chalcogenides, such as MoS₂ VSe₂, NbSe₃ etc., were identified for reversible Li-intercalation.^{9–11} Among such Li-metal batteries, Li/TiS₂ (at EXXON) and Li/MoS₂ (at Moli Energy) system was initially considered very promising.^{8,12} However, due to the safety risks originated from the dendritic lithium growth at the metallic-Li anode, the EXXON’s batteries could not be commercialized and Moli’s batteries had to be recalled from the market after fire accidents.^{12,13}

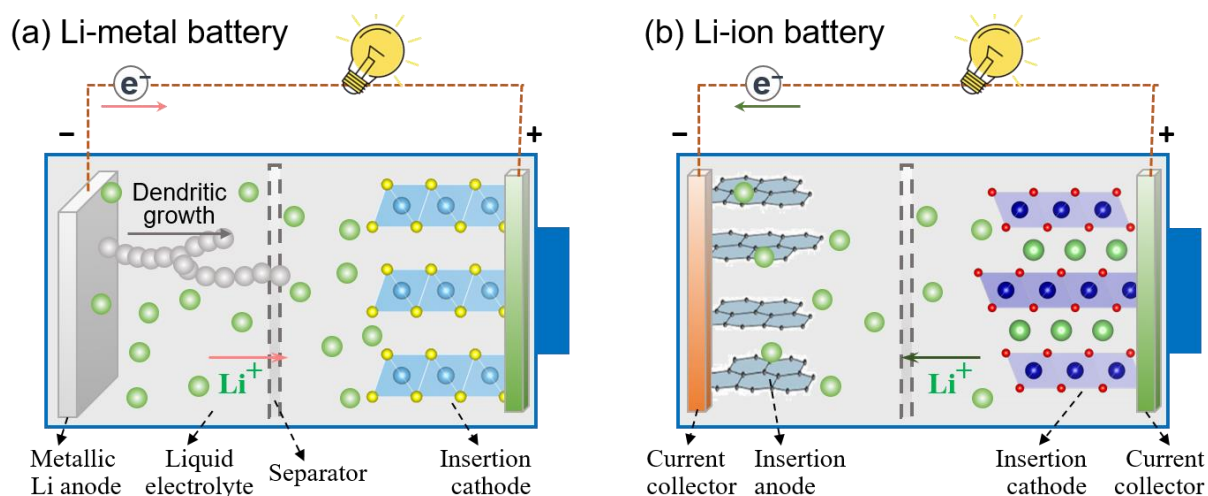
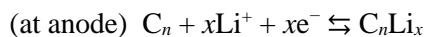
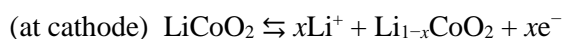


Figure I.1. Schematic configuration of Li-metal and Li-ion batteries. (a) Li-metal battery with Li-free insertion cathode (e.g., TiS_2) and Li metal anode, which shows dendritic Li growth that can cause short-circuit. (b) Li-ion battery having a Li-containing insertion cathode (e.g., LiCoO_2) with an insertion anode (i.e., graphitic-carbon) material.

I.1.2 Li-ion batteries with oxide cathodes for higher voltage

Even though early Li-metal batteries were rapidly terminated, research for safer and viable Li-battery system was intense. In 1979, Goodenough proposed LiCoO_2 as a Li-insertion host which demonstrated successive Li deintercalation-intercalation for $\text{Li}_{1-x}\text{CoO}_2$ with $0 < x < 0.5$.^{14,15} Furthermore, as LiCoO_2 contains Li, the metallic Li metal anode was not needed anymore and use of graphite was proposed as Li-insertion anode.¹⁶ This led Akira Yoshino (at the Asahi Kasei Corporation) to use carbonaceous materials (with a certain crystalline structure that does not decompose in organic propylene carbonate (PC) electrolyte, e.g., vapor phase grown carbon fiber¹⁷) as Li-insertion anode and demonstrated the first Li-ion rechargeable battery in 1986 (see Figure I.1b), according to the reaction scheme shown below.^{18–20} This configuration of LIB was commercialized by Sony in 1991.^{8,19,20}



Followed by the successful demonstration by layered LiCoO_2 , electrochemical properties were discovered in other family of compounds, such as, ‘spinel’ LiMn_2O_4 and ‘polyanionic’ LiFePO_4 , etc., and also in other layered oxides.^{4,21} Amongst the compounds, majority of today’s batteries still use LiCoO_2 , and its derivatives as positive electrode. Both TiS_2 and LiCoO_2 has similar layered crystal structure (Figure I.1) and Li-(de)intercalation in them is charge compensated by cationic redox, i.e., the redox of the transition metals ($\text{TM}^{n+/n+1}$). The voltage profiles of the sulfide and oxide electrodes are illustrated by their schematic band positions in Figure I.2. In sulfides the cationic redox level ($\text{Ti}^{3+/4+}$) has a higher energy (i.e., closer to the Li/Li^+ redox level) than the cationic redox level ($\text{Co}^{2+/3+}$) in oxides.^{21,22} Consequently, low voltage can only be obtained from TiS_2 sulfide. The voltage difference is

reflected into their specific energies, as TiS_2 offers much lower ($\sim 450 \text{ Wh}\cdot\text{kg}^{-1}$) than the commercialized LiCoO_2 ($\sim 600 \text{ Wh}\cdot\text{kg}^{-1}$).

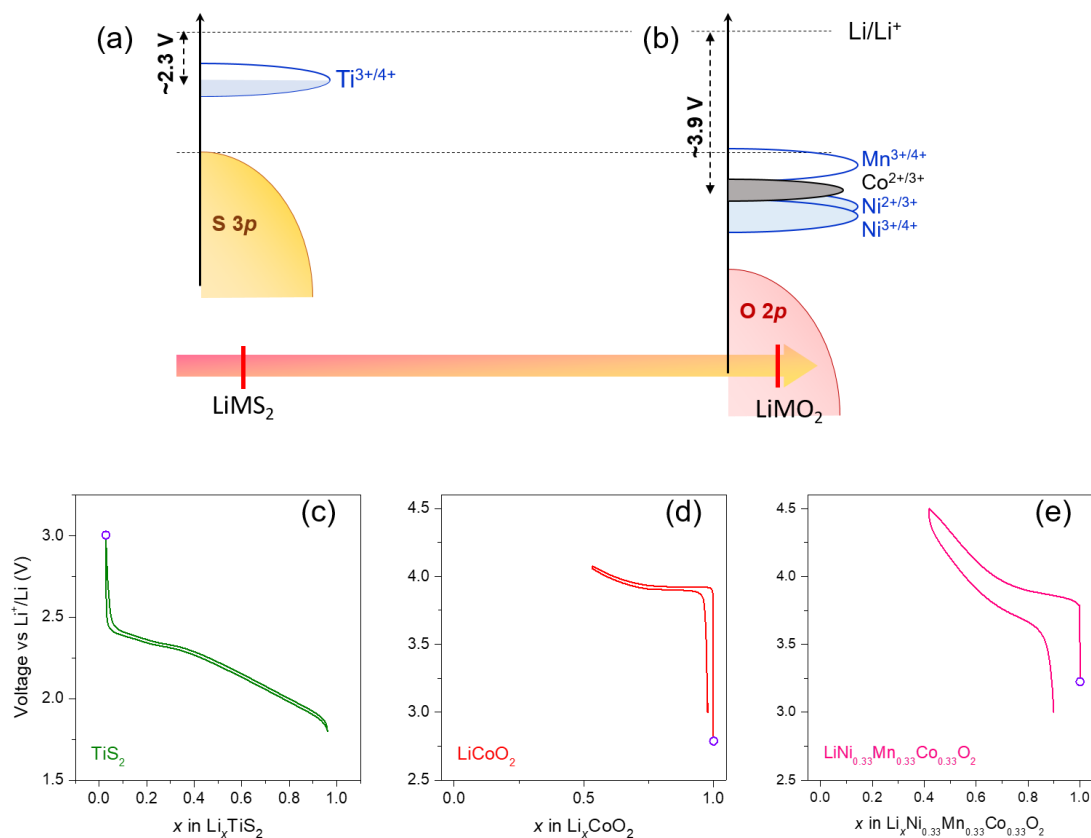


Figure I.2. Comparison of band positions and voltage profiles in LiMS_2 sulfides and LiMO_2 oxides. Simple schematics of the band positions of $\text{LiTi}^{3+}\text{S}_2$ (a) and LiCoO_2 (b) are shown. The relative band positions are estimated based on references^{23,24}. The voltage profiles (1st cycle) of TiS_2 , LiCoO_2 (LCO), and $\text{LiNi}_{0.33}\text{Mn}_{0.33}\text{Co}_{0.33}\text{O}_2$ (NMC) are shown in c-d. The purple circles show the starting points. TiS_2 was discharged first (starting with $x = 0$) and LCO and NMC were charged first (starting with $x = 1$).

Despite low operating potential, the increased covalency in sulfides than in oxides plays a crucial role. In LiCoO_2 , only ~ 0.5 Li can be reversibly (de)intercalated (i.e., capacity up to $\sim 140 \text{ mAh}\cdot\text{g}^{-1}$), as more Li extraction leads to gradual collapse of the O3 lattice structure.^{25,26} LiNiO_2 with similar crystal structure could deliver a capacity $>150 \text{ mAh}\cdot\text{g}^{-1}$, however its thermal instability posed a major safety drawback.²⁷ Contrarily, in TiS_2 , fully ~ 1 Li can be intercalated reversibly (i.e., capacity up to $\sim 220 \text{ mAh}\cdot\text{g}^{-1}$), because of the robustness of the crystal structure due to greater covalency and bigger size of the S atoms.

The limited capacity could be pushed further by designing compounds such as $\text{Li}[\text{Ni}_{1-y-z}\text{Mn}_y\text{Co}_z]\text{O}_2$ (NMC), and $\text{Li}[\text{Ni}_{1-y-z}\text{Co}_y\text{Al}_z]\text{O}_2$ (NCA) etc. This was made possible by partially replacing Co with Ni/Mn or by Ni/Al. The crystal structures of the LCO and NMC are compared in Figure I.3, which show that the Co is partially mixed with Ni/Mn in the metallic layer. “NMC 111” ($\text{LiNi}_{1/3}\text{Mn}_{1/3}\text{Co}_{1/3}\text{O}_2$, with equal parts of TM in metal layer) was reported in 2001, which showed reversible capacity of $>150 \text{ mAh}\cdot\text{g}^{-1}$.²⁸ In subsequent years the capacity in NMC could be increased by

leading to unprecedented capacity of $>270 \text{ mAh}\cdot\text{g}^{-1}$ for $\text{Li}_{1.2}\text{Ni}_{0.13}\text{Mn}_{0.54}\text{Co}_{0.13}\text{O}_2$, which is known as today's Li-rich NMC (Figure I.4b).^{35,36} Note that in this Li-rich phases Mn^{4+} remains redox-inactive throughout charge and discharge, while the $\text{Ni}^{2+/3+/4+}$ and $\text{Co}^{2+/3+}$ redox can only account for part of the capacity (denoted by blue dotted circle in Figure I.4b,d).

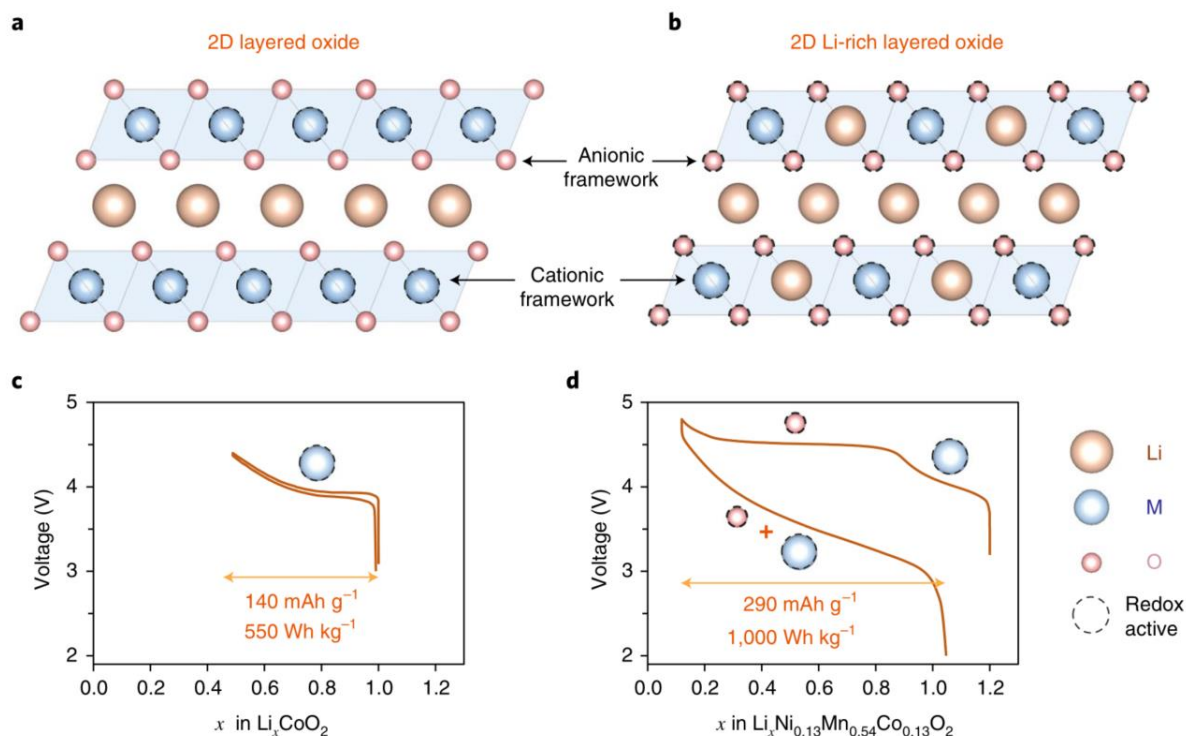


Figure I.4. Illustrating cationic and anionic redox. In Li-stoichiometric layered oxides, such as LiCoO_2 (a), only transition metals (TM) are redox active (indicated by blue dotted circle). The Li-rich layered oxides, such as $\text{Li}_{1.2}\text{Ni}_{0.13}\text{Mn}_{0.54}\text{Co}_{0.13}\text{O}_2$ (Li-rich NMC) (b) that contains extra Li within the metal layers, both TMs and the ligand O atoms (indicated in pink color) are redox active. The corresponding voltage profiles (c and d) indicate a near-doubling of capacity and specific energy for the Li-rich NMC due to cumulative cationic and anionic redox processes. Figure reproduced from reference³⁷.

Thanks to a decade of intense research, it is now well established that the anomalous extra capacity of Li-rich cathodes arises from the redox of O^{2-} anions (denoted by red dotted circle in Figure I.4b,d), more specifically the ‘non-bonding’ O 2p orbitals that point towards excess-Li in the metal layers.^{23,38–42} This new redox has been termed as ‘anionic redox’ which has emerged as a new paradigm to design higher energy Li-rich cathode materials. Invigorated by this fundamental understanding, solid-state chemists have extended the concept of oxygen redox to cation-disordered $\text{Li}_{1+y}\text{M}_{1-y}\text{O}_2$ ($\text{M} = \text{Nb}, \text{Mn}, \text{Ti}, \text{Fe}, \text{V} \dots$) as well as Na-based layered oxides.^{43–45}

Despite this rich materials design-space, certain practical issues, such as voltage fade, poor kinetics, voltage hysteresis, and irreversible O_2 loss, have delayed the commercialization of Li-rich NMCs.^{37,46,47} As shown in the voltage profile of Li-rich NMC in Figure I.5a, the staircase charging profile converts to S-shaped discharge profile in the 1st cycle (known as ‘activation cycle’) with a large

irreversibility of >0.25 Li, along with huge voltage hysteresis. Furthermore, the voltage fades continually in long cycling. In 2013, Sathiya *et al.* reported the electrochemical behavior of the $\text{Li}_2\text{Ru}_{1-y}\text{Sn}_y\text{O}_3$ solid solution that possesses a similar voltage profile (Figure I.5b).⁴⁸ But, due to increased covalency of Ru–O bonds, a reversible capacity $>200 \text{ mAh}\cdot\text{g}^{-1}$ could be obtained with good capacity retention and very little voltage decay. Although the crucial role of oxygen redox towards these issues was clearly highlighted by detailed investigations on a ‘practical’ Li-rich NMC and also on a ‘model’ $\text{Li}_{1.33}\text{Ru}_{0.5}\text{Sn}_{0.17}\text{O}_2$ electrode, much remains to be understood for further fundamental insights that will ultimately lead to implementable solutions.^{37,49,50} Moving further down to $5d$ Ir, the oxygen redox could be stabilized in α - Li_2IrO_3 .⁵¹ Pearce *et al.*, reported the electrochemical properties of β - Li_2IrO_3 which has a layered 3D structure and it showed negligible voltage hysteresis due to the increased covalency of Ir–O bonds and robustness of the crystal structure.^{52,53} Another approach was increasing the Li-rich character to access higher capacity in Li_3IrO_4 .⁵⁴ More recently, a third approach with mild success has emerged, that is to tune the ligand by increasing electronegativity of the anionic sublattice via substituting fluorine for oxygen, but so far limited only to disordered rocksalt structures.^{55,56}

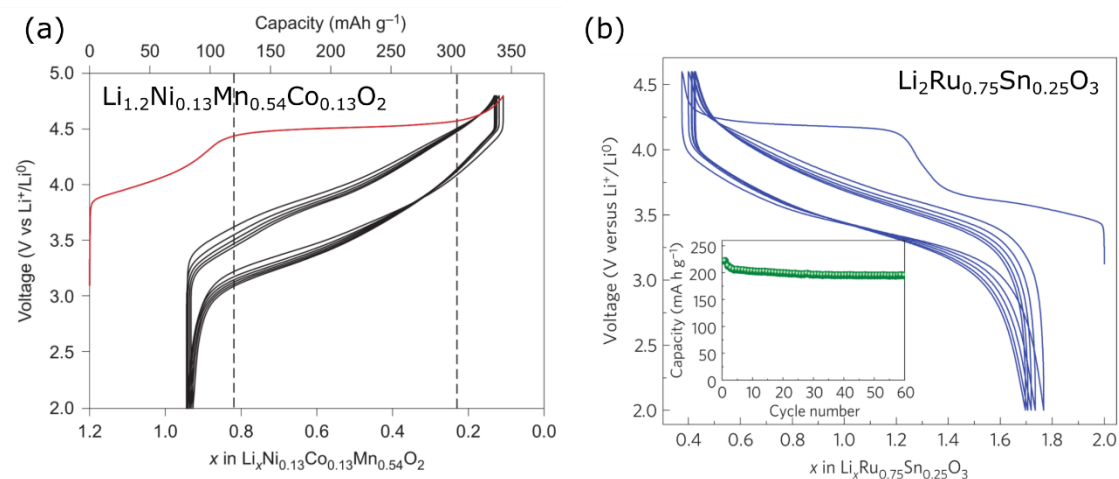


Figure I.5. Voltage profiles of some Li-rich oxides. Figures are reproduced from references^{23,48}.

Now the question arises, that under what circumstances the ‘non-bonding’ O $2p$ orbitals take part in ‘anionic’ redox? Over the past five years, experimental and theoretical studies have correlated the origin of anionic redox as arising from oxygen lone-pair states to the compound’s electronic structure. In classical layered oxides (LiMO_2), the redox is limited to the oxidation/reduction of antibonding M–O^* levels (often called as $\text{M } d$ band for simplicity sake), which remains mostly cationic by nature (Figure I.6a). In compounds having higher O/M ratios, e.g. Li-rich Li_2MO_3 (i.e., $\text{Li}[\text{Li}_{1/3}\text{M}_{2/3}]\text{O}_2$), one of the O $2p$ orbitals (the one pointing towards Li in the $[\text{Li}_{1/3}\text{M}_{2/3}]\text{O}_2$ layer) is weakly bonded because of its relatively small overlap with the Li $2s$ orbital. Hence, it behaves like an O non-bonding state and is located above the stabilized (M–O) bonding band (Figure I.6b). This non-bonding O $2p$ orbital can donate electron once the (M–O) * is emptied, without destabilizing the structure. But the reversibility of the anionic redox depend on relative band positioning of (M–O) * antibonding and O $2p$ non-bonding bands. To describe, we need to introduce the d - d Coulomb

interaction term U , that splits the partially filled $(M-O)^*$ band due to on-site electron repulsion within the d orbitals, as known as Mott-Hubbard splitting, leading to empty upper- and filled lower-Hubbard bands (UHB and LHB, respectively). Depending on the relative values of U vs. Δ (the energy difference between $(M-O)$ and $(M-O)^*$), three different scenarios can occur.

(1) $U \ll \Delta$, electrons are extracted from the filled LHB, as observed in case of classical one-band cationic redox (Figure I.6c). Widely applies to oxides and fluorides having highly ionic (large Δ) M-L bonds (L being the ligand).

(2) $U/2 \approx \Delta$, resulting in overlapping LHB and O $2p$ non-bonding bands, that are simultaneously available for electrochemical activity leading to reversible anionic redox (Figure I.6d).

(3) $U \gg \Delta$, when electrons are being removed directly from the non-bonding O $2p$ band situated above the filled LHB (Figure I.6d), where the highly reactive O^{n-} species formed upon charging may not be stabilized and oxygen loss occurs, as observed in Li_2MnO_3 .

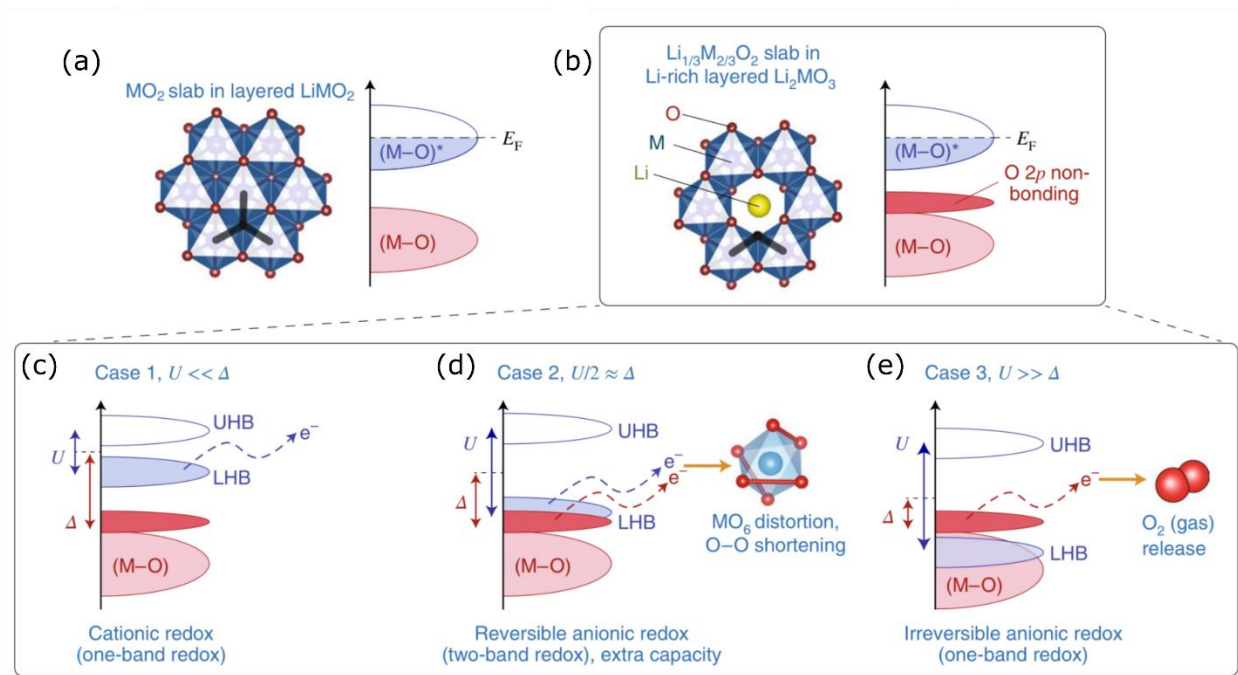


Figure I.6. Schematic band diagrams that governs the anionic redox. In $LiMO_2$ (a), no non-bonding O $2p$ exists, whereas in Li-rich $Li[Li_{1/3}M_{2/3}]O_2$ (b), O atoms are coordinated by only two metals, so that part of the O $2p$ orbitals that does not have the good symmetry to participate in M-O bonds and remain as pure O non-bonding states. (c-e) Different relative positioning of the band that control the redox. Figure taken from reference³⁷.

Hence for sustainable anionic redox, the second situation is favorable. The exemplary cases are evidenced in $Li_{1.33}Ru_{0.5}Sn_{0.17}O_2$ or in Li_2IrO_3 , as shown before. This is a result of increased covalency in the $4d/5d$ metals, leading to lower energy difference between M d and O p orbitals (i.e., lower Δ). Now, instead of adjusting the metal d level, another direction to lower the Δ consists in raising the ligand p level, by replacing the oxygen with ligands X = S, Se, Te, etc., that has lower electronegativity compared to O. Taking the case of sulfides (X = S), the S $3p$ band, having a higher energy than the O $2p$ band (i.e.,

S 3p band is closer to the Li/Li⁺ redox level), can help for reversible anionic redox, however with a lower voltage. Hence, when designing a Li-rich layered sulfides alike the oxides, the S 3d band will largely overlap with the M d bands, see Figure I.7a,b. In fact, sulfide like LiCoS₂ cannot form, since the high-energy sulfur 3p bands will pour electrons into the low-lying Co 3d bands, which can also be interpreted as the oxidation of S²⁻ by Co, resulting into the (S—S)²⁻ dimer.⁵⁷ Further intercalation of lithium ions into CoS₂ will generate metallic Co and Li₂S, via conversion reaction.^{58–60} Hence, for Li intercalation, only few light transition metals (left side of the periodic table), e.g., Ti, and V, etc., can combine with sulfur, as the 3d redox level of these metals are situated above the S 3p band (Figure I.7b).²⁴ Works on anionic redox in sulfides will be carried out as a part of this thesis.

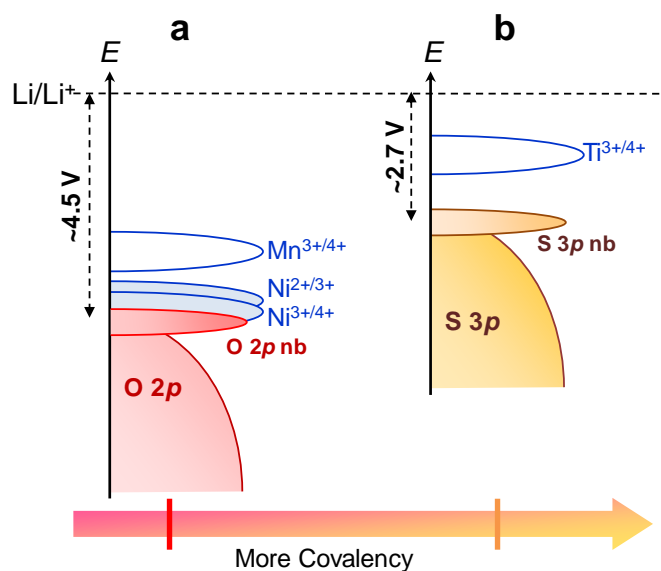


Figure I.7. Moving from Li-rich layered oxides to sulfides. Schematic band structure of Ni²⁺ substituted Li₂MnO₃ (a), and Li_{1.33}Ti_{0.67}S₂ or Li₂TiS₃ (b). The relative band positions are estimated based on references^{23,24}. The label *nb* stands for non-bonding.

Based on this findings, anionic redox chemistry was extended to Na-cathode materials. Na-rich layered oxide Na₂MnO₃ had drawn tremendous attraction, as shown by theoretical studies.^{61,62} Interestingly, for Na, despite having larger ionic radius than Li, similar migration barrier (~0.7 eV) was predicted due to elongated Na–O bond. Furthermore, possibility of better performance was predicted for Na₂MnO₃, because of enhanced electronic conductivity, for smaller band gap that arises from weaker octahedral crystal field.⁶¹ However, experimentally the Na-rich Na₂MnO₃ could not be synthesized yet.⁶³ Rather, phases with Li or vacancy (□) in place of Na in the metal layer have been reported in literature, such as Na[Li_{0.2}Mn_{0.8}O₂], Na[Li_{0.2}Ni_{0.2}Mn_{0.6}O₂], Na_{0.57-x}[□_{0.14}Mn⁴⁺_{0.86}O₂], etc., that shows only cationic redox (with O3-type crystal structure, space group *C2/m*).^{45,64,65} Nevertheless, few phases, like Na_{0.67}[Mg_{0.28}Mn_{0.72}O₂], Na_{0.67}[Mn_{1-y}Zn_yO₂], and Na_{0.67}[Ni_{0.33}Mn_{0.67}O₂], etc., were reported which possess anionic redox capability (with P2-type crystal structure, space group *P6₃/mmc*).^{44,66–69} Along this line, in sulfides, NaCrS₂, NaCr_{1-y}Ti_yS₂, etc., were reported showing anionic activity.^{70,71} Interestingly, these studies reveal that excess Na is not required to activate oxygen redox, that demands further studies. Stoichiometric Na-rich layered Na₂MO₃ could be successfully synthesized, only by

moving to $4d$ or $5d$ TMs, such as Na_2RuO_3 , $\text{Na}_2\text{Ru}_{1-\gamma}\text{Sn}_\gamma\text{O}_3$, Na_2IrO_3 , $\text{Na}_{1.2}\text{Mn}_{0.4}\text{Ir}_{0.4}\text{O}_2$ etc.^{72–77} Contrarily, sulfides show the possibility to be synthesized as Na-rich Na_2TMS_3 with $3d$ metals, as recently electrochemical properties of Na_2TiS_3 (O3-phase) were reported,^{78,79} that will be discussed later as a part of this thesis.

I.2 From LIBs to all-solid-state batteries (ASSBs)

I.2.1 Why all-solid-state batteries

In addition to the ongoing efforts to further increase the energy density of Li-ion batteries (LIBs), their safety has raised more serious safety concerns. Steps to increase energy density by raising the upper cutoff voltages (that causes poorer stability of electrode-electrolyte interfaces),⁸⁰ using ultrathin ($< 10 \mu\text{m}$) polymeric separators (despite reinforcements using ceramic materials),⁸¹ etc. have exposed more vulnerability toward internal short circuits and thermal runaway. Even though today's LIBs and battery management systems (BMS) are well-advanced to prevent the flammability of the liquid electrolytes, several news of fires due to LIBs have been reported in the last decade (Figure I.8).^{82–84} Furthermore, the push for large-scale applications of LIBs, such as batteries for electric vehicles, and grid energy storages, etc. imposed more safety requirements for LIBs.



Figure I.8. Reported pictures of LIBs causing fire in electronic devices and vehicles. Figures taken from references^{85–88}.

Therefore, replacing the conventional flammable organic liquid electrolytes with safer solid electrolytes (SEs) is considered to be an ideal solution, and bulk-type all-solid-state Li-ion batteries have been reinvestigated intensively in recent years.^{5,89,90} Several other advantages of solid electrolytes can be beneficial in this regards,

- 1) Possibility of electrochemical stability over higher voltages.^{91,92}
- 2) Longer cycle life, with low self-discharge.⁹³
- 3) Higher energy density, due to possibility of using Li-metal anode, and with other promising battery systems (e.g., Li-air, Li-S, etc.).⁹⁴
- 4) Capability of increasing cell-level energy density by designing ASSBs with stacked bipolar electrodes that allows minimization of inactive encasing materials.^{95,96} Next, we will describe how SEs could be incorporated in actual batteries.

I.2.2 Battery technologies using solid electrolytes (SEs)

Battery technologies using SEs can be traced long back. In 1967, researchers at Ford discovered in sodium β -alumina (with conductivity $\sim 10^{-3} \text{ S}\cdot\text{cm}^{-1}$) which successfully led to commercialization of high-temperature Na-S batteries operating at $\sim 300^\circ\text{C}$ (Figure I.9a).⁹⁷⁻⁹⁹ However, oxide materials like β -alumina are synthesized and sintered at very high temperatures ($>1200^\circ\text{C}$), to eliminate grain boundary resistance, and thus impose difficulties in the fabrication of batteries. In 1992, researchers at the Oak Ridge National Laboratory developed amorphous glassy SE LiPON (e.g., $\text{Li}_{3.3}\text{PO}_{3.8}\text{N}_{0.24}$) that was commercially utilized by various companies, e.g., Sakti3, Excellatron, etc., in thin film Li-microbatteries (Figure I.9b) with capacity of $\sim 10 - 50 \text{ mAh}$.¹⁰⁰ The LiPON has a low Li-conductivity ($2 \times 10^{-6} \text{ S}\cdot\text{cm}^{-1}$ at RT), but has good electrochemical stability and negligible interfacial resistance with both metallic Li and the transition metal cathodes.^{101,102} However, because of the high cost (synthesized by RF Magnetron deposition from Li_3PO_4 target in N_2) and low Li-conductivity, the applications of LiPON were limited to microbatteries. In contrast, in the last decade, the field have been revisited intensely in order to realize bulk-type ASSBs that can replace the traditional high-energy LIBs (Figure I.9c), which is quite challenging as will be described next.

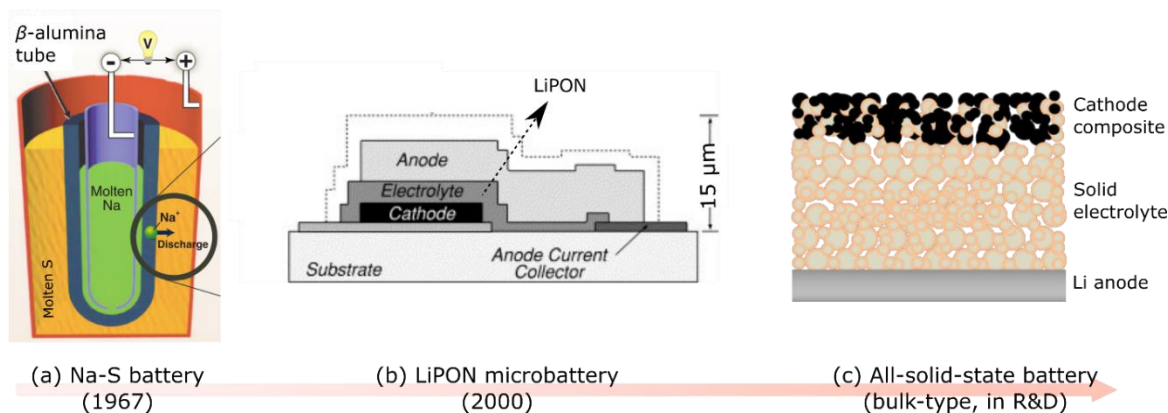


Figure I.9. Battery technologies using solid electrolyte. Na-S battery with molten-Na | β -alumina | molten-S configuration. Based on similar concept Na- NiCl_2 battery (so called ZEBRA battery) was also commercialized using molten- NiCl_2 cathode that operates at $\sim 250^\circ\text{C}$.^{99,103} (b) LiPON microbattery with LiCoO_2 or LiMn_2O_4 cathode and vapor-deposited Li or Sn_3N_4 anode with Si_3N_4 insulation casing (Vacuum deposition for all layers), and (c) all-solid-state battery for future commercialization. Figures in a-b are adapted from references^{99,100}.

I.2.3 Requirements for ASSBs

In bulk-type ASSB, the use of the SEs in powder form allows the adoption of battery configuration that was developed for LIBs. To comply with minimum requirements for a functional battery, the SEs must possess,

- 1) High ionic conductivity ($>10^{-4} \text{ S}\cdot\text{cm}^{-1}$ at RT)
- 2) A wide electrochemical stability window (preferably 0 - 5 V), and,

- 3) Excellent chemical stability with anode (Li-metal) and cathode materials.
- 4) Facile processing capability for ASSB fabrication

In this regard, as Li-ion conductivities for SEs (will be discussed in Section I.3) is comparable to liquid electrolyte ($>10^{-3} \text{ S}\cdot\text{cm}^{-1}$), ASSBs show potential to compete with conventional LIBs. To estimate the merit, the required thickness of the SEs can be calculated from Li-conductivity according to the equation,

$$R = \frac{1}{\sigma} \cdot \frac{l}{A}$$

where R is the resistance, σ is the conductivity, l is the thickness, and A is the area of the electrolyte. Therefore the required thickness range of the SE can be calculated to meet an estimated range of resistance comparable to liquid electrolytes. As shown in Figure I.10, thin ($< 40 \mu\text{m}$) layer of SEs are required. Therefore this task is challenging, and will require materials processing techniques such as thin film deposition, SE casting etc., in future.^{104–106} Nevertheless, the thickness can be increased further for SEs, because of its high Li-ion transference number t_+ , according to the relation $D^+ \propto \sigma \times t_+$, where D^+ is the diffusion coefficient of Li^+ ions. In SEs $t_+ \approx 1$ (i.e., only Li^+ moves, anions are immobile), whereas for liquid electrolytes typically t_+ in the range of 0.3 - 0.4.⁸¹

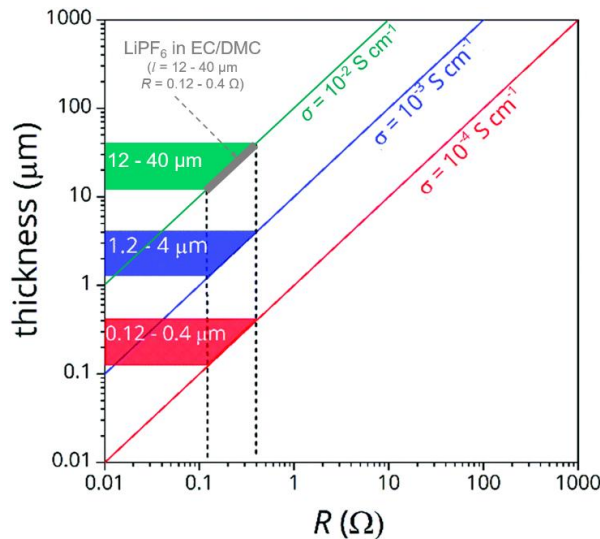


Figure I.10. Minimum thickness required for a SE to match the resistance of liquid electrolytes. LiPF_6 in EC/DMC with an area of 1 cm^2 was used for comparison. Note that the effect of Li-ion lithium-ion transference number t_+ was not accounted in the calculation. Figure adapted from reference¹⁰⁵.

But, the advantage of single-ion conducting character of SEs is often offset by difficulties in forming and maintaining intimate ionic contacts with active materials in the composite electrodes. Hence the need of sintering SEs prior to cycling and high pressure during the cycling of ASSBs. Furthermore the kinetic issues, such as, the interfacial impedance of the SE/electrode interface, space charge layer, etc., and chemical compatibility, e.g., inter-diffusion and chemical reactions interface must be considered. Overall, to achieve bulk-type ASSBs that show comparable performance with conventional

LIBs, several critical challenges must be addressed, thus highlighting the need of fundamental studies and exploration of various directions. As the SEs are the most important parameter, they will be discussed next, starting with its historical account till now.

I.3 Evolution of solid electrolytes (SEs)

I.3.1 Journey towards conductivity surpassing liquid electrolytes

The journey of ‘electrolytes’ is considered to be started way back in the 1830s, when Michael Faraday discovered ion conduction in solid materials. In 1834, the recorded remarkable property of conduction in heated solid Ag_2S and PbF_2 ,¹⁰⁷ as he described following,

“I formerly described a substance, sulfuret of silver, whose conducting power was increased by heat; and I have since then met with another as strongly affected in the same way: this is fluoride of lead. When a piece of that substance, which had been fused and cooled, was introduced into the circuit of a voltaic battery, it stopped the current. Being heated, it acquired conducting powers before it was visibly red hot in daylight; and even sparks could be taken against it whilst still solid.”¹⁰⁸

This was probably the first observations of transition (Figure I.11) from a poor conducting state to superionic conducting states in a materials which is now called ‘solid electrolytes’.¹⁰⁸ During this period, he discovered the motion of mobile ions in both liquid and solid electrolytes, which subsequently took two different paths of ‘*Electrochemistry*’ and ‘*Solid State Ionics*’.¹⁰⁸

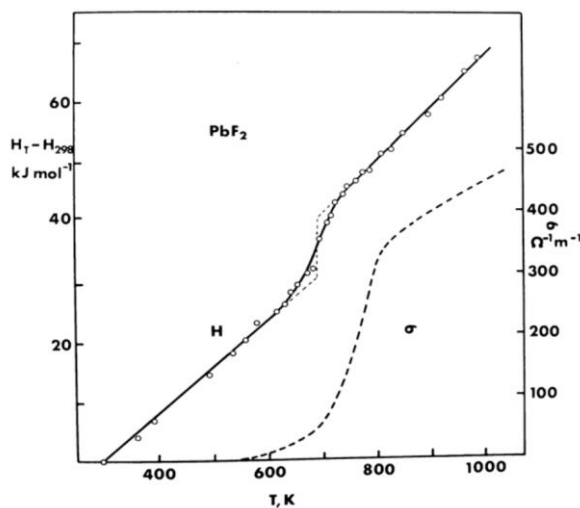


Figure I.11. Heat content (left y-axis) and ionic conductivity (right y-axis) of PbF_2 . Figure adapted from reference¹⁰⁸.

However, the 1960s are generally considered the turning point for solid electrolytes (SEs) when they were studied extensively. Subsequent development of SEs are outlined in Figure I.12. Though started with report of high Li-conducting Li_3N , discovery of fast 2D Na^+ -transport phenomenon in sodium β -alumina ($\text{Na}_2\text{O} \cdot 11\text{Al}_2\text{O}_3$) marked the era, as it was readily used for high-temperature Na-S batteries, as discussed earlier.^{97–99,109} Following this, Goodenough *et al.* in 1976, discovered the fast Na-

conduction in NASICON-type compounds ($\text{Na}_{1+x}\text{Zr}_2\text{Si}_x\text{P}_{3-x}\text{O}_{12}$, $0 \leq x \leq 3$).¹¹⁰ Inspired by this, Li-ion conductivity in NASICON-like structures was investigated, as Subramanian *et al.* reported a NaSICON-type $\text{LiTi}_2(\text{PO}_4)_3$ in 1986 (with an conductivity of $2 \cdot 10^{-6} \text{ S} \cdot \text{cm}^{-1}$ at RT).¹¹¹ The ionic conductivity of $\text{LiTi}_2(\text{PO}_4)_3$ could be further improved by partially substitution as the compounds $\text{Li}_{1.3}\text{Al}_{0.3}\text{Ti}_{1.7}(\text{PO}_4)_3$ (LATP) exhibits a conductivity of $7 \cdot 10^{-4} \text{ S} \cdot \text{cm}^{-1}$ at RT.¹¹² During this time sulfide-based solid electrolytes, especially glassy sulfides, were also investigated intensely. Binary $\text{Li}_2\text{S}-\text{P}_2\text{S}_5$ and $\text{Li}_2\text{S}-\text{SiS}_2$ glasses doped with LiI, were reported to possess ionic conductivity higher than $10^{-4} \text{ S} \cdot \text{cm}^{-1}$.¹¹³⁻¹¹⁷ The sulfide glasses, and also oxide glasses (e.g., $\text{Li}_{3.6}\text{Si}_{0.6}\text{P}_{0.4}\text{O}_4$, $\sim 10^{-6} \text{ S} \cdot \text{cm}^{-1}$ at RT) were mostly used for thin film batteries.^{117,118} Perovskite type $\text{Li}_{3x}\text{La}_{2/3-x}\text{TiO}_3$ was reported also with high conductivity.¹¹⁹ Thus, though this fruitful period has seen the discovery of many new Li-ion conducting compounds, the conductivities of these solid electrolytes were far behind practical utilization and this research fall into oblivion.^{101,110,120,121}

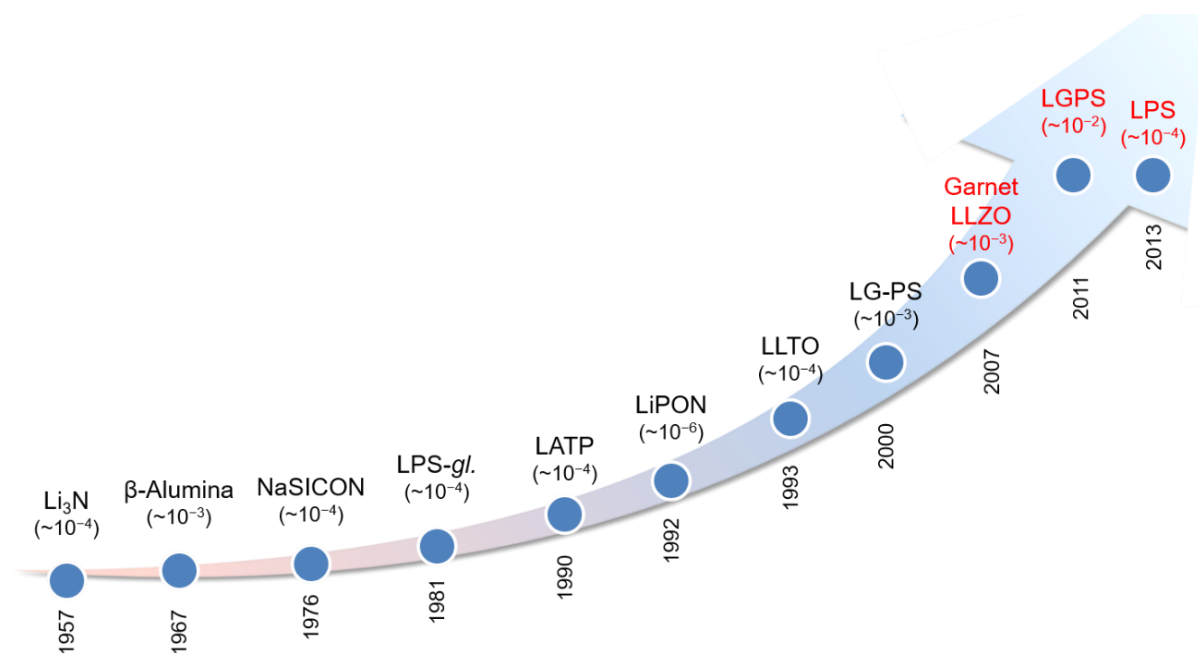


Figure I.12. Development of solid electrolytes towards superionic conductivity. The ionic conductivities (in $\text{S} \cdot \text{cm}^{-1}$) are indicated in the parentheses. Note that ionic conductivity comparable to liquid electrolytes was achieved in 2011. Based on references^{97-99,101,109-117,119-128}.

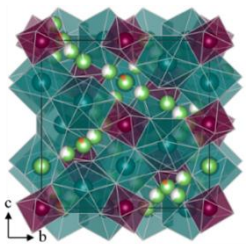
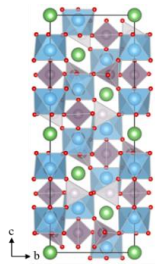
Recent safety issues of LIB's in the early 20th century and foreseen aspiration of industries has led researchers to re-visit the field intensely in the past decade and several new interesting compounds were found or their conductivities were improved.^{123,124} The conductivity of $\text{Li}_{1.3}\text{Al}_{0.3}\text{Ti}_{1.7}(\text{PO}_4)_3$ (LATP) could be much improved to of $1.12 \cdot 10^{-3} \text{ S} \cdot \text{cm}^{-1}$ at RT by using spark plasma sintering to decrease the grain boundary resistance.¹²² Garnet-type $\text{Li}_7\text{La}_3\text{Zr}_2\text{O}_{12}$ (LLZO) with a cubic structure was revisited in 2007 and a high ionic conductivity of $3.7 \cdot 10^{-4} \text{ S} \cdot \text{cm}^{-1}$ at RT was demonstrated,¹²³ which could be further improved to $>10^{-3} \text{ S} \cdot \text{cm}^{-1}$ at RT in 2013, by partial hypervalent substitution of Zr with Al, Ga, Ta, Nb, etc.^{129,130} However the ionic conductivities achieved ($\sim 10^{-3} - 10^{-6} \text{ S} \cdot \text{cm}^{-1}$) were still trailing behind the liquid electrolytes¹²⁵. In 2000, based on LISICON-type oxides, by replacing O with S, Kanno *et al.*

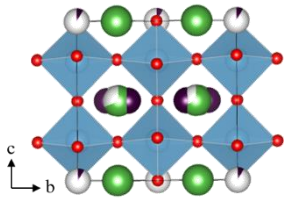
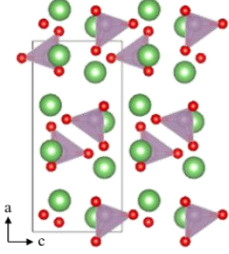
discovered a new crystalline material family $\text{Li}_{4-x}\text{Ge}_{1-x}\text{P}_x\text{S}_4$ (thio-LISICON) with conductivity of $2 \cdot 10^{-3} \text{ S}\cdot\text{cm}^{-1}$ at RT.¹²⁶ Along this family, it is only recently, the ionic conductivities comparable to the liquids ($\sim 10^{-2} - 10^{-3} \text{ S}\cdot\text{cm}^{-1}$) have been achieved with the discovery of thio-phosphates $\text{Li}_{11-x}\text{M}_{2-x}\text{P}_{1+x}\text{S}_{12}$ (M = Si, Ge, Sn). The $\text{Li}_{10}\text{GeP}_2\text{S}_{12}$ (LGPS), reported by Kanno and coworkers, exhibits a very high lithium ionic conductivity of $1.2 \cdot 10^{-2} \text{ S}\cdot\text{cm}^{-1}$ at RT.¹²⁷ Seino *et al.* (2014) reported a heat-treated glass-ceramic conductor $\text{Li}_7\text{P}_3\text{S}_{11}$ with an extremely high ionic conductivity of $1.7 \cdot 10^{-2} \text{ S}\cdot\text{cm}^{-1}$ at RT.¹³¹ Thus, improvement in ionic conductivities has been stellar, however, achieved only with few special crystal structure, which will be summarized in next section.

I.3.2 State of the art

Inorganic solid electrolytes (oxide and sulfide- based), can be crystalline, glassy, and glass-ceramics, and they are summarized here briefly in Table I.1 and Table I.2.

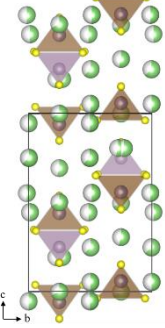
Table I.1. Different classes of oxide-based solid electrolytes (crystalline).^a

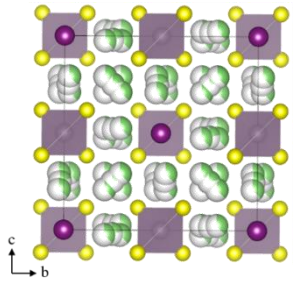
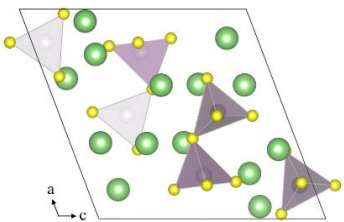
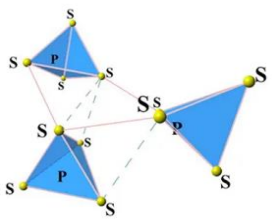
Solid Electrolyte	σ_{RT} ($\text{S}\cdot\text{cm}^{-1}$)	Performance
Garnet-type $\text{Li}_7\text{La}_3\text{Zr}_2\text{O}_{12}$ (LLZO) ^{123,129,130}  e.g., $\text{Li}_{7-3x}\text{M}'_x\text{La}_{3-x}\text{Zr}_2\text{O}_{12}$ (M' = Al^{3+} , Ga^{3+}) or, $\text{Li}_{7-x}\text{La}_3\text{M}''_{2-x}\text{Ta}_x\text{O}_{12}$ (M'' = Nb^{5+} , Te^{6+})	$\sim 10^{-3}$ - 10^{-4}	Pros- Electrochemical stability up to $\sim 5 \text{ V}^{92}$ High mechanical strength Thermally stable at HT Cons- Brittle in nature HT annealing for densification Does not wet Li metal
NaSICON-type $\text{LiM}_2(\text{PO}_4)_3$, M = Zr, Ti ^{112,132}  e.g., $\text{Li}_{1.3}\text{Al}_{0.3}\text{Ti}_{1.7}(\text{PO}_4)_3$ (LATP), ¹³³ $\text{Li}_{1.5}\text{Al}_{0.5}\text{Ge}_{1.5}(\text{PO}_4)_3$ (LAGP) ¹³⁴	$\sim 10^{-4}$	Pros- High bulk (grains) conductivity ($\sim 10^{-3} \text{ S}\cdot\text{cm}^{-1}$) Air-stable Cons- High grain-boundary resistance Brittle in nature HT annealing for densification Instability of Ti^{4+} (reduces to Ti^{3+})

<p>Perovskite-type $\text{Li}_{3x}\text{La}_{2/3-x}\square_{1/3-2x}\text{TiO}_3$¹³⁵</p>  <p>e.g., $\text{Li}_{0.35}\text{La}_{0.55}\text{TiO}_3$ (LLTO)</p>	<p>$\sim 10^{-3}$</p>	<p>Pros- High conductivity</p> <p>Cons- Instability of Ti^{4+} (reduces to Ti^{3+}) Reduces vs Li at ~ 1.5 V</p>
<p>LiSICON-type $\text{Li}_3\text{PO}_4$¹³⁶</p>  <p>e.g., $\text{Li}_{2+2x}\text{Zn}_{1-x}\text{GeO}_4$¹³⁷ or, $\text{Li}_{3+y}\text{Si}_y\text{P}_{1-y}\text{O}_4$¹³⁸</p>	<p>$< 10^{-6}$</p>	<p>Pros- High thermodynamic stability</p> <p>Cons- Low conductivity</p>

^aNote that amorphous glassy-type SEs, such as $\text{Li}_3\text{PO}_4/\text{Li}_3\text{BO}_3/\text{Li}_2\text{SO}_4$ glass, LiPON (composition varies from $\text{Li}_{3.3}\text{PO}_{3.8}\text{N}_{0.24}$ to $\text{Li}_{3.6}\text{PO}_{3.3}\text{N}_{0.69}$), Li-La-Zr-O, etc. (with conductivities $< 10^{-6}$ $\text{S}\cdot\text{cm}^{-1}$ at RT) were also explored that were prepared by mechanochemical synthesis, RF magnetron sputtering, etc.^{139–142}

Table I.2. Different classes of sulfide-based solid electrolytes.

	Solid Electrolyte	σ_{RT} ($\text{S}\cdot\text{cm}^{-1}$)	Performance
Crystalline	<p>Thio-LiSICON-type Li_3PS_4^{121,143}</p>  <p>e.g., $\text{Li}_{10}\text{MP}_2\text{S}_{12}$ (M= Si, Ge, Sn),^{127,144,145} $\beta\text{-Li}_3\text{PS}_4$¹²⁸</p>	<p>$\sim 10^{-2}$ - 10^{-4}</p>	<p>Pros- Very high conductivity ($\sim 10^{-2}$ $\text{S}\cdot\text{cm}^{-1}$) Low grain-boundary resistance Mechanically robust due to deformable nature RT pressure sintering</p> <p>Cons- Relatively low potential window Costly due to Ge High moisture sensitivity Low conductivity of $\beta\text{-Li}_3\text{PS}_4$ ($\sim 10^{-4}$)</p>

	<p>Argyrodite-type $\text{Li}_6\text{PS}_5\text{X}^{146-148}$ (X= I / Br / Cl)</p> 	$\sim 10^{-2}$ - 10^{-5}	<p>Pros-</p> <ul style="list-style-type: none"> High conductivity Low grain-boundary resistance High ductility RT pressure sintering <p>Cons-</p> <ul style="list-style-type: none"> High moisture sensitivity Relatively low potential window
Glass-ceramics	<p>$\text{Li}_7\text{P}_3\text{S}_{11}^{149}$</p> 	$\sim 10^{-2}$	<p>Pros-</p> <ul style="list-style-type: none"> Very high conductivity ($\sim 10^{-2} \text{ S}\cdot\text{cm}^{-1}$) Low grain-boundary resistance High ductility RT pressure sintering <p>Cons-</p> <ul style="list-style-type: none"> High moisture sensitivity Decomposes vs Li metal¹⁵⁰
Glassy	<p>$\text{Li}_2\text{S}-\text{P}_2\text{S}_5/\text{SiS}_2$ Glass^{151,152}</p>  <p>(no crystallinity, with randomly oriented $\text{PS}_4/\text{P}_2\text{S}_7/\text{SiS}_3$ polyhedra¹⁵³) e.g., 75·Li_2S-25·P_2S_5 (mol%) (1-x) Li_2S-P_2S_5·xLiI</p>	$\sim 10^{-4}$	<p>Pros-</p> <ul style="list-style-type: none"> Mechanochemical synthesis Relatively high potential window No grain-boundary resistance Very high ductility and processability RT pressure sintering¹⁵⁴ <p>Cons-</p> <ul style="list-style-type: none"> Low conductivity

Na ion conductors. In parallel, the pursuit of Na-ion conductors also has been intense in the last decade. As solid state electrolytes, though the research started as early as in 1970s, only few inorganic materials have been found, e.g., β -alumina, NaSICON ($\text{Na}_{1+x}\text{Zr}_2\text{P}_{3-x}\text{Si}_x\text{O}_{12}$), and Na_3PS_4 , etc., which offer Na-ion conductivity close to the liquid electrolytes.^{110,155} However, oxide materials like β -alumina and NaSICON are synthesized and sintered at very high temperatures ($>1200^\circ\text{C}$), to eliminate grain boundary resistance and furthermore show interfacial incompatibility with metallic Na anode.¹⁵⁶ Cubic Na_3PS_4 has been reported for its potential application in a RT solid-state Na-ion battery, but the conductivity was still low ($\sim 10^{-4} \text{ S}\cdot\text{cm}^{-1}$).¹⁵⁷ Further efforts to design new Na-ion conductor is concentrated on Na_3PS_4 -based structure, for example, substitution of P to synthesize $\text{Na}_{11}\text{Sn}_2\text{PS}_{12}$,

Na_3SbS_4 etc., and even substitution of S leading to $\text{Na}_{3-x}\text{PS}_{4-x}\text{Cl}_x$, Na_3PSe_4 , etc., and slight increase in conductivity up to $\sim 10^{-3} \text{ S}\cdot\text{cm}^{-1}$ was obtained (except in recently reported $\text{Na}_{2.88}\text{Sb}_{0.88}\text{W}_{0.12}\text{S}_4$, $32 \text{ mS}\cdot\text{cm}^{-1}$).¹⁵⁸⁻¹⁶² However, due very small stability window and interfacial incompatibility, these sulfide-based electrolytes could not be implemented in practical ASSBs.^{156,163} From theoretical calculation, a small electrochemical stability window has been predicted for Na_3PS_4 (1.55 – 2.25 V) and Na_3PSe_4 (1.8 – 2.15 V).¹⁶¹

I.3.3 Design principle of superionic conductors

Conductivities in different families being discussed, question arises about what is behind the conductivity in these solids? Inorganic solids usually exhibit low ionic conductivity than traditional liquid electrolytes. In liquids, ion-conduction involves the following process- solvation and dissociation of electrolyte salt by/in polar solvent molecules, and migration of solvated ions through solvent media (Figure I.13a). Contrarily, in solids, the ionic conduction is mediated by empty Li/Na sites and due to their strong bonding inside the lattice, a large energy barrier ΔH_{mig} must be overcome for the ion migration to occur (Figure I.13b).

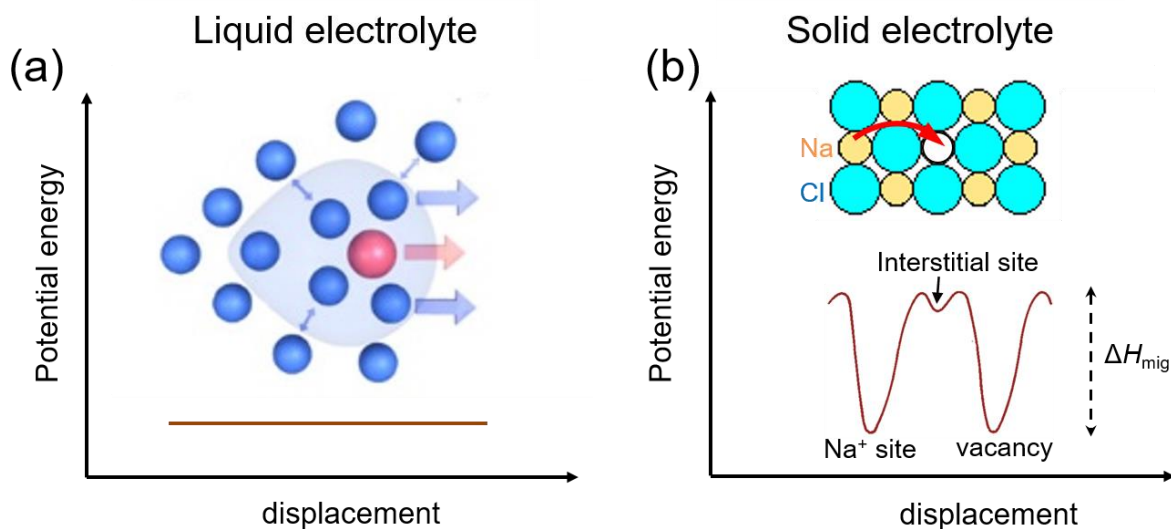


Figure I.13. Simplified schematics illustration of ionic conduction process in liquid (a) and solid (b) electrolytes.^{125,164}

In general, crystalline solid electrolytes consists of a fixed anionic sublattice (generally 3D), and a mobile Li(/Na) sublattice. Ionic conduction occurs by means of a series of definite hopping of individual ions between adjacent lattice sites through inter-connected diffusion channels, in one, two or three dimensions. The structure is illustrated for $\text{Li}_{10}\text{GeP}_2\text{S}_{12}$ (LGPS) in Figure I.14.¹²⁷

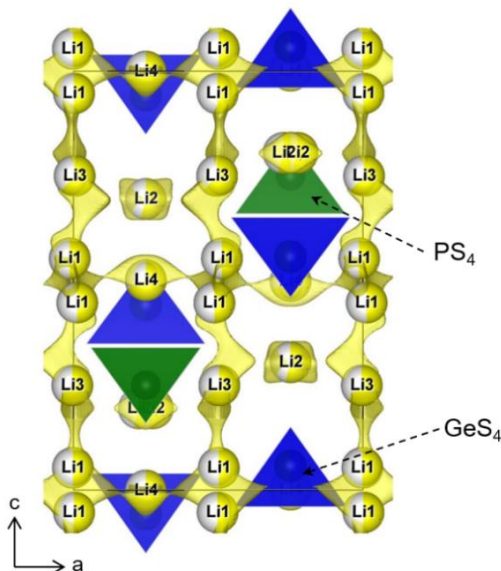


Figure I.14. Illustration of Li-conduction in $\text{Li}_{10}\text{GeP}_2\text{S}_{12}$ (LGPS). The LGPS shows an average Li-conductivity σ_{RT} of $12 \text{ mS}\cdot\text{cm}^{-1}$ ($E_a = 0.27 \text{ eV}$).¹²⁷ Li, P, and Ge atoms are shown in yellow, green, and blue. The anionic backbone consists of immobile PS_4/GeS_4 tetrahedra. The Li-ions forms the mobile sublattice. The Li-conduction pathways are highlighted in yellow. The Li1 and Li3 conducts along b direction (with $\sigma_{[001]} = \sim 27 \text{ mS}\cdot\text{cm}^{-1}$) and Li4 connect the 1D conduction channel (with $\sigma_{[110]} = \sim 7 \text{ mS}\cdot\text{cm}^{-1}$), while Li2 remains almost immobile.^{165–170}

In addition to the long-range connectivity of Li^+ sites, Li-ion diffusion probability depends on the relative energies of the lattice sites involved in hopping and the energy barriers that separate them. Hence, percolation of low energy pathways throughout the crystal lattice is also important to achieve good long range diffusivity.¹⁷¹ Thus, a number of factors regarding crystalline structure and materials chemistry affect the overall ionic conductivity, σ , which can be expressed by,

$$\sigma = \frac{q^2}{k_{\text{B}}T} n_c D_0 \exp\left(-\frac{E_a}{k_{\text{B}}T}\right)$$

where, n_c is the concentration of mobile-ion carriers (e.g., vacancies or interstitials), D_0 is the diffusion coefficient, E_a is the activation energy for ion transport, T is temperature, and k_{B} is the Boltzmann constant. Following the equation, the prerequisites to improve ionic conductivities are,

- 1) An open crystal structural framework with 3D conduction pathways with optimum free volume for ion migration.
- 2) A high n_c , with low E_a .
- 3) Highly polarizable ions to lower the migration energy barriers.¹⁷²

As a consequence, high ionic conductivity is generally obtained in few SE families that have ‘special’ crystal structures including channel size, free volume, polarizability, etc. Furthermore, within a SE family, the maximum ionic conductivity is obtained upon introducing configurational disorder

(partial site occupancies or site disorder) resulting from either vacancies or interstitials.¹⁷¹ Therefore, aliovalent substitution is generally adopted to create Li vacancies or interstitials, to increase disorder in the Li/Na-sublattice.^{110,120,136}

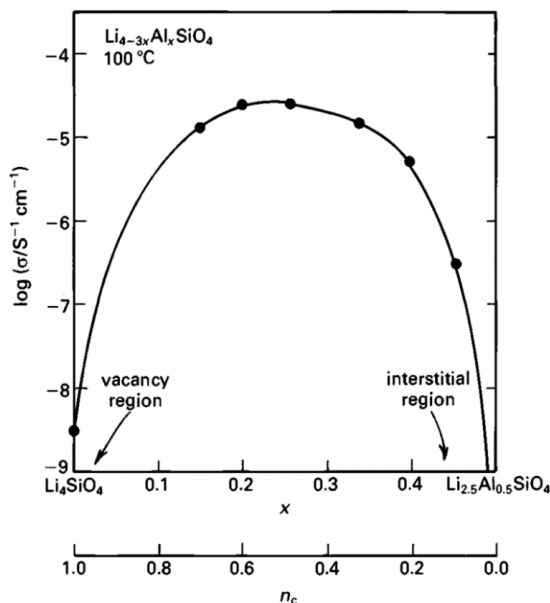


Figure I.15. Ionic conductivity of $\text{Li}_{4-3x}\text{Al}_x\text{SiO}_4$. The fraction of occupied mobile ion sites, n_c varies from 1 (at $x = 0$) to 0 (at $x = 0.5$) and a broad conductivity maximum occurs around $x = 0.25$. Figure taken from reference¹⁷³.

In aliovalent solid solution, ions are substituted by other ions of different charge, which consequently causes additional changes involving creation of vacancies or interstitials (ionic compensation) to conserve the electro-neutrality and thereby increasing the value of n_c . To illustrate, let us take the example of $\text{Li}_{4-3x}\text{Al}_x\text{SiO}_4$ solid solutions (Figure I.15).¹³⁶ In this case, it is possible to fill a set of interstitial sites completely or to empty completely a particular set of lattice sites. At the half-stage, the ionic conductivity should pass through a maximum, as the product of the concentration of mobile species, n_c and sites to which they may migrate ($1 - n_c$) is maximum when the concentrations of filled and empty sites are equal. Indeed the same has been observed for the solid solution.¹⁷³

But where to find disorder? Often, SEs possess polymorphism and the high temperature polymorph (HTP) are generally highly disordered with higher crystal symmetry. For example, the garnet-type $\text{Li}_7\text{La}_3\text{Zr}_2\text{O}_{12}$ (LLZO, Figure I.16), crystallizes in a thermodynamically more stable tetragonal phase at RT with a σ_{RT} of $\sim 10^{-6} \text{ S}\cdot\text{cm}^{-1}$.¹⁷⁴ At a temperature $>650^\circ\text{C}$, it transforms to a high-conducting cubic polymorph, which exhibits an extrapolated σ_{RT} of $\sim 10^{-4} \text{ S}\cdot\text{cm}^{-1}$.^{174,175} It is evident that in both polymorphs, the crystal framework formed by dodecahedral LaO_8 and octahedral ZrO_6 is influenced very little but Li-distribution is greatly disordered in the HTP. To stabilize the cubic phase at RT, the most efficient way is to introduce Li vacancy into the Li-sublattice by hypervalent substitutions.^{129,130} Highest conductivity of $\sim 1.4 \times 10^{-3} \text{ S}\cdot\text{cm}^{-1}$ at RT was obtained for Ga-substituted LLZO ($\text{Li}_{6.25}\text{Ga}_{0.25}\text{La}_3\text{Zr}_2\text{O}_{12}$)¹⁷⁶. Small amount of Ga-substitution creates Li-vacancy (though the

framework remains invariant) which makes the crystal structure inherently disorder, hence the stabilization.

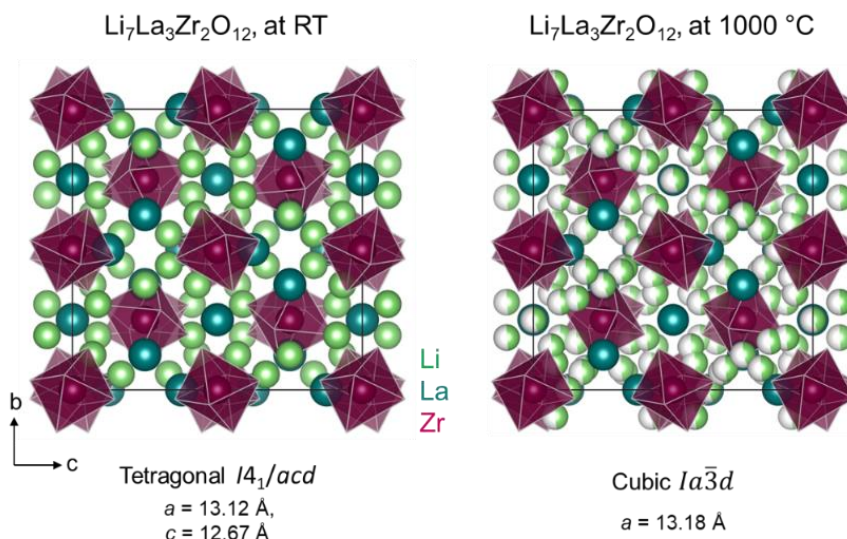


Figure I.16. Crystal structures of LLZO. O atoms are not shown. Li, La, and ZrO_6 are shown in green, cyan, and purple, respectively. Note that the cubic phase can be stabilized at RT via hypervalent substitutions, e.g., by Al^{3+} , Ga^{3+} etc. (in Li site, i.e., $\text{Li}_{7-3x}\text{Ga}_x\text{La}_{3-x}\text{Zr}_2\text{O}_{12}$), or by Ta^{5+} , Nb^{5+} , Te^{6+} , W^{6+} etc. (in Zr site, i.e., $\text{Li}_{7-x}\text{La}_3\text{Zr}_{2-x}\text{Ta}_x\text{O}_{12}$), etc.^{129,130}

Similarly, the high-conducting thio-phosphate $\text{Li}_{11-x}\text{M}_{2-x}\text{P}_{1+x}\text{S}_{12}$ ($M = \text{Si}, \text{Ge}, \text{Sn}$) phases were designed by aliovalent substitution in Li_3PS_4 .¹²¹ Ionic conductivity of Li_3PS_4 at RT was reported back in 1984 by Tachez *et al.*,¹²¹ (Figure I.17) to be $\sim 3 \cdot 10^{-7} \text{ S} \cdot \text{cm}^{-1}$. However, with increasing temperature, a jump in the conductivity was observed due to an order-disorder phase transition at $\sim 200^\circ\text{C}$.¹⁴³ Therefore, the Li-disorder leads to 4 times higher conductivity and a smaller activation energy (E_a) of 0.46 eV, compared to 0.49 eV for the low temperature polymorph (LTP).^{121,143,177}

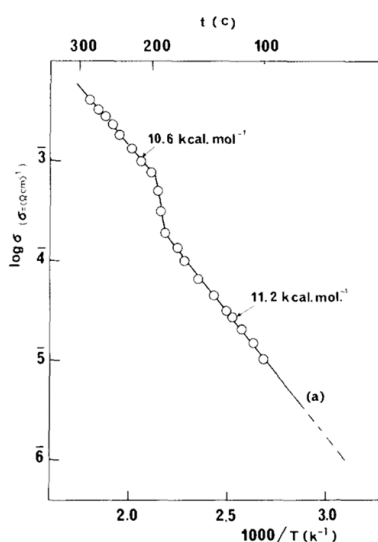


Figure I.17. Ionic conductivity of Li_3PS_4 . Figure taken from Reference¹²¹.

Kanno *et al* (2003) demonstrated partial substitution of P^{5+} by Ge^{4+} in Li_3PS_4 .¹²⁶ Thus prepared $Li_{4-x}Ge_{1-x}P_xS_4$ (or $Li_{3+y}Ge_yP_{1-y}S_4$) solid solution showed gradual increase of ionic conductivity with increasing substitution and highest conductivity of $2 \cdot 10^{-3} \text{ S} \cdot \text{cm}^{-1}$ was reported at RT for $Li_{3.25}Ge_{0.25}P_{0.75}S_4$, where $x = 0.75$ (or $y = 0.25$). Nevertheless, in quest for higher conductivity, Kanno and coworkers (2011) discovered further optimized $Li_{10}GeP_2S_{12}$ (or $Li_{3.33}Ge_{0.33}P_{0.67}S_4$), as known as LGPS composition. Furthermore, the HTP can be stabilized by changing synthesis method also, as Liu *et al* reported stabilization of the β - Li_3PS_4 by nano-structuring ($\sim 80 - 100 \text{ nm}$) via wet-chemical synthesis.¹²⁸ Stabilization of HTPs will be carried out as a part of this thesis.

What are the other factors ? The anionic sublattice has a significant effect on Li^+ diffusivity in SEs. Larger and more polarizable framework is preferable for ionic conduction, as it decreases the interaction of $Li-X$ bond ($X = \text{anions}$), thus making the Li 's more mobile. Hence, replacement of larger and more polarizable S for O improves the conductivity by magnitude of orders (Figure I.18a).^{126,178} Furthermore, it was exemplified by Ong *et al*, with the LGPX ($Li_{10}GeP_2X_{12}$, $X = O, S, Se$) structure. Li^+ diffusivity is significantly slower in $Li_{10}GeP_2O_{12}$ with higher activation energy than in $Li_{10}GeP_2S_{12}$ (Figure I.18b).¹⁷² In contrary, cation substitution within the SE family has much lesser impact.¹⁷²

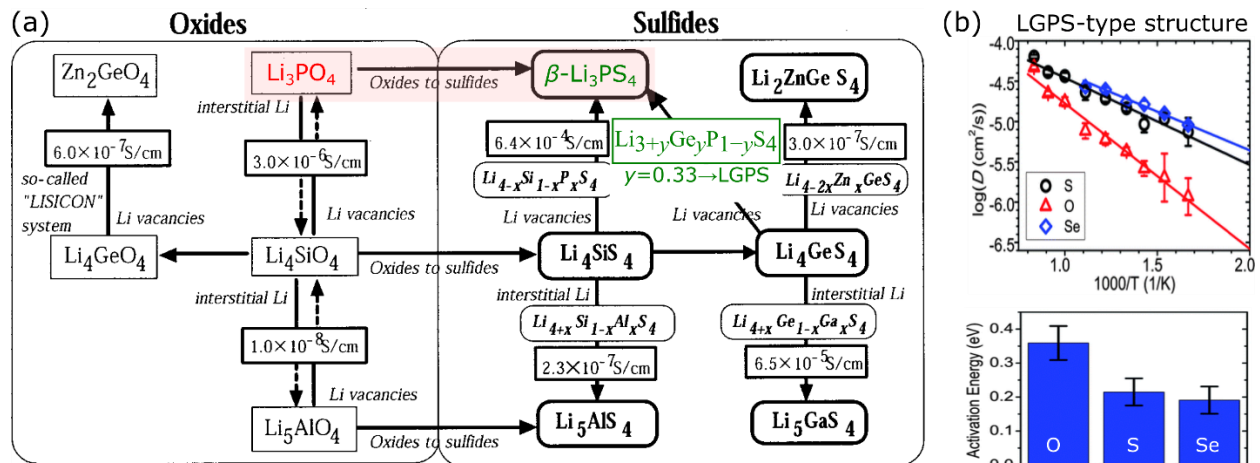


Figure I.18. Enhancement of ionic conductivity by moving from oxides to sulfides. (a) Optimizing ionic conductivity by introducing defects (Li vacancies or interstitials).¹²⁶ Note that the LGPS was designed by optimizing Li-concentration in $Li_{3+y}Ge_yP_{1-y}S_4$ with $y = 0.33$.¹²⁷ (b) Variation in diffusivities (D) and activation energies (E_a) upon anion tuning in $Li_{10}GeP_2X_{12}$ ($X = O, S, \text{ and } Se$), calculated from MD simulations.¹⁷² Figures adapted from references^{126,172}.

However, only disordered crystal structure is not enough for superionic conductivity. From, first principles computational studies, crystal structural frameworks with body-center cubic (bcc) packing of anions (e.g., S^{2-}) are found to be superior for Li-ion diffusion, than in other close-packed frameworks. In bcc anion packing, Li ions occupy and migrate between face-sharing tetrahedral sites, leading to a low migration barrier of $\sim 0.2 \text{ eV}$ (Figure I.19a), that is typical in Li sulfides, e.g., LGPS, $Li_7P_3S_{11}$, β - Li_3PS_4 , etc.¹⁷⁹ In addition to crystal structural features, from AIMD (Ab Initio Molecular Dynamics)

simulations, it was shown that Li superionic conductors in sulfides, and specially in oxides (despite having bcc packing, e.g., LLZO), exhibit a unique diffusion mechanism distinctive from typical solid materials.¹⁸⁰ Here, multiple Li ions migrate simultaneously through a concerted mechanism instead of an isolated ion hopping in typical solids. During the concerted migration of multiple ions, when ions located at the high-energy sites migrate downhill, they cancel out a part of the energy barrier felt by other uphill-climbing ions. Hence, the concerted migration with a decreased migration barrier is kinetically favorable (Figure I.19b). Therefore, to activate super-ionic conduction, one needs to insert mobile ions into high-energy sites that activates the concerted ion migration.

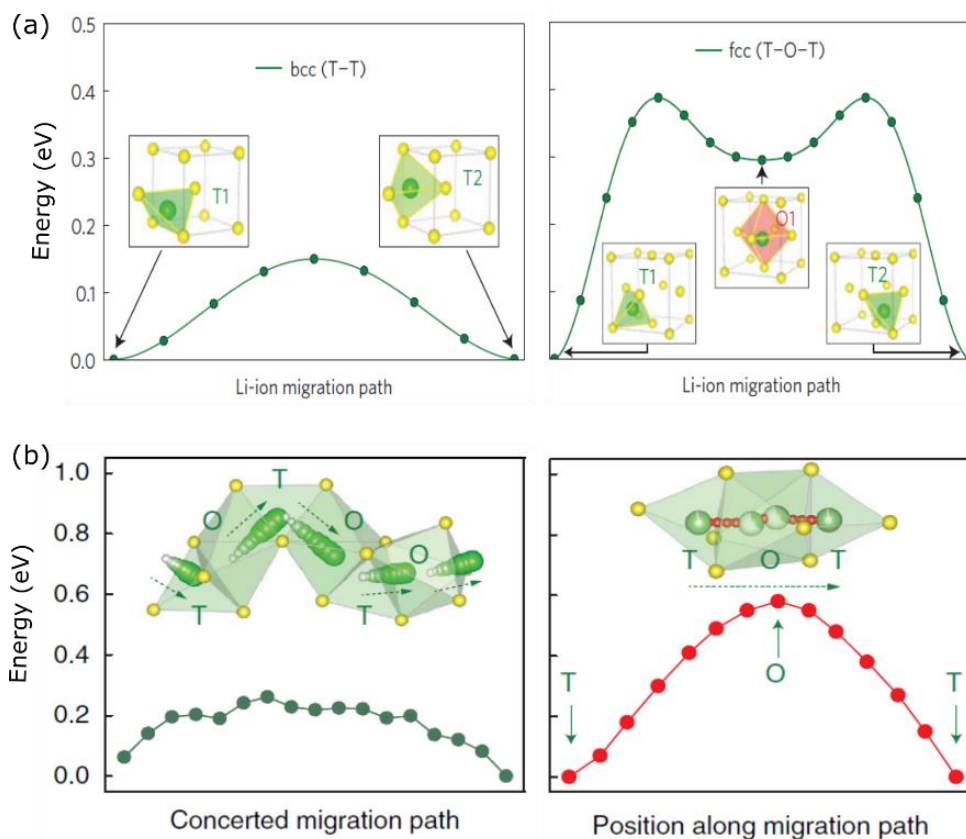


Figure I.19. Structural and configurational features of superionic conductors. (a) Calculated energy path in bcc and fcc sulfur-lattices (for single Li⁺ migration). (b) Migration energy barrier LLZO for concerted migration of multiple Li⁺ (in left) and single Li⁺ (in right) along the diffusion channel. The Li⁺/path are shown as green spheres and O/S atoms as yellow spheres. T and O represent Li tetrahedra or octahedra. Note that the bcc lattice of concerted migration decreases the energy barrier of migration. Figures taken from references^{179,180}.

I.3.4 Choosing the electrolyte: Oxides or Sulfides ?

High ionic conductivities has been obtained in both oxide and sulfide based SEs, as shown above. So which is better for practical applications ? To answer this, few other properties, such as, electrochemical and chemical stability and compatibility, and, processing capability for fabrication of

ASSB, etc., must be considered. In this regard, oxide and sulfide based solid electrolytes possess various advantages over one other, as compared overall in Figure I.20.

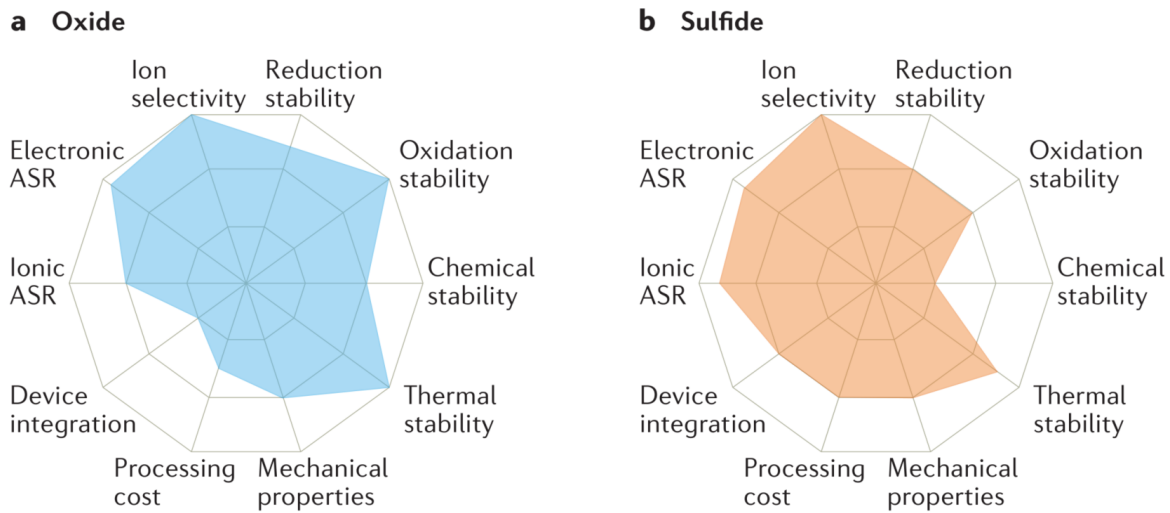


Figure I.20. Comparison of advantages/disadvantages between oxide and sulfide solid electrolytes. Figure taken from reference⁹⁴.

As clear from the spider plot, the oxide SEs possess much better chemical, electrochemical thermal stability than the sulfides. Based on first-principles calculations, the intrinsic thermodynamic stabilities of existing solid electrolytes were calculated by Zhu *et al*, as shown in Figure I.21a.¹⁸¹ As shown, most of the solid electrolytes, except LLZO, are unstable against Li. Oxides have higher thermodynamic reduction potential compared to the sulfide electrolytes.

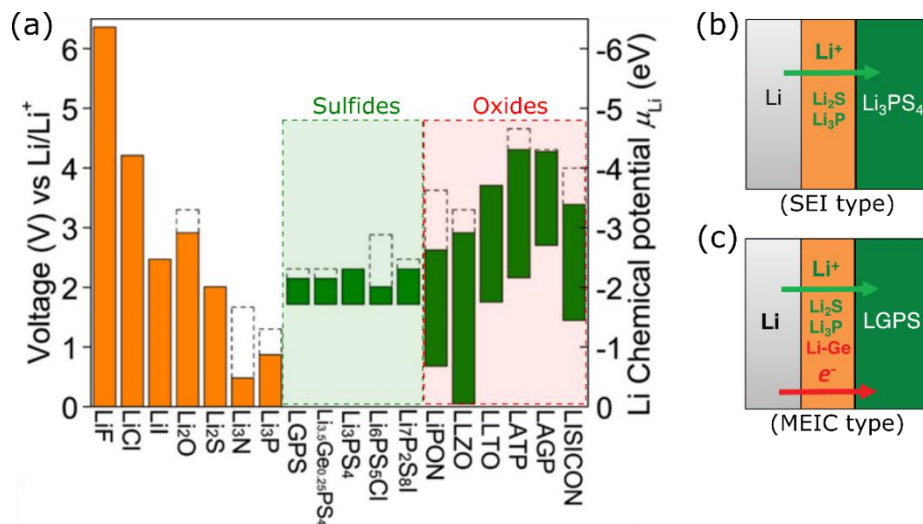


Figure I.21. Electrochemical stability and decomposition of solid electrolytes. (a) Electrochemical stability window (shown in solid color bar) and the oxidation potential to fully delithiate the material (marked in dashed line). (b-c) Schematic illustration of interphase layer of Li_3PS_4 and LGPS against Li

metal. SEI and MEIC denote solid electrolyte interface, mixed electronic-ionic conductor, respectively. Figures adapted from reference^{181,182}.

Because of the low electrochemical stability, the solid electrolytes decompose at low and high voltage. Upon Li contact, few SEs, e.g., LiPON, Li₃PS₄, etc., decomposes to Li binary compounds like as Li₂O, Li₃P, Li₃N, Li₂S, etc., that are stable against the high chemical potential (μ_{Li}) of Li metal, which passivate the solid electrolyte and inhibit further decomposition (Figure I.21b).^{183,184} The passivation mechanism relies on the electronic insulating properties of the decomposition interphase layers and is not protective if the layer is electronically conductive. In LGPS, the decomposition layer consists Li₃P, Li₂S and in addition electronically conductive Li-Ge alloys (Li₁₅Ge₄) or Ge metal that helps to propagate the decomposition and increase of interfacial impedance, as shown experimentally (Figure I.21c).¹⁸⁵⁻¹⁸⁷ Similarly, the absence of passivation mechanism explains the lithiation and reduction of LLTO^{188,189}, LATP¹⁹⁰, LAGP¹⁹¹, and LISICON¹⁹², etc., that were observed experimentally.

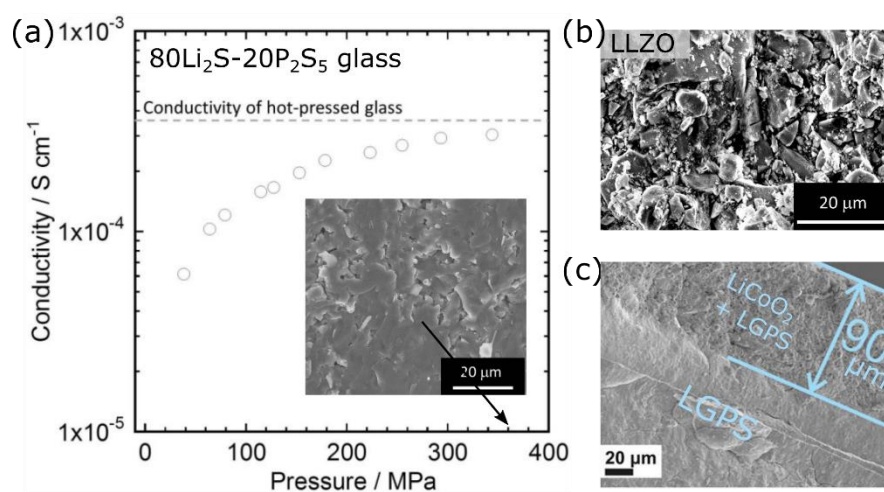


Figure I.22. RT sinterability of sulfide SEs. Ionic conductivity of Li₂S-P₂S₅ glass pellets pressed at RT. Inset shows the SEM image of cross sections of the pellet that was pressed at 360 MPa. Note that good ionic conductivity could be obtained only pelletizing at moderate pressure.¹⁵⁴ (b) SEM image of cross sections of the pellet of RT pressed LLZO oxide, showing inefficient densification.¹⁵⁴ (c) SEM image of cross sections of the RT-pressed pellet of stacked LGPS and LGPS-LiCoO₂ showing good densification.¹⁹³ Figures adapted from references^{154,193}.

In short, even though oxide based SEs are desired over sulfides because of their higher voltage stability window and ease of handling, sulfide SEs provide advantages in terms of ionic conductivity, and more importantly for device integration (Figure I.20). Sulfides are suitable for room-temperature processing, as they possess the unique mechanical properties of ‘RT pressure sintering’, see Figure I.22. Furthermore, due to its moderate elastic modulus, sulfide SEs can sustain the volume changes of electrode during cycle. Whereas, oxide SEs, being mechanically rigid, need high temperature and pressure sintering and prone to fragmentations and contact loss during cycling. Therefore, sulfide-based

SEs, e.g., LGPS, β -Li₃PS₄ etc., have been mostly used for ASSBs, and some examples will be shown next.

I.4 Progress in full ASSBs

The SEs, especially sulfide SEs, have a narrow electrochemical stability window. Thus the cyclability of the ASSBs depend on the SEI formation which effectively extends the electrochemical window of the SEs. Figure I.23a shows performance of LiCoO₂ with LGPS-type SEs (indicated on the figure) and Li metal anode.¹⁹⁴ However because of interfacial reactions, full capacity from LiCoO₂ could not be obtained. Moreover, dendrite issues were also shown persist with sulfide SEs and this is the reason why In-Li alloy is generally used.^{195–197} NMC-811 cathode materials were used in ASSB with β -Li₃PS₄ SEs and In anode (Figure I.23b).¹⁹⁸ However, much less capacity could be obtained than the capacity obtained in LIBs with liquid electrolyte.

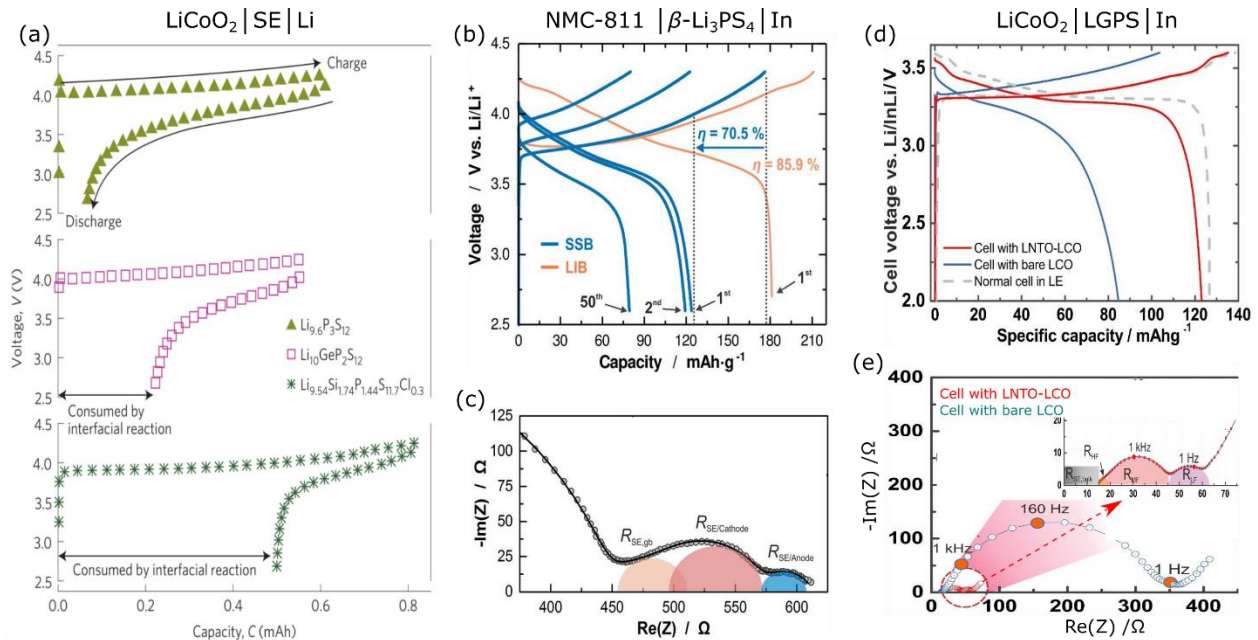


Figure I.23. Performances of ASSBs with different sulfide SEs. Voltage profiles of LiCoO₂ in ASSB using the SEs indicated on the figure. (b) Voltage profiles of NMC-811 (LiNi_{0.8}Co_{0.1}Mn_{0.1}O₂) in ASSB with β -Li₃PS₄ SE and in LIB. The EIS spectra of the ASSB is shown in (c). (d) Voltage profiles of surface-coated (with LiNb_{0.5}Ta_{0.5}O₃, LNTO) and uncoated LCO (LiCoO₂) in ASSB and LIB. The EIS spectra of the ASSBs are shown in (e). Figures adapted from references^{193,194,198}.

High resistance at SE/cathode interface, due to resistive decomposition products, was confirmed by the electrochemical impedance spectroscopy (EIS, Figure I.23c), that further grows upon charge-discharge.^{150,189,198,199} The oxidative degradation at the cathode side represents a major factor contributing to the capacity fading of ASSBs. In particular, for the application of high-capacity nickel-

rich layered oxides or high-voltage cathode materials, the electrochemical stability of thiophosphate electrolytes toward high potentials is insufficient and requires surface-coatings by ZrO_2 , LiNbO_3 , $\text{LiNb}_{0.5}\text{Ta}_{0.5}\text{O}_3$ (LNTO) or $\text{Li}_2\text{O-ZrO}_2$ etc.^{193,200–202} Indeed, the LNTO-coated LiCoO_2 performs much better in ASSB than uncoated LiCoO_2 (Figure I.23d).¹⁹³ The interfacial resistance was decreased largely (Figure I.23e), but still remains due to the formation of Li-depleted layer at the interface originated from μ_{Li} differences at S–O interface.^{203–205} In short, though sulfide-based SEs are preferred for its higher conductivity and facile integration for ASSB fabrication, tackling the interfaces has become the next big challenge. Works on compatibility of sulfide-based electrolyte/electrode will be carried out as a part of this thesis.

I.5 Chapter Conclusions

This chapter initially discussed how to increase the energy density of cathode materials, via the utilization of materials that accumulate both cationic and anionic redox process, provided we are able to solve the bottlenecks associated with the anionic redox. This is our motivation to work on anionic redox in sulfides, which will be discussed in Chapter III. Secondly, we recalled that the safety of LIBs need to be improved. This could be achieved via fabricating safe all-solid-state-batteries (ASSBs), where solid electrolytes (SEs) are used in place of flammable liquid electrolytes. To realize functional ASSBs, SEs must possess good electrochemical/chemical stability with capability of easy handling. Oxide based SEs with improved ionic conductivity are desired in this regard. Hence, we decided search new ionically conducting oxides by selecting and optimizing disordered polymorphs, what exactly will be addressed in the next chapter.

Chapter II

Searching Ionic Conductors in the Li(Na)-Zn-P-O phase diagram[#]

[#]This chapter includes the following publications that I co-authored: *Chem. Mater.* 2018, 30, 1379–1390; *Inorg. Chem.* 2019, 58, 1774–1781; and Saha *et al.*, manuscript under preparation.

II.1 Chapter Introduction.

This chapter deals with searching new oxide-based SEs for application in ASSBs. In oxides, despite sufficiently high conductivity (up to $\sim 10^{-3} \text{ S}\cdot\text{cm}^{-1}$) in few materials, conductivities are still lower than the liquid electrolytes, which furthermore is affected by high interfacial resistance.^{125,206} Owing to greater stability, ease of handling and larger electrochemical window, oxides can be better candidates than the sulfide SEs, provided that we improve the conductivity, hence our efforts to develop new materials.

Usually superionic conductivity is observed, when the material is highly disordered. As disorder increases in high-temperature polymorphs, numerous materials show temperature driven phase transition with the higher temperature polymorphs (HTPs) showing the best ionic conductivity. Thus, intense research is devoted to the stabilization of the HTPs at RT, by various methods, such as quenching, nano-structuring, varying synthesis condition like using certain precursors, and by aliovalent substitution, etc., as has been discussed in Chapter I. Following this line, we have concentrated our search towards new Li-conducting oxides in the Li(Na)-Zn-P-O phase diagram (Figure II.1), based on the facts that:

- 1) Zn-based phosphates are known to possess disordered polymorphs,²⁰⁷
- 2) Zn^{2+} (d^{10}) is electrochemically redox-inactive, and finally, that,
- 3) Zn-based phosphates can be synthesized at relatively lower temperature ($< 800 \text{ }^\circ\text{C}$), whereas most oxide SEs require high temperature ($> 1000 \text{ }^\circ\text{C}$) synthesis/sintering.

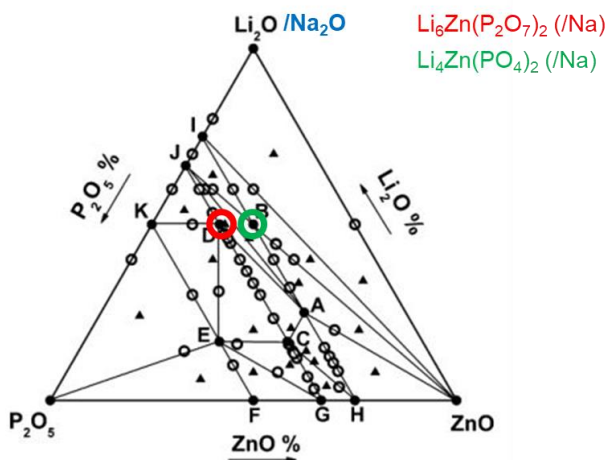


Figure II.1. Phase diagram of the Li(Na)-Zn-P-O System. Diagram adapted from Rao *et al*, 2009.²⁰⁷

In this family, several compounds are shown to exhibit polymorphism extensively,²⁰⁷ and we have spotted $\text{Li}/\text{Na}_6\text{Zn}(\text{P}_2\text{O}_7)_2$, and $\text{Li}/\text{Na}_4\text{Zn}(\text{PO}_4)_2$ as potential candidates (Figure II.1). We furthermore decided to explore their Na-counterpart also, provided they can be synthesized. We have studied the relation between the polymorphism and disorder in these ‘model compounds’ along with the variation of conductivities with structural modifications. Finally, we have explored various ways to stabilize the

high temperature polymorphs (HTP) at RT, with the conduction mechanisms rationalized by bond valence energy landscape (BVEL) maps, which confirms the high sensitivity of ionic conductivity on disorder. Our studies on Li-ion conductors $\text{Li}_6\text{Zn}(\text{PO}_4)_2$ and $\text{Li}_4\text{Zn}(\text{PO}_4)_2$ will be presented in Section II.2 and II.3, followed by its extension to Na-ion conductor $\text{Na}_4\text{Zn}(\text{PO}_4)_2$ (Section II.4).

II.2 $\text{Li}_6\text{Zn}(\text{P}_2\text{O}_7)_2$

The low temperature phase (LTP) of $\text{Li}_6\text{Zn}(\text{P}_2\text{O}_7)_2$, that was reported by Rao *et al.*,²⁰⁷ was shown to transform to a HTP following a phase transition at 365 °C. XRD patterns for both the phases were reported, indexed with a possible monoclinic unit cells, but no structural model was presented. Herein we choose this compound to study the influence of polymorphism and disorder upon ion conduction.

II.2.1 Probing the polymorphism with temperature

$\text{Li}_6\text{Zn}(\text{P}_2\text{O}_7)_2$ sample was prepared by classical solid state reaction of Li_2CO_3 , ZnO , and $\text{NH}_4\text{H}_2\text{PO}_4$ at 700 °C, detailed method is described in the Appendix (Section A1.1). The X-ray powder diffraction (XRD) pattern of the sample, when prepared by quenching from the synthesis temperature, is in agreement with the list of peak positions reported by Rao *et al.*²⁰⁷, but our pattern indicates that the powder is composed of a mixture of different polymorphs of $\text{Li}_6\text{Zn}(\text{P}_2\text{O}_7)_2$. Hence, the quenched samples were further annealed at 300 °C (i.e. below the phase transition temperature) to get pure α - $\text{Li}_6\text{Zn}(\text{P}_2\text{O}_7)_2$. However, by annealing at temperatures higher than the phase transition temperature and successive quenching we could not succeed in stabilizing the other high-temperature polymorphs in pure form. For such a reason, hereafter if not otherwise specified, the pure α - $\text{Li}_6\text{Zn}(\text{P}_2\text{O}_7)_2$ sample was used as the starting material and its polymorphism was studied both via thermo-gravimetric analysis (TGA) and *in situ* X-ray diffraction as a function of the temperature.

Figure II.2a shows the DSC profile of $\text{Li}_6\text{Zn}(\text{P}_2\text{O}_7)_2$ heated to 600°C and cooled to RT.^A Several endothermic peaks of different amplitudes were observed, as opposed to the single peak reported earlier²⁰⁷ indicating the existence of multiple phase transitions upon heating. During the cooling, existence of fewer exothermic peaks suggests that the compound undergoes different structural transitions.

To grasp deeper insights in the phase transitions and the associated structural transformations, we have performed temperature dependent *in situ* synchrotron-XRD (SXR) experiments over a broad temperature range up to 650 °C and the diffractograms are gathered in Figure II.2b,c. Diffraction patterns were collected at 5 °C intervals. They are plotted as 2D contour diagrams in Figure II.2b and as a function

^A All DSC experiments were performed by Matthieu Courty, at Laboratoire de Réactivité et Chimie des Solides (LRCS), Amiens.

of diffraction angle in Figure II.2c. From the evolution of the patterns, five phase transitions could be identified and they occur at temperatures corresponding to peaks in the DSC measurement, as indicated by the red arrows in Figure II.2a.

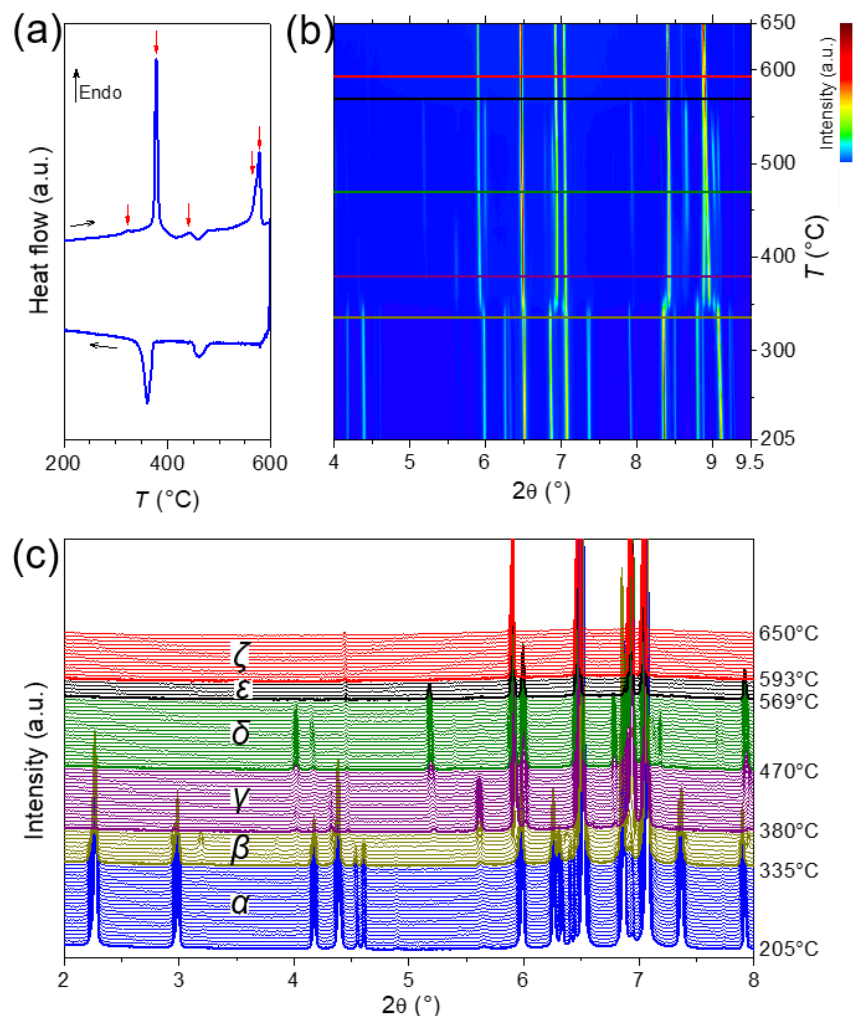


Figure II.2. Probing temperature-dependent structural modifications by DSC and SXRD. (a) DSC curve of the $\text{Li}_6\text{Zn}(\text{P}_2\text{O}_7)_2$ sample. (b) 2D contour plot showing the temperature dependence of the SXR patterns indicating different phases with temperature. (c) Evolution of the SXR patterns during heating of the $\text{Li}_6\text{Zn}(\text{P}_2\text{O}_7)_2$ sample observed in the temperature dependent synchrotron-XRD experiment. Successive phase transitions have been denoted on the plot and corresponding temperatures has been indicated at the right. In (b) the horizontal lines correspond to the phase transition temperatures indicated in (c).

One should first mention that all patterns present similarities and only differ in peak's positions and in the presence, or not, of small additional peaks. This indicates that all six polymorphs are likely structurally related. The first transition was observed at ~ 335 °C. Till this temperature the compound crystallizes in α - $\text{Li}_6\text{Zn}(\text{P}_2\text{O}_7)_2$ form, but increasing the temperature to 380°C leads to a disappearance of its low angle peaks to the expense of new one at $2\theta = 3.2^\circ$, hence leading to another polymorph denoted as the β -phase. Then upon further heating we observe the subsequent growth of the γ -polymorph (380°C

to 470°C) and δ -polymorph (470°C to 569°C) which presents characteristic peaks at $2\theta = 5.6^\circ$ and $2\theta = 4.1^\circ$ and 5.18° , respectively. Afterwards, there is appearance of the ε -polymorph, whose existence is limited to a narrow temperature range (569-593°C), and XRD exhibits a pattern very close to the δ -one with however the disappearance of the doublet around $2\theta = 4.1^\circ$. Lastly, for temperature above 593°C, there is the appearance of the ζ -polymorph which shows XRD pattern with fewer peaks, indicative of a higher symmetry and/or smaller unit cell of this polymorph.

The synchrotron-XRD patterns collected during cooling (Figure II.3) indicate, in contrast to heating, two phase transitions are observed which start at $\sim 487^\circ\text{C}$ and $\sim 369^\circ\text{C}$, in agreement with the DSC data (Figure II.2a). Moreover, upon cooling to RT, the sample does not transform back to pure α - $\text{Li}_6\text{Zn}(\text{P}_2\text{O}_7)_2$ polymorph, since its RT XRD consists in a mixture of the α -polymorph with other high temperature phases. However, we believe such a difference to be rooted in the slow kinetics of phase transitions upon cooling, as supported by the feasibility to transform the multiphase cooled sample into the pure α -polymorph by a short reannealing step at 300°C .

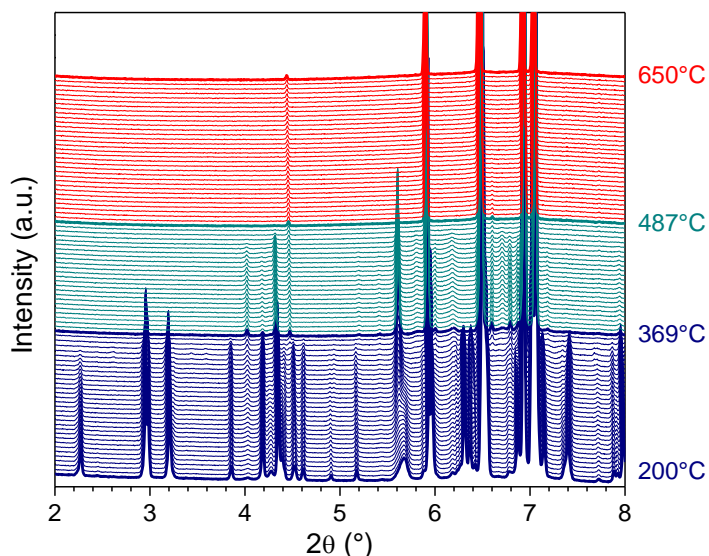


Figure II.3. Evolution of the SXRD patterns during cooling of the $\text{Li}_6\text{Zn}(\text{P}_2\text{O}_7)_2$ sample.

II.2.2 Structural solution of ordered α -phase

Next, in the absence of any single crystal, we directly used the powder XRD patterns to solve the crystal structure of the two main phases. The pattern recorded at RT for the α -phase was indexed using the DICVOL program²⁰⁸ with a monoclinic unit cell with lattice parameters $a = 25.66942(10) \text{ \AA}$, $b = 10.25856(4) \text{ \AA}$, $c = 9.10213(3) \text{ \AA}$, and $\beta = 104.7074(3)^\circ$. This leads to a unit cell volume of $V = 2313.0(1) \text{ \AA}^3$ which can accommodate eight formulas per unit cell ($Z = 8$). Systematic extinctions were found to be consistent with $C 2/c$ space group (S.G.). Then a first set of Zn, P and O atomic positions were found using the 'FOX' program, the PO_4 groups being treated as rigid bodies.²⁰⁹ All Zn, P and O atoms are placed on general position $8f$ (except two oxygen atoms, denoted as O22 and O44), which

bridge PO_4 tetrahedra to form the pyrophosphate groups. Neutron powder diffraction (NPD) pattern recorded at RT was then used to determine the Li positions using Fourier difference maps. Finally, all atoms were refined using combined Rietveld refinement of both SXR and the NPD. The refinements present good reliability parameters ($\chi^2=3.5$, $R_B=5.08\%$ for NPD) and are shown in Figure II.4, with the structural parameters gathered in the Appendix Table A1.1.

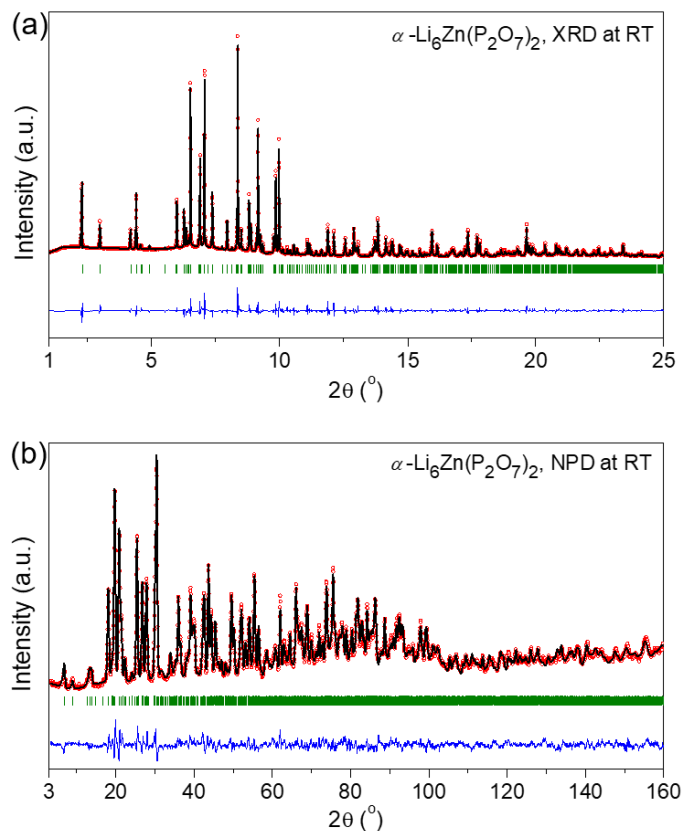


Figure II.4. Combined Rietveld refinement of the XRD (a) and NPD patterns (b) of $\alpha\text{-Li}_6\text{Zn}(\text{P}_2\text{O}_7)_2$. The red circles, black continuous line, blue line and green tick bars represent the observed, calculated, and difference patterns, and Bragg positions, respectively.

The deduced crystal structure is shown in Figure II.6a,c. Four crystallographically distinct P atoms and fifteen crystallographically distinct O atoms form the pyrophosphate $\text{P}_2\text{O}_7^{4-}$ groups which are all oriented in a parallel way. Zn and Li are placed in between those pyrophosphate groups and only coordinated by oxygen atoms from $\text{P}_2\text{O}_7^{4-}$. The Zn atoms (on a single Wyckoff site $8f$) stay in a distorted trigonal bipyramidal coordination with three equatorial Zn–O bond lengths of ~ 2 Å and two slightly longer axial bonds of ~ 2.3 Å. The Li atoms are distributed upon six crystallographic sites and all sit in a distorted tetrahedral positions with average Li–O bond length of ~ 1.96 Å.

II.2.3 Structural solution of disordered ζ -phase

Similarly we proceed to solve the structure of the high temperature ζ -phase from SXR and NPD patterns recorded at 600°C . The best fit ($\chi^2=3.51$, $R_B=9.38\%$, for NPD) could be found in a monoclinic unit cell with space group $C2/c$, but with much smaller unit cell than the α -phase. The lattice

parameters were found to be $a = 13.24574(6)$ Å, $b = 5.19764(2)$ Å, $c = 8.92388(4)$ Å, and $\beta = 105.1842(4)^\circ$, leading to a unit cell volume $V = 592.8(2)$ Å³ that is one fourth of the volume of the RT monoclinic unit cell and therefore can accommodate two formulae per unit cell ($Z = 2$). The high temperature ζ - unit cell vectors are linked to the RT α -Li₆Zn(P₂O₇)₂ ones by the following relation:

$$\begin{pmatrix} \mathbf{a}_\zeta \\ \mathbf{b}_\zeta \\ \mathbf{c}_\zeta \end{pmatrix} = \begin{pmatrix} 1/2 & 0 & 0 \\ 0 & 1/2 & 0 \\ 0 & 0 & 1 \end{pmatrix} \begin{pmatrix} \mathbf{a}_\alpha \\ \mathbf{b}_\alpha \\ \mathbf{c}_\alpha \end{pmatrix}$$

The structural model for the ζ -phase was obtained from atomic positions of the α -phase at RT to which the transformation matrix was applied. Its a and b unit cell parameters being twice smaller than for the α -phase, we must have a mixing of Li and Zn atoms to comply with the invariance of the molecular formulae. This was supported by combined SXRD/NPD refinement (Figure II.5), which indicates that Li and Zn are statistically distributed over two Wyckoff sites (general position 8f). The preexisting Zn trigonal-bipyramidal positions in the P₂O₇⁴⁻ layer are converted to tetrahedral Li₂/Zn₂ positions with 0.9/0.1 occupancy and the preexisting Li positions in the Li layer lead to a trigonal-bipyramidal mixed Li₁/Zn₁ position with 0.85/0.15 occupancy in the ζ -phase. The structural parameters are gathered in the Appendix Table A1.2 and the deduced crystal structure is shown in Figure II.6b,d.

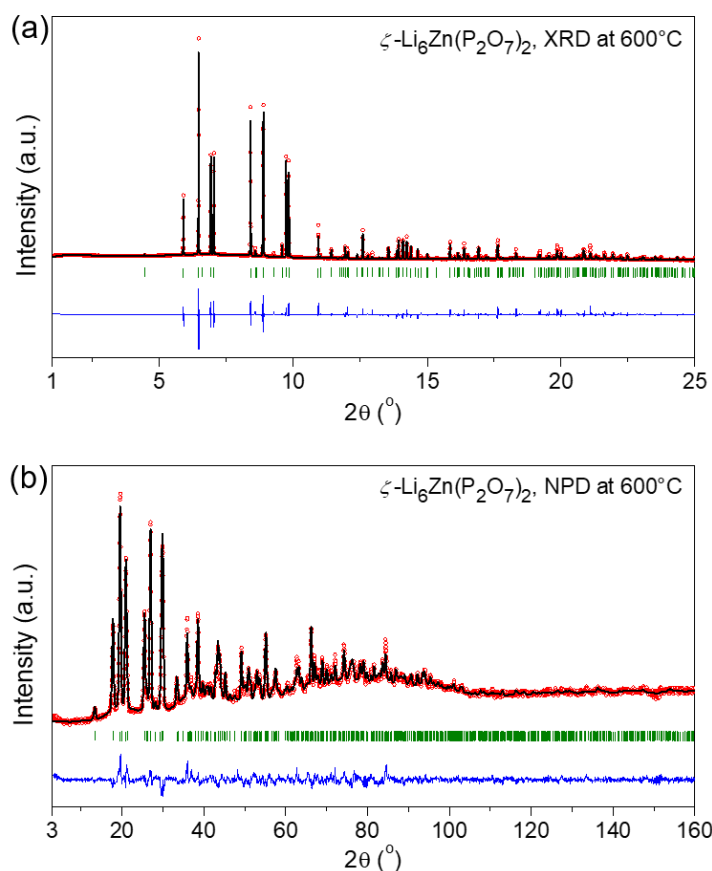


Figure II.5. Rietveld refinement of the XRD and NPD patterns of ζ -Li₆Zn(P₂O₇)₂, recorded at 600 °C. For legends refer to Figure II.4.

By comparing α - and ζ - structures, we see that the $\text{P}_2\text{O}_7^{4-}$ backbone remains conserved. The main difference is that the high temperature ζ - polymorph possesses disorder and mixing between Li and Zn positions, whereas the RT α - polymorph is fully ordered.

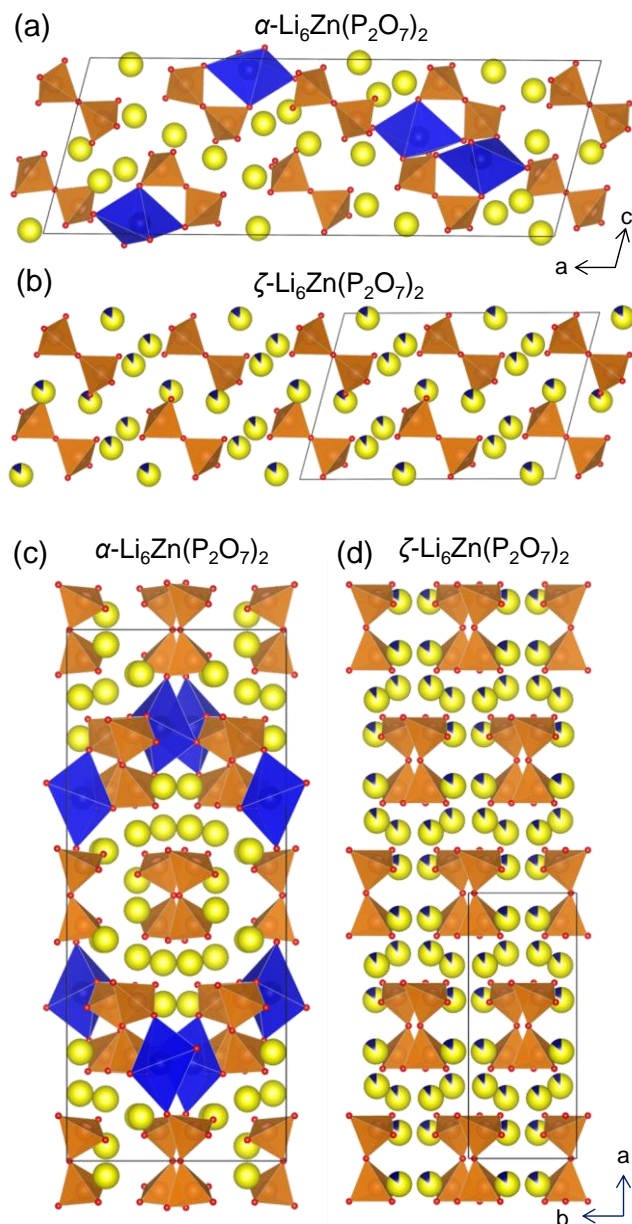


Figure II.6. Crystal structure of the polymorphs of $\text{Li}_6\text{Zn}(\text{P}_2\text{O}_7)_2$. (a-d) Along [010] direction (a,b) and along [001] direction (c,d). Li is shown in yellow; ZnO_4 and PO_4 tetrahedra are colored in blue and orange, respectively.

The structural determinations of the two main phases at RT and 600 °C shed light on the four β , γ , δ , and ε intermediate phases, even if it is out of the goal of the present study to solve all structures. None of these phase present XRD patterns that can be fully indexed with the α - or the ζ -unit cells. However, the resemblance in the main peaks indicates that the $\text{P}_2\text{O}_7^{4-}$ backbone remains identical,

whereas gradual disappearance of low angle peaks in successive polymorphs indicates increasing disorder. We expect that further differences between structures arise from complex and partial Li/Zn orderings that may lead to pretty large unit cells, if not incommensurate. Nevertheless, looking at the subtle differences in the SXRD patterns of the β - with the α -polymorph, it could be inferred that the polymorphs have similar structure where both of the polymorphs possess the low angle peaks ($2\theta < 3.5^\circ$). Similarly γ - and δ - phases have similar structure with characteristic mid-low angle peaks at $2\theta = 3.5^\circ - 5.8^\circ$ and ε - and ζ - are similar where these two sets of peaks are absent. Further studies, including a thorough NPD exploration versus temperature, will be needed to solve these intermediate structures. Also, the phases observed on cooling remain largely unexplored since the kinetics of phase transformation seems to be fast on heating but slow on cooling, as three days of annealing the cooled phase at 300°C are needed to recover the α phase.

II.2.4 Influence of disorder on ionic conductivity

The ionic conductivity of the compound was measured from the AC impedance spectra recorded on a sintered pellet of $\alpha\text{-Li}_6\text{Zn}(\text{P}_2\text{O}_7)_2$ (see Appendix Section A1.1 for details). Representative Nyquist impedance plots are shown in Figure II.7a. All recorded spectra consist of a depressed semicircle at the high frequency region followed by a Warburg tail at lower frequency region, which confirms the ionic nature of the ac conductivity. The slightly flattened semicircle sums up the impedance responses of the sample made of grains (g) and grain boundaries (gb). All the contributions were decoupled by fitting the whole impedance spectra to an equivalent circuit model $(R_g//Q_g)(R_{gb}//Q_{gb})W_o$ (inset of Figure II.7b); where R and Q represent the resistance and constant phase element associated with the grains (g) or grain boundaries (gb) of the sample, respectively, and W_o is the Warburg resistance.

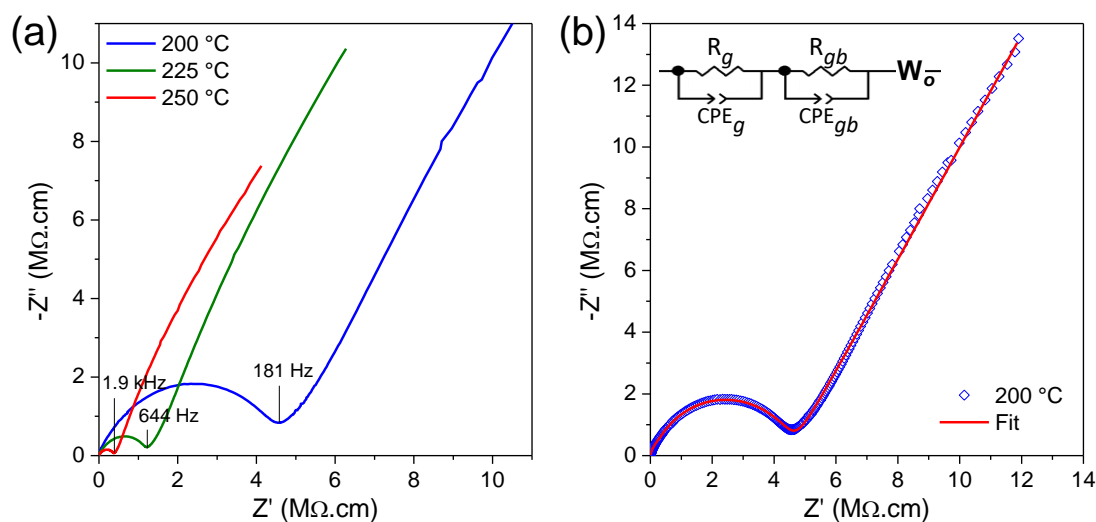


Figure II.7. AC impedance spectra of the $\text{Li}_6\text{Zn}(\text{P}_2\text{O}_7)_2$. (a) Representative AC impedance spectra of $\alpha\text{-Li}_6\text{Zn}(\text{P}_2\text{O}_7)_2$ recorded at 200, 225 and 250 $^\circ\text{C}$. Some typical frequencies have also been indicated.

(b) The fitting of the impedance spectra recorded at 200 °C. Inset shows the equivalent circuit used to fit the spectra.

A typical fitting is shown in Figure II.7b. The fitting decouples the flattened semicircle into two deconvoluted semicircles and lead to capacitance values of $\sim 10^{-12}$ F and $\sim 10^{-11}$ F associated with the Q of the deconvoluted semicircles at higher and lower frequency, respectively. Such values are respectively reflecting the grains (σ_g) and the grain boundaries (σ_{gb}) contributions, to the overall conductivity (see Appendix Section A1.1 for details).

The ionic conductivity of the α - $\text{Li}_6\text{Zn}(\text{P}_2\text{O}_7)_2$ sample is summarized in Figure II.8. The plot exhibits a linear variation of $\ln(\sigma T)$ with inverse temperature indicating a thermally activated Arrhenius-type behavior, $\sigma(T) = A/T \cdot \exp(-E_a/k_B T)$, where k_B is the Boltzmann constant, A is a pre-exponential factor and T is the temperature. The bulk ionic conductivity (σ_g) at 200°C was found to be $\sim 6 \times 10^{-8}$ $\text{S}\cdot\text{cm}^{-1}$ with an E_a of 0.9 eV and σ_g of $\sim 2 \times 10^{-12}$ $\text{S}\cdot\text{cm}^{-1}$ at RT could be deduced by extrapolation of the Arrhenius plot. Variation of the total ionic conductivity (σ_{tot}) is also plotted (line **a** in Figure II.8b), which indicates a much lower σ_{tot} value of $\sim 1 \times 10^{-14}$ $\text{S}\cdot\text{cm}^{-1}$ and $E_a = \sim 1.1$ eV at RT. This indicates that the conductivity in this material is limited by the grain boundary conductivity (σ_{gb}), which is $\sim 1.4 \times 10^{-14}$ $\text{S}\cdot\text{cm}^{-1}$ at RT ($E_a = \sim 1.1$ eV).

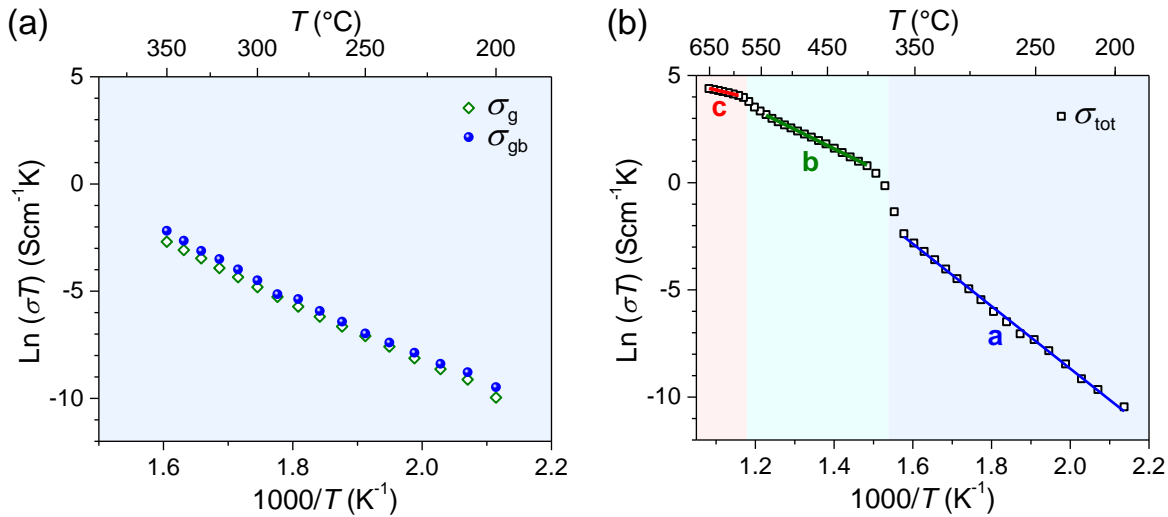


Figure II.8. Arrhenius plot of Ionic Conductivity of the $\text{Li}_6\text{Zn}(\text{P}_2\text{O}_7)_2$ sample. (a) Grains conductivity (σ_g) and grain boundary conductivity (σ_{gb}), (b) total conductivity (σ_{tot}). The blue, green and red background refers to the three regions of ionic conductivity. In (b) a, b, and c denote the solid lines in blue, green, and red, respectively.

However, since this compound undergoes several order-disorder phase transitions at higher temperatures, we next measured the conductivity of the sample over a broader temperature range up to 650 °C. The variation of the measured σ_{tot} values are shown in Figure II.8b. Three jumps in conductivity can be observed in the Arrhenius plot, as denoted by lines **a**, **b** and **c** in the plot. First jump was observed at ~ 390 °C, as shown by line **b**, which probably is induced by the transition to the γ -polymorph. Extrapolation of the line **b** to RT indicates a σ_{tot} value of $\sim 3.3 \times 10^{-10}$ $\text{S}\cdot\text{cm}^{-1}$, with E_a of 0.73 eV.

Further increase was observed at ~ 590 °C, adhering to the phase transition to the ζ -polymorph (line **c** in Figure II.8b) and gives an extrapolated σ_{tot} value of $\sim 1.5 \times 10^{-5} \text{ S}\cdot\text{cm}^{-1}$ at RT, with E_a value of 0.35 eV. For these polymorphs, the behavior of σ_g and σ_{gb} could not be obtained, because of the shift of the grains and grain boundary responses toward higher frequencies with temperature, which finally moves beyond the measurable frequency window of the instrument leaving only the Warburg tail observable (see Figure II.9). At this point, it's worth noting that while SXRD revealed multitude phase transitions, only two of them have a strong effect on the ionic conductivity.

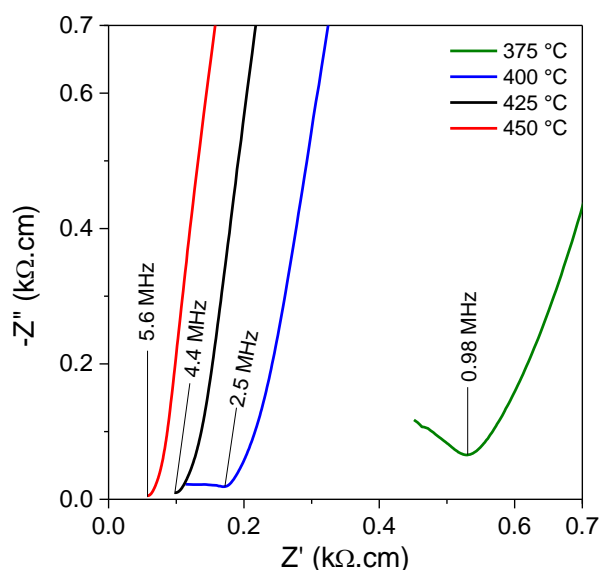


Figure II.9. AC impedance spectra of $\alpha\text{-Li}_6\text{Zn}(\text{P}_2\text{O}_7)_2$ recorded at high temperatures. Some typical frequencies have also been indicated.

II.2.5 Mechanism of Li-conduction from BVEL calculations

As an attempt to correlate the observed increase in ionic conductivity with the structural transition, we have performed bond valence energy landscape (BVEL) calculations of the α - and ζ -polymorphs. The details of the calculations are described in the Appendix Section A1.1. The BVEL maps representing the Li^+ conduction pathways in the $\text{Li}_6\text{Zn}(\text{P}_2\text{O}_7)_2$ polymorphs are shown in Figure II.10. The calculations predict for $\alpha\text{-Li}_6\text{Zn}(\text{P}_2\text{O}_7)_2$ an infinite 2-D Li^+ percolation path along the b-c plane at 1.05 eV above the minimum energy (Figure II.10a) which most likely results from the layered structure of the polymorph.

This contrast with the calculated BVEL map for the ζ - polymorph which predicts infinite 3-D Li^+ percolation paths at 0.65 eV above the minimum energy (Figure II.10b). From a comparison of the Li^+ conduction channels in both polymorphs we can deduce that the onset of the Li/Zn inter-sites mixing associated to the ζ - polymorph creates new migration channels. Thus interlayer Li^+ hopping become possible through mixed $\text{Li}^+/\text{Zn}^{2+}$ sites in agreement with the highest ionic conductivity measured for the ζ - as compared to the α - polymorph.

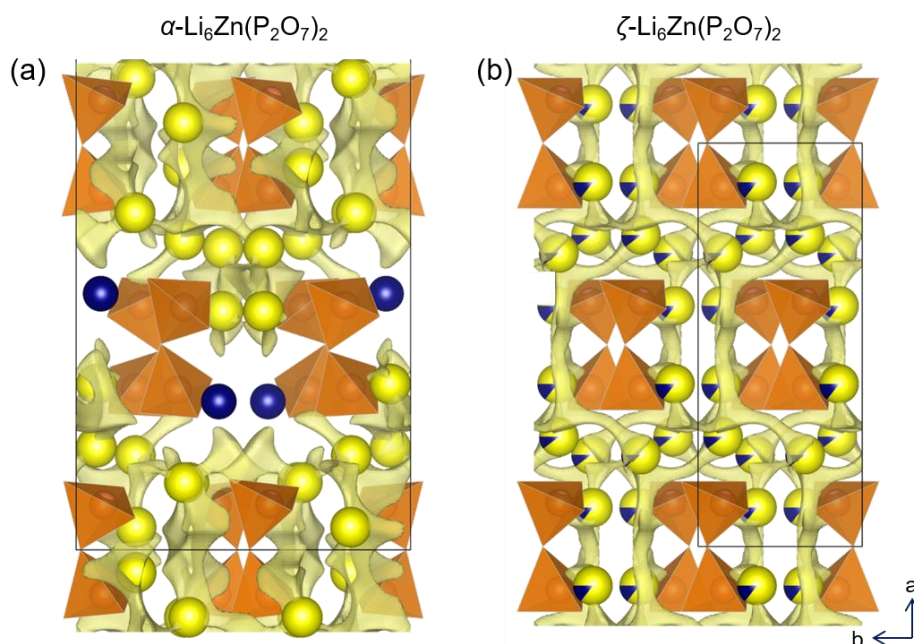


Figure II.10. BVEL map of (a) α - $\text{Li}_6\text{Zn}(\text{P}_2\text{O}_7)_2$ and (b) ζ - $\text{Li}_6\text{Zn}(\text{P}_2\text{O}_7)_2$ at the percolation energies. The yellow domains indicate the migration paths for Li^+ in the structure, obtained using an iso-surface value of 1.05, and 0.65 eV above the minimum energy, respectively. For the color codes, refer to Figure II.6.

In short, we thoroughly studied the polymorphism in $\text{Li}_6\text{Zn}(\text{P}_2\text{O}_7)_2$ and explored its impact on ionic conductivity. It showed two jumps in ionic conductivity with increasing temperature, with a high activation barrier for Li^+ conduction for the α than the ζ -polymorph (0.9 eV vs. 0.35 eV). Altogether, these results suggest that not only disorder, but also cation-mixing can lead to new conduction pathways, which can increase the ionic conductivity. However, despite our efforts we could not stabilize the ζ -polymorph at RT by hypervalent synthesis. Next, we move to similar studies on $\text{Li}_4\text{Zn}(\text{PO}_4)_2$ to verify whether the HTPs can be stabilized.

II.3 $\text{Li}_4\text{Zn}(\text{PO}_4)_2$

The $\text{Li}_4\text{Zn}(\text{PO}_4)_2$ was reported as early as in 1976, it was never explored in details for its transport properties despite its rich chemistry.²¹⁰ This compound received further attention in 1986 by West *et al.*, who explored its thermal stability by differential thermal analysis of Li_3PO_4 - $\text{Zn}_3(\text{PO}_4)_2$ solid solutions.²¹¹ Interestingly, they reported three polymorphs, low temperature the α - $\text{Li}_4\text{Zn}(\text{PO}_4)_2$ and the high temperature β - and γ - $\text{Li}_4\text{Zn}(\text{PO}_4)_2$, and moreover they speculated that the β -phase derives from the α -phase by cation disordering. One year later, the same group, prepared the pure compound by solid state synthesis and explored its ionic conductivity.²¹² They found that $\text{Li}_4\text{Zn}(\text{PO}_4)_2$ is a poor Li^+ conductor, but noticed an increase of conductivity for the β -phase. Fifteen years later, Jensen *et al.*, have

prepared the compound by hydrothermal method and described an accurate structural model for the α -phase.²¹³ However, nobody has described the crystal structures of the high temperature phases till date.

β - $\text{Li}_4\text{Zn}(\text{PO}_4)_2$ has been speculated to be isostructural to γ - Li_3PO_4 ,^{211,213} which is well-known since long as a good Li^+ conductor.¹³⁸ More specifically, this compound can be viewed as Li_3PO_4 with two Li^+ substituted by one Zn^{2+} , and since there is no twofold positions in Li_3PO_4 to accommodate the extra Zn^{2+} , the Zn^{2+} and vacancies are probably disordered in fourfold Li sites. This could explain the higher conductivity reported for the β phase, bearing in mind that in solid electrolytes, disordered polymorphs possess greater conductivity than their ordered counterparts.^{130,177,214} In this study, we studied its conductivity governed by its disorder in the structure and explored various ways to stabilize the β -polymorph at RT.

II.3.1 Crystal structure of $\text{Li}_4\text{Zn}(\text{PO}_4)_2$

$\text{Li}_4\text{Zn}(\text{PO}_4)_2$ sample was prepared by following classical solid state reaction of Li_2CO_3 , ZnO , and $\text{NH}_4\text{H}_2\text{PO}_4$ at 700 °C, see the Appendix Section A1.1 for details. The XRD pattern of the as-prepared pristine sample, α - $\text{Li}_4\text{Zn}(\text{PO}_4)_2$ (RT form), can be perfectly fitted with a monoclinic unit cell having a $P 2_1/c$ space group and lattice parameters $a = 8.11990(16)$ Å, $b = 10.24192(13)$ Å, $c = 8.10549(15)$ Å, $\beta = 104.8589(9)^\circ$, $V = 651.538(2)$ Å³, with $Z = 4$, using the structural model reported earlier²¹³.

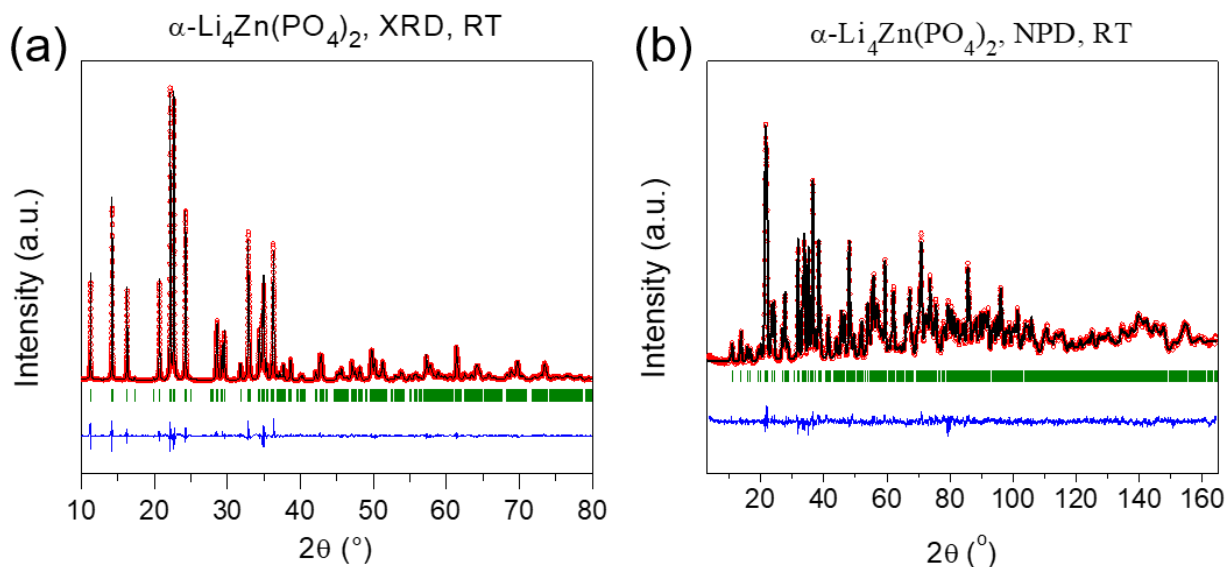


Figure II.11. Rietveld refinement of the XRD and NPD patterns of α - $\text{Li}_4\text{Zn}(\text{PO}_4)_2$, measured at RT. The red circles, black continuous line, blue line and green tick bars represent the observed, calculated, and difference patterns, and Bragg positions, respectively.

The combined Rietveld refinement of the neutron and XRD patterns is shown in Figure II.11a,b and the resulting structural parameters are reported in the Appendix Table A1.3. The structure of α -

$\text{Li}_4\text{Zn}(\text{PO}_4)_2$ is drawn in Figure II.12. It consists of corner sharing ZnO_4 and PO_4 tetrahedra forming layers along the b - c plane, which are stacked along $[100]$. These layers are separated by Li atoms, which are also in tetrahedral coordination.

II.3.2 Order-disorder transition with temperature

The α - $\text{Li}_4\text{Zn}(\text{PO}_4)_2$ phase is known to undergo phase transition at high temperature to β - $\text{Li}_4\text{Zn}(\text{PO}_4)_2$,^{213,212} but the crystal structure of β - $\text{Li}_4\text{Zn}(\text{PO}_4)_2$ was never reported, to our best knowledge. Hence we have carried out systematic investigations of the phase transition and finally have been able to deduce a structural model for the β - $\text{Li}_4\text{Zn}(\text{PO}_4)_2$ phase. Differential scanning calorimetry (DSC), shown in Figure II.13a, of the as-prepared $\text{Li}_4\text{Zn}(\text{PO}_4)_2$ sample clearly depicts the $\alpha \rightarrow \beta$ transitions at ca. 443 °C on heating, with an activation enthalpy of 11.7 kJ/mol (endothermic). On cooling, the DSC trace shows the reversible process with a thermal hysteresis of ~15 °C indicating that the transition is of first order. This phase transition was monitored by temperature dependent XRD experiments and the diffractograms are gathered in Figure II.13b. Upon heating, XRD patterns of α - $\text{Li}_4\text{Zn}(\text{PO}_4)_2$ show a small shift towards lower angles due to thermal expansion, until the temperature reaches 430°C. Above this temperature, the XRD pattern changes and looks similar to the one previously reported for the β form. On cooling, this process is reversible and the α -phase is recovered below 420°C, see Figure II.14.

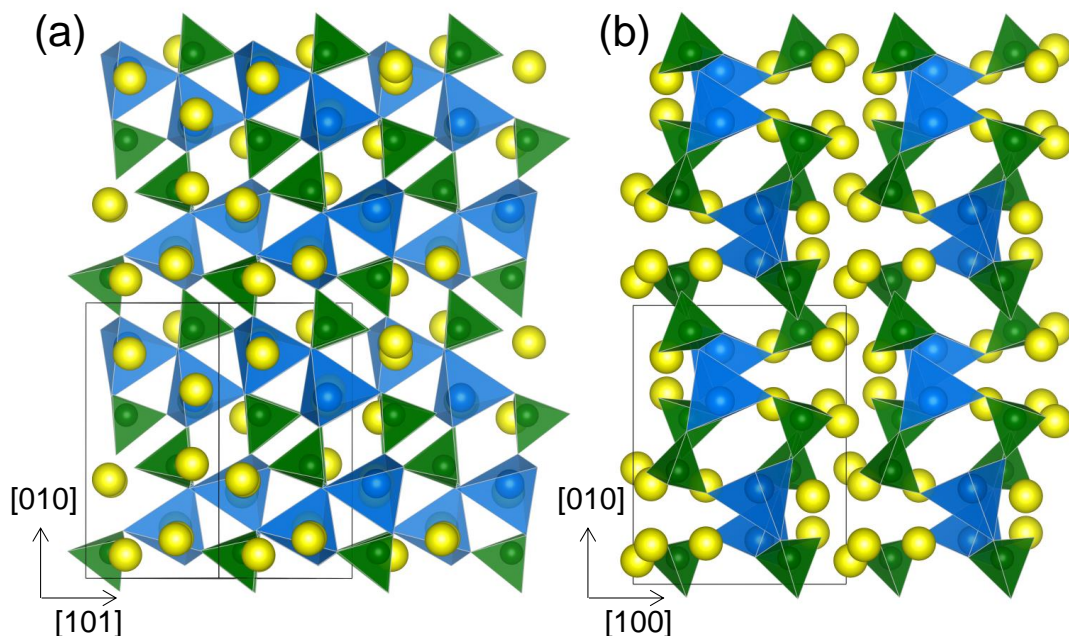


Figure II.12. Crystal structure of α - $\text{Li}_4\text{Zn}(\text{PO}_4)_2$. (a) along $[\bar{1}01]$, (b) along $[001]$. Li is shown in yellow; ZnO_4 and PO_4 tetrahedra are colored in blue and green, respectively.

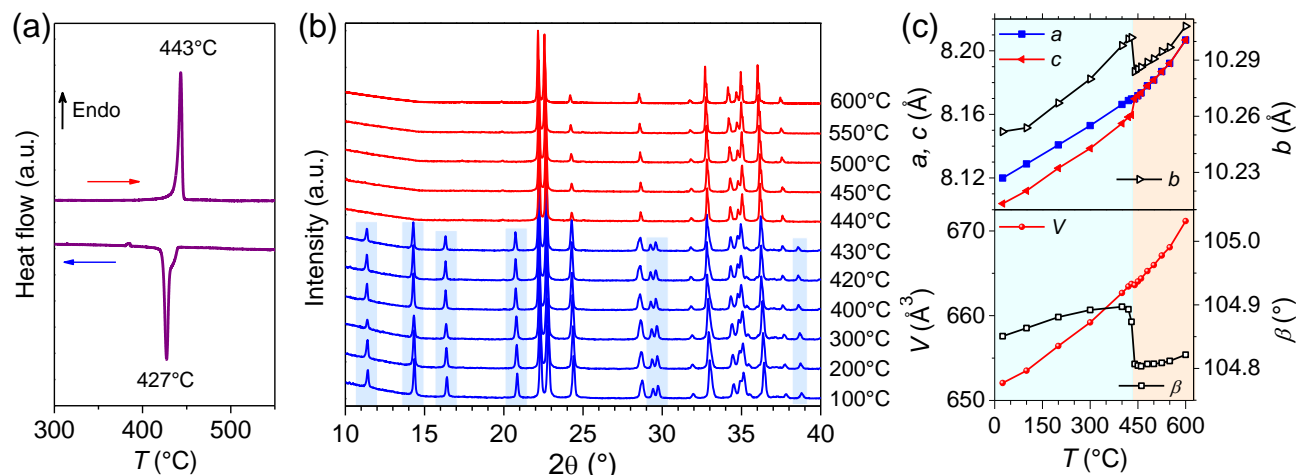


Figure II.13. Probing temperature-dependent structural modifications of $\text{Li}_4\text{Zn}(\text{PO}_4)_2$ by DSC and XRD. (a) DSC curve of $\text{Li}_4\text{Zn}(\text{PO}_4)_2$, measured in air with a heating and cooling rate of $10^\circ\text{C}/\text{min}$. (b) Evolution of the XRD patterns of $\text{Li}_4\text{Zn}(\text{PO}_4)_2$ between 100 and 600°C on heating. Values of temperatures corresponding to the patterns are indicated at the right. The patterns colored in blue and red corresponds to the α - and β - polymorphs, respectively, and the peaks that disappear for the β - phase has been indicated by blue backgrounds. (c) Evolution of lattice parameters with respect to temperature. The lattice parameters have been converted to monoclinic unit cell setting pertaining to the α - crystal structure for comparison. The blue and red regions correspond to the α - and β - phases, respectively.

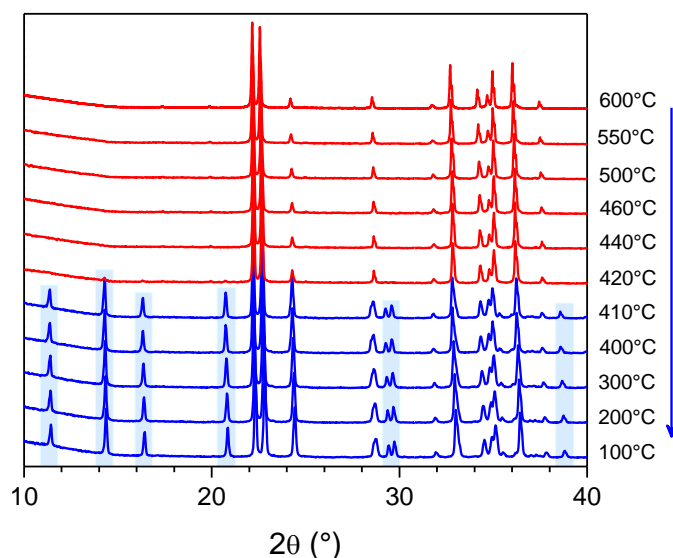


Figure II.14. Evolution of XRD patterns of $\text{Li}_4\text{Zn}(\text{PO}_4)_2$ with temperature during cooling. Values of temperatures corresponding to the patterns are indicated at the right. The patterns colored in blue and red corresponds to the α - and β - polymorphs, respectively, and the peaks that reappear for the α - phase has been indicated by blue backgrounds.

II.3.3 Structural solution of the β -polymorph

Note that our efforts to quench the high temperature β phase at RT were unsuccessful; therefore we directly used the pattern recorded at 600°C to solve the structure for the β phase. The β phase presents

a powder pattern similar to the α -phase, except for some peaks that have disappeared, especially in the low angle region. This relative similarity in diffraction pattern hints for a structural relationship between the α - and the β - structures. The XRD pattern of β -Li₄Zn(PO₄)₂ at 600°C could be indexed using the Dicvol program²⁰⁸ with an orthorhombic unit cell with lattice parameters $a = 10.30571(4)$ Å, $b = 6.50156(3)$ Å and $c = 5.00496(2)$ Å, leading to a unit cell volume $V = 335.348(2)$ Å³ that is half the volume of the RT monoclinic unit cell and therefore can accommodate two formulas per unit cell ($Z = 2$). The orthorhombic unit cell vectors are linked to the monoclinic α -Li₄Zn(PO₄)₂ ones by the following relation:

$$\begin{pmatrix} \mathbf{a}_{\text{ortho}} \\ \mathbf{b}_{\text{ortho}} \\ \mathbf{c}_{\text{ortho}} \end{pmatrix} = \begin{pmatrix} 0 & 1 & 0 \\ 1/2 & 0 & -1/2 \\ 1/2 & 0 & 1/2 \end{pmatrix} \begin{pmatrix} \mathbf{a}_{\text{mono}} \\ \mathbf{b}_{\text{mono}} \\ \mathbf{c}_{\text{mono}} \end{pmatrix}$$

Systematic extinctions were found to be consistent with $Pnma$ space group. The orthorhombic unit cell is plotted on top of the α structure in Figure II.16a, and where, looking at two adjacent orthorhombic unit cells, it clearly appears that the high temperature β phase should involve a disorder between Zn and Li2 atoms to comply invariance through lattice translation. Therefore, the XRD and NPD of the β -phase recorded at 600°C were then simultaneously refined by the Rietveld method, introducing mixing between Zn and Li cations.

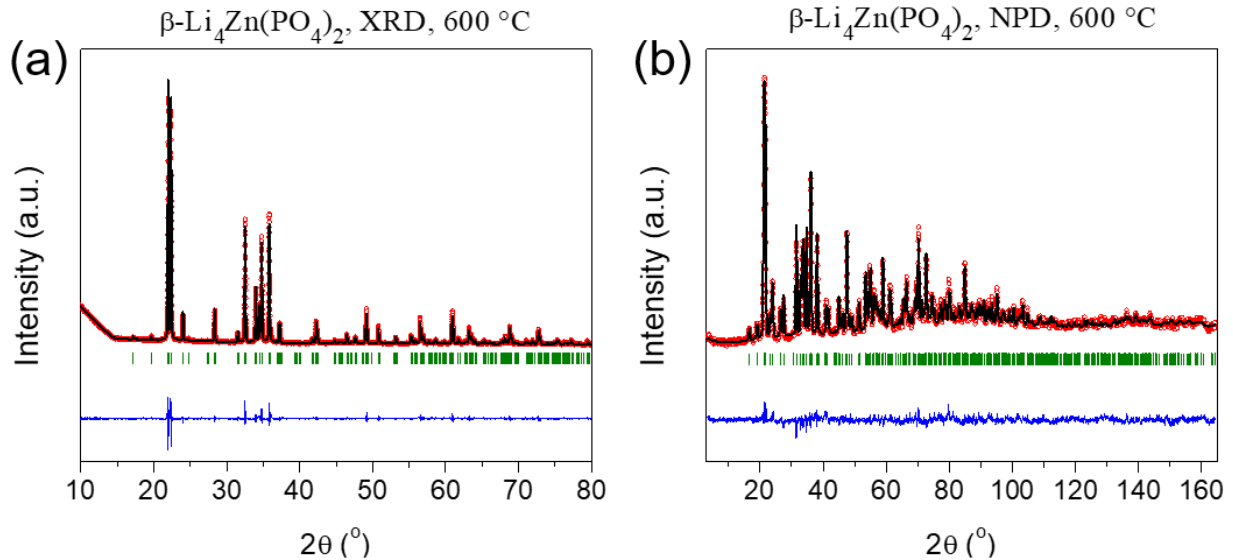


Figure II.15. Rietveld refinement of the XRD and NPD patterns of β -Li₄Zn(PO₄)₂, measured at 600°C. The red circles, black continuous line, blue line and green tick bars represent the observed, calculated, and difference patterns, and Bragg positions, respectively.

The corresponding Rietveld refinements in Figure II.15 and the deduced structural model is shown in Figure II.16b, with the structural parameters are gathered in the Appendix Table A1.4. Lastly, all temperature-dependent XRD patterns were Rietveld refined and the evolution of lattice parameters of the Li₄Zn(PO₄)₂ with temperature is summarized in Figure II.2c using the monoclinic description for the β phase for an easier comparison. It can be noticed that the unit cell volume monotonously increases with T and exhibits a slight discontinuity at the transition, as expected from a first order phase transition.

Moreover, it should be noted that this volume increase results from anisotropic changes in the b , c and β unit cell parameters.

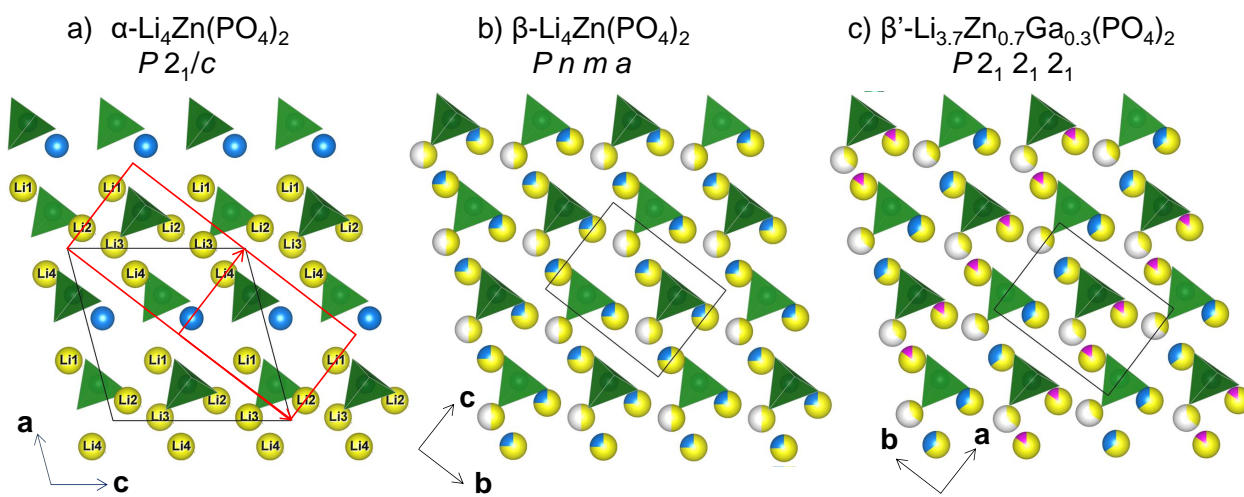


Figure II.16. Crystal structure of (a) α - $\text{Li}_4\text{Zn}(\text{PO}_4)_2$, (b) β - $\text{Li}_4\text{Zn}(\text{PO}_4)_2$ and (c) β' - $\text{Li}_{3.7}\text{Zn}_{0.7}\text{Ga}_{0.3}(\text{PO}_4)_2$. In (a), the monoclinic α unit cell is plotted in black and the orthorhombic β cell is shown in red. For sake of clarity, only half of the unit cell content ($0 \leq y \leq \frac{1}{2}$ in the monoclinic setting) is shown. Li, Zn, P and Ga are shown in yellow, blue, green and pink, respectively and PO_4 tetrahedra are colored in green.

II.3.4 Stabilization of β -phase by ball-milling

Having found that the β - $\text{Li}_4\text{Zn}(\text{PO}_4)_2$ is a disordered counterpart of the α - $\text{Li}_4\text{Zn}(\text{PO}_4)_2$ polymorph, it became interesting to stabilize this phase at RT. Since ball-milling is known to increase disorder by repeated particles fracturing and welding, as was demonstrated recently for sulphates²¹⁵, we tried to stabilize the β phase by ball-milling. More specifically, the as-prepared α - $\text{Li}_4\text{Zn}(\text{PO}_4)_2$ was ball milled for 2 hours.

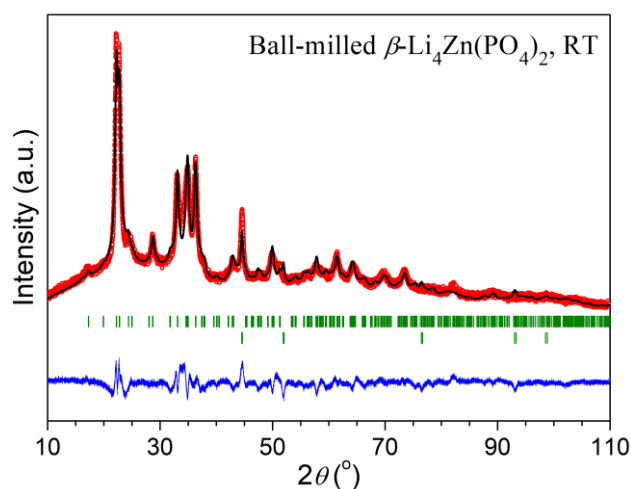


Figure II.17. Rietveld refinement of the XRD pattern of the ball-milled β - $\text{Li}_4\text{Zn}(\text{PO}_4)_2$ sample, measured at RT. The red circles, black continuous line, blue line and green tick bars represent the observed, calculated, and difference patterns, and Bragg positions, respectively.

The XRD pattern of the obtained powder shows broad peaks that can be nicely fitted with the structural model of the β -Li₄Zn(PO₄)₂ polymorph deduced earlier (Figure II.17). From the width of the Bragg peaks, we could further deduce that the ball-milled powder is made of particles with crystallites size of 10(±2) nm.

II.3.5 Stabilization of β -phase by aliovalent substitution

Chemical substitution was then explored as an alternative to ball milling to introduce disorder. More precisely, we attempted the partial substitution of Zn²⁺ with M = Al³⁺, Ga³⁺ and In³⁺ in Li₄Zn(PO₄)₂ with the hope to create disorder in Li-sublattice by introducing Li⁺ deficiency for charge compensation and hence to promote the β -phase stabilization. All samples of nominal compositions of Li_{4-x}Zn_{1-x}M_x(PO₄)₂ were prepared by quenching the pellet from the synthesis temperature (800°C). We found that Al³⁺ and In³⁺ are unable to form solid solutions with Li₄Zn(PO₄)₂, leading to impurity phases (Appendix Figure A1.3 and Appendix Figure A1.4).

This contrasts with the incorporation of Ga³⁺ that was successful for $x \leq 0.5$ mol pfu., beyond which secondary phases were found to form. The RT SXRD patterns of as-prepared Li_{4-x}Zn_{1-x}Ga_x(PO₄)₂ samples with $0 \leq x \leq 0.5$ are shown in Figure II.18 (and the XRD patterns in Figure II.19a). The Bragg peaks gradually shift towards higher 2θ angles, indicating that the unit cell volume decreases with insertion of Ga³⁺, as expected from the smaller ionic radii of Ga³⁺ versus Zn²⁺ (Figure II.19b and Figure II.18b). Moreover, low angle peaks gradually broaden and their intensity decreases with increasing the Ga content, prior to finally disappear completely for 0.3 mol Ga pfu.

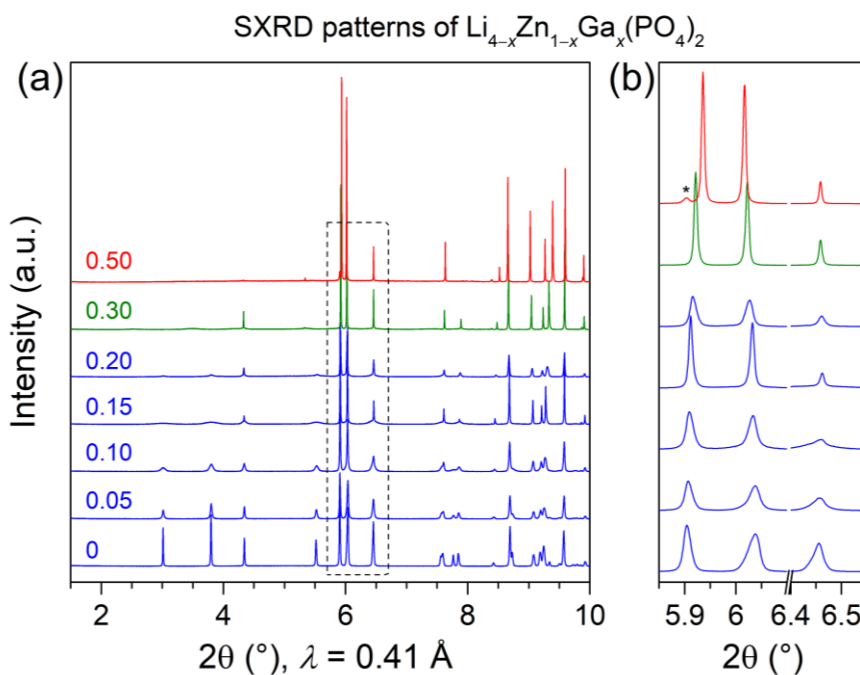


Figure II.18. SXRD patterns of the Li_{4-x}Zn_{1-x}Ga_x(PO₄)₂ samples. (a) SXRD patterns for the compositions with x values indicated in the figure. (b) Zoom of the SXRD patterns of selected 2θ range, marked in (a) with a rectangle. In (b), the peak marked by * is from some minor unknown impurity.

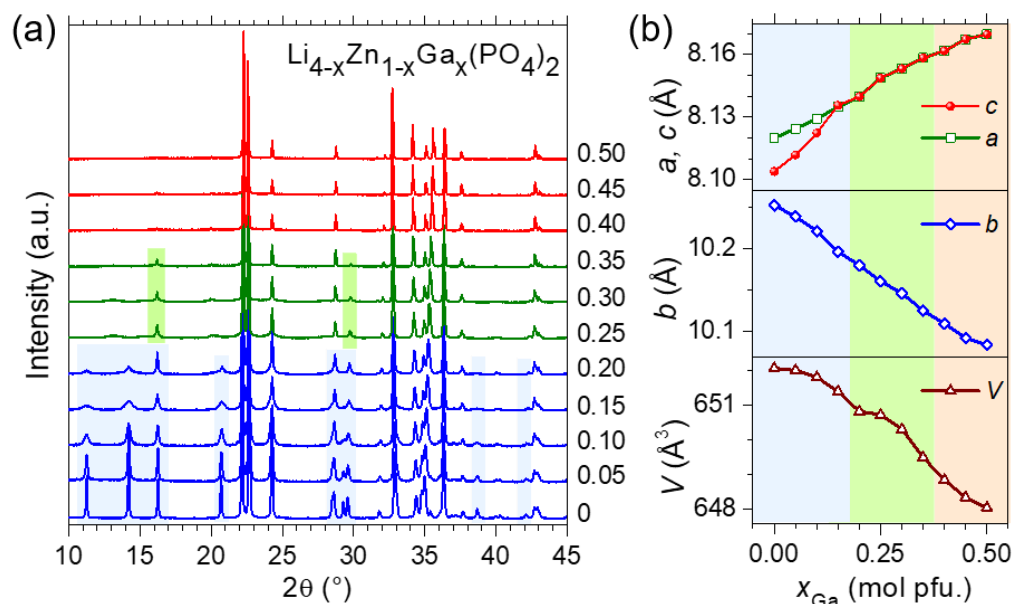


Figure II.19. XRD patterns of the $\text{Li}_{4-x}\text{Zn}_{1-x}\text{Ga}_x(\text{PO}_4)_2$ samples. (a) XRD patterns of the samples, measured at RT. In (a), and (b), the values of x corresponding to the patterns are indicated at the right. The patterns colored in blue, green and red corresponds to the α -, β' -, and β - polymorphs, respectively, and the peaks that disappear from the α - and β - phases have been indicated by blue and green backgrounds, respectively. (b) Evolution of lattice parameters with respect to Ga content. The lattice parameters have been converted to monoclinic unit cell setting for comparison. The blue, green, and red regions correspond to the α -, β' -, and β - phases, respectively.

II.3.6 Structural solution of the Ga-substituted phases

Note that for $x = 0.3$ the collected XRD/SXRD pattern appears similar, at first sight, to the one of the high temperature β - $\text{Li}_4\text{Zn}(\text{PO}_4)_2$ phase, hence suggesting that Ga-substitution is efficient to preserve some Li/Zn disorder even at RT. Taking a closer look at the $\text{Li}_{3.7}\text{Zn}_{0.7}\text{Ga}_{0.3}(\text{PO}_4)_2$ pattern, it appears that all peaks can be indexed with the same orthorhombic cell as β - $\text{Li}_4\text{Zn}(\text{PO}_4)_2$ with slightly smaller lattice parameters, $a = 4.9391(2)$ Å, $b = 6.4803(3)$ Å, $c = 10.1468(5)$ Å, and $V = 324.77(3)$ Å³. However the presence of peaks at 2θ values of 16.2° and 29.8° , rules out the $Pnma$ space group, and suggests its $P2_12_12_1$ subgroup (011 and 013 peaks, respectively).

A structural model was therefore constructed and Rietveld refined against both NPD and XRD patterns, simultaneously. The best structural model (shown in Figure II.16c), as deduced by combined NPD and XRD refinements (Figure II.20), was obtained by mixing Li and Zn on one site, and Li and Ga on another site. This structure (structural parameters are gathered in the Appendix Table A1.5) will be denoted as β' - hereafter, only differs from the β - structure by the fact that the $8d$ site in $Pnma$ splits into two crystallographic sites of multiplicity 4, indicating that introducing Ga segregates Zn and Ga on two distinct positions in $P2_12_12_1$, both of them being mixed with Li. Note that at high temperature (above 300°C , Appendix Figure A1.5a), the β' - $\text{Li}_{3.7}\text{Zn}_{0.7}\text{Ga}_{0.3}(\text{PO}_4)_2$ transforms to the β -phase (Appendix Figure A1.6)

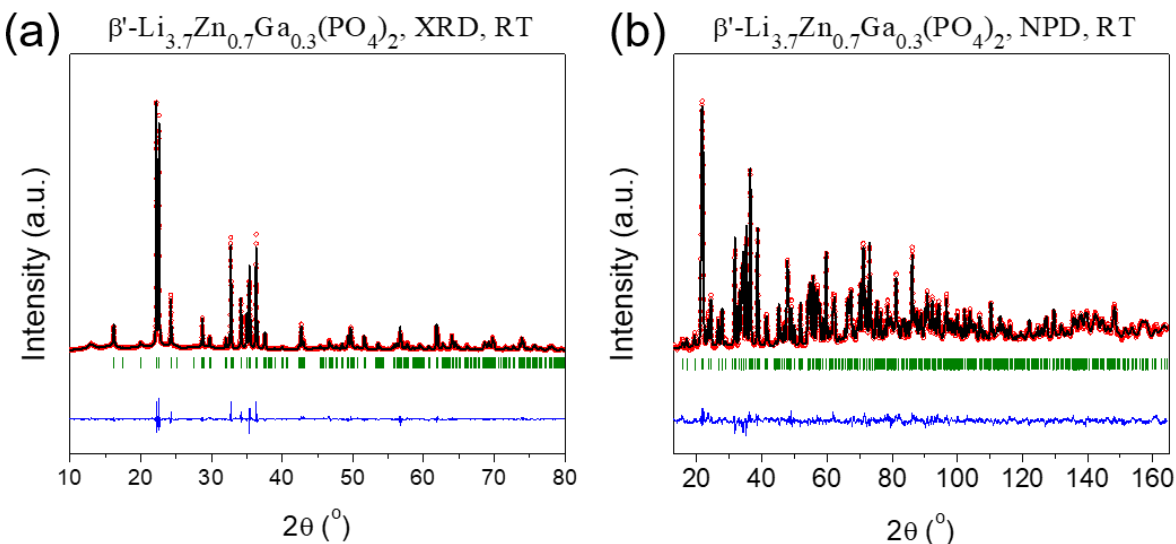


Figure II.20. Rietveld refinement of (a) XRD, and (b) NPD patterns of β' - $\text{Li}_{3.7}\text{Zn}_{0.7}\text{Ga}_{0.3}(\text{PO}_4)_2$, measured at RT. The red circles, black continuous line, blue line and green tick bars represent the observed, calculated, and difference patterns, and Bragg positions, respectively.

Further substitution of Zn with Ga leads to disappearance of the (011) and (013) peaks in the XRD patterns, as evident from Figure II.19b. This confirms the stabilization of the β -polymorph at RT with Ga concentration ≥ 0.35 mol pfu. The $\text{Li}_{3.5}\text{Zn}_{0.5}\text{Ga}_{0.5}(\text{PO}_4)_2$ compound produces a XRD pattern fully consistent with the $Pnma$ space group involving a full Li/Zn/Ga disorder, as the high temperature pure Zn compound. In order to deduce a structural model for Ga-substituted β -phase, we performed a combined Rietveld refinement of the NPD and XRD patterns of $\text{Li}_{3.5}\text{Zn}_{0.5}\text{Ga}_{0.5}(\text{PO}_4)_2$ recorded at RT, as shown in Figure II.21. The patterns could be fitted perfectly in $Pnma$ space group with lattice parameters of $a = 10.08917(3)$ Å, $b = 6.51079(2)$ Å, $c = 4.935843(16)$ Å, and $V = 324.16(5)$ Å³. The crystal structure is shown in Figure II.22 and the structural parameters are summarized in the Appendix Table A1.7.

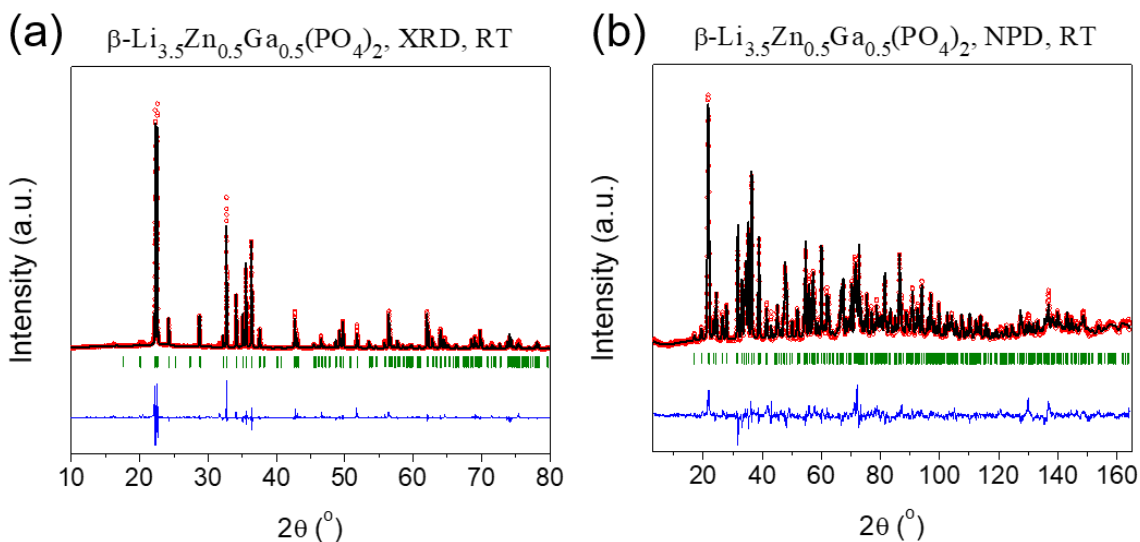


Figure II.21. Rietveld refinement of the RT XRD (a), and NPD (b) patterns of β - $\text{Li}_{3.5}\text{Zn}_{0.5}\text{Ga}_{0.5}(\text{PO}_4)_2$. The red circles, black continuous line, blue line and green tick bars represent the observed, calculated, and difference patterns, and Bragg positions, respectively.

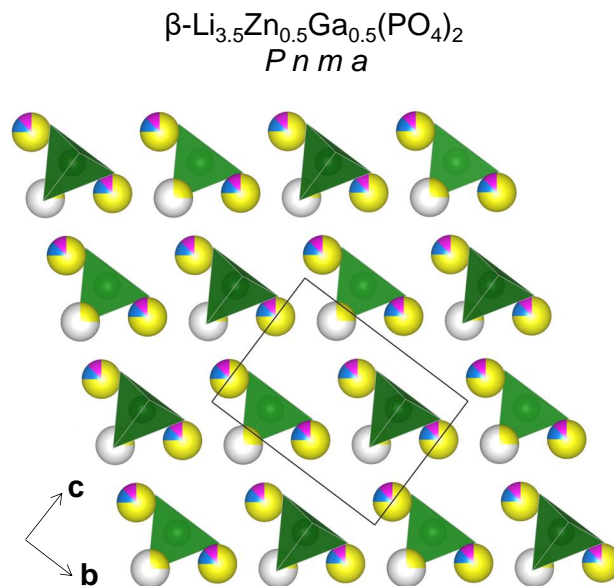


Figure II.22. Crystal structure of $\beta\text{-Li}_{3.5}\text{Zn}_{0.5}\text{Ga}_{0.5}(\text{PO}_4)_2$ at RT. The unit cell is shown in black parallelogram. For sake of clarity, only half of the unit cell content ($0 \leq y \leq \frac{1}{2}$ in the monoclinic setting) is shown. Li, Zn and Ga are shown in blue, yellow and pink, respectively and PO_4 tetrahedra are colored in green.

At this stage, it is worth reminding that all Ga-substituted samples mentioned previously were prepared by quenching from their synthesis temperature (800°C). Samples prepared by slow-cooling (sc) to RT ($1^\circ\text{C}/\text{min}$) show slight but notable discrepancy in the XRD patterns compared to those prepared by quenching, for Ga contents of $x \geq 0.3$. Two compounds, sc- $\text{Li}_{3.7}\text{Zn}_{0.7}\text{Ga}_{0.3}(\text{PO}_4)_2$ and sc- $\text{Li}_{3.5}\text{Zn}_{0.5}\text{Ga}_{0.5}(\text{PO}_4)_2$, were examined with special care. At RT, both samples present a XRD pattern characteristic of the β' -phase ($P2_12_12_1$) along with many additional small superstructure peaks. The temperature-dependent XRD study (Appendix Figure A1.5) of the compositions mentioned above shows that the XRD patterns of the sample transforms into the β structure ($Pnma$ space group, see Appendix Figure A1.6) above 380°C .

Finally, to confirm the phase transitions with temperature in the quenched Ga-substituted samples, we measured the DSC curve of all quenched samples. The data have been summarized in Figure II.23a and are in perfect agreement with high-temperature XRD experiments. We see that the phase-transition temperatures to the high temperature β phase slightly decrease with increased Ga content, while the enthalpy of the phase transition reduces drastically and finally disappears for $x_{\text{Ga}} = 0.45$. This confirms that the substitution creates Li^+ deficiency and an inherently disordered Li-sublattice, which in turn reduces the free energy associated with the ordering of Li-sublattice, eventually leading to stabilization of the disordered phase. Hence stabilization of the β -phase at RT can become

possible by quenching. The phase transitions in the Ga-substituted samples are summarized in the temperature-composition phase diagram in Figure II.23b, c.

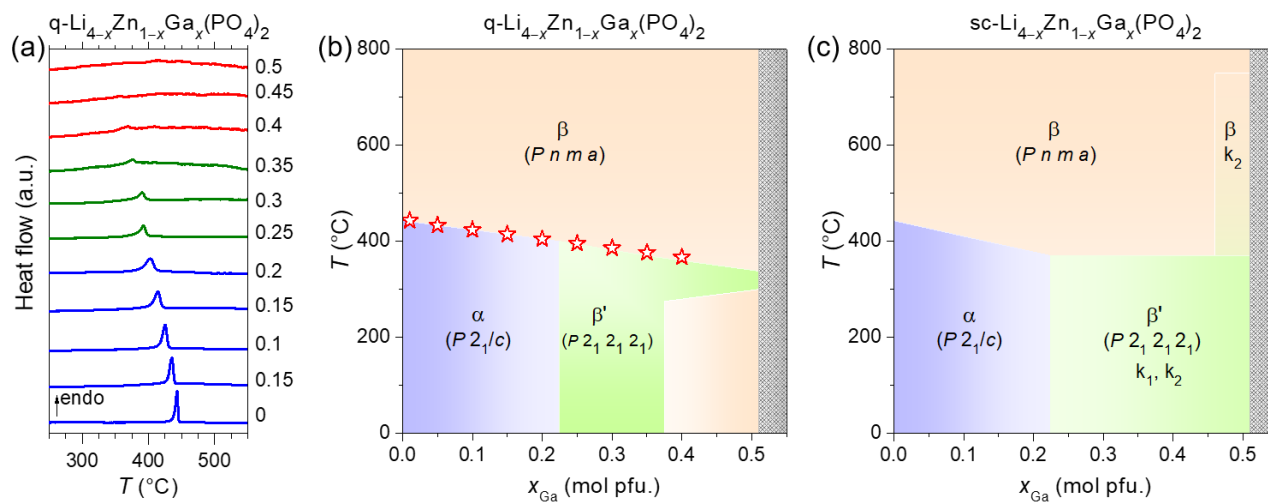


Figure II.23. DSC curves and simplified temperature-composition phase diagram of $\text{Li}_{4-x}\text{Zn}_{1-x}\text{Ga}_x(\text{PO}_4)_2$ samples. ‘q’ and ‘sc’ denotes the quenched and slow-cooled samples, respectively. (a) DSC curves of the samples, measured in air with a heating and cooling rate of $10\text{ }^\circ\text{C}/\text{min}$. The values of x corresponding to the patterns are indicated at the right. (b,c) The phase diagram, deduced from temperature-dependent XRD and DSC experiments (red stars). In (c), k_1 and k_2 are indicative of superstructure peaks. The black shaded region indicates the presence of secondary phases for Ga contents above 0.5 mol pfu .

II.3.7 Transition in Ionic Conductivity

We measured the ionic conductivity of all compounds by ac impedance spectroscopy over a broad frequency and temperature range. The impedance spectra were recorded on sintered pellets between ionically blocking platinum electrodes (see the Appendix section A1.1 for details). Figure II.24a shows a typical Nyquist impedance plot of the sintered pellets of the pristine $\text{Li}_4\text{Zn}(\text{PO}_4)_2$ sample at $300\text{ }^\circ\text{C}$. Each recorded spectra shows a depressed semicircle at high frequencies followed by a Warburg tail at lower frequency region. The low frequency spike represents the impedance response due to the blocking of mobile Li ions at the electrode interface with Pt electrode and it confirms that The total ionic conductivity (σ_{tot}) was obtained by using the value of intercept of the Warburg tail with the semicircle. We have explored the impedance spectra further by examining the depressed semicircle at high frequency. The depression of the semicircle cannot be accounted by the inhomogeneities at the sample-electrode interface, hence the need of deconvolution of the semicircle to separate the different contributions.

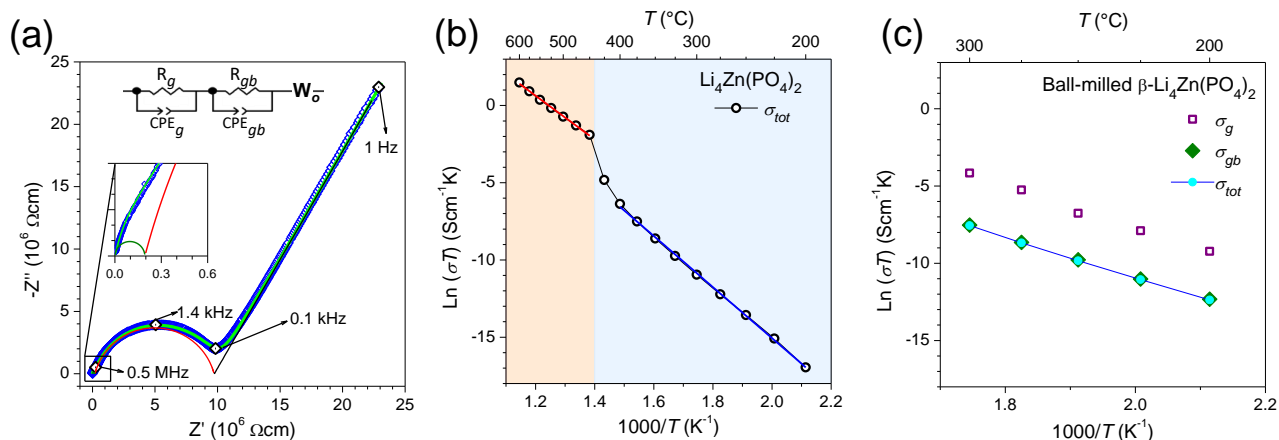


Figure II.24. Ionic conductivities of the $\text{Li}_4\text{Zn}(\text{PO}_4)_2$ sample. (a) Representative AC impedance spectra of $\text{Li}_4\text{Zn}(\text{PO}_4)_2$ sample recorded at 300 °C, the fitting has been shown by light green line on the curve. The deconvolution to different contributions, as obtained from the fitting, has been shown in the same curve and also zoomed in the inset. Contributions from the grains and grain boundary, has been indicated by green and red semicircles, respectively, and Warburg tail by black line. Some typical frequencies has also been indicated, the highest two of them are the resonance frequencies corresponding to grains and grain boundaries, respectively. Inset shows the equivalent circuit used to fit the spectra. Arrhenius plot of σ_{tot} of $\text{Li}_4\text{Zn}(\text{PO}_4)_2$ (b) and ball-milled $\beta\text{-Li}_4\text{Zn}(\text{PO}_4)_2$ (c); in (b) the blue and red background refers to α - and β - $\text{Li}_4\text{Zn}(\text{PO}_4)_2$ polymorph, respectively.

Since the impedance response of polycrystalline materials is expected to be composed of grain (bulk) and grain boundaries (surface) contributions, we decouple the semicircle to two contributions by fitting the whole impedance spectra to an equivalent circuit model $(R_g//Q_g)(R_{gb}//Q_{gb})W_o$ (inset of Figure II.24a); where R and Q represent the resistance and constant phase element associated with the grains (g) or grain boundaries (gb) of the sample, respectively, and W_o is the Warburg resistance. The fitting produces an capacitances of $\sim 10^{-12}$ F and $\sim 10^{-11}$ F associated with the constant phase element, for the high and low frequency deconvoluted semicircles, respectively and hence can be assigned to grains (σ_g) and grain boundaries (σ_{gb}) contributions, respectively²¹⁶. A typical fitting is shown in Figure II.24a. This assignment was further confirmed by calculating the characteristic resonance frequencies (f_r) of the semicircles which generally appear at the apexes of the deconvoluted semicircles; as indicated in Figure II.24a. However, with increasing temperature, both grains and grain boundary responses gradually shift towards higher frequencies and finally move beyond the measurable frequency window of the instrument leaving only the Warburg tail observable. Hence deconvolution of grain conductivity (σ_g) and grain boundary conductivity (σ_{gb}) was not possible above ~ 300 -400 °C for the samples and only σ_{tot} was obtained.

The variations of the ionic conductivity for the pristine $\text{Li}_4\text{Zn}(\text{PO}_4)_2$ over a temperature range are shown in Figure II.24b. There is a linear variation for the $\ln(\sigma T)$ with temperature, indicative of a thermally activated Arrhenius type behavior $\sigma(T) = A/T \cdot \exp(-E_a/k_B T)$, where k_B is the Boltzmann constant, A is a pre-exponential factor and T is temperature). The RT σ_b , σ_{gb} , and σ_{tot} values of $\sim 5.5 \cdot 10^{-18}$, $\sim 3.5 \cdot 10^{-19}$, and $\sim 1.8 \cdot 10^{-19}$ S·cm⁻¹, respectively, were deduced by linear extrapolation of the Arrhenius

plot to the RT, with a similar E_a of ~ 1.3 eV for all the conduction processes. Altogether, this implies that this compound is not a good conducting material at low temperature, at least in its α -form.

We measured the conductivity of the pristine $\text{Li}_4\text{Zn}(\text{PO}_4)_2$ sample over a broader temperature range of 200 - 600 °C and reported the measured σ_{tot} values in Figure II.24b. A sudden change in the slope of the Arrhenius plot occurs at ~ 425 °C; temperature at which the $\alpha \rightarrow \beta$ structural transition was shown to occur. Note that the high temperature β - $\text{Li}_4\text{Zn}(\text{PO}_4)_2$ polymorph shows a much higher conductivity with an E_a of 1.1 eV and a RT σ_{tot} of $1.8 \times 10^{-15} \text{ S}\cdot\text{cm}^{-1}$. For sake of completion we also measured the transport properties of our new RT β - $\text{Li}_4\text{Zn}(\text{PO}_4)_2$ phase obtained by ball-milling of the α - $\text{Li}_4\text{Zn}(\text{PO}_4)_2$ phase (Figure II.24c). Interestingly, the ball-milled β - sample shows an extrapolated RT σ_{tot} value of $2.4 \cdot 10^{-15} \text{ S}\cdot\text{cm}^{-1}$, nearly similar to that obtained from the high-temperature β -phase of $\text{Li}_4\text{Zn}(\text{PO}_4)_2$ with however a slightly lower activation energy ($E_a = 1.0$ eV). We exploited this data further by decoupling the grains and grain boundaries contributions and found activations energies of 1.1 and 1.0 eV, respectively, with corresponding RT conductivities of $1.7 \cdot 10^{-14} \text{ S}\cdot\text{cm}^{-1}$ (σ_g) and $3 \cdot 10^{-15} \text{ S}\cdot\text{cm}^{-1}$ (σ_{gb}). Overall, this further confirms the better transport properties of the β -polymorph even when prepared at RT.

II.3.8 Higher conductivity in RT-stabilized phases

Encouraged by these findings, we also explored the transport properties of the quenched $\text{Li}_{4-x}\text{Zn}_{1-x}\text{Ga}_x(\text{PO}_4)_2$ samples. The results, shown in Figure II.25, reveal a steady increase of the ionic conductivities together with a progressive smearing of the jump in conductivity at the $\alpha \rightarrow \beta'/\beta$ transition with increasing the Ga^{3+} substitution (x_{Ga}). More specifically, the change of slope in conductivity at the structural transition gradually decreases till a Ga^{3+} content of 0.15 pfu. and then disappears completely with further increase of Ga content. This is consistent with the results obtained from XRD experiments which show that the β' -phase is formed beyond $x_{\text{Ga}} = 0.25$ and also from DSC measurements which indicate a shift/smearing of the phase transition with increasing x_{Ga} content.

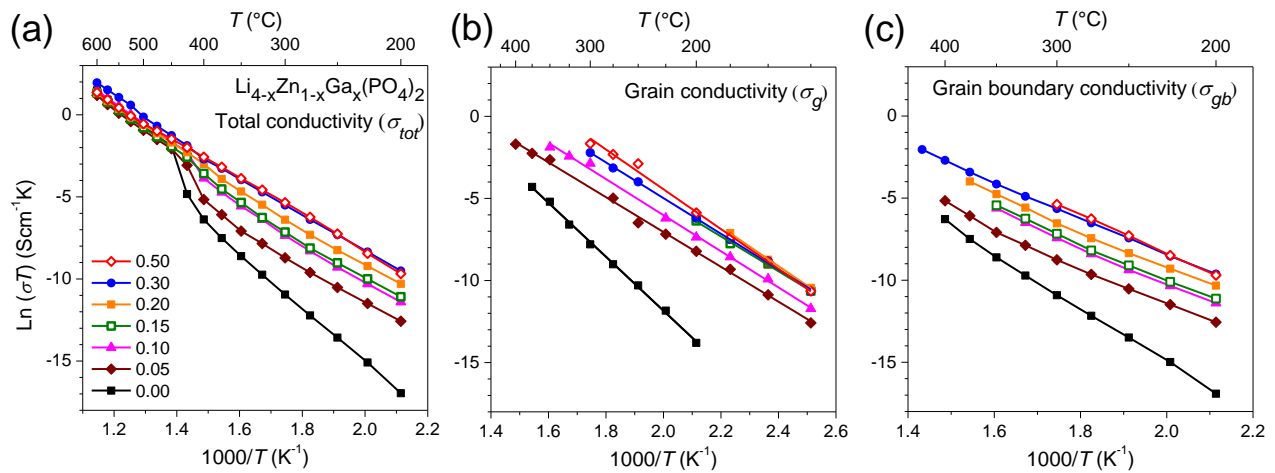


Figure II.25. Arrhenius plot ionic conductivity of $\text{Li}_{4-x}\text{Zn}_{1-x}\text{Ga}_x(\text{PO}_4)_2$ samples. The σ_{tot} (a), σ_g (b) and σ_{gb} (c) are shown. Values of x are indicated in (a).

Table 3. Ionic conductivities of the $\text{Li}_{4-x}\text{Zn}_{1-x}\text{Ga}_x(\text{PO}_4)_2$ samples at RT obtained by extrapolation of the Arrhenius plot and at 200 °C and their activation energies (E_a).

x_{Ga}		σ_g ($\text{S}\cdot\text{cm}^{-1}$)			σ_{gb} ($\text{S}\cdot\text{cm}^{-1}$)			σ_{tot} ($\text{S}\cdot\text{cm}^{-1}$)		
		RT	200 °C	E_a (eV)	RT	200 °C	E_a (eV)	RT	200 °C	E_a (eV)
α -	0	$5.6\cdot 10^{-18}$	$2.1\cdot 10^{-9}$	1.32	$3.5\cdot 10^{-19}$	$9.5\cdot 10^{-11}$	1.30	$3.6\cdot 10^{-19}$	$9.1\cdot 10^{-11}$	1.3
	0.05	$1.4\cdot 10^{-12}$	$5.7\cdot 10^{-7}$	0.87	$4.2\cdot 10^{-14}$	$7.4\cdot 10^{-9}$	0.82	$4.1\cdot 10^{-14}$	$7.3\cdot 10^{-9}$	0.82
	0.1	$1.9\cdot 10^{-12}$	$1.3\cdot 10^{-6}$	0.92	$8.3\cdot 10^{-14}$	$2.4\cdot 10^{-8}$	0.85	$8.1\cdot 10^{-14}$	$2.3\cdot 10^{-8}$	0.85
	0.15	$6.5\cdot 10^{-12}$	$3.6\cdot 10^{-6}$	0.89	$2.7\cdot 10^{-13}$	$3.1\cdot 10^{-8}$	0.79	$1.8\cdot 10^{-13}$	$3.1\cdot 10^{-8}$	0.82
	0.2	$5.2\cdot 10^{-12}$	$1.9\cdot 10^{-6}$	0.95	$3.5\cdot 10^{-13}$	$6.9\cdot 10^{-8}$	0.82	$3.4\cdot 10^{-13}$	$6.7\cdot 10^{-8}$	0.83
β' -	0.25	$6\cdot 10^{-12}$	$5.9\cdot 10^{-6}$	0.93	$4.9\cdot 10^{-13}$	$1.1\cdot 10^{-7}$	0.84	$4.5\cdot 10^{-13}$	$1.1\cdot 10^{-7}$	0.84
	0.3	$5.7\cdot 10^{-12}$	$4.3\cdot 10^{-6}$	0.91	$3.9\cdot 10^{-13}$	$1.4\cdot 10^{-7}$	0.86	$3.6\cdot 10^{-13}$	$1.4\cdot 10^{-7}$	0.87
β -	0.4	$5.6\cdot 10^{-12}$	$9.2\cdot 10^{-6}$	0.95	$2.1\cdot 10^{-13}$	$8.7\cdot 10^{-8}$	0.88	$2.7\cdot 10^{-13}$	$8.6\cdot 10^{-8}$	0.87
	0.5	$1.6\cdot 10^{-12}$	$5.9\cdot 10^{-6}$	1.02	$1.4\cdot 10^{-13}$	$1.3\cdot 10^{-7}$	0.93	$1.3\cdot 10^{-13}$	$1.3\cdot 10^{-7}$	0.93

Further insight onto these transport properties of members of the $\text{Li}_{4-x}\text{Zn}_{1-x}\text{Ga}_x(\text{PO}_4)_2$ series can be gained by further analyzing the impedance data with the key values reported in Table 3. Firstly, there is an increase by several orders of magnitude of the σ_g RT values with increasing the x_{Ga} content so that σ_g of $\sim 1\text{--}2 \times 10^{-12} \text{ S}\cdot\text{cm}^{-1}$ can be obtained for $x_{\text{Ga}} = 0.05$, and 0.10 as compared to $\sigma_g = 5.55 \cdot 10^{-18} \text{ S}\cdot\text{cm}^{-1}$ for $x_{\text{Ga}}=0$, while structure-wise the samples are still pertaining to the α -phase in the composition range. Such an effect is most likely nested in the increasing amount of disorder that we can spot by XRD from the broadening of Bragg reflections characterizing the α -polymorph (Figure II.19b). Moreover, we notice a drastic fall in the E_a to 0.8 and 0.9 eV, respectively for the above-mentioned compositions. Interestingly, we could observe that σ_{gb} tracks σ_g and increases to $\sim 4\text{--}8 \times 10^{-14} \text{ S}\cdot\text{cm}^{-1}$ at RT, with σ_{tot} reaching $\sim 4\text{--}8 \times 10^{-14} \text{ S}\cdot\text{cm}^{-1}$ at RT. Upon further increasing the x_{Ga} content beyond 0.05, the RT σ_g values slightly increase prior to saturate at values of $\sim 6 \times 10^{-12} \text{ S}\cdot\text{cm}^{-1}$ (β -phase, Table 3) while structure-wise the compounds evolve from the α -phase to the β' -phase. Similarly, σ_{gb} follows the same variation over this composition range while the activation energy remains nearly constant. It is only for samples having higher Ga contents ($x_{\text{Ga}} > 0.40$) and crystallizing in the β -structure that we observe a noticeable decrease in σ_g to $\sim 2 \times 10^{-12} \text{ S}\cdot\text{cm}^{-1}$ and an increase in E_a from 0.9 to 1.0 eV. Altogether, these findings fail to establish a direct correlation between structure and conductivity and further analysis is required to interpret this trend. Nevertheless, the ac conductivity is ionic in nature, and this was further confirmed by direct current (DC) polarization experiments, which indicates that the electronic contribution is negligible, see Figure II.26.

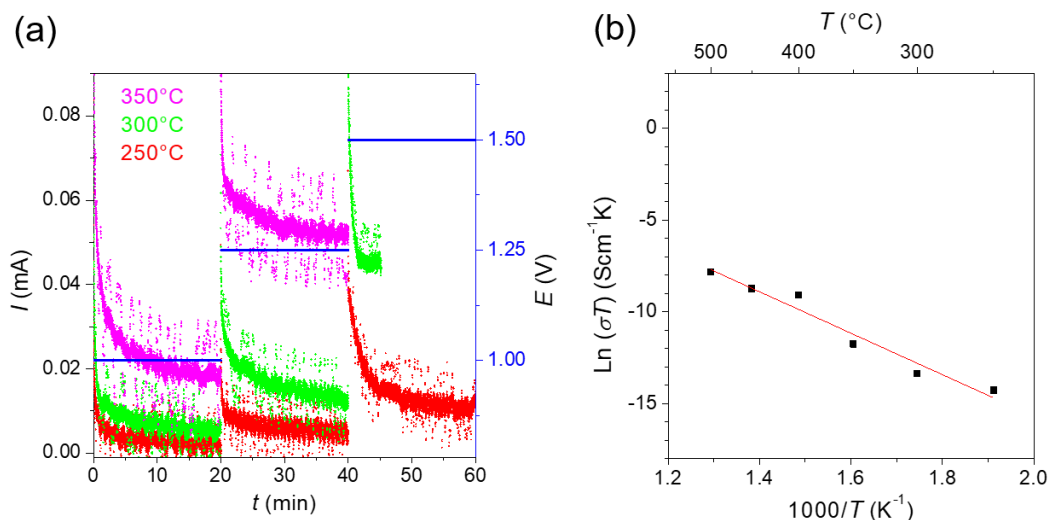


Figure II.26. DC polarization of β' - $\text{Li}_{3.7}\text{Zn}_{0.7}\text{Ga}_{0.3}(\text{PO}_4)_2$ sample. (a) DC polarization plots at different potentials and temperatures, and, (b) Arrhenius plot of DC conductivity of the sample.

II.3.9 Conduction mechanism

To retrieve qualitative information concerning the connection existing between structure and conductivity, BVEL was employed. The BVEL maps representing the Li^+ conduction pathways in the $\text{Li}_{4-x}\text{Zn}_{1-x}\text{Ga}_x(\text{PO}_4)_2$ polymorphs are shown in Figure II.27. For α - $\text{Li}_4\text{Zn}(\text{PO}_4)_2$, infinite 2-D Li^+ percolation paths, involving Li2, Li3 and Li4 sites and not the sterically hindered Li1 site, appear along the b-c plane at 1.05 eV above the minimum energy. This is fully consistent with its layered crystal structure and Li^+ percolation occurs along the layers, whereas hopping of Li^+ between layers is not possible because of the Zn hindrance between the Li layers. This explains the high E_a and very low σ_g of the sample.

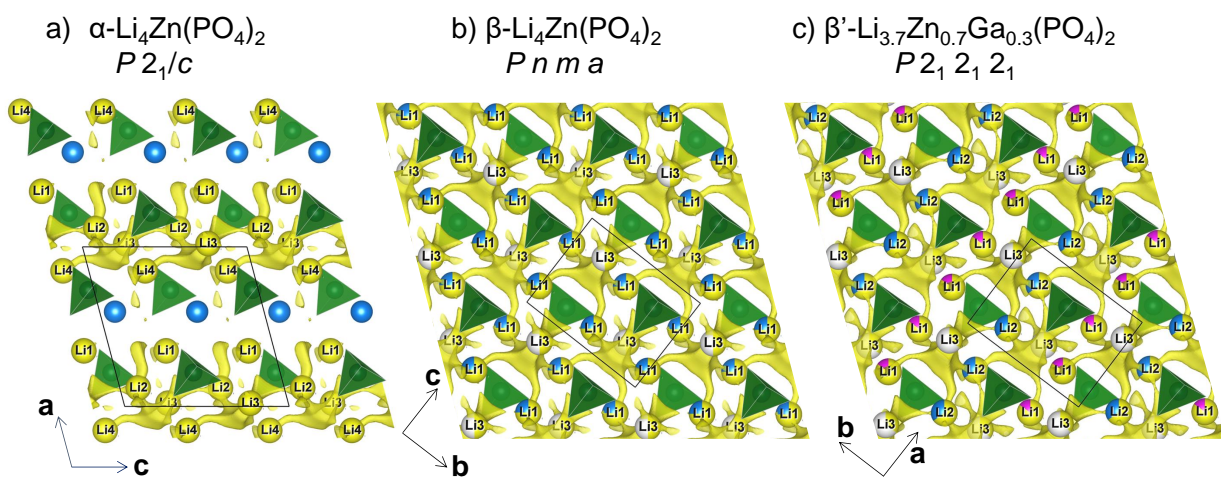


Figure II.27. BVEL of (a) α - $\text{Li}_4\text{Zn}(\text{PO}_4)_2$, (b) β - $\text{Li}_4\text{Zn}(\text{PO}_4)_2$ and (c) β' - $\text{Li}_{3.7}\text{Zn}_{0.7}\text{Ga}_{0.3}(\text{PO}_4)_2$ at the percolation energies. The yellow domains indicates the migration paths for Li^+ in the structure, obtained using an iso-surface value of 1.05, 0.7, and 0.9 eV above the minimum energy, respectively.

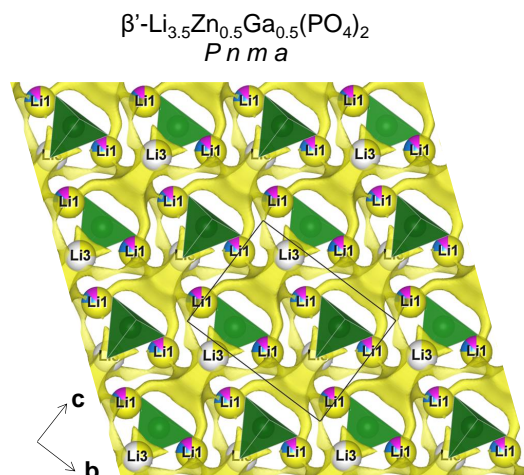


Figure II.28. BVEL of β' -Li_{3.5}Zn_{0.5}Ga_{0.5}(PO₄)₂, at the percolation energies. The yellow domains indicate the migration paths for Li⁺ in the structure, obtained using an iso-surface value of 1.1 eV above the minimum energy.

For the high temperature β -Li₄Zn(PO₄)₂ and β' -Li_{3.7}Zn_{0.7}Ga_{0.3}(PO₄)₂ phases, BVEL maps indicate a 3-D Li⁺ percolation at 0.7 and 0.9 eV above the minimum energy, respectively. This comes in no surprise, because, in β - and β' -phases, the mixing between Li and Zn/Ga atoms on the same crystallographic positions breaks the layered nature of the α -polymorph, for which Li atoms are confined in the b-c planes. Thus in the β - and β' -polymorphs, Li ions can hop from sites to sites three-dimensionally. This is consistent with the lower E_a in the β - and β' - sample compared to the α -phase. Moreover, in β'/β - structures that present the same (PO₄)³⁻ framework, Li3 is the only Li site not being mixed with Zn or Ga which accommodates the vacancies resulting from the charge compensation, (Figure II.27), and BVEL maps indicate that ionic conduction takes place preferentially through this site. Therefore, this explains the little changes in σ_g values when the structure changes from β' to β -Li_{3.5}Zn_{0.5}Ga_{0.5}(PO₄)₂.

Although BVEL could account for the greater conductivity for the β'/β -polymorph as opposed to the α -one, the feasibility to obtain ionic conductivities for the α -polymorph as high as the β -phase at low Ga substitution level is not well understood. First let's recall that ionic conductivity is the result of a delicate balance between vacancies, disorder, and defects among others¹²⁵. Numerous ionic conductors show order-disorder phase transition with the high temperature phase having usually a higher ionic conductivity, owing to its higher structural symmetry which flattens the potential landscape hence leading to reduced activation barrier for Li⁺ jump as well as to its enhanced disorder that increases the number of energy equivalent Li-sites having partial occupancies.²¹⁷ The Ga-substitutions, besides promoting structural disorder in the samples, introduces Li vacancies. However, the role of the vacancies remains questionable for the above observation as the ionic conductivity is nearly similar for α -Li_{3.9}Zn_{0.9}Ga_{0.1}(PO₄)₂ and β' -Li_{3.9}Zn_{0.9}Ga_{0.1}(PO₄)₂. To understand the respective contributions of vacancies and disorder, we plotted the variation of the log(σ_g) as a function of the concentration of Li vacancies and of the broadening of the Bragg peaks characteristic to the α -polymorph as an estimation

of disorder in the samples, see Figure II.29. Note that the ionic conductivity drastically increases with increasing the amount of vacancies ($x = 0.05$) with afterwards another increase from $x = 0.15$ which seems to be related to an increase in structural disorder. We thus believe that the disorder, as evidenced from the peak broadening which indicates the presence of antiphase boundaries and/or small disordered β'/β domains in the structure, as was also observed in rocksalt-type oxides,²¹⁸ could trigger β'/β -like conduction even at low Ga-substitution level.

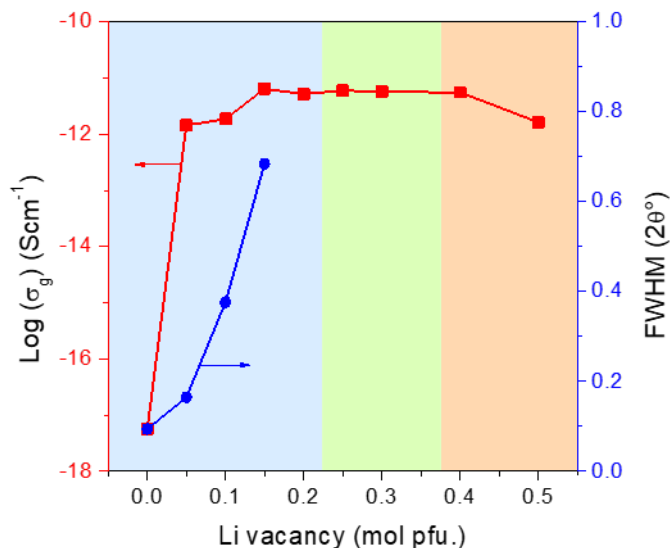


Figure II.29. Variation of ionic conductivity and broadening of XRD peak with concentration of Li vacancy. The (100) peak of the XRD pattern at $2\theta = 16.3^\circ$ was chosen to estimate the FWHM. The light blue, green and red background represent α -, β' -, and β - polymorphs, respectively.

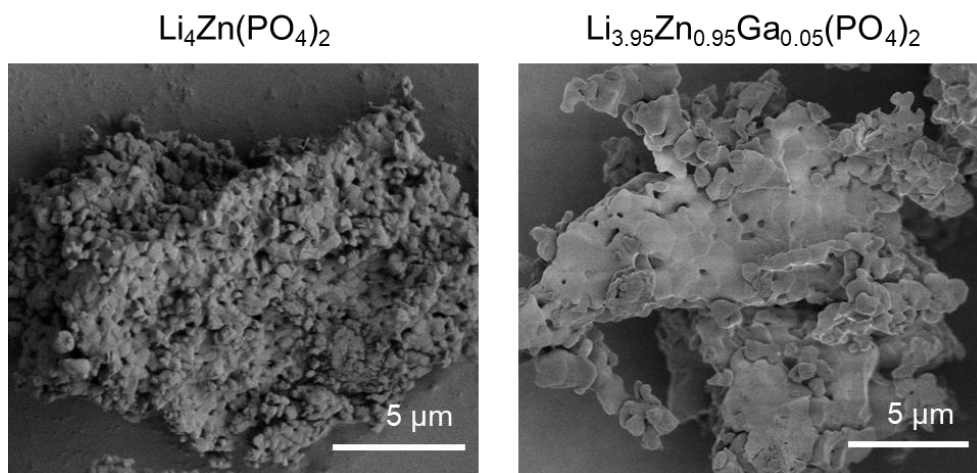


Figure II.30. FESEM images of the cross-section of the sintered pellets.

Additionally, the conductivity of a sample depends upon the surface contact of a grain with its neighbors, hence stressing the importance of grain boundaries vs. grain. A simultaneous increase of (σ_b) and (σ_{gb}) with increasing the doping content is frequently reported^{219,220}. Our samples, being synthesized and sintered identically, are expected to have similar grain size and surface contacts. Thus for compounds having the highest conducting grains, the number of charge carriers crossing the grain

boundaries will be greater as well, hence providing a possible explanation to the systematic tracking of grain and grain boundary conductivities observed in our samples. Furthermore, we have collected FESEM images of the cross-sections of pellets of $\text{Li}_4\text{Zn}(\text{PO}_4)_2$, and $\text{Li}_{3.95}\text{Zn}_{0.95}\text{Ga}_{0.05}(\text{PO}_4)_2$, and they are shown in Figure II.30. As evident, Ga-substitution improves the grain boundaries also, which could be another reason for the improvement of the grain boundary conductivity. However, further studies, such as, TEM studies on grain boundaries for space charge region,²²¹ or for amorphous second phase,²²² etc., are needed to understand this behaviour. Next we extended our studies to Na-ion conductors, to study the implications in structural and conductivity aspects, when Li is replaced by Na.

II.4 $\text{Na}_4\text{Zn}(\text{PO}_4)_2$

Conductivity in the Na-counterparts of these Li-phases, i.e., $\text{Na}_6\text{Zn}(\text{P}_2\text{O}_7)_2$, and $\text{Na}_4\text{Zn}(\text{PO}_4)_2$, were not explored before in the literature. Our effort to synthesize the $\text{Na}_6\text{Zn}(\text{P}_2\text{O}_7)_2$ was not successful (shown in the Appendix Figure A1.7). In contrast, the $\text{Na}_4\text{Zn}(\text{PO}_4)_2$ could be successfully synthesized, as indicated by Irvine and West (1989),²²³ which can be visualized as Zn-substituted Na_3PO_4 . Indeed Na_3PO_4 based systems are quite interesting, because they comprise dynamic rotational disorders in the anionic sublattice, which can provide an extra parameter for ionic conductivity, alongside the usual cationic disorder. The rotational disorders can enhance ionic conductivity, by the “paddle wheel” mechanism, where the cation hopping is accompanied by a simultaneous rotation of the anion leading to lowering of the activation barrier for Na-hopping.^{224–226} Indeed research in 1980s on Na_3PO_4 showed quite promising Na-conductivity, as it shows high ionic conductivity, $\sim 5 \cdot 10^{-3} \text{ S} \cdot \text{cm}^{-1}$ at 300 °C.^{224,227,228} At RT, if quenched, it crystallizes into tetragonal polymorph (space group $P\bar{4}2_1c$), which progressively transforms to hydrated phases with time by absorbing moisture.^{228–230} The tetragonal polymorph has been stabilized at RT by making solid solution with AlPO_4 , Na_2SO_4 , and Na_4SiO_4 , but without any significant improvement in ionic conductivity yet.^{227,231} Therefore, the Na_3PO_4 based systems not only provide an excellent playground to solid state chemists, but also significantly interesting to design new Na-ionic conductors.

II.4.1 Polymorphism in $\text{Na}_4\text{Zn}(\text{PO}_4)_2$

$\text{Na}_4\text{Zn}(\text{PO}_4)_2$ was synthesized by solid state reactions of Na_2CO_3 , ZnO , and $\text{NH}_4\text{H}_2\text{PO}_4$ in stoichiometric amounts, at 700 °C (details in the Appendix Section A1.1). As-synthesized $\text{Na}_4\text{Zn}(\text{PO}_4)_2$ samples present different X-ray diffraction (XRD) patterns when the pellet is recovered by quenching from 700 °C (denoted hereafter as β -polymorph), or by cooling slowly (1 °C/min) to RT (denoted hereafter as α -polymorph), see the patterns at 50 °C in Figure II.31a,c. The origin of the differences in the XRD patterns were investigated by probing the temperature-dependent structural evolution of the as-synthesized $\text{Na}_4\text{Zn}(\text{PO}_4)_2$ samples, as described next.

Figure II.31a,b summarizes the evolution of the XRD patterns with temperature of α - $\text{Na}_4\text{Zn}(\text{PO}_4)_2$. During heating (1 °C/min), a phase transition at 380 - 400 °C is observed, characterized by disappearance of many diffraction peaks to keep only a few and transforms to the HT γ -polymorph (Figure II.31a). On cooling, when cooled slowly (1 °C/min), two phase transitions are observed, at ~320 °C and ~260 °C, respectively, and the sample transforms back to the α -polymorph, as observed from the evolution of the XRD patterns (Figure II.31b). Hence on slow-cooling an intermediate β - phase is observed, whose pattern only differs from the γ - phase by the presence of a peak at $2\theta = 35.8^\circ$. This indicates that the γ and β structure are very close, as will be shown later. If the sample is quenched during synthesis, the β phase can be stabilized at RT (Figure S1). However the β - $\text{Na}_4\text{Zn}(\text{PO}_4)_2$ is a metastable phase, as the phase converts to the thermodynamically stable α -phase upon mild heating above ~ 260 °C, as evidenced in Figure II.31c.

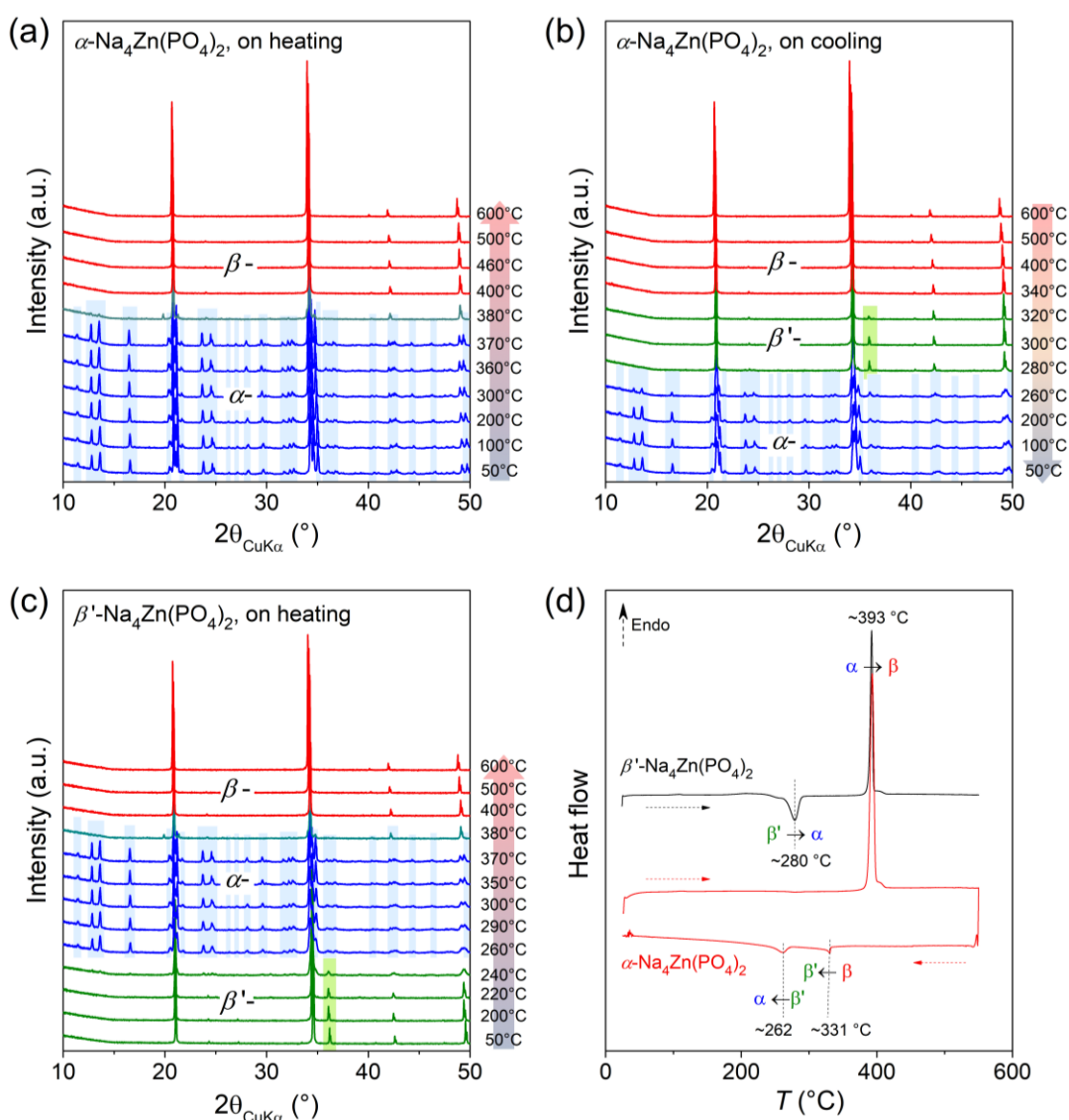


Figure II.31. Evolution of as-synthesized $\text{Na}_4\text{Zn}(\text{PO}_4)_2$ with temperature. (a-b) Evolution of the XRD patterns of the α - $\text{Na}_4\text{Zn}(\text{PO}_4)_2$ sample (prepared by slow-cooling) on heating (a), and following

slow-cooling (b). (c) Evolution of the XRD patterns of the β - $\text{Na}_4\text{Zn}(\text{PO}_4)_2$ sample (prepared by quenching) on heating. For heating and cooling, a rate of 1 °C/min was used. The corresponding temperatures are indicated at the right side of the XRD patterns. (d) DSC curves of the $\text{Na}_4\text{Zn}(\text{PO}_4)_2$ samples measured in air (with a rate of 10 and 5 °C/min, respectively).

The phase transitions were further probed by differential scanning calorimetry (DSC) and are summarized in Figure II.31d. The DSC curve of α - $\text{Na}_4\text{Zn}(\text{PO}_4)_2$ (red curve) shows the $\alpha \rightarrow \gamma$ transition (endothermic) at ~393 °C. During cooling, two exothermic transitions were observed, peaking at ~331, and 280 °C, corresponding to the $\gamma \rightarrow \beta$, and $\beta \rightarrow \alpha$, respectively. This observation is fully consistent with the evolution of XRD patterns, as discussed above. The DSC trace of the quenched β - $\text{Na}_4\text{Zn}(\text{PO}_4)_2$ was also recorded. For this sample, as expected an exothermic $\beta \rightarrow \alpha$ transition was observed at ~280 °C, prior the endothermic $\alpha \rightarrow \gamma$ transition. Interestingly, this kinetic behaviour is different than what was observed in the Li-counterpart of this compound, $\text{Li}_4\text{Zn}(\text{PO}_4)_2$, that was reported previously.

II.4.2 Structural solutions

The newly synthesized $\text{Na}_4\text{Zn}(\text{PO}_4)_2$ not only shows polymorphic behaviour under the influence of temperature, but also presents interesting kinetic behaviour owing to the presence of Na. Hence, to explain the phenomena, we first explored the crystal structures of the polymorphs in detail. The structures were attempted to solve by studying their selected area electron diffraction (SAED) patterns, SXRD, and neutron powder diffraction (NPD) patterns and are described below.

a) Structure of γ - $\text{Na}_4\text{Zn}(\text{PO}_4)_2$

The structure of γ - $\text{Na}_4\text{Zn}(\text{PO}_4)_2$ was solved by treating its SXRD pattern (collected at 500 °C), which can be indexed in the $Fm\bar{3}m$ space group with lattice parameter $a = 7.46901(4)$ Å, i.e., a structure similar to the one adopted by γ - Na_3PO_4 , with a slightly smaller (3%) unit cell.²³² Several structural models were constructed from Na_3PO_4 , replacing one Na by one Zn and a vacancy, either on the $8c$ or on the $4b$ Wyckoff sites. The best Rietveld refinement was obtained by placing Na and Zn on the $8c$ site, while the $4b$ site is only 50% occupied by Na. O was placed on the $96k$ site, instead of $24e$ in γ - Na_3PO_4 , so that this structure exhibits a fully rotational disorder on PO_4 with are seen as balls. The final refinement is shown in Figure II.36 and the structural parameters are gathered in Appendix Table A1.8.

b) Structure of β - $\text{Na}_4\text{Zn}(\text{PO}_4)_2$

The structure of β - $\text{Na}_4\text{Zn}(\text{PO}_4)_2$ was solved using SXRD and NPD patterns recorded on a quenched sample. As mentioned before, the XRD pattern of the β -phase shows one extra peak compared to the γ pattern. This indicates a close relation between both structures. Indexation of these peaks requires a doubling of the cubic unit cell parameters (see Figure S2). The pattern can be indexed with the cubic $F23$ space group and lattice parameter $a = 14.786037(10)$ Å. Structural models were constructed from the high temperature γ -structure, and refined against both SXRD and NPD patterns. Thus, the obtained model led to a good Rietveld refinement, as shown in Figure II.33. The structural model is summarized in Appendix Table A1.9 and the resulting structure is shown in Figure 6.

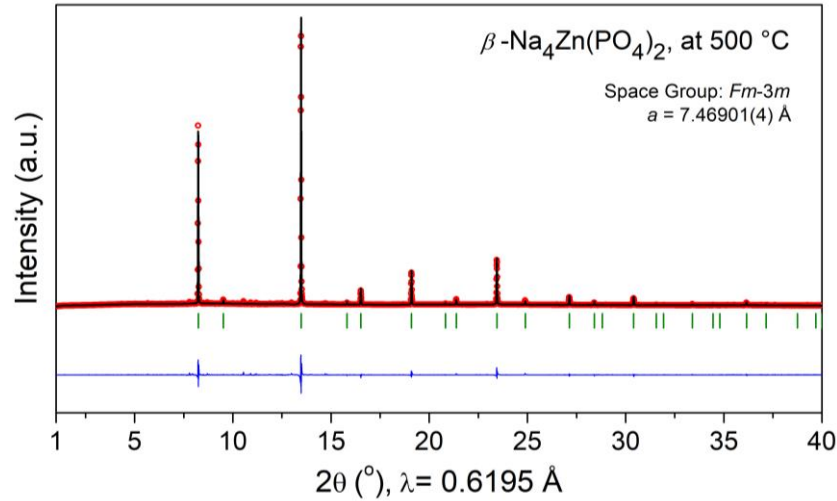


Figure II.32. Rietveld refinement of the SXRD pattern of β - $\text{Na}_4\text{Zn}(\text{PO}_4)_2$ recorded at 500 °C. For symbol code, refer to the Figure II.31.

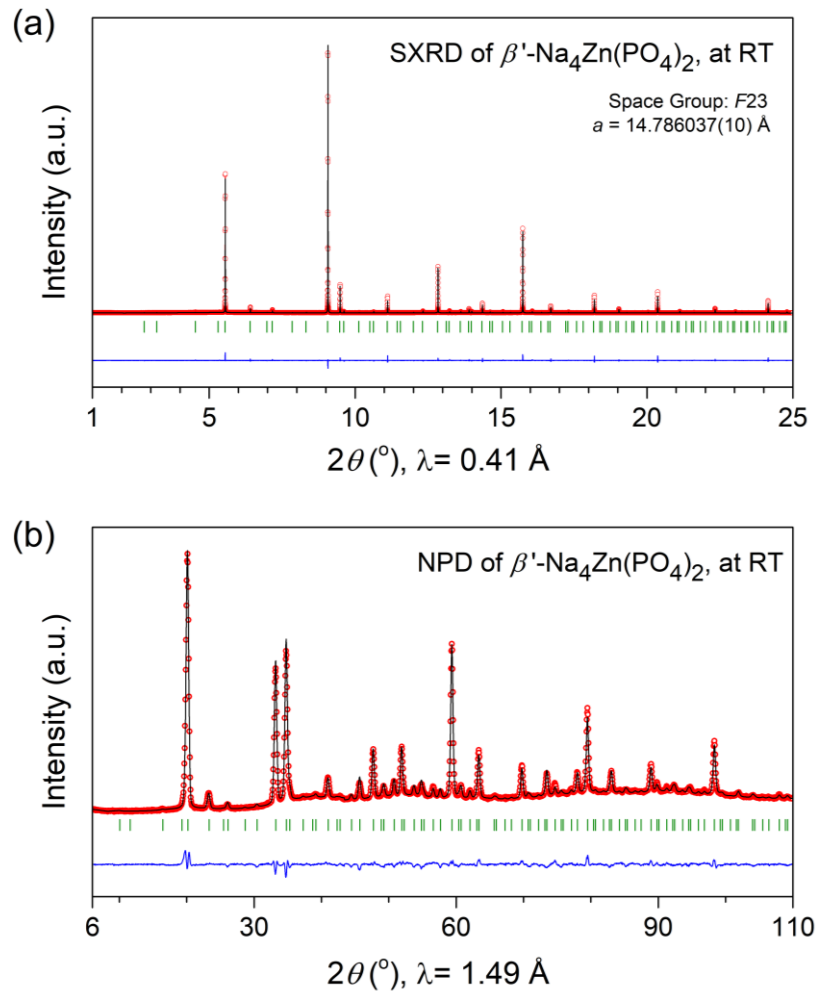


Figure II.33. Combined Rietveld refinement of the SXRD (a), and NPD (b) patterns of β - $\text{Na}_4\text{Zn}(\text{PO}_4)_2$ recorded at RT. For symbol code, refer to the Figure II.31.

In β - $\text{Na}_4\text{Zn}(\text{PO}_4)_2$, the distribution of Na, Zn and vacancies is similar as in γ - $\text{Na}_4\text{Zn}(\text{PO}_4)_2$. The main difference, and reason for the doubling of the lattice parameter, is that 75% of the PO_4 groups get ordered (namely P2 linked to O21 and O22) and are no longer described with oxygen being placed on a Wyckoff position with high multiplicity, while 25% of PO_4 remain rotationally disordered (P1 and P3), see Appendix Table A1.9. This partial-crystallization of the PO_4 tetrahedra, i.e., breaking of the rotational disorder for those tetrahedra, drives the γ to β transition on cooling.

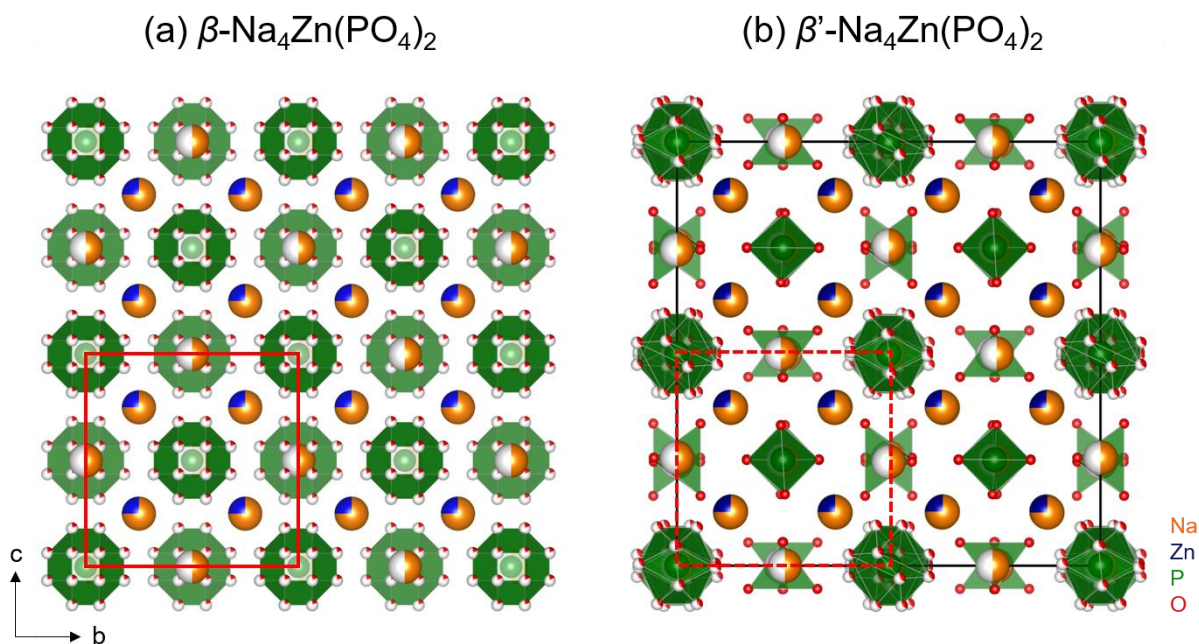


Figure II.34. Crystal structures of the γ - $\text{Na}_4\text{Zn}(\text{PO}_4)_2$ (a), and β - $\text{Na}_4\text{Zn}(\text{PO}_4)_2$ (b). The γ - unit cell (red line, a) is superposed on the β - unit cell (black line, in b) as dashed red line.

c) Structure of α - $\text{Na}_4\text{Zn}(\text{PO}_4)_2$

The XRD pattern of α - $\text{Na}_4\text{Zn}(\text{PO}_4)_2$ presents many additional peaks compared to the patterns of γ - and β - $\text{Na}_4\text{Zn}(\text{PO}_4)_2$, indicating again a structural filiation between phases, α - $\text{Na}_4\text{Zn}(\text{PO}_4)_2$ having a lower symmetry. The SXRD pattern could be indexed with a unit cell parameters $a = 8.99824(4)$ Å, $b = 21.05794(10)$ Å, $c = 9.08501(4)$ Å, and $\beta = 110.51598(28)^\circ$. The lattice vectors of the α -phase can be deduced from those of the β one using the following relation:

$$(\mathbf{a}_\alpha, \mathbf{b}_\alpha, \mathbf{c}_\alpha) = \begin{pmatrix} 1/4 & 1 & 1/4 \\ 1/4 & -1 & 1/4 \\ 1/2 & 0 & -1/2 \end{pmatrix} (\mathbf{a}_{\beta'}, \mathbf{b}_{\beta'}, \mathbf{c}_{\beta'}) + \left(\frac{1}{4}, 0, \frac{1}{4}\right)$$

The reflections conditions in the selected area electron diffraction (SAED) patterns of the α - $\text{Na}_4\text{Zn}(\text{PO}_4)_2$ suggest that the probable space group is monoclinic $P2_1/n$. Figure II.35 shows the Le Bail refinement of both SXRD and NPD pattern of α - $\text{Na}_4\text{Zn}(\text{PO}_4)_2$ with the above mentioned unit cell.

Solving the structure from powder diffraction with such a large unit cell is a challenge; however, one can suggest that the α -phase presents a complete PO_4 ordering without any rotational disorder, and Zn/Na/Vacancy ordering. Further investigations using single crystals will be necessary to elucidate this unambiguously.

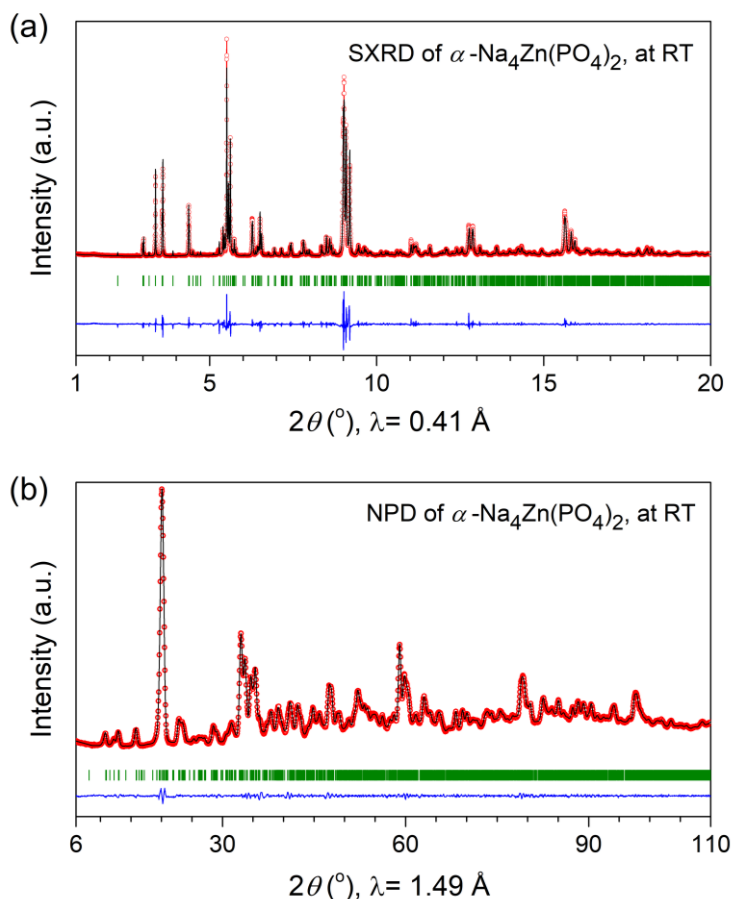


Figure II.35. Le Bail refinement of the SXR pattern (a) and the NPD pattern (b) of $\alpha\text{-Na}_4\text{Zn}(\text{PO}_4)_2$. The red circles, black, and blue lines, and green tick bars represent the observed, calculated, and difference patterns, and Bragg positions, respectively.

II.4.3 Stabilization of the β -polymorph.

Since the high-temperature $\gamma\text{-Na}_4\text{Zn}(\text{PO}_4)_2$ presents a disordered crystal structure, we tried to stabilize the polymorph at RT by deliberately creating disorder in the system. For this purpose we have partially substituted Zn^{2+} with hypervalent M^{3+} ($\text{M} = \text{In}, \text{Ga}, \text{and Al}$) to create Li^+ vacancies, so that the inherently disordered phase is stabilized at RT. We found that $\text{M}^{3+} = \text{In}^{3+}$ does not form solid solution with $\text{Na}_4\text{Zn}(\text{PO}_4)_2$, see Appendix Figure A1.8.

However, $\text{M}^{3+} = \text{Al}^{3+}$, and Ga^{3+} , was found to be successfully incorporated in the crystal structure. We prepared a series of compounds with nominal composition of $\text{Na}_{4-x}\text{Zn}_{1-x}\text{M}_x(\text{PO}_4)_2$, with

M = Ga, and Al. When prepared by quenching the Ga/Al substituted compositions crystallize in the β -form (Figure II.36), alike the pristine β - $\text{Na}_4\text{Zn}(\text{PO}_4)_2$. But interestingly, even when they are prepared by cooling slowly to RT (1 °C/min), the compositions are also stabilized as the β -polymorph, see Figure II.37.

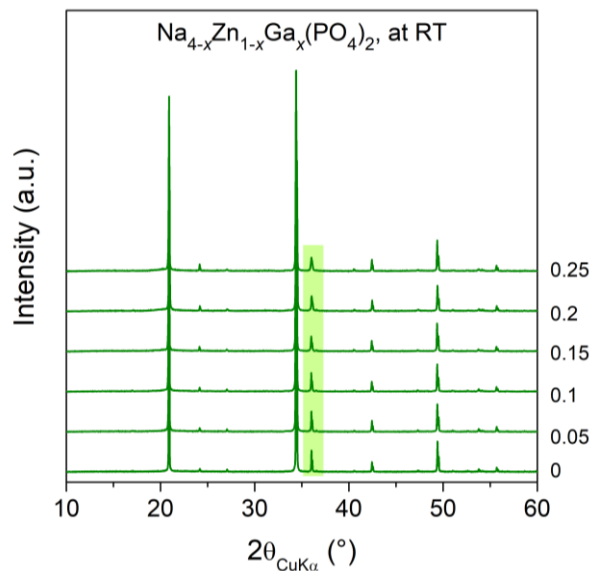


Figure II.36. XRD patterns of the $\text{Na}_{4-x}\text{Zn}_{1-x}\text{Ga}_x(\text{PO}_4)_2$ synthesized by quenching. The values of x are indicated at the right of the patterns. All the compositions show XRD patterns like the pristine β - $\text{Na}_4\text{Zn}(\text{PO}_4)_2$ ($x = 0$) phase.

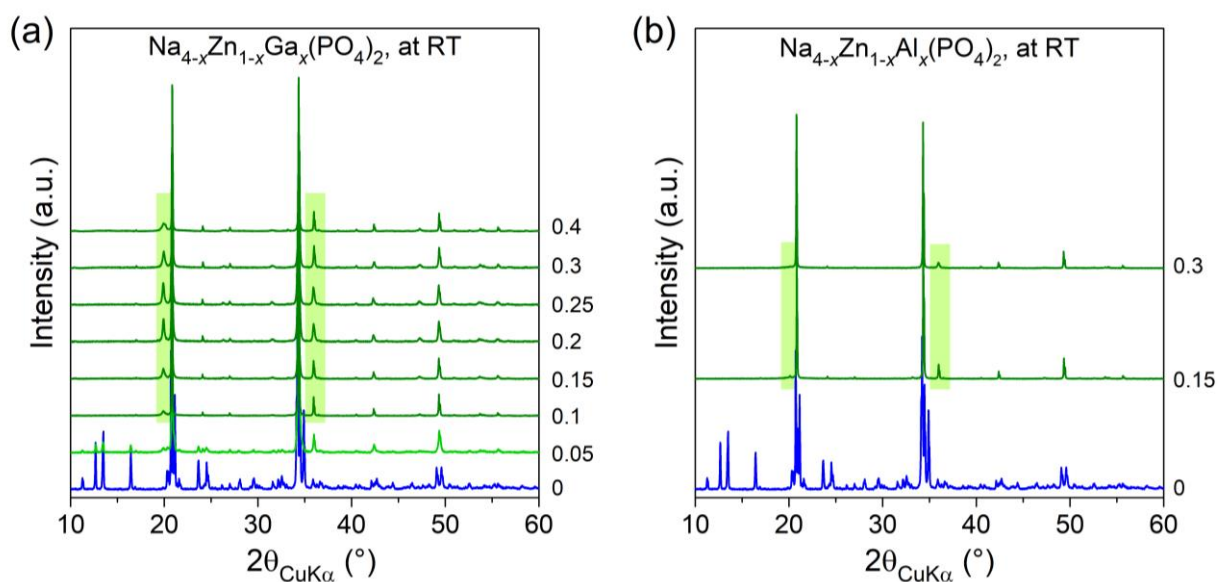


Figure II.37. XRD patterns of the $\text{Na}_{4-x}\text{Zn}_{1-x}\text{M}_x(\text{PO}_4)_2$ synthesized by slow cooling for M = Ga (a) and Al (b). The values of x are indicated at the right of the patterns. For comparison, the pattern corresponding to the pristine α - $\text{Na}_4\text{Zn}(\text{PO}_4)_2$ (slow-cooled) is also shown (blue pattern).

Closer look at the XRD patterns of the quenched and slow-cooled $\text{Na}_{4-x}\text{Zn}_{1-x}\text{M}_x(\text{PO}_4)_2$ ($\text{M} = \text{Ga}$, and Al) samples reveal the presence of the peak at $2\theta = 35.8^\circ$, characteristic to the β -phase (Figure II.36 and Figure II.37). Difference lies in the intensities of the peak at $\sim 19.9^\circ$ (Figure II.37a). Note that the (531) peak (at $2\theta = 35.8^\circ$) characteristic to the β -phase is present in both the patterns. Furthermore, the (311) peak (at 19.9°) shows intensity for the slow-cooled sample, but shows zero intensity for the quenched sample, thus indicating minor differences in the atomic arrangements. The SXRD pattern of slow-cooled and quenched samples could be indexed in $F23$ space group (shown in Appendix Figure A1.9 for the $\beta\text{-Na}_{3.85}\text{Zn}_{0.85}\text{Ga}_{0.15}(\text{PO}_4)_2$).

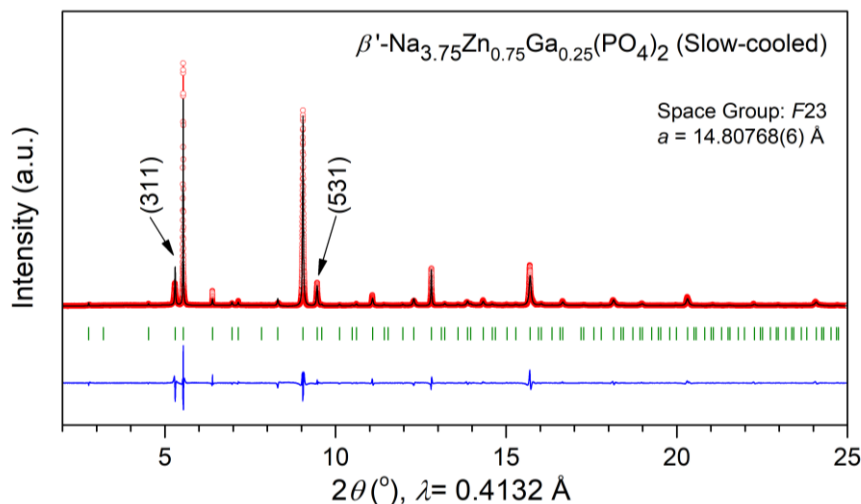


Figure II.38. Le Bail refinement of the SXRD pattern of slow-cooled $\beta\text{-Na}_{3.85}\text{Zn}_{0.85}\text{Ga}_{0.15}(\text{PO}_4)_2$ sample. The red circles, black, and blue lines, and green tick bars represent the observed, calculated, and difference patterns, and Bragg positions, respectively.

The Le Bail refinement of the SXRD pattern for the slow-cooled $\beta\text{-Na}_{3.75}\text{Zn}_{0.75}\text{Ga}_{0.25}(\text{PO}_4)_2$ sample ($x = 0.25$) shown in Figure II.38, that was fitted in $F23$ space group with unit cell parameters $a = 14.80768(6) \text{ \AA}$, $V = 3246.842(22) \text{ \AA}^3$. Turning to the Al-substituted phases, the SXRD pattern of the slow-cooled $\beta\text{-Na}_{3.85}\text{Zn}_{0.85}\text{Al}_{0.15}(\text{PO}_4)_2$ sample was also collected, which could be fitted similarly in $F23$ space group, and details are shown in the Appendix Figure A1.10. However, despite our best efforts, we could not find unique structural solutions for the Ga/Al-substituted phases. Further study with single crystal samples are required to unveil the complexity of the crystal structures of the phases.

At this stage, observing the stabilization of the β -polymorph for the Ga-substituted phases, the next legitimate question arises about the structural behaviour under the influence of temperature. Hence, we have performed temperature-dependent XRD experiments of the slow-cooled $\beta\text{-Na}_{3.85}\text{Zn}_{0.85}\text{Ga}_{0.15}(\text{PO}_4)_2$ and $\beta\text{-Na}_{3.75}\text{Zn}_{0.75}\text{Ga}_{0.25}(\text{PO}_4)_2$ samples. For the $\text{Na}_{3.85}\text{Zn}_{0.85}\text{Ga}_{0.15}(\text{PO}_4)_2$ sample, the β -phase to the α' -phase at $\sim 280^\circ \text{C}$ (Figure II.39a). This transition is followed by transition to the β -phase (at $\sim 360^\circ \text{C}$) and the to the γ -phase (at $\sim 400^\circ \text{C}$), see Figure II.39a. To recall, the $\beta \rightarrow \alpha$ phase transition was observed for the $\beta\text{-Na}_4\text{Zn}(\text{PO}_4)_2$ samples also. In contrary, for the $\text{Na}_{3.75}\text{Zn}_{0.75}\text{Ga}_{0.25}(\text{PO}_4)_2$

sample, only $\beta \rightarrow \alpha$ phase transition was observed at ~ 320 °C. During cooling, only one phase transition, back to the β -phase was observed (at ~ 300 °C) for both the phases (Appendix Figure A1.11).

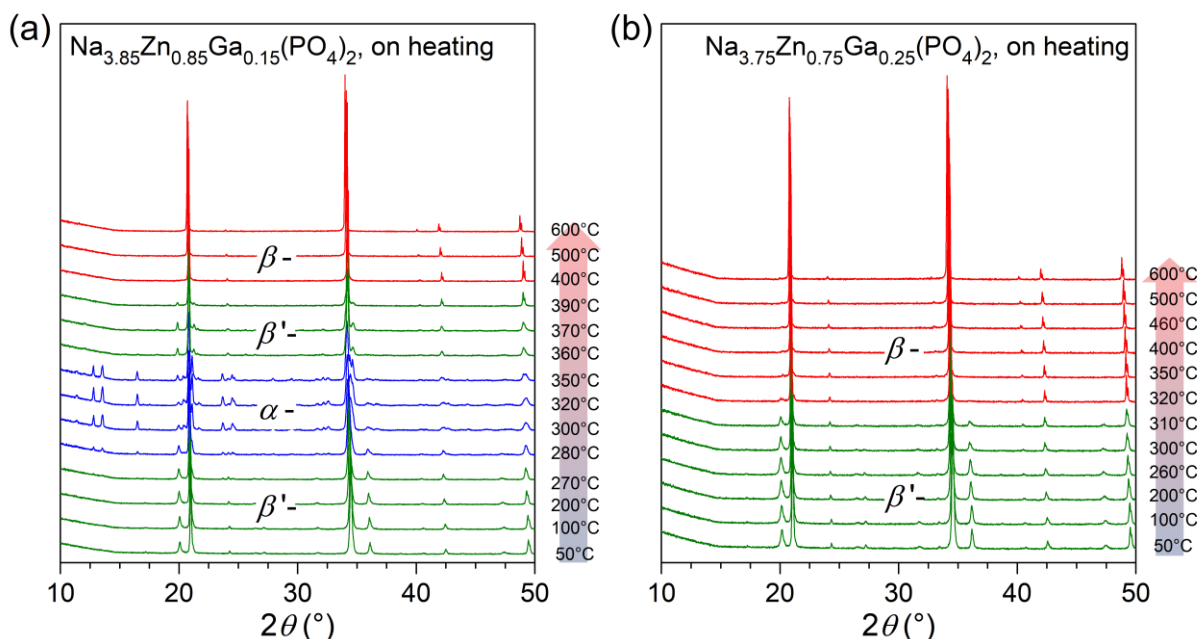


Figure II.39. Evolution of XRD patterns of as-synthesized $\text{Na}_{4-x}\text{Zn}_{1-x}\text{Ga}_x(\text{PO}_4)_2$ samples (prepared by slow-cooling) with temperature upon heating (at 1 °C/min), for $x_{\text{Ga}} = 0.15$ (a), and $x_{\text{Ga}} = 0.25$ (b). The corresponding temperatures are indicated at the right side of the XRD patterns.

II.4.4 Ionic Conductivity transition in pristine $\text{Na}_4\text{Zn}(\text{PO}_4)_2$

The variations of ionic conductivities of the $\text{Na}_4\text{Zn}(\text{PO}_4)_2$ samples synthesized by quenching or cooling slowly are summarized in Figure II.40. The linear variation for the $\ln(\sigma T)$ with inverse temperature confirms the thermally activated Arrhenius type behavior $\sigma(T) = A/T \cdot \exp(-E_a/k_B T)$, where k_B is the Boltzmann constant, A is a pre-exponential factor and T is temperature. The thermodynamically stable α - $\text{Na}_4\text{Zn}(\text{PO}_4)_2$ presents a poor ionic conductor at RT (extrapolated $\sigma_{\text{tot}} \approx 1 \times 10^{-14}$ S·cm $^{-1}$ at 25 °C with $E_a \approx 0.92$ eV). However, the quenched β - $\text{Na}_4\text{Zn}(\text{PO}_4)_2$ sample, at low temperature, shows higher conductivity ($\sigma_{\text{tot}} \approx 3 \times 10^{-8}$ S·cm $^{-1}$ at 150 °C) than the slow-cooled α - $\text{Na}_4\text{Zn}(\text{PO}_4)_2$ sample ($\sigma_{\text{tot}} \approx 9 \times 10^{-10}$ S·cm $^{-1}$ at 150 °C). Since at RT the quenched sample is in β -form, which is disordered, it shows higher conductivity than the slow-cooled α -form. Interestingly, at higher temperature, when $T \geq 250$ °C, the conductivity of β - $\text{Na}_4\text{Zn}(\text{PO}_4)_2$ decreases and traces the conductivity of the α - $\text{Na}_4\text{Zn}(\text{PO}_4)_2$. But this behaviour is consistent with the structural analysis as portrayed before (Figure II.31). At slight higher temperature, the quenched sample transforms again to the α -form (Figure II.31c), hence showing same conductivity.

Upon increasing the temperature further, when $T \geq 375$ °C, both the samples undergo a transition in ionic conductivity at ~ 375 °C, driven by the order-disorder transition ($\alpha \rightarrow \gamma$) in the compound,

showing much higher ionic conductivity. Since the disordered phase favors fast ionic conduction, it becomes interesting to explore the transport properties of the RT-stabilized γ/β phases.

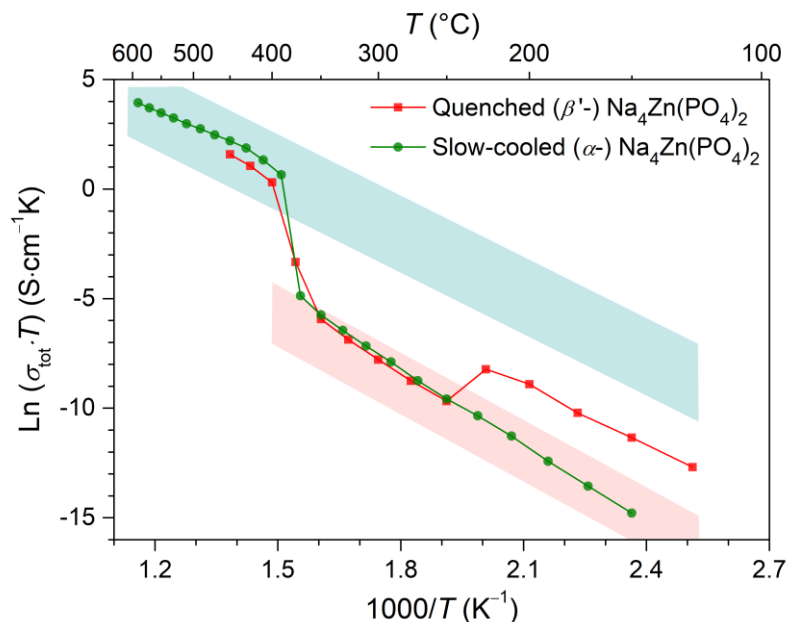


Figure II.40. Arrhenius plot of total ionic conductivity of the $\text{Na}_4\text{Zn}(\text{PO}_4)_2$ samples.

II.4.5 Higher conductivity in Ga/Al-substituted β -phases

Figure II.41 summarizes the total ionic conductivities (σ_{tot}) of all Ga-substituted samples and the conductivity values are gathered in Table 4. Note that Al-substitution over Ga exhibits similar transport properties and is shown in Appendix. For all the Ga-substituted samples, high ionic conductivities, comparable to the γ - $\text{Na}_4\text{Zn}(\text{PO}_4)_2$, have been obtained even at RT. However, the Ga-substituted samples ($x_{\text{Ga}} = 0.05 - 0.2$ mol pfu) show interesting behaviour after slight heating, that the conductivity decreases (blue background in Figure II.41), but at $T \geq 390$ °C it again increases. Furthermore, the conductivity transition temperature increases with increasing Ga content, but was not seen for the $x_{\text{Ga}} = 0.25$ sample. This behaviour is similar to what was observed for the quenched β - $\text{Na}_4\text{Zn}(\text{PO}_4)_2$ sample. Hence this behaviour pertains to the $\gamma \rightarrow \alpha$ transition, as was confirmed by the temperature dependent XRD measurement for the representative sample with $x_{\text{Ga}} = 0.15$ mol pfu (Figure II.39a). From the evolution of the XRD patterns, it is evident that the samples transform to the α -phase at 280°C, before transforming back to the β -phase. Hence, the decreased conductivity can be attributed to the α -phase. Furthermore, it is interesting to note, that the transition temperature of the $\gamma \rightarrow \alpha$ conductivity-transition moves to higher temperature (see blue background in Figure II.41) with increasing Ga-content for the $\text{Na}_{4-x}\text{Zn}_{1-x}\text{Ga}_x(\text{PO}_4)_2$ samples with $x = 0.05 - 0.2$. For the $x_{\text{Ga}} = 0.25$ sample, the structural $\gamma \rightarrow \alpha$ transition was not observed (Figure II.39b), hence the transition was not observed in ionic conductivity as well. Thus, total ionic conductivity of $\sim 1.1 \cdot 10^{-10}$ at RT was obtained for the x_{Ga}

= 0.25 sample, which is several order of magnitudes higher than the pristine $\text{Na}_4\text{Zn}(\text{PO}_4)_2$. The Al-substituted sample shows ionic conductivity in similar order and shown in Appendix Figure A1.12.

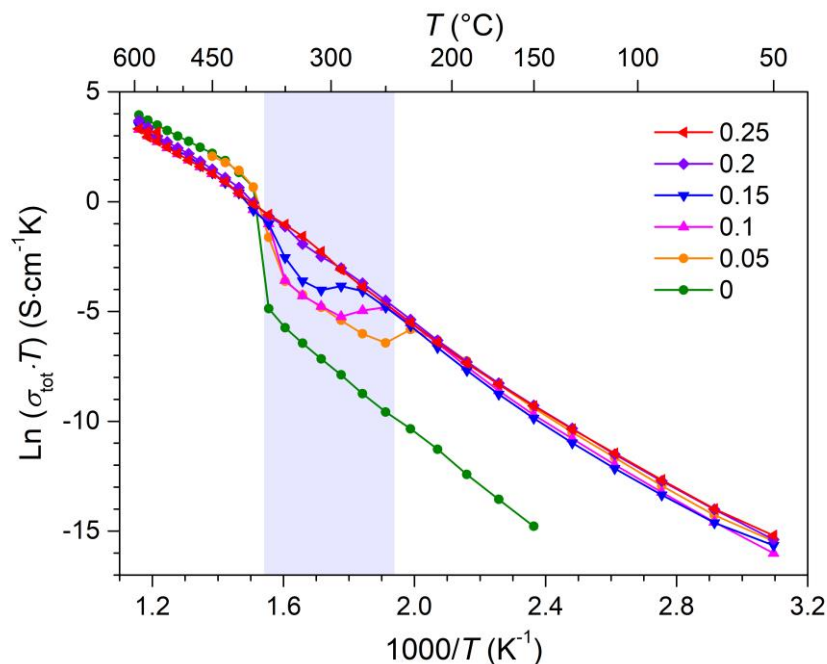


Figure II.41. Arrhenius plot of total ionic conductivity of the $\text{Na}_{4-x}\text{Zn}_{1-x}\text{Ga}_x(\text{PO}_4)_2$ samples synthesized by slow cooling. The values of x are indicated in the legends.

Table 4. Ionic conductivities and activation energies of the $\text{Na}_{4-x}\text{Zn}_{1-x}\text{M}_x(\text{PO}_4)_2$ samples ($\text{M} = \text{Ga}, \text{Al}$). Conductivities at RT were obtained by extrapolation of the Arrhenius plot. The red, and blue background denotes the Ga, and Al substitution, respectively.

x_{Ga}	σ_{g} ($\text{S}\cdot\text{cm}^{-1}$)			σ_{gb} ($\text{S}\cdot\text{cm}^{-1}$)			σ_{tot} ($\text{S}\cdot\text{cm}^{-1}$)		
	RT	150 °C	E_{a} (eV)	RT	150 °C	E_{a} (eV)	RT	150 °C	E_{a} (eV)
0	$1.3\cdot 10^{-13}$	$9.2\cdot 10^{-9}$	0.95	$2.2\cdot 10^{-14}$	$1\cdot 10^{-9}$	0.92	$1.8\cdot 10^{-14}$	$9.6\cdot 10^{-10}$	0.92
0.05	$6.2\cdot 10^{-10}$	$3.8\cdot 10^{-6}$	0.75	$3.4\cdot 10^{-11}$	$1.9\cdot 10^{-7}$	0.74	$3.2\cdot 10^{-11}$	$1.8\cdot 10^{-7}$	0.74
0.15-Ga	$1.5\cdot 10^{-9}$	$1.4\cdot 10^{-5}$	0.73	$5.4\cdot 10^{-11}$	$1.1\cdot 10^{-7}$	0.65	$5\cdot 10^{-11}$	$1.1\cdot 10^{-7}$	0.65
0.15-Al	$2\cdot 10^{-9}$	$2.2\cdot 10^{-5}$	0.7	$7.7\cdot 10^{-11}$	$1.8\cdot 10^{-7}$	0.63	$7.5\cdot 10^{-11}$	$1.8\cdot 10^{-7}$	0.63
0.25	$2.7\cdot 10^{-9}$	$8.6\cdot 10^{-5}$	0.75	$1.1\cdot 10^{-10}$	$2\cdot 10^{-7}$	0.62	$1.1\cdot 10^{-10}$	$2\cdot 10^{-7}$	0.62

Furthermore, we observed that, for the Ga-substituted compositions the conductivities in α -form (see blue background in Figure II.41) is higher than the pristine α - $\text{Na}_4\text{Zn}(\text{PO}_4)_2$ ($x_{\text{Ga}} = 0$ in Figure II.41).

This goes in line with the common observation in ionic conductors that the conductivity increases with increasing Na/Li vacancy leading to disorder. To recall, this also observed for the $\text{Li}_4\text{Zn}(\text{PO}_4)_2$ (Section II.3) also where, despite pertaining to the α -phase, the $\alpha\text{-Li}_{4-x}\text{Zn}_{1-x}\text{Ga}_x(\text{PO}_4)_2$ compositions (i.e., $x = 0.05 - 0.2$) show higher conductivity with higher Ga-content, due to the increased disorder for Li-vacancy.

To summarize this section, a new compound $\text{Na}_4\text{Zn}(\text{PO}_4)_2$ has been designed and synthesized, which shows a phase transition to disordered γ -phase at $\sim 390^\circ\text{C}$. Ga^{3+} , and Al^{3+} substitution for Zn^{2+} successfully stabilizes the γ -phase at RT. As a consequence, Li-conductivity similar to the HT-stable $\gamma\text{-Na}_4\text{Zn}(\text{PO}_4)_2$ was possible to obtain in the $\beta\text{-Na}_{4-x}\text{Zn}_{1-x}\text{M}_x(\text{PO}_4)_2$ phases ($\text{M} = \text{Ga}, \text{Al}$) at RT.

II.5 Chapter Conclusions.

We thoroughly studied polymorphism in $\text{Li}_6\text{Zn}(\text{P}_2\text{O}_7)_2$, and $\text{Li}(\text{Na})_4\text{Zn}(\text{PO}_4)_2$, and explored its impact on ionic conductivity. The $\text{Li}_6\text{Zn}(\text{P}_2\text{O}_7)_2$ undergoes multiple phase transitions with temperature, elucidating the existence of six polymorphs. Full structural resolution for the α - and ζ - polymorphs has been deduced enabling us to account the variation of the ionic conductivity in the compound. The ζ -polymorph was found to crystallize in a monoclinic unit cell ($C2/c$ S.G.) as the α -polymorph but with a four-time smaller unit cell having a highly disordered and cation-mixed Li/Zn sublattice. We performed BVOL calculations on such newly resolved structures and found that the Li^+ ionic conduction in the α -polymorph is two dimensional in contrast to three-dimensional for the ζ -polymorph owing to the Li/Zn mixed sites which promote interlayer ion hopping. Such predictions were confirmed by AC-impedance measurements which besides showing two jumps in ionic conductivity with increasing temperature, has confirmed an high activation barrier for Li^+ conduction for the α than the ζ -polymorph (0.9 eV vs. 0.35 eV). Altogether, these results suggest that not only disorder, but also cation-mixing can lead to new conduction pathways, which can increase the ionic conductivity.

In $\text{Li}_4\text{Zn}(\text{PO}_4)_2$ and $\text{Na}_4\text{Zn}(\text{PO}_4)_2$, we have explored the rich crystal chemistry in great details and described how we could improve its ionic conductivity. We showed that both compounds undergo an order-disorder phase transition at HT, accompanied by a jump in its ionic conductivity. We solved the crystal structure of the high temperature β/β' -polymorphs, which appears to be derived from the low temperature α -structure by preserving the PO_4^{3-} backbone, but presenting a disordered Li(Na)/Zn sublattice. The γ -polymorph was found to have a higher conductivity than the α -phase. We have demonstrated the feasibility to stabilize the γ -polymorph at RT either by ball-milling the α phase, or by partial substitution of Zn^{2+} by Ga^{3+} in $\text{Li}_4\text{Zn}(\text{PO}_4)_2$ (also by Al^{3+} in case of $\text{Na}_4\text{Zn}(\text{PO}_4)_2$). With 0.5 mol pfu Ga, we could successfully stabilize the $\text{Li}_{3.5}\text{Zn}_{0.5}\text{Ga}_{0.5}(\text{PO}_4)_2$ as γ -polymorph at RT, with a crystal structure pertaining to the $\beta\text{-Li}_4\text{Zn}(\text{PO}_4)_2$ phase, but with the Zn and Ga ions fully mixed in a disordered Li-sublattice. The $\beta\text{-Li}_{4-x}\text{Zn}_{1-x}\text{Ga}_x(\text{PO}_4)_2$ samples exhibit ionic conductivities up to $\sim 2 - 5 \times 10^{-13} \text{ S}\cdot\text{cm}^{-1}$ at RT, by several orders of magnitudes higher than $\alpha\text{-Li}_4\text{Zn}(\text{PO}_4)_2$. This could be explained by the higher crystal symmetry of the disordered $\beta\text{-Li}_4\text{Zn}(\text{PO}_4)_2$ that enables to switch the conduction mechanism from

2-D to 3-D. Similarly, the β - $\text{Na}_{4-x}\text{Zn}_{1-x}\text{M}_x(\text{PO}_4)_2$, $\text{M} = \text{Ga}$ and Al , samples exhibit ionic conductivities up to $\sim 2.7 \times 10^{-9} \text{ S} \cdot \text{cm}^{-1}$ at RT, by several orders of magnitudes higher than α - $\text{Na}_4\text{Zn}(\text{PO}_4)_2$.

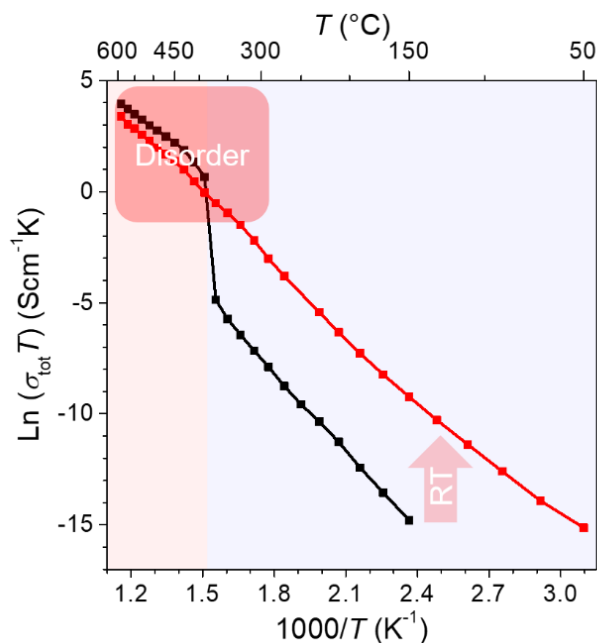


Figure II.42. Strategy to design new ionic conductors. The conductivity plots are of $\text{Na}_4\text{Zn}(\text{PO}_4)_2$ (in black) and of $\text{Na}_{3.75}\text{Zn}_{0.75}\text{Ga}_{0.25}(\text{PO}_4)_2$, and shown as representatives.

Despite such a rich chemistry of $\text{Li}_6\text{Zn}(\text{P}_2\text{O}_7)_2$, $\text{Li}_4\text{Zn}(\text{PO}_4)_2/\text{Na}_4\text{Zn}(\text{PO}_4)_2$ and its Ga/Al substitutes, the ionic conductivity is still far from the targeted value ($10^{-3} \text{ S} \cdot \text{cm}^{-1}$). However, through this work we illustrate the role of disorder to ionic conduction and demonstrates how to use chemical substitutions to trigger RT stabilization of disordered high-temperature polymorphs (Figure II.42). Next, to fabricate practical all-solid-state-batteries (ASSB), we decided to implement sulfide-based solid electrolytes, e.g., β - Li_3PS_4 , $\text{Li}_2\text{S}-\text{P}_2\text{S}_5$ (LPS) glass, etc., which showed high ionic conductivity and easiness to be implemented in ASSB, as discussed in Chapter I.^{154,177,233} In order to study interfacial compatibility in all-sulfide ASSBs²³⁴, we have revisited some sulfide cathode materials, and designed highly reversible Li-rich $\text{Li}_{1.33-2y/3}\text{Ti}_{0.67-y/3}\text{Fe}_y\text{S}_2$ electrode for LIBs, that offer high energy density capitalizing the benefit of anionic redox,³⁷ and this will be the topic of the next chapter.

Chapter III

Sulfide-based cathode materials: Anionic redox in Li-rich sulfides[#]

[#]This chapter includes the following publication: Saha *et al.*, *Nature Energy* 2019.

III.1 Chapter Introduction

Layered sulfide TiS_2 , was one of the very first intercalation host that was considered to develop rechargeable Li-metal batteries (Figure III.1a).²³⁵ However, with the emergence of Li-ion batteries (LIBs), layered oxide LiCoO_2 (Figure III.1b) was proposed as positive electrode because of its high energy density, and today's commercial batteries use LiCoO_2 (LCO), and its derivatives such as $\text{LiNi}_x\text{Mn}_y\text{Co}_{1-x-y}\text{O}_2$ (NMC), etc., as positive electrode, as discussed in Section I.1.3.^{15,236} For LiCoO_2 , only ~ 0.5 Li can be deintercalated reversibly. Even though there are ongoing efforts to push the limit by doping,^{26,237} deintercalation of >0.5 Li leads to a harmful phase transformation.^{238–240} Nevertheless, Tarascon and colleagues (1999) showed the possibility of charge transfer from O $2p$ in the fully-delithiated “ CoO_2 ”, which gave hints about anionic activity (Figure III.1b).^{241,242} Then Li-rich NMC's ($\text{Li}[\text{Li}_z\text{Ni}_x\text{Mn}_y\text{Co}_{1-x-y-z}\text{O}_2]$) was designed by partially substituting the transition metals with Li, where >1 Li can be extracted, thus leading to high capacity (Figure III.1c), by capitalizing the benefit of anionic redox (i.e., electrochemical participation of O anions).^{29,33,34,36} However, this comes with several limitations, as discussed before.

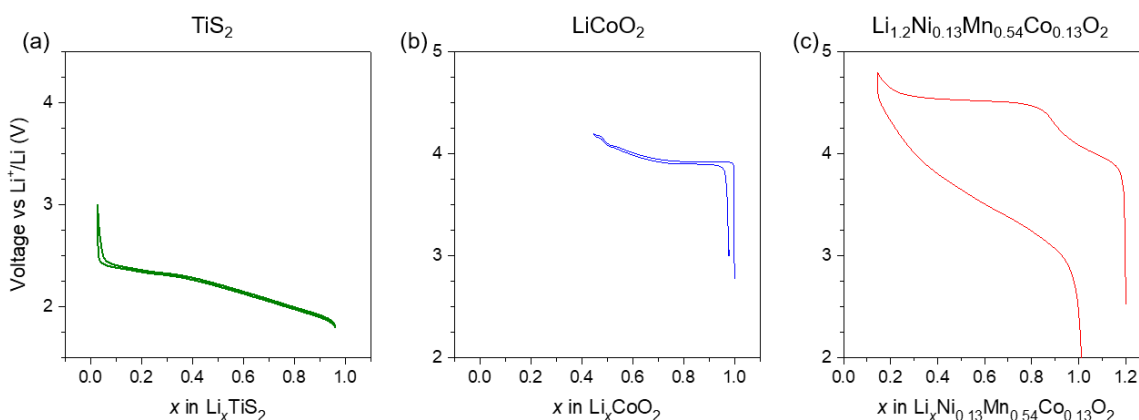


Figure III.1. Voltage profiles of TiS_2 , LiCoO_2 , and $\text{Li}_{1.2}\text{Ni}_{0.13}\text{Mn}_{0.54}\text{Co}_{0.13}\text{O}_2$ (Li-rich NMC).

The Li (de)intercalation in TiS_2 is charge-compensated mostly by cationic $\text{Ti}^{3+/4+}$ redox process, with possibly very little contribution of S due to its high covalency, as pointed out by few reports.^{243–245} Furthermore, possibility of oxidation of S upon Li-intercalation in $\text{LiTi}_{0.5}\text{Fe}_{0.5}\text{S}_2$ was discussed by Tarascon *et al* (1983).²⁴⁶ Interestingly, ligand to metal charge-transfer in layered disulfides, can be triggered upon lowering the metal d level, by tuning the transition metals (TM). Lowering the d -level energy on moving to the right-hand side of the periodic table can lead to holes on S $3s$ states by electron transfer to TM d -states, e.g., in FeS_2 .^{242,247–249} Therefore, unlike oxides, stable ligand-hole chemistry was well-known in sulfides, e.g., TiS_3 ($\text{Ti}^{4+}\text{S}^{2-}(\text{S}_2)^{2-}$), $\text{Fe}^{2+}(\text{S}_2)^{2-}$, and $\text{V}^{4+}(\text{S}_2)^{2-}$ etc., since the pioneering works by Rouxel *et al*.^{247,248,250} Quasi-layered dichalcogenide FeS_2 , and trichalcogenides MQ_3 ($\text{M} = \text{Ti}, \text{Zr}, \text{Hf}, \text{Nb}, \text{Ta}; \text{Q} = \text{S}, \text{Se}$), especially TiS_3 , TaS_3 and NbSe_3 , have been subject of immense interest owing to the possibility of multielectron redox reaction, in early works, which presents the classical examples of anionic redox chemistry.^{10,242,251–254} In these electrode materials, S (or Se) fully or partially

exists as dimerized $S^{2-}-S^{2-}$ pairs, and undergo breaking of S—S bonds to form standard S^{2-} states in discharge. Thus, the study of sulfide materials is quite important while discussing anionic redox and we decided to explore the practicability anionic redox in sulfides. In this chapter, we will present the investigation of anionic redox, in ‘pseudo-layered’ TiS_3 first, and then, in layered Li-rich sulfides.

III.2 Pseudo-layered TiS_3

We first explore anionic S_2^{2-}/S^{2-} redox and its structural consequence in pseudo-layered TiS_3 . The anionic redox in TiS_3 was known since 1980s, even much before the oxygen redox.^{10,242,255,256} We decided to revisit the anionic redox in TiS_3 in order to reinvestigate in detail its structural aspects and assess the reversibility of the anionic redox together with the practical issues, such as voltage fade, kinetics, and voltage hysteresis, etc.

The crystal structure of TiS_3 , determined on single crystal, was reported by Furuseth *et al*, way back in 1975.²⁵⁷ The reported structures are shown in Figure III.2a,b. It crystallizes in monoclinic crystal structure (space group $P2_1/m$), with $a = 4.958 \text{ \AA}$, $b = 3.4006 \text{ \AA}$, $c = 8.778 \text{ \AA}$, and $\beta = 97.32^\circ$. The structure consists TiS_8 polyhedra linked via shared faces into an infinite chain parallel to the b axis with the neighboring chains offset by $b/2$ (Figure III.2a,c). The Ti bilayered chains bonded by van der Waals forces along c and connected via longer Ti—S bonds (2.86 \AA) along a axis, which makes the structure quasi-layered (Figure III.2b,c), with Ti residing in an irregular eightfold coordination with S atoms (Figure III.2c).

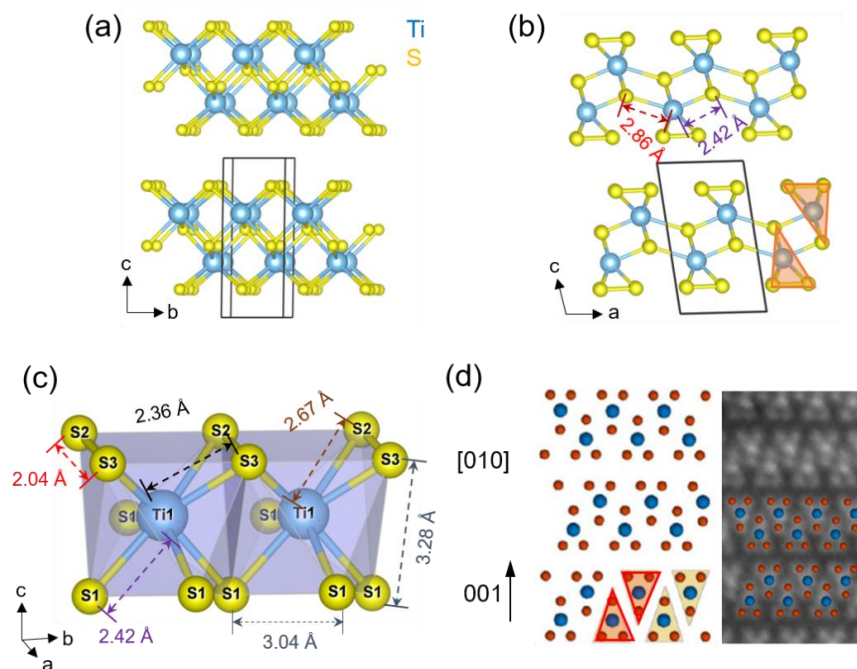


Figure III.2. Reported crystal structure of TiS_3 . (a-c) Structural model reported by Furuseth *et al* in 1975.²⁵⁷ The structure is drawn along $[100]$ (a), and, $[010]$ (b) direction. Typical bond distances and Ti coordination is shown in (c). Ti and S atoms are shown in blue and yellow, respectively. Ti—S bonds

distances were cut at 2.9 Å. (d) Structure proposed by Guilmeau *et al* in 2014 with HRTEM image shown in right panel.²⁵⁸ S atoms are shown in red here. Figure adapted from Reference²⁵⁸. Note the differences in the delimiting triangle around Ti in panel (b) and (d).

Interestingly, TiS_3 contains two kind of S atoms; bridging (S1) and disulfide pair (S2 and S3), see Figure III.2c, with the presence of the S–S dimer (S_2^{2-}) with a bond length of 2.04 Å (S2–S3, marked in red). TiS_3 remains the origin of great interest for various applications dealing with energy storage, photocatalytic, electronic, optoelectronic, etc.^{10,259–268} However, despite immense attention, the crystal structure was taken for granted, until Guilmeau *et al* revisited the structure in 2014 and proposed slight different arrangement of the S atoms (Figure III.2d).²⁵⁸ Thus, owing to these contradictory findings, we decided to revisit the structure and electrochemical properties of TiS_3 .

III.2.1 Synthesis of TiS_3

TiS_3 was synthesized as powder, by solid-state synthesis route. Required amount of TiS_2 or Ti metal powder was reacted with S powder (20 wt% extra) in a vacuum-sealed quartz tube at 550 °C for one week (conditions were optimized). Thus shiny black colored TiS_3 lumps were obtained (Figure III.3a) which was hand-grinded to powder for further use. For precaution, the TiS_3 was always handled inside an Ar-filled glovebox.

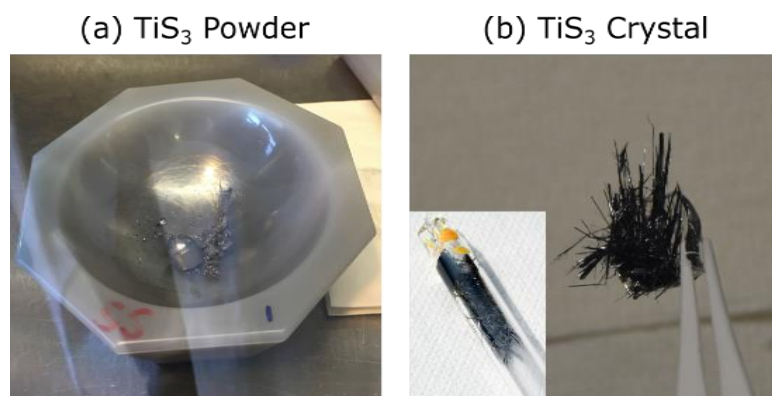


Figure III.3. Picture of the as-synthesized TiS_3 . (a) Synthesized powder and (b) TiS_3 crystals. Inset in (b) shows the ampule after the synthesis.

In parallel, we also tried to synthesize single crystals of TiS_3 by vapor transport method. Ti powder and S powder (50 wt% excess) was mixed and vacuum sealed in quartz ampule (10 - 13 cm long). The ampule were heated in furnaces at 600 °C, with a temperature gradient of ~50 °C to the cooler end and was kept for 2 weeks. Occasionally, up to 50 wt% of iodine was also added as additional vapor transporter, but no noticeable differences were observed. Ribbon shaped TiS_3 crystals (up to ~1 cm long, with up to 1 mm of breadth and submicron thickness) could be obtained. A picture of the crystals is shown in Figure III.3b. However, closer look at the crystals by optical microscopy reveals that the crystals always consist a bunch of single crystals stick together, or with local exfoliations.

III.2.2 Structural characterizations: a different variant of TiS_3

The purity of the as-synthesized TiS_3 powder was confirmed by XRD. Regardless the precursor, whether TiS_2 or Ti powder, was used, the XRD patterns of the synthesized TiS_3 were found to be always similar. We collected scanning electron microscopy (SEM) images of the TiS_3 powder (Figure III.4). Interestingly we found that the powder is comprised of micrometer sized ribbons.

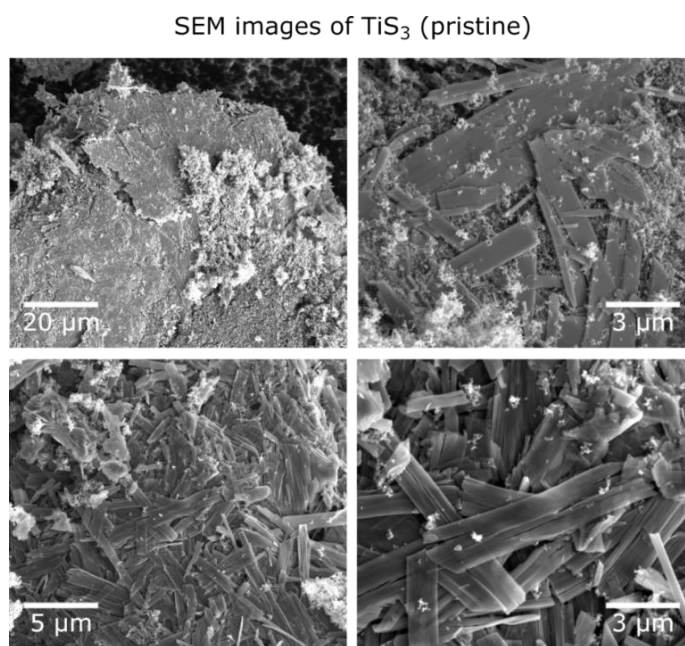


Figure III.4. SEM images of the pristine TiS_3 powders. Images were taken after the powders mixed and hand-grinded with 20 wt% Csp. The amorphous whitish Csp can be seen also in the SEM images.

Next, we used synchrotron-XRD pattern (SXRD), and neutron powder pattern (NPD) for structural characterization. The SXRD pattern was collected at the 11-BM beamline of Argonne National Lab with a wavelength $\lambda = 0.41 \text{ \AA}$. The NPD was collected at the D1B powder diffractometer (Institut Laue-Langevin) with a wavelength $\lambda = 1.291 \text{ \AA}$, for details see the Appendix. The Rietveld refinement of the SXRD pattern of TiS_3 is shown in Figure III.5. The pattern could be refined using the reported model, with a monoclinic unit cell of $P2_1/m$ space group. Profiles of the peaks present a strong anisotropic broadening arising from size effects. Refinements indicate that the crystallite shapes are platelets-like, and that the platelets are oriented perpendicular to the $[001]$ direction. The structure obtained from the Rietveld refinement was further refined with the NPD pattern (Figure III.6) to obtain the final structural model. The corresponding structural model is summarized in Appendix Table A2.1 with the crystal structure is shown in Figure III.7a.

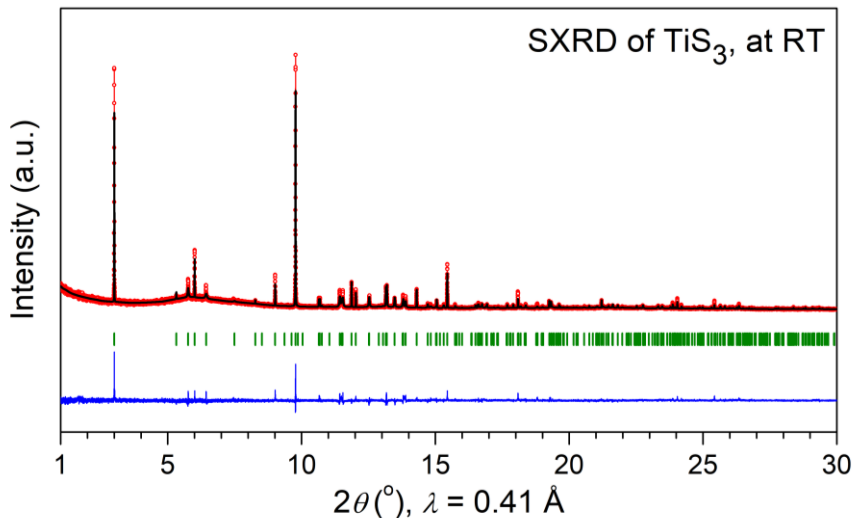


Figure III.5. Rietveld refinement of the SXRD pattern of the pristine TiS_3 powder. The red circles, black continuous line, blue line, and green tick bars represent the observed, calculated, and difference patterns, and Bragg positions, respectively.

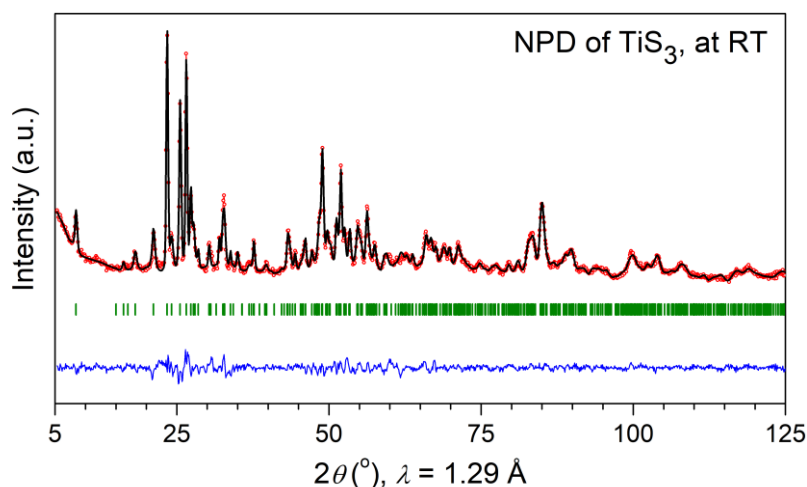


Figure III.6. Rietveld refinement of the NPD pattern of the pristine TiS_3 powder collected at D1b. The red circles, black continuous line, blue line, and green tick bars represent the observed, calculated, and difference patterns, and Bragg positions, respectively.

The deduced structural model shows S–S dimer of 2.054(10) Å. The model is similar to the reported by Furuse *et al* (1975),²⁵⁷ however with slight differences in the atomic arrangements. The as-synthesized TiS_3 can be perceived as an array of 2D slabs consisting of ‘isosceles triangles’ with alternating up and down orientations, where the triangles are formed by S atoms (red triangle in Figure III.7a). In contrast, the reported model, the S atoms form nearly ‘right triangles’ (orange triangle in Figure III.7b). Such a subtle difference in the atomic arrangement is not drastic, but produces slightly different bond lengths, hence confirming the crystal structure pointed out by Guilmeau *et al* (2014), which was described as A-variant (ZrSe_3 -type).²⁵⁸

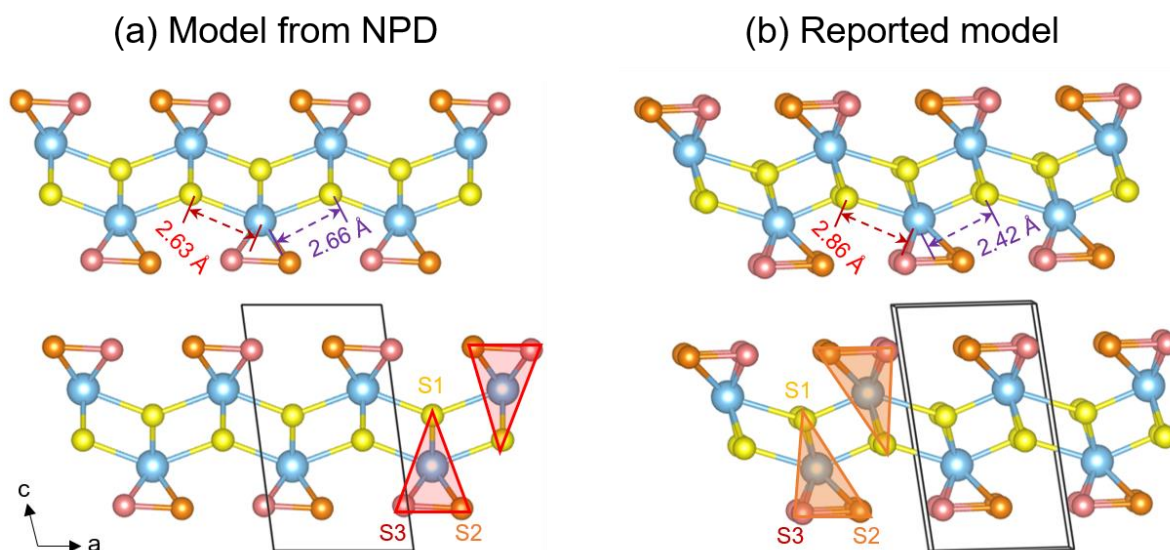


Figure III.7. The crystal structure of as-synthesized TiS_3 . The structure deduced from Rietveld refinement of the NPD pattern (a) is compared with the reported model by Furuseth *et al.*, 1975²⁵⁷ (b).

As SXR/NPD give the long range crystal structure, we used the crystals of TiS_3 to confirm the deduced structural model, by transmission electron microscopy (TEM) studies.^B High angle annular dark field scanning transmission electron microscopy (HAADF-STEM) images of the TiS_3 crystals were recorded and are shown in Figure III.8. Visually the atomic resolution HAADF-STEM image of the TiS_3 can be perceived as an array of 2D slabs consisting of isosceles triangles with alternating “up” and “down” orientations. The vertices of each triangle are formed with the dots of the S atomic columns and each triangle is centered with a slightly brighter dot of the Ti column. The periodicity of the TiS_3 structure along the c -axis is traced with a white line in Figure III.8. Kinks in the line mark the domains with flipped orientation of the monoclinic c -axis, so that the domains are classified as nanoscale mirror twins with the (001) twin plane. The Ti and S atomic positions within the triangles fully support the TiS_3 crystal structure refined from the NPD pattern. The positions of the Ti and S columns fully coincide with the positions of the corresponding dots in the triangles (inset a, Figure III.8). The crystal structure reported in Furuseth *et al.*, 1975²⁵⁷ provides a distorted shape of the triangles, which does not match the contrast in the HAADF-STEM image (inset b, Figure III.8).

^B TEM studies were performed by Prof Artem M. Abakumov, Skolkovo Institute of Science and Technology (Russia).

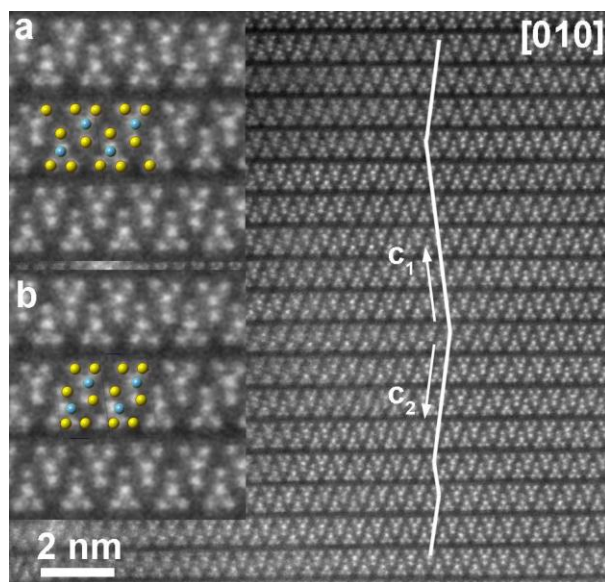


Figure III.8. HAADF-STEM image of TiS_3 single crystal showing the atomic arrangement. Twinned nano domains with mirrored orientation of the c -axis are traced with the kinked white line. The inserts show the enlarged images with overlaid structural model obtained from the NPD Rietveld refinement (a) and from Furuset *et al*²⁵⁷ (b). Note that the reported model (b) does not match the HAADF-STEM image. The Ti and S atoms are shown as blue and yellow spheres, respectively.

In short, our structural studies confirm the structure of TiS_3 in accordance with Guilmeau *et al* (2014),²⁵⁸ where the S atoms form ‘isosceles triangles’ around the Ti atoms (see Figure III.7).

III.2.3 Electrochemistry of TiS_3

Then the TiS_3 powder was characterized for electrochemical performance. They were mixed with 20 wt% conductive Csp and hand-grinded for 5 mins prior to cycling (SEM images were shown in Figure III.4). The powders were galvanostatically cycled in Li-half cells with LP30 electrolyte between 1.7 V and 3 V at a rate of $C/20$ and the voltage profiles are summarized in Figure III.9.

The TiS_3 was discharged first (red curve in Figure III.9a) and up to 2 Li could be inserted till a cut off discharge potential of 1.75 V. At the beginning of first discharge we always observe a deep voltage drop (peak at ~ 2 V in dQ/dV curve in Figure III.9b), which is usually associated to nucleation of a second phase.^{10,255,269–271} The discharge plateau observed afterwards corresponds to the intense peak at 1.97 V in the dQ/dV curve. During the subsequent charge, a small nucleation overpotential followed by a charging plateau is obtained (peaking at 2.57 V in dQ/dV curve). However, the material does not go back to the initial composition (i.e., Li_0TiS_3), since ~ 0.2 Li remains in the charged phase (with an approximate composition of $\text{Li}_{0.2}\text{TiS}_3$). In the 2nd discharge, the nucleation overpotential is not observed, and the intercalation takes place at slightly higher potential than the 1st discharge. Overall a high polarization of >0.5 V is obtained.

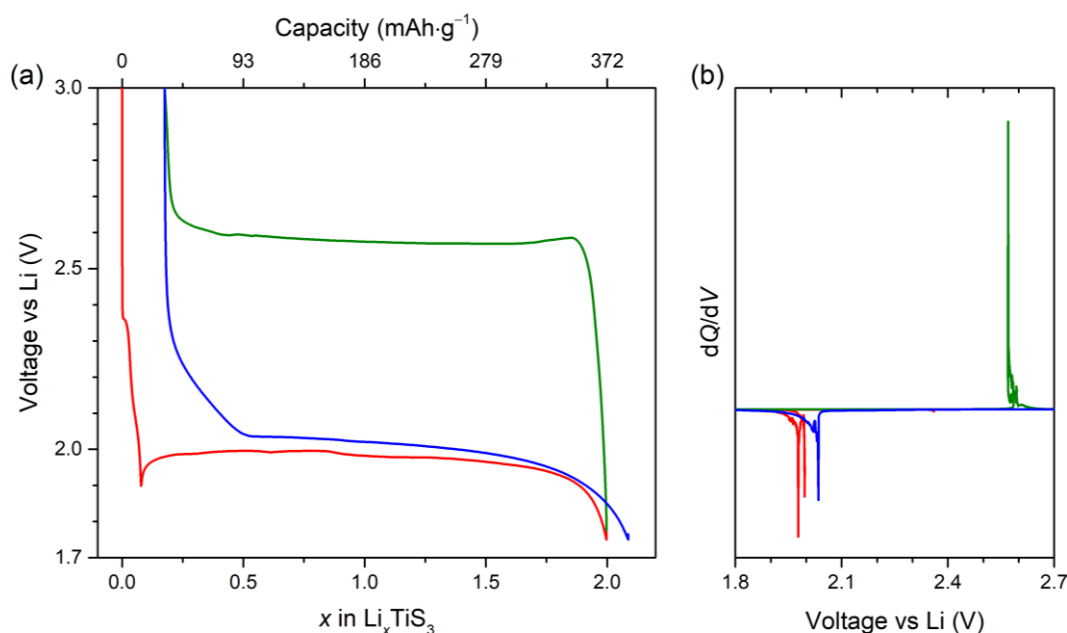


Figure III.9. Charge-discharge profile of TiS_3 in the 1st cycle. The first Li-intercalation (discharge) and, subsequent second charge and discharge are shown in red, green and blue colors, respectively. The voltage profile are shown in (a) and the corresponding dQ/dV curves are in (b).

III.2.4 Evolution of crystal structure during discharge-charge

To understand the structural change upon Li-(de)intercalation, we performed *operando* XRD during charge-discharge of the TiS_3 powder and the results are summarized in Figure III.10a. During the first discharge, it goes through a biphasic process, as indicated by the appearance of a 2nd phase. At mid-discharge, the Li_1TiS_3 composition (shown in blue color) is a mixture of phases, with second phase solely remaining at the end of discharge (Li_2TiS_3 , red pattern). Upon charging back, the evolution of the XRD patterns follows the reverse pathway. Note that, the full charged phase $\text{Li}_{-0.2}\text{TiS}_3$ shows a XRD pattern (shown in green) similar to the TiS_3 , but with much broader peaks. This indicates that, upon cycling, TiS_3 loses crystallinity largely.

For more accurate characterization, we have also collected *ex situ* SXR patterns (at 11-BM) of the samples at various SoCs (state of charges). The patterns are gathered in Figure III.10b. The mid-charged LiTiS_3 is clearly a mixture of the TiS_3 and Li_2TiS_3 , in agreement with the previously described the *operando* XRD. Mention must be made, that the SXR pattern of the fully-discharged Li_2TiS_3 is different from the layered Li-rich Li_2TiS_3 (will be discussed in Section III.3).²⁷² This indicates that the crystal structure of the Li_2TiS_3 prepared electrochemically (by Li intercalating in TiS_3) is different from the layered LiMS_2 (M= transition metal, space group $C2/m$) family.

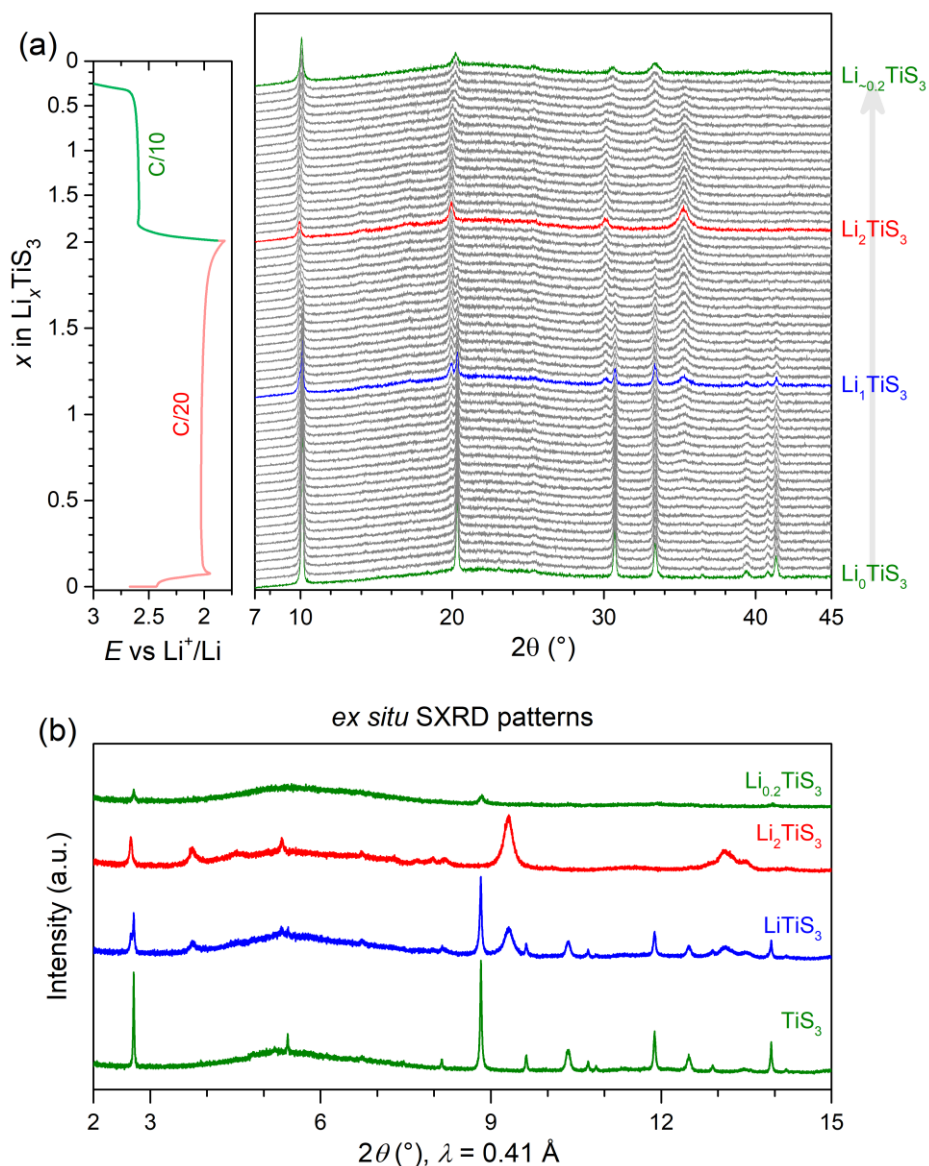


Figure III.10. Operando XRD of TiS_3 . The corresponding charge (at C/20 rate) and discharge (at C/10 rate) profile is shown in the left panel. Some important compositions are indicated at the right of the patterns. (b) *Ex situ* SXR patterns of some composition indicated on the figure.

In contrast to the layered Li_2TiS_3 phase,²⁷² the crystal structure of this electrochemically prepared Li_2TiS_3 has never been reported in literature, hence our attempt to solve it by combined TEM and SXR studies. Firstly, TEM studies were performed on Li_2TiS_3 crystals that were recovered from discharged TiS_3/Li cell (i.e., few TiS_3 crystals were cycled, without Csp additive, at a rate of C/50). The HRTEM images are shown in Figure III.11. We noticed significant exfoliation of the TiS_3 crystals upon lithiation (Figure III.11a). HAADF-STEM image of Li_2TiS_3 shows that the crystal structure is retained, but the gap between the Ti–S slabs disappears (along a direction, compare Figure III.11b). However, we could reconstruct a reciprocal space by rotating the crystals around $[010]$, and then it could be indexed with a primitive monoclinic unit cell with $a = 6.35 \text{ \AA}$, $b = 3.51 \text{ \AA}$, $c = 17.87 \text{ \AA}$, $\beta = 91.2^\circ$.

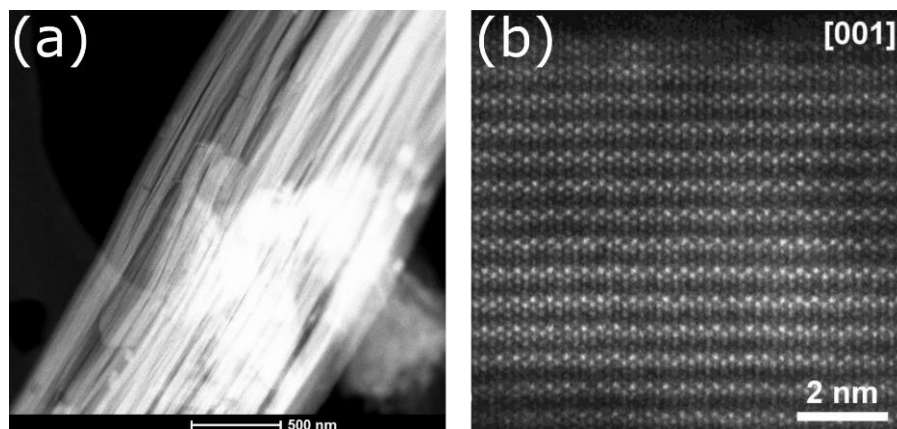


Figure III.11. HRTEM images of Li_2TiS_3 single crystals. (a) Low magnification HAADF-STEM image, and (b) HAADF-STEM image of the Li_2TiS_3 .

SEM images of Li_2TiS_3 (discharged TiS_3)

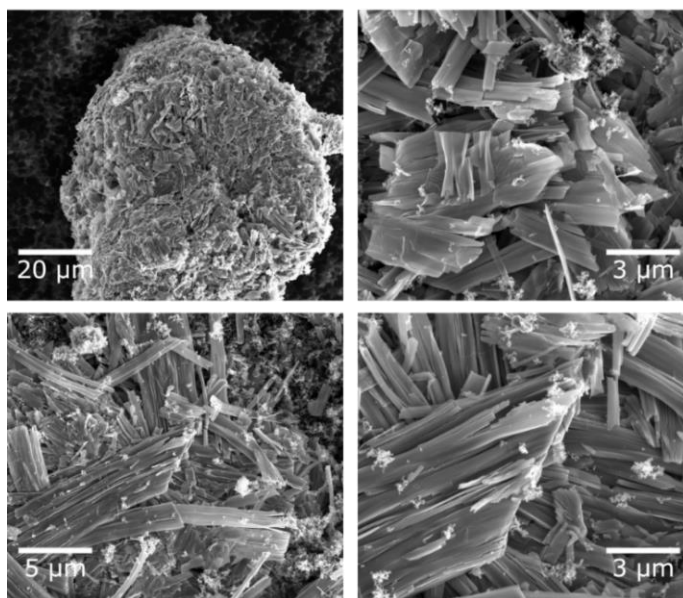


Figure III.12. SEM images of the *ex situ* Li_2TiS_3 (discharged TiS_3) powder. Images were taken after washing and drying of the cycled sample. The amorphous whitish region corresponds to the C_{sp} that was added prior to cycling.

At this point, this unit cell was used to refine the *ex situ* SXRD pattern collected for the Li_2TiS_3 powder sample (that preserve the submicron-sized ribbon like morphology, see the SEM images in Figure III.12). The Le Bail refinement of the SXRD pattern is shown in Figure III.13. The SXRD pattern could be indexed with a monoclinic unit cell of $a = 6.34670(32) \text{ \AA}$, $b = 3.51879(18)$, $c = 17.86683(4) \text{ \AA}$, $\beta = 91.19907(1)^\circ$, and $V = 398.927 \text{ \AA}^3$. Compared to the pristine TiS_3 , we observe an expansion along a direction and doubling along c direction, whereas b remains almost similar (to recall, $a = 4.9667(3) \text{ \AA}$, $b = 3.40157(10) \text{ \AA}$, $c = 8.8008(4) \text{ \AA}$, and $V = 147.419(11) \text{ \AA}^3$ for TiS_3 , see Appendix Table A2.1). Consequently, in Li_2TiS_3 , the unit cell is doubled along c direction (i.e., $Z = 2$), with $\sim 35\%$ expansion (normalized by Z) in unit cell volume is observed upon lithiation of TiS_3 .

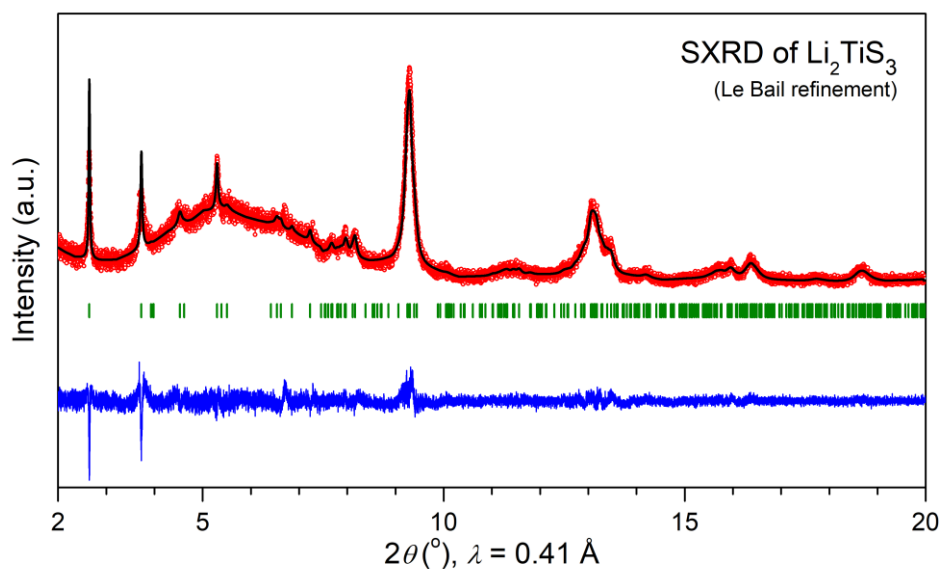


Figure III.13. Le Bail refinement of *ex situ* Li_2TiS_3 powder. The red circles, black continuous line, blue line, and green tick bars represent the observed, calculated, and difference patterns, and Bragg positions, respectively.

However, we could not obtain the complete structural model yet. For Li_2TiS_3 , the work is still under progress. Lastly, the crystal structure of the $\text{Li}_{-0.2}\text{TiS}_3$ formed upon charging back was examined. The HAADF-STEM image of the phase (Figure III.14) shows close resemblance to the corresponding image of the pristine TiS_3 , with however, a wavy appearance in the Ti–S slabs, indicating large residual strain. Such strain does not come as surprise, bearing in mind the breaking/reformation of S–S dimers upon cycling.

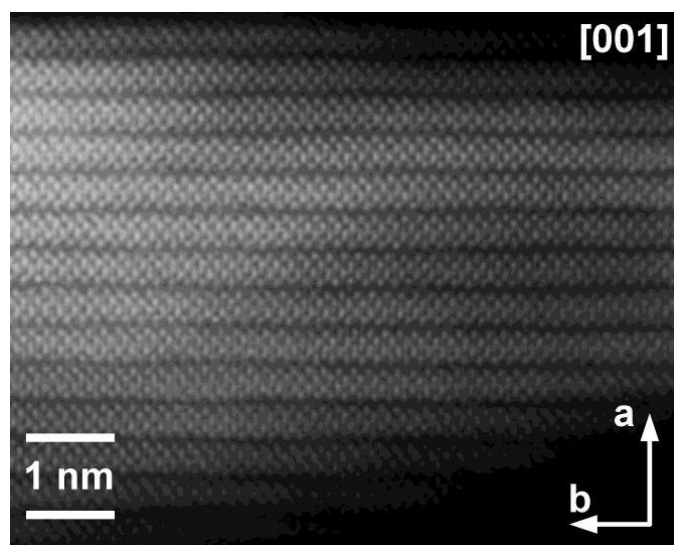


Figure III.14. HAADF-STEM image of $\text{Li}_{-0.2}\text{TiS}_3$ after 1st cycle.

III.2.5 Tracking oxidation states during Li (de)intercalation

Next, we examined the charge compensation mechanism during the Li (de)intercalation in TiS_3 , which will also be used as a reference later. The ionic charge of TiS_3 is expected to be formulated as $\text{Ti}^{4+}(\text{S}_2)^{2-}\text{S}^{2-}$. The oxidation changes in S and in Ti were probed at various SoCs. Figure III.15a shows the S 2p core XPS spectra collected on the cycled samples.^c The pristine TiS_3 shows S 2p core XPS peak containing both S^{2-} and S_2^{2-} (dimer) at a ratio 32:68 %, consistent with the crystal structure drawn in Figure III.2, where the isolated S1 atom (bridging) is characterized by a larger negative charge than the S atoms in S2–S3 pair.^{255,268,273,274} At mid-discharge (Li_1TiS_3), the intensity of the S_2^{2-} peak decreases (56:44 %). The fully-discharged Li_2TiS_3 shows only the peak for S^{2-} (and similar to TiS_2), as the S_2^{2-} gets reduced to S^{2-} upon Li-intercalation. On charging back, in $\text{Li}_{0.2}\text{TiS}_3$, the spectra is almost restored back as the pristine.

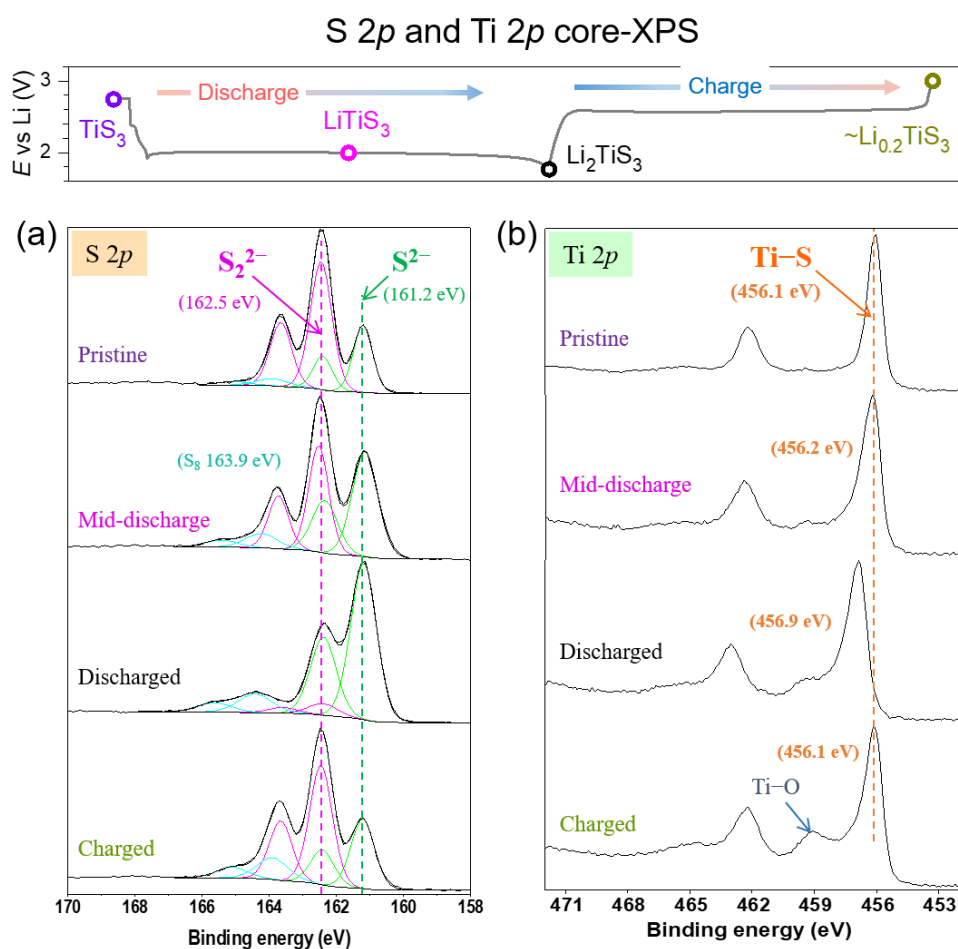


Figure III.15. S 2p and Ti 2p core XPS spectra of the cycled TiS_3 powder samples. The corresponding voltage profile during cycling is shown in the top panel. In (a), the spectra are deconvoluted by fitting to the doublets as indicated on the figure. In (b), the spectra shows traces of Ti–O, which is probably due to the reactivity with electrolyte.

^c XPS studies were performed by Dr Dominique Foix, Université de Pau.

Ti $2p$ core XPS spectra were also collected on the same samples and they are shown in Figure III.15b. The spectra for the pristine TiS_3 and mid-discharged LiTiS_3 are positioned at same binding energies, indicating their formal oxidation state to be +4.²⁵⁵ However, drastic change happens for the full-discharged Li_2TiS_3 , where the peak moves to higher binding energy. Following the existing literature, this shift could be explained by the increase of ionicity of Ti-environment that arises from reduction of all S_2^{2-} dimers to S^{2-} , while Ti stays as Ti^{4+} .^{255,256,273,275,276} However, we believe that the possibility of reduction of Ti^{4+} cannot be discarded and we will continue working on this further. Furthermore, we are exploring the possibility of change in the Ti coordination from trigonal prismatic site to the more stable octahedron site. On charging back, the position of the Ti XPS peak is restored back, despite the irreversibility of electrochemistry ($\text{Li}_{-0.2}\text{TiS}_3$).

To further probe the changes in the oxidation states, we performed Electron energy loss spectroscopy (EELS) in combination with X-ray absorption spectroscopy (XAS) studies.^D The S L -edge EELS spectra of the pristine TiS_3 and fully-discharged Li_2TiS_3 powders (Figure III.16a) comprise a weak pre-edge and intense broad edge feature. The spectra correspond to a series of transitions from the S $2p$ core level to unoccupied S $3s$ σ^* , S $3d$, etc. states, which are further split because of transitions from the S $2p_{3/2}$ (L_3 edge) and S $2p_{1/2}$ (L_2 edge) states due to spin-orbit coupling.²⁷⁷ The S- L edge of the TiS_3 and Li_2TiS_3 shows similar spectra, except the spectra for TiS_3 contains more broad peaks. Worth noting that for the TiS_3 , the broad peaks may be associated to possibly presence of different coordinations of S atoms.

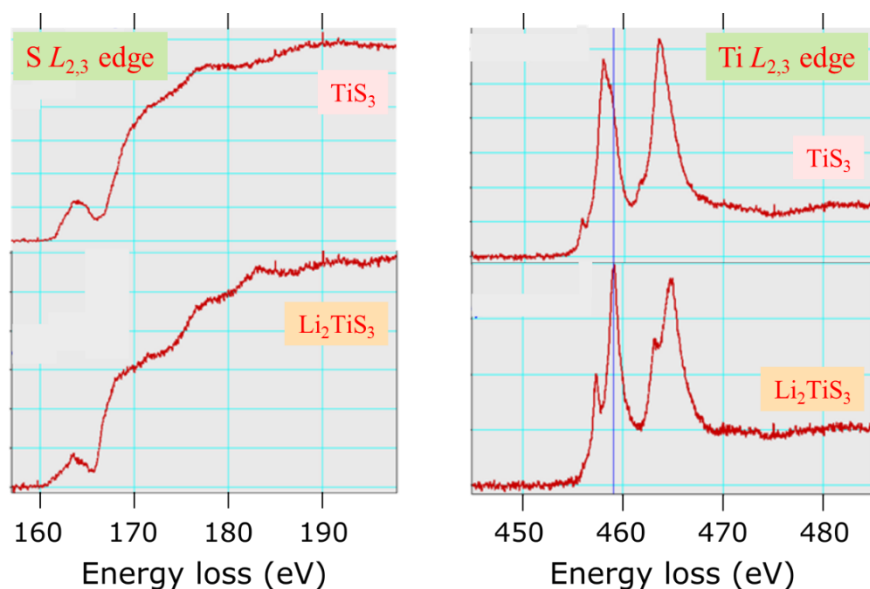


Figure III.16. EELS spectra of the S $L_{2,3}$ and Ti $L_{2,3}$ edge of the cycled TiS_3 samples. The corresponding voltage profile during cycling is shown in Figure III.15.

Turning to the Ti L -edge EELS of TiS_3 powder (Figure III.16b), we found that the spectra is in good agreement with the previously reported Ti L -edge XANES (X-ray absorption near edge structure)

^D EELS studies were performed by Prof Artem M. Abakumov.

spectra of TiS_3 ^{268,276} and has been associated to the Ti^{4+} (in TiS_8 coordination, as portrayed in the structural characterizations). Upon Li-intercalation (Li_2TiS_3), the spectra shifts towards higher energy by ~ 0.98 eV (similar to that of TiS_2 ²⁴³ suggesting an octahedrally-coordinated of Ti^{4+}). Note that the observation in XPS (Figure III.15b) supports this shift.

To get further insights of S states, X-ray absorption spectroscopy (XAS) studies were performed at the 4-ID-C beamline (Argonne National Laboratory).^E XANES spectra were collected in both total electron yield (TEY, probe depth is ~ 10 nm) and total fluorescent yield (TFY, probe depth is ~ 100 nm) modes. Both TEY and TFY spectra produces similar spectra and hence only TFY spectra (more bulk sensitive) has solely reported here, with the TEY spectra been described in the Appendix Figure A2.1. See the Appendix for details of the methods of XANES acquisition.

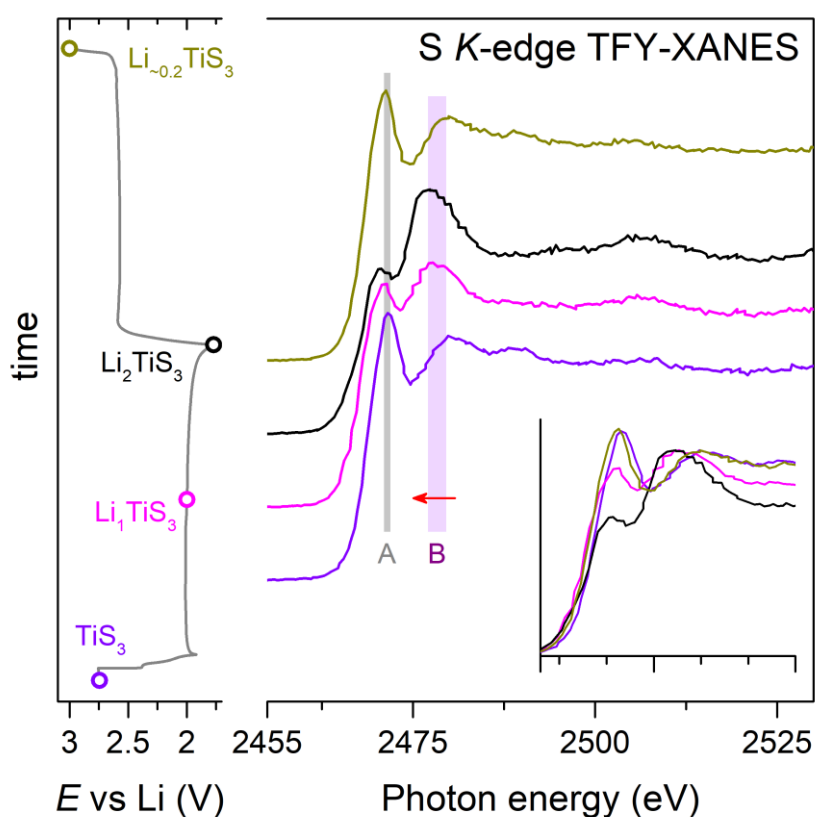


Figure III.17. S K-edge TFY-XANES spectra collected for TiS_3 and LiTiS_3 , (mid-discharged), Li_2TiS_3 (full-discharged), and $\text{Li}_{-0.2}\text{TiS}_3$ (fully-charged) samples.

The TFY-XANES spectra for pristine TiS_3 consists a broad edge centered at ~ 2472 eV (denoted as **B** and an intense pre-edge at ~ 2471.5 eV (denoted as **A**).^{243,268} The **B** edge (at ~ 2479.8 eV) represents

^E XAS studies were performed by Haifeng Li and Prof Jordi Cabana, University of Illinois at Chicago (USA).

multiple photoelectron transitions enlisting hybridized sulfur $1s \rightarrow 3p\sigma^*$ transition with the latter state being hybridized with metal $4s$ and $4p$ states. The pre-edge **A**, in contrast, depends on the degree of hybridization of the S unoccupied antibonding states with the empty transition metal $3d$ states.²⁵⁰ The shape and position of the spectra are consistent with reported spectra of the TiS_3 .^{256,268} Remarkable variations are observed upon Li intercalation, specifically decrease in the intensity of pre-edge **A**, and shift of edge **B** towards lower energy. In LiTiS_3 , the edge shifts to ~ 2477.3 eV, and the pre-edge becomes weak, whereas in Li_2TiS_3 , the pre-edge further weakens. This is consistent with the reduction of S_2^{2-} to S^{2-} , as similar shift in the edge **B** is observed during lithiation of VS_4 .²⁵⁰ The S_2^{2-} dimers having a lower energy $1s$ orbital compared to S^{2-} , hence leading to a higher energy edge peak.^{250,268} Upon charging back, in $\text{Li}_{0.2}\text{TiS}_3$, the spectra is almost restored back. Overall, these studies unambiguously point towards the $\text{S}^{2-}/\text{S}_2^{2-}$ redox.

III.2.6 Practicability of the anionic redox

Having explored the strong involvement of anionic redox in TiS_3 leading to an energy density as high as >700 $\text{Wh}\cdot\text{kg}^{-1}$, the next legitimate question pertains to its practicability. To evaluate, first we cycled TiS_3 powder over long cycling (Figure III.18), which shows that the capacity falls very rapidly.

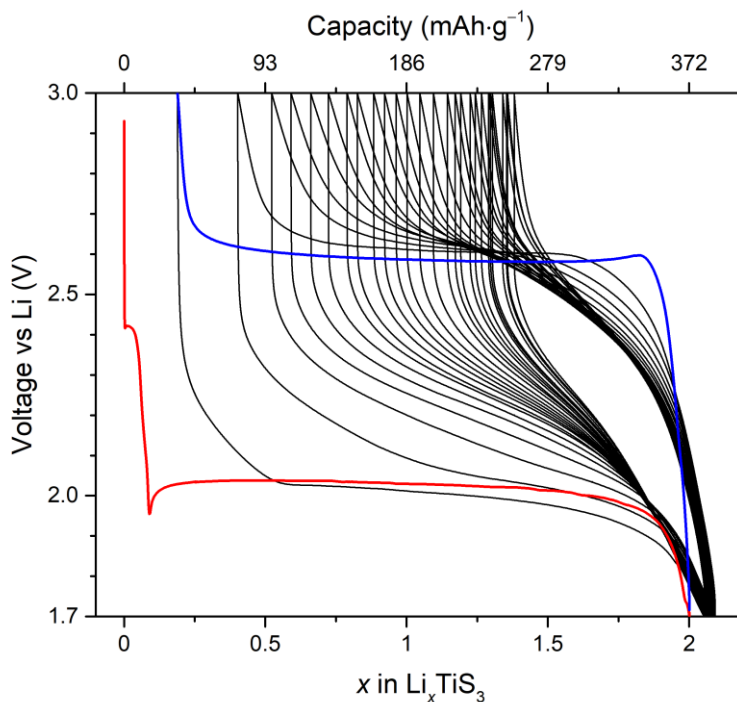


Figure III.18. Charge-discharge profile of TiS_3 over first 25 cycles. The TiS_3 (powder) was cycled in Swagelok cell as powder (hand-ground with 20 wt% Csp) at a rate of $C/20$.

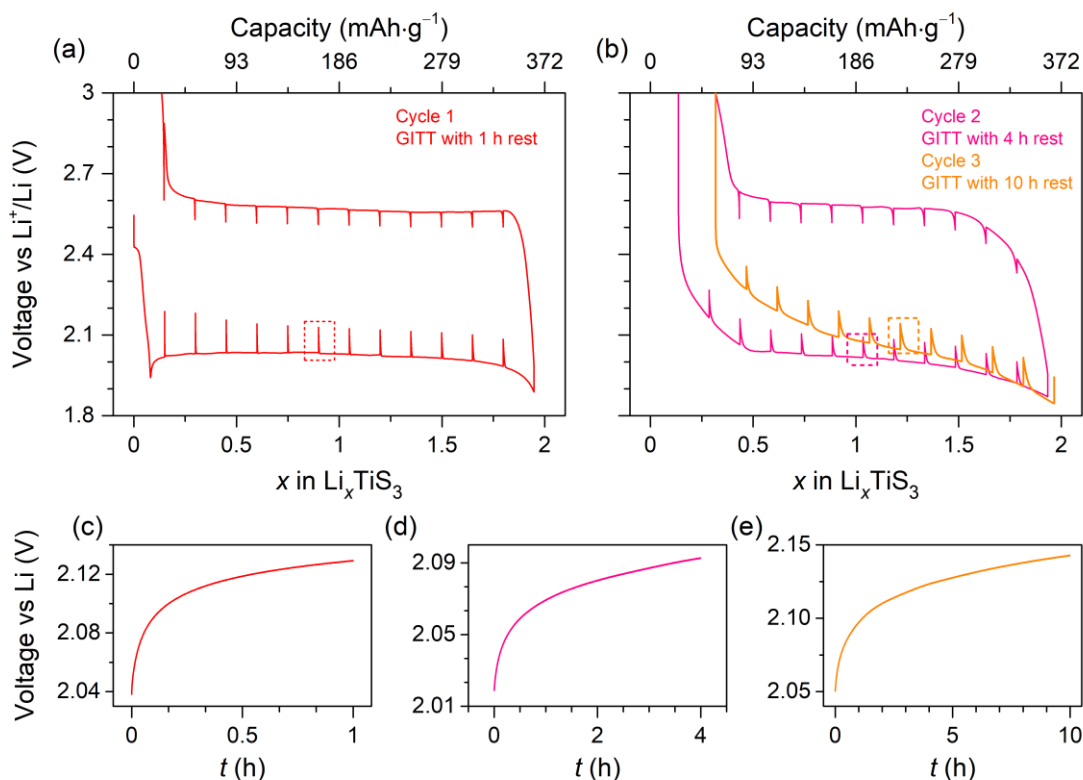


Figure III.19. Voltage profile of TiS_3 recorded with a GITT protocol. The TiS_3 was cycled in a two-electrode cell at a rate of $C/20$ with relaxation time indicated in the figure. (a-b) Voltage profile in first 3 cycles with varying relaxation time. (c-f) Voltage profile during the relaxation indicated by boxes with dashed in a,b.

Furthermore, a huge polarization of ~ 0.6 mV in the charge-discharge profile reveals that the Li uptake/removal in TiS_3 lead to poor energy efficiency. To understand whether the polarization is nested in kinetic limitation, we performed galvanostatic intermittent titration technique (GITT) of TiS_3 . The voltage profile of the first 3 cycles recorded with GITT protocol (3 h pulse at $C/20$ followed by relaxation) is shown in Figure III.19. After a rest of 1 h a large hysteresis still remains as shown in the 1st cycle (Figure III.19a). The relaxation time was increased gradually in the 2nd and 3rd cycle (Figure III.19b), but even after rests of 4 h (2nd cycle) or 10 h (3rd cycle) the hysteresis does not improve. Typical voltage profile during the rest period is shown in Figure III.19c-e, which shows a never-ending voltage relaxation even for rest periods of 10 h. Therefore, the anionic redox process in TiS_3 has a large time constant and is inherently limited thermodynamically.²⁷⁸

In summary, the rich crystallochemistry and electrochemistry of TiS_3 has been explored in details. The structural change upon S–S bond breaking and reformation accompanied by Li (de)insertion is yet to be understood completely. Turning back to electrochemistry, utilization of the anionic $\text{S}_2^{2-}/\text{S}^{2-}$ redox lead to attractive capacity of ~ 370 $\text{mAh}\cdot\text{g}^{-1}$, but to the expense of large hysteresis, and rapid capacity fading. Hence, to circumvent the issue, we decided to explore the feasibility of designing Li-rich layered sulfides, alike the Li-rich oxides, which do not trigger complete S–S dimerization.

III.3 Li-rich layered sulfides

In layered family, Li-rich NMC oxides were derived from the layered $\text{Li}_{1.33}\text{Mn}_{0.67}\text{O}_2$ (commonly written as Li_2MnO_3) with their anionic redox activity being a function of the competition between U (d - d coulomb interaction) and Δ (charge transfer) terms.²⁷⁹ Preparing a similar Li-rich Mn-based layered sulfide is not possible, simply because the S $3p$ band is situated much closer to the Li/Li⁺ reference than the O $2p$ band, leaving the Mn^{3+/4+} redox band too low-lying, as already discussed in Chapter 1 (recall Figure I.7a,b). Hence, to design an analogous layered sulfide $\text{Li}_{1.33}\text{M}_{0.67}\text{S}_2$, (i.e., Li_2MS_3) an appropriate transition metal M needs to be chosen first. Amongst $3d$ metals, $\text{M} = \text{Ti}^{4+}$ presents the best choice for sulfides, because the Ti^{3+/4+} redox band is located above the S $3p$ band. The $\text{Li}_2\text{Ti}^{4+}(\text{S}^{2-})_3$ offers a high theoretical capacity of $339 \text{ mAh}\cdot\text{g}^{-1}$ (considering removal of all Li's). Therefore, we decided to study anionic redox in Li_2TiS_3 -based Li-rich layered sulfides, which will be described next.

III.3.1 Li_2TiS_3

III.3.1.1 Structural Characterizations

Li_2TiS_3 was prepared by reacting Li_2S , and TiS_2 in stoichiometric amounts in vacuum-sealed quartz tubes at $750 \text{ }^\circ\text{C}$ (see the Appendix for details). The SXRD pattern of the as-synthesized Li_2TiS_3 could be refined in the in $C2/m$ space group alike for Li_2MnO_3 . The Rietveld refinement of its synchrotron XRD (SXRD) pattern is shown in Figure III.20a, with the obtained parameters summarized in the Appendix Table A2.2. This crystal structure of Li_2TiS_3 is shown in Figure III.20b, that indicates the similarity to honeycomb-ordered structure reported for Li-rich layered oxides family. However with an expectedly expansion of unit cell in Li-rich sulfides than in oxides, to accommodate the bulkier S atoms.

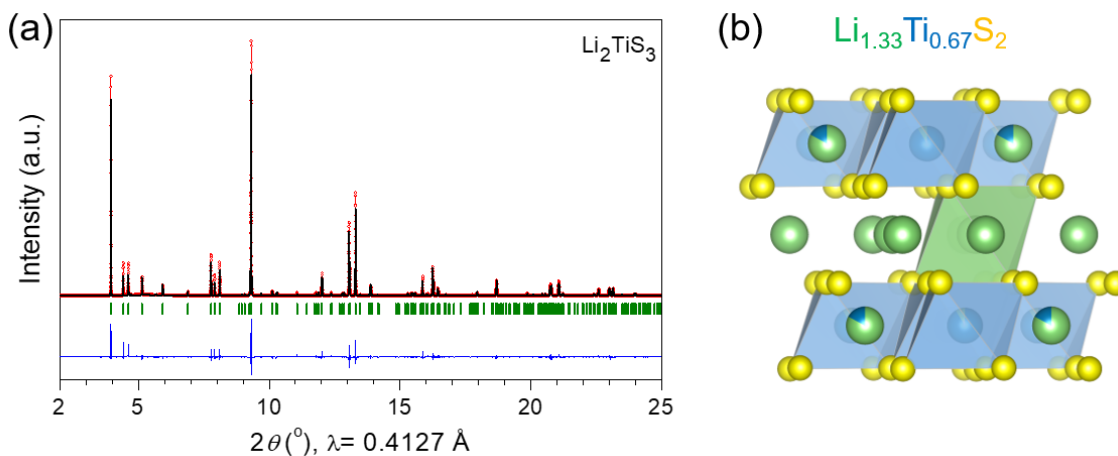


Figure III.20. Crystal structure of Li_2TiS_3 from Rietveld refinement of the SXRD pattern. (a) The Rietveld refinement. The red circles, black continuous line, blue line, and green tick bars represent the

observed, calculated, and difference patterns, and Bragg positions, respectively. (b) The corresponding crystal structure. Li, Ti, and S atoms are shown in green, blue, and yellow, respectively.

III.3.1.2 Electrochemical activity

The electrochemical performance of the Li_2TiS_3 sample was tested in Li-half cell between 1.8 V and 3 V at a rate of $C/20$ and the voltage profiles are summarized in Figure III.21.

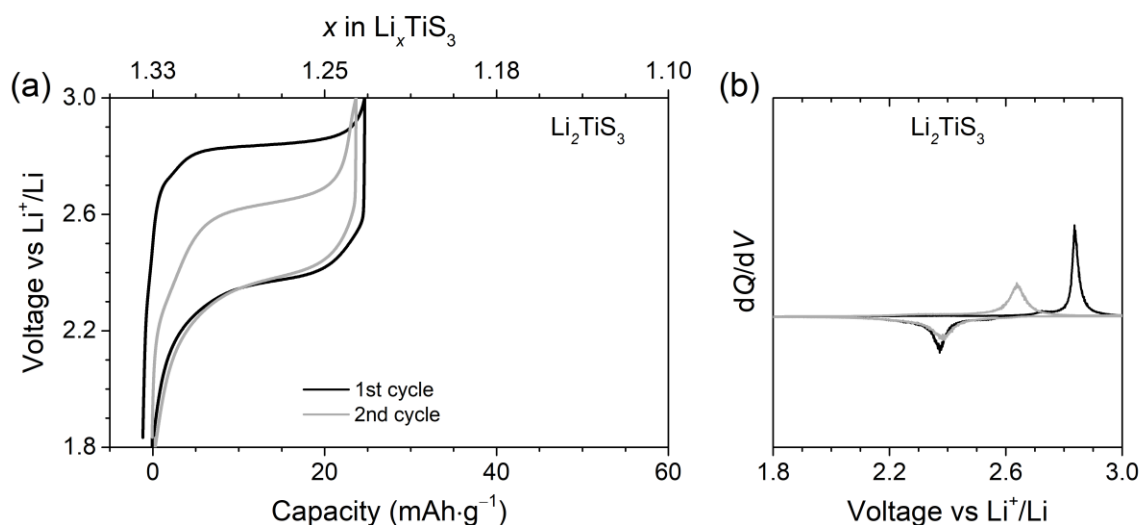


Figure III.21. The electrochemical performance of Li_2TiS_3 . (a) The voltage profile, and, (b) corresponding dQ/dV curves, are shown here. The curves in lighter color denote the 2nd cycle.

The Li_2TiS_3 shows very poor electrochemical activity, since only ~ 0.1 Li could be extracted reversibly. This is in accordance with some recent literature also.^{280,281} Attempts to enhance the activity by either ball milling the sample or by adding larger amounts of carbon additive were unsuccessful. Note that Li_2TiS_3 has a sufficiently high electronic conductivity ($\sim 2.7 \cdot 10^{-5} \text{ S} \cdot \text{cm}^{-1}$, Appendix Figure A2.2), and ionic conductivity ($\sim 5.5 \cdot 10^{-4} \text{ S} \cdot \text{cm}^{-1}$, Appendix Figure A2.3). This leads us to conclude that such a non-activity is intrinsic to the phase. Interestingly we noticed, that the voltage profile of Li_2TiS_3 changes in the 2nd cycle (Figure III.21a) and interestingly the 2nd charge occurs at a lower potential than the 1st one (Figure III.21b). Hence, the 1st cycle act as an ‘activation cycle’, alike the Li-rich NMC. This phenomenon is observed for all Li_2TiS_3 -based compounds, as we will see in the subsequent sections.

Nevertheless, the pristine Li_2TiS_3 did not show any substantial electrochemical activity, which most likely nested in the fact that the $\text{Ti}^{3+/4+}$ redox band is empty ($3d^0$) and is situated far above the S $3p$ band, hence unable to stabilize oxidized sulfur (Figure I.7b). Hence, we move now for suitable partial substitution for Ti^{4+} . Here onwards, the Li_2TiS_3 will be written as $\text{Li}_{1.33}\text{Ti}_{0.67}\text{S}_2$, to be consistent with the layered $\text{LiMO}_2/\text{LiMS}_2$ formalism.

III.3.2 Fe^{2+} -substituted Li_2TiS_3

In order to initiate electrochemical activity in $\text{Li}_{1.33}\text{Ti}_{0.67}\text{S}_2$, suitable transition metal substituent M needs to be chosen. Since Ti^{4+} has $3d^0$ electronic configuration, $\text{Li}_{1.33}\text{Ti}_{0.66}\text{S}_2$ (i.e., Li_2TiS_3) is apparently electrochemically inactive. This situation reminds that of the $\text{Li}_{1.33}\text{Mn}_{0.67}\text{O}_2$ phase (poor electrochemical performance without nano-sizing) that required partial substitution with Ni^{2+} to instigate electrochemical activity (Figure I.7a).^{29,33,34} A first hint to address this problem in sulfides consists, as discussed by Li *et al.*, in using Co^{2+} as a substituent to initiate reversible anionic redox. Pursuing their idea, the authors succeeded in preparing $\text{Li}_{1.2}\text{Ti}_{0.6}\text{Co}_{0.2}\text{S}_2$ showing anionic redox activity.²⁸¹ Following similar substitution strategy, another approach to overcome this unfavorable band situation in Li_2TiS_3 is to prepare Ti^{3+} -doped $\text{Li}_{1.33-2y/3}\text{Ti}^{4+}_{0.67-2y/3}\text{Ti}^{3+}_y\text{S}_2$ so that the partially reduced Ti^{3+} ($3d^1$) leads to a half-filled $\text{Ti}^{3+/4+}$ redox couple, as shown by Flamary-Mespoulie *et al* (2016).²⁷² Other successful strategies to electrochemically activate the Li_2TiS_3 are either preparing $\text{Li}_{1.33}\text{Ti}^{4+}_{0.67}\text{S}_2$ having disordered rock-salt structures, or triggering anionic redox activity via antisite occupation as shown for $\text{NaCr}^{3+}\text{S}_2$ (leading to ~ 0.5 Na removal despite $\text{Cr}^{3+/4+}$ redox level is buried inside the S $3p$ band).^{70,282,283} We herein chosen Fe as a substituent to demonstrate the feasibility to activate the anionic redox activity in Li-rich layered $\text{Li}_{1.33-2y/3}\text{Ti}^{4+}_{0.67-y/3}\text{Fe}^{2+}_y\text{S}_2$. This situation is favourable for reversible sulfur redox, since the $\text{Fe}^{2+/3+}$ redox couple with available electrons ($3d^6$) is expected to be pinned at the top of the S $3p$ band (Figure III.22).²⁴

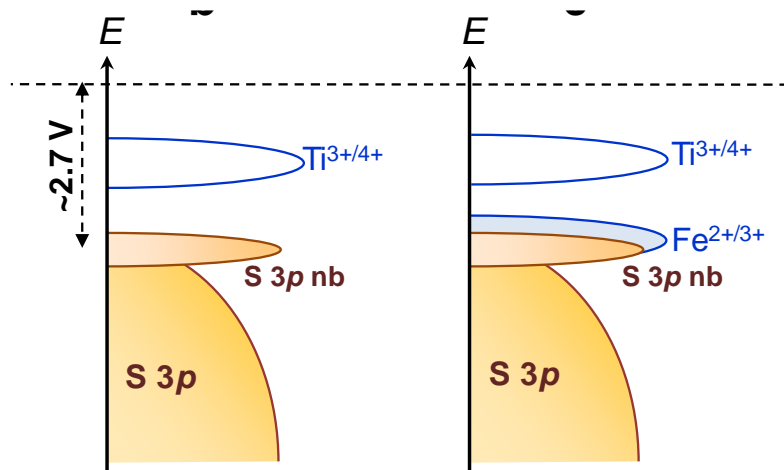


Figure III.22. Fe-substitution in Li_2TiS_3 . Schematic band structure of $\text{Li}_{1.33}\text{Ti}_{0.67}\text{S}_2$ (i.e., Li_2TiS_3 , in left), and its Fe^{2+} substituted derivative (in right). The relative band positions are estimated based on Ref²⁴. The label *nb* stands for non-bonding.

We prepared a series of materials of nominal composition $\text{Li}_{1.33-2y/3}\text{Ti}_{0.67-y/3}\text{Fe}_y\text{S}_2$, with $y = 0 - 0.5$, whose structural and electrochemical properties will be described below.

III.3.2.1 Structural Characterizations

The $\text{Li}_{1.33-2y/3}\text{Ti}_{0.67-y/3}\text{Fe}_y\text{S}_2$ compositions were prepared by reacting Li_2S , TiS_2 and FeS in stoichiometric amounts in vacuum-sealed quartz tubes at 750°C (see the Appendix Section A2.1 for

details). The lab X-ray diffraction (XRD) patterns are gathered in Figure III.23a for all the compositions. For more accurate characterization, SXRD patterns were also collected at the 11-BM in transmission mode with $\lambda = 0.41 \text{ \AA}$ and the patterns are gathered in Figure III.23b.

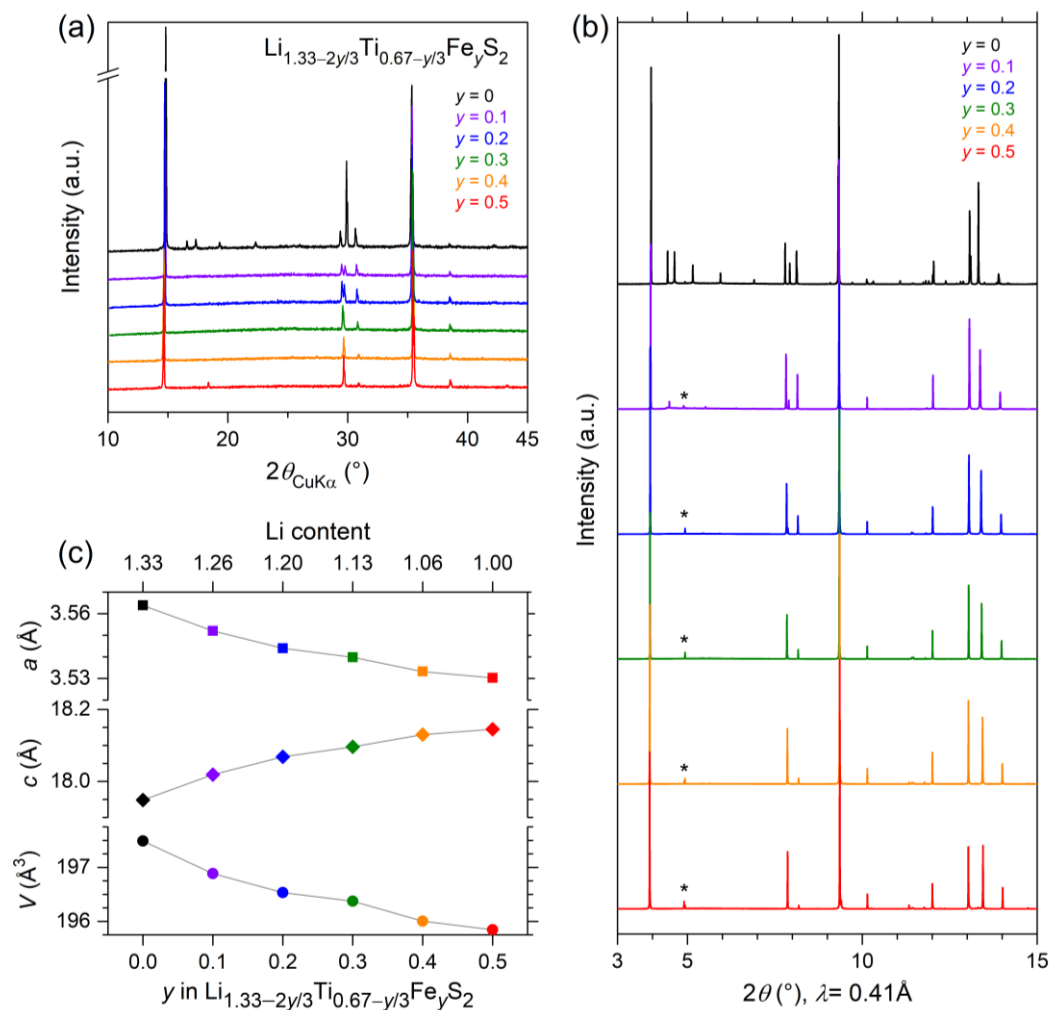


Figure III.23. Structural behavior of the $\text{Li}_{1.33-2y/3}\text{Ti}_{0.67-y/3}\text{Fe}_y\text{S}_2$ series. (a) XRD patterns, and (b) SXRD patterns of the as-synthesized $\text{Li}_{1.33-2y/3}\text{Ti}_{0.67-y/3}\text{Fe}_y\text{S}_2$ samples. (c) Variation of lattice parameters (obtained from the Rietveld refinement of the SXRD patterns). For the $y = 0$ composition, the lattice parameters have been converted to the $R\bar{3}m$ description.

Upon increasing the Fe content y , there is a progressive shift of the Bragg peaks (Figure III.24a) indicating the existence of a solid solution. Moreover, Fe-containing compositions ($y = 0.1 - 0.5$) do not show the superstructure peaks, most likely because Fe^{2+} disrupts the honeycomb $\text{Li}^+/\text{Ti}^{4+}$ ordering. Therefore, the Fe-containing phases could be fitted in a hexagonal $R\bar{3}m$ description analogous to the well-known Li-rich layered $\text{Li}_{1+y}\text{M}_{1-y}\text{O}_2$ phases, with the obtained lattice parameters shown in Figure III.23c. With increasing Fe content, we observe a monotonic increase in the c parameter that is accompanied by a decrease in the a parameter, such that the overall effect is a monotonic decrease in unit cell volume (V).

Since among the $\text{Li}_{1.33-2y/3}\text{Ti}_{0.67-y/3}\text{Fe}_y\text{S}_2$ series, the compound with $y = 0.3$ will be the center of interest in this study, we have characterized its structure in detail. The $\text{Li}_{1.13}\text{Ti}_{0.57}\text{Fe}_{0.3}\text{S}_2$ ($y = 0.3$) sample consists of submicron sized (5 - 30 μm) particles (shown in the Appendix Figure A2.4). We performed the Rietveld refinement of its SXRD pattern (Figure III.24b), which confirms that Fe, Ti and Li occupy same site in the metal layer (see the structural model in the Appendix). This structure was further confirmed by Rietveld refinement of its neutron powder diffraction (NPD) pattern also (see Figure III.24c).

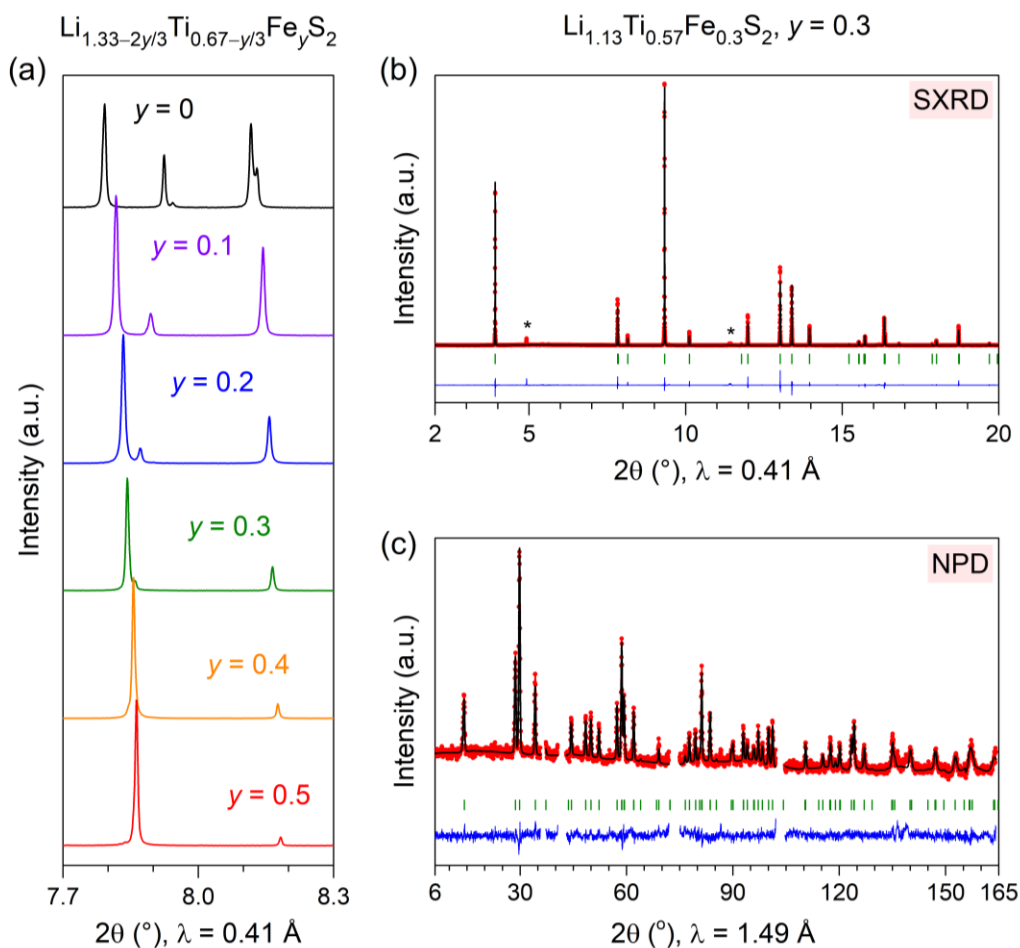


Figure III.24. Structural characterization of the $\text{Li}_{1.13}\text{Ti}_{0.57}\text{Fe}_{0.3}\text{S}_2$ ($y = 0.3$) sample. (a) Progressive shift of the peaks in SXRD patterns of the $\text{Li}_{1.33-2y/3}\text{Ti}_{0.67-y/3}\text{Fe}_y\text{S}_2$ samples. (b) Rietveld refinement of the SXRD pattern of the $\text{Li}_{1.13}\text{Ti}_{0.57}\text{Fe}_{0.3}\text{S}_2$ sample. (c) Rietveld refinement of the NPD pattern of $\text{Li}_{1.13}\text{Ti}_{0.57}\text{Fe}_{0.3}\text{S}_2$ using the model deduced from the SXRD pattern. The refinement returns the cell parameters of $a = 3.53563(4)$ \AA , $b = 18.08630(38)$ \AA , and $V = 195.801(5)$ \AA^3 with GoFs of $\chi^2 = 1.6$, $R_{\text{wp}} = 0.355\%$, and $R_{\text{B}} = 1.15\%$. Few 2θ regions have been excluded to avoid peaks from the vanadium-container. The red circles, black continuous line, blue line, and green tick bars represent the observed, calculated and difference patterns, and Bragg positions, respectively.

The structures of the $\text{Li}_{1.13}\text{Ti}_{0.57}\text{Fe}_{0.3}\text{S}_2$ is compared with the Li-rich NMC (LrNMC) in Figure III.25, which indicates the similarity of the structures of Li-rich sulfides and oxides. In both cases the excess Li's are mixed and disordered with the transition metals in the metal layer (MX_2 layer, $\text{X} = \text{S}$,

O), while for the sulfides the layer gap and TM–X (X= S, O) bond lengths are increased to accommodate the bulkier S atoms. Hence, now we move to explore their electrochemical properties.

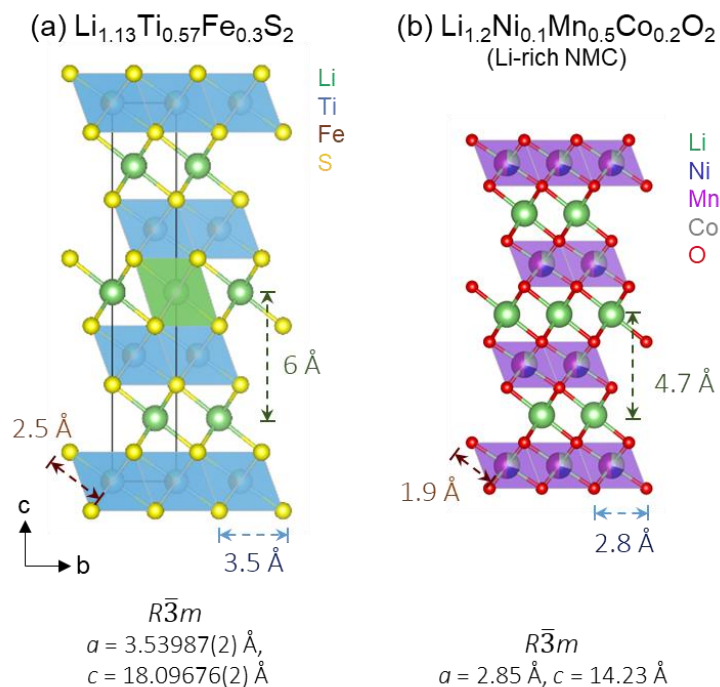


Figure III.25. Comparing the crystal structures of $\text{Li}_{1.13}\text{Ti}_{0.57}\text{Fe}_{0.3}\text{S}_2$ (a) and Li-rich NMC (b).

III.3.2.2 Electrochemical Properties

The electrochemical performances of the $\text{Li}_{1.33-2y/3}\text{Ti}_{0.67-y/3}\text{Fe}_y\text{S}_2$ samples (mixed and hand-ground with 20 wt% Csp) were tested in Li-half cells (in Swagelok type cells) between 1.8 V and 3 V at a rate of C/20 and the voltage profiles are summarized in Figure III.26. The Fe^{2+} -containing phases are electrochemically active, as shown in Figure III.26, which furthermore shows that, with increasing Fe-content, more amount of Li's can be extracted from the compositions up to $y = 0.3$. With $y > 0.3$, the extractable amount of Li's does not increase anymore, because of the available amount of Li (i.e., $1.33 - 2y/3$) decreases in the compositions. This improvement is most likely nested in the gradual amelioration of the band positioning with introduction of Fe content that triggers reversible anionic redox activity. However, despite the gradual electrochemical activation in the series, complete delithiation was not observed, as ~ 0.1 Li remains after full-charge of the compositions with $y \geq 0.3$.

The voltage profiles shows a specificity that is nested in the second cycle's charge-discharge which occurs at a lower potential than the first cycle. Note also the appearance of a short sloppy voltage profile (marked by 'S' in Figure III.26) at the early stage of charge, and most likely related to Fe redox activity. This follows by a long plateau-like (marked by 'P') activity on further oxidation, and presumably from the $\text{S}^{2-}/\text{S}_2^{n-}$ redox.

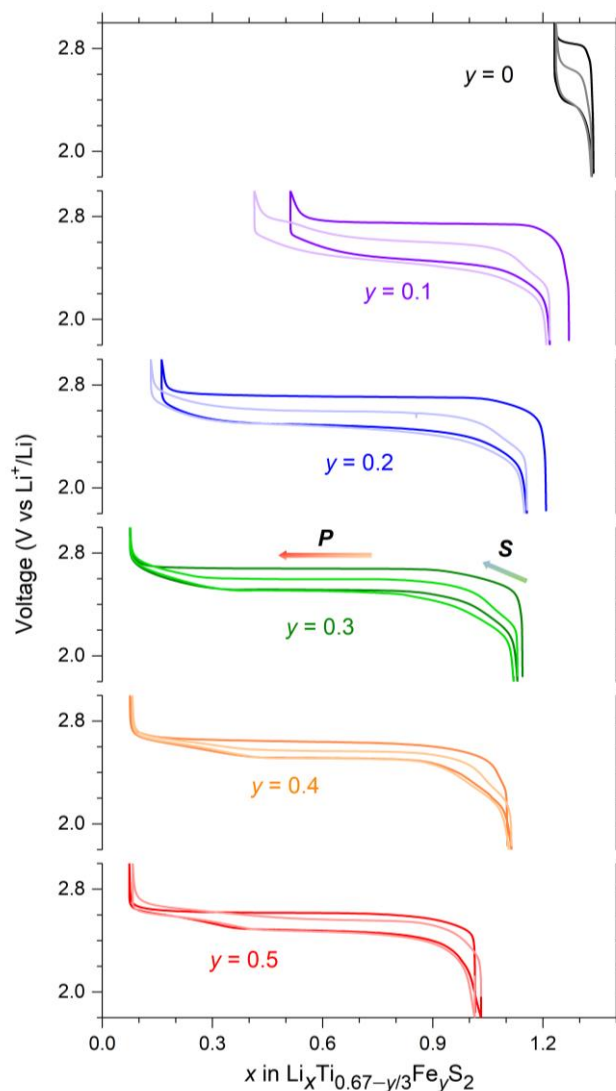


Figure III.26. Electrochemical behavior of $\text{Li}_{1.33-2y/3}\text{Ti}_{0.67-y/3}\text{Fe}_y\text{S}_2$. Voltage profiles of the compositions obtained over cycling vs Li at C/20 for the first two cycles. The curves in lighter colors denote the second cycles. The arrows marked by ‘S’ and ‘P’ denote the slope and the plateau, respectively (d) Performance of the $\text{Li}_{1.13}\text{Ti}_{0.57}\text{Fe}_{0.3}\text{S}_2$ ($y = 0.3$) composition over cycling at a rate of C/2.5 (except the first formation cycle at C/20).

The capacity obtained for all the compositions are summarized in Figure III.27a, which shows increase in capacity up to $y = 0.3$, and then decreases simply due to the lower amount of available Li. The maximum capacity of $\sim 245 \text{ mAh}\cdot\text{g}^{-1}$ was obtained for the composition $\text{Li}_{1.13}\text{Ti}_{0.57}\text{Fe}_{0.3}\text{S}_2$ ($y = 0.3$). The maximum capacities available from the cationic $\text{Fe}^{2+/3+}$ redox for the compositions are shown in Figure III.27a (purple line), which constitute parts of the measured capacities. Even by assuming full utilization of the multi-electron oxidation of Fe^{2+} to Fe^{4+} (blue dotted line in Figure III.27a), which is quite unlikely to occur in sulfide frameworks, we cannot account for all the measured capacity, hence implying the activity of the anionic network. Lastly, the corresponding dQ/dV profiles are shown in

Figure III.27b, which highlights that the respective oxidation potentials shift to lower voltage with increasing the Fe content.

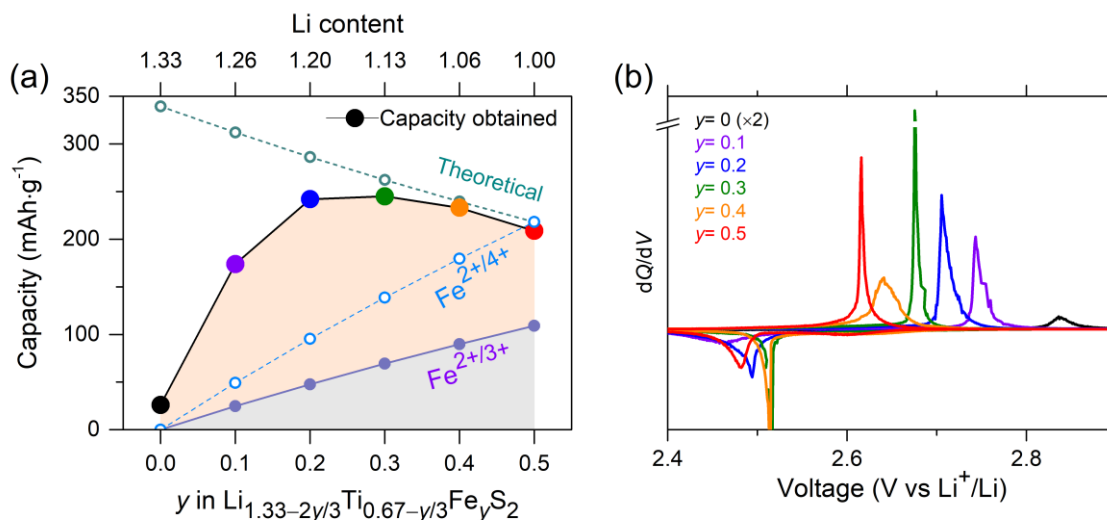


Figure III.27. Capacity and dQ/dV of $\text{Li}_{1.33-2y/3}\text{Ti}_{0.67-y/3}\text{Fe}_y\text{S}_2$. (a) Theoretical capacity (considering total Li-removal) and the actual discharge capacity obtained for the compounds over cycling at C/20. The capacity expected from cationic $\text{Fe}^{2+/3+}$ and hypothetical $\text{Fe}^{2+/4+}$ redox is also shown. (b) dQ/dV curves obtained in the first cycle for the various compositions.

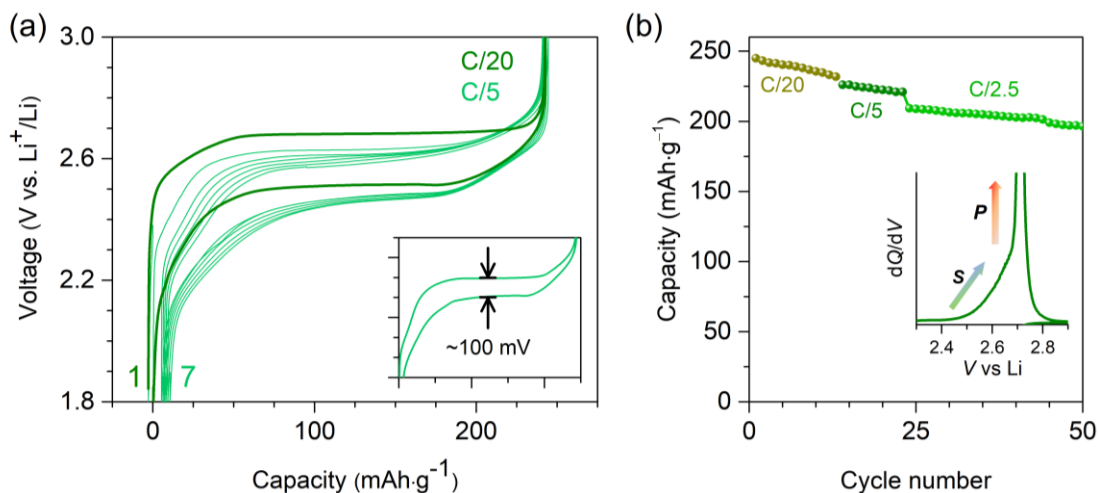


Figure III.28. More details of the electrochemical properties of $\text{Li}_{1.13}\text{Ti}_{0.57}\text{Fe}_{0.3}\text{S}_2$ ($y = 0.3$). (a) Evolution of the charge-discharge profile in first 7 cycles, at rates as indicated in the figure. The inset shows the zoom of the 2nd cycle, illustrating the overall voltage gap. (b) Cycling performance in Li-halfcell (at a rate indicated). The materials were cycled in Swagelok type cells, with samples as powders (mixed with 20 wt% Csp) only, without any further optimization. Inset shows zoom on the dQ/dV curve in the 1st cycle, illustrating the slope (S) and the plateau (P) features.

The voltage profile of the $\text{Li}_{1.13}\text{Ti}_{0.57}\text{Fe}_{0.3}\text{S}_2$ is shown in Figure III.28a. Note that the voltage profile changes after the 1st cycle and then stable cycling has been observed. 2nd cycle onward, the polarization reduces to ~ 100 mV (inset, Figure III.28a), instead of ~ 220 mV during the first cycle. This indicates that the first cycle acts as an ‘activation’ cycle alike the Li-rich NMC oxides. The dQ/dV profile

for $\text{Li}_{1.13}\text{Ti}_{0.57}\text{Fe}_{0.3}\text{S}_2$ is enlarged in Figure III.28b, which shows that the initial sloppy voltage profile (S) appears as a shoulder in the dQ/dV curve, whereas the plateau (P) manifests itself as an intense peak (recall Figure III.26 and Figure III.27b, green curves). The $y = 0.3$ sample not only shows the largest capacity, but also a respectable capacity retention (Figure III.28b) with also barely noticeable irreversible capacity in the first discharge. Therefore, we chose this composition for further investigations.

III.3.2.3 Cycling behaviour over larger voltage range

From the electrochemical behaviour described above (within 1.8 - 3 V), it is clear that ~ 0.1 Li remained electrochemically inaccessible, irrespective of the Fe-content. Hence, the legitimate question arises, is it possible to delithiate further ?

To verify this we decided to cycle the $\text{Li}_{1.13}\text{Ti}_{0.57}\text{Fe}_{0.3}\text{S}_2$ with an increased the upper voltage cutoff (> 4 V). The resulting voltage profile is shown in Figure III.29a, which shows that it does not lead to success, rather cell failure was observed above 3.8 V. Furthermore, it was confirmed by *operando* UV spectra that electrolyte decompositions occur at high voltage (as indicated by appearance of new absorption peak at ~ 250 -300 nm wavelength) and furthermore by *operando* XRD that shows sample decomposition to unidentified phases (details in the Appendix Figure A2.5 and Appendix Figure A2.6), which is responsible for the short circuit like behaviour. Worth recalling, that this situation is alike the Li-rich oxides, where even pushing at higher voltage does not enable fully delithiation prior decomposition, and oxygen release.^{54,284}

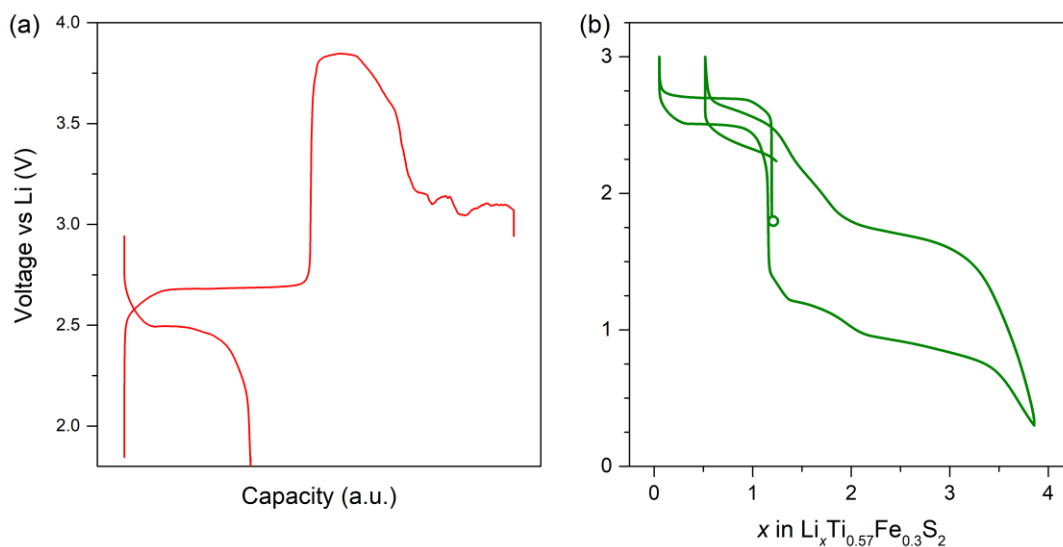


Figure III.29. Cycling $\text{Li}_{1.13}\text{Ti}_{0.57}\text{Fe}_{0.3}\text{S}_2$ in a broader voltage range. (a) Voltage profiles of the $\text{Li}_{1.13}\text{Ti}_{0.57}\text{Fe}_{0.3}\text{S}_2$ /Li half-cell cycled with a cutoff potential of 4.5 V (at a rate of C/20). Note that, even the cutoff potential was never reached because of sample decomposition, or parasitic reactions etc. (b)

Voltage profiles of the $\text{Li}_{1.13}\text{Ti}_{0.57}\text{Fe}_{0.3}\text{S}_2$ /Li half-cell cycled in low voltage (up to 0.2 V, at a rate of C/20). The green circle denotes the starting point.

Lastly, it remains to verify the electrochemical behaviour of the Li-rich sulfide at low voltage. Therefore, we have cycled the $\text{Li}_{1.13}\text{Ti}_{0.57}\text{Fe}_{0.3}\text{S}_2$ vs Li, up to 0.2 V (Figure III.29b). The sample indeed shows a staggering capacity increase, due to uptake of ~ 3 extra Li in discharge and consequently increase of the energy density up to $\sim 800 \text{ mAh} \cdot \text{g}^{-1}$. This can simply be explained by the conversion reaction type mechanism,²⁸⁵ where the metal ions (Fe^{2+} and Ti^{4+}) are reduced according to the following reaction,



However, a large polarization and rapid capacity loss upon cycling is observed which again highlight the drawbacks of the conversion type redox.⁵⁸

Lastly, to assess the practical application of this cathode material, we tried to cycle the $\text{Li}_{1.13}\text{Ti}_{0.57}\text{Fe}_{0.3}\text{S}_2$ sample at 55 °C, which could not succeed (details can be found in Appendix Figure A2.7).

In short, the Li-rich sulfide shows excellent reversibility of Li-(de)intercalation process only within voltage range of 1.8 - 3 V. Hence we will concentrate hereafter on the cycling performance of this compound within this range, starting with exploration of the structural aspects.

III.3.2.4 Structural integrity during charge-discharge

We first explore the effect Li uptake-removal process on the crystal structure of the $\text{Li}_{1.13}\text{Ti}_{0.57}\text{Fe}_{0.3}\text{S}_2$, by *operando* XRD measurements. XRD patterns were collected for every change in lithium stoichiometry of ~ 0.01 and summarized in Figure III.30. Upon charge, we observed a slight initial shift of the main peaks, indicating solid-solution behaviour. Over this regime, the unit cell volume decreases as a consequence of an anisotropic variation of the a and c lattice parameters (Figure III.30). Then, as the voltage reaches the first plateau, there is a gradual change in the intensity of the peaks with some peaks disappearing at the expense of new ones, which sharpen to give a well-defined XRD powder pattern at the end of the full charge, hence suggesting a two-phase de-intercalation process. This new phase with approximate composition $\sim \text{Li}_{0.1}\text{Ti}_{0.57}\text{Fe}_{0.3}\text{S}_2$, whose structure remains as layered one as described in detail in the next paragraph, has a lower unit cell volume (by $\sim 12.2\%$) than the pristine one.

On discharge, the compound undergoes first a solid-solution process for which both the a and c lattice parameters strongly increase (Figure III.30). Then, a biphasic process is observed with the growth of a phase with increased volume, followed again by solid-solution behaviour. We therefore have, for the first cycle, charge and discharge processes that proceed through different structural paths, even though the pattern returns close to the one for the pristine phase. This path-difference can be clearly observed from the evolution of the unit cell volume and of the a and c lattice parameters (Figure III.30).

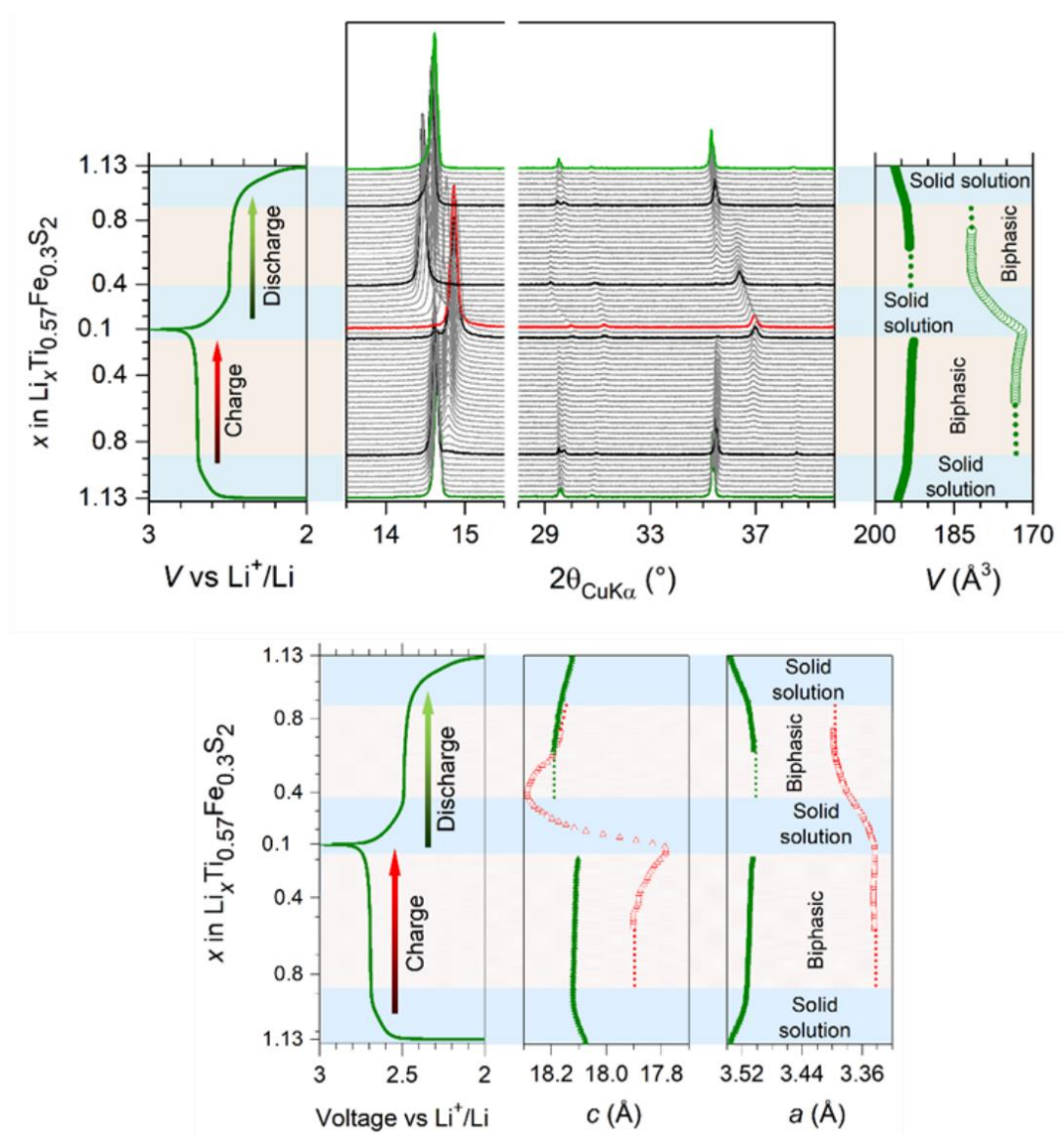


Figure III.30. Probing the Li (de)intercalation in operando. (a) Evolution of the *in situ* XRD patterns in the first cycle of a $\text{Li}_{1.13}\text{Ti}_{0.57}\text{Fe}_{0.3}\text{S}_2$ /Li half-cell at a rate of C/20. The left panel shows the corresponding voltage profile and the right panel shows the evolution of the unit cell volume (V), as obtained from the Rietveld refinements of the XRD patterns. Note that the dotted lines represent extrapolations, where the XRD patterns could not be refined because of poor intensity of the peaks. (b-c) Rietveld refinement of the SXRDR patterns (b) and the HAADF-STEM image (c) of the full-charged phase. The peaks denoted by * in (b) show minor Li_2TiO_3 impurity. (d) The bond-lengths observed in the pristine, full-charged and full-discharged phase (as obtained from the Rietveld refinement of the corresponding SXRDR patterns).

We further continued the operando XRD in the 2nd cycle (Figure III.31). Here also, the structural evolution goes through a biphasic process, as indicated by the evolution of the XRD patterns. However, the lattice parameters evolves via more symmetric, although not perfect, pathways on charge

and discharge, compared to the 1st cycle. Overall, throughout cycling the phase remains crystalline with well-preserved long-range layered crystal structure.

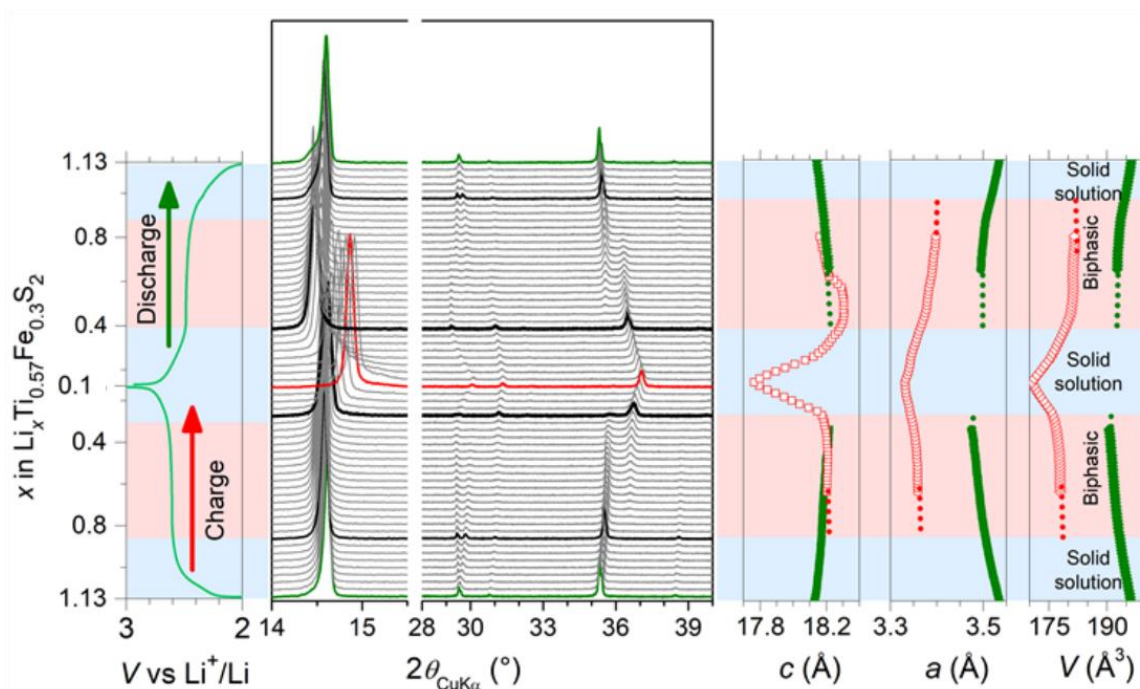


Figure III.31. 2nd cycle of the *in situ* cycling of $\text{Li}/\text{Li}_{1.13}\text{Ti}_{0.57}\text{Fe}_{0.3}\text{S}_2$ half-cell. The evolution of the XRD patterns during the *in situ* cycling of $\text{Li}/\text{Li}_{1.13}\text{Ti}_{0.57}\text{Fe}_{0.3}\text{S}_2$ half-cell at a rate of C/20 with the evolution of the unit cell parameters a , c , and V are also shown.

III.3.2.5 Crystal structures of charged-discharged phases

Next, we performed an in-depth exploration of the crystal structures at different states of charge (pristine, fully-charged and fully-discharged after first cycle) using SXRD. In agreement with the lab XRD data, the patterns can be indexed in the $R\bar{3}m$ space group. The pristine $\text{Li}_{1.13}\text{Ti}_{0.57}\text{Fe}_{0.3}\text{S}_2$ ($V = 196.384(2) \text{ \AA}^3$) presents an average Ti–S bond-length of $2.4792(3) \text{ \AA}$, with average S–S distances of $\sim 3.505 \text{ \AA}$ (structural model in Appendix Table A2.3). The Rietveld refinement of the SXRD pattern for the fully-charged $\text{Li}_{0.13}\text{Ti}_{0.57}\text{Fe}_{0.3}\text{S}_2$ phase is shown in Figure 4b. The corresponding crystal structure indicates a much smaller unit cell ($V = 172.338(6) \text{ \AA}^3$) (see the Appendix Table A2.4 for the structural model). This corresponds to $\sim 12\%$ contraction of the unit cell upon delithiation. Moreover, the average Ti–S bond length was found to shrink to $2.3635(1) \text{ \AA}$, leading to decreased average S–S distances of $\sim 3.344 \text{ \AA}$.

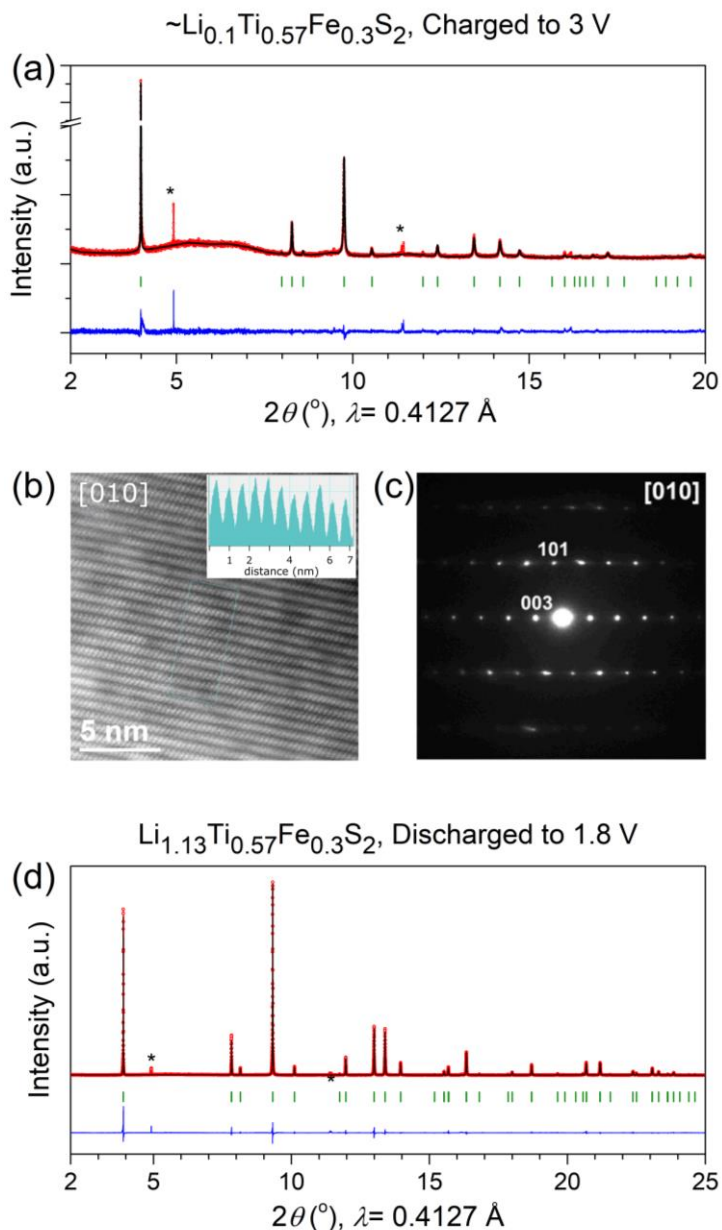


Figure III.32. Structural characterization of $\text{Li}_{1.13}\text{Ti}_{0.57}\text{Fe}_{0.3}\text{S}_2$ after Li (de)intercalation. (a-c) Rietveld refinement of the SXR D pattern (a), the HAADF-STEM image (b), and, SAED patterns of the fully-charged sample along the [010] axis (c) of the full-charged phase. The inset in (c) shows the HAADF intensity profile. (d) Rietveld refinement of the SXR D pattern of the discharge phase of the $\text{Li}_{1.13}\text{Ti}_{0.57}\text{Fe}_{0.3}\text{S}_2$. The red circles, black continuous line, blue line, and green tick bars represent the observed, calculated and difference patterns, and Bragg positions, respectively. The peaks denoted by * are from minor Li_2TiO_3 impurity.

In parallel, we conducted transmission electron microscopy (TEM) studies of the fully charged phase to verify whether cationic migration²⁸⁶ occurs. The HAADF-STEM image shows only the $[\text{Li}_{0.1}\text{Ti}_{0.57}\text{Fe}_{0.3}]\text{S}_2$ layers and thus discards the possibility of transition-metal migration to the interlayer sites (Figure III.32b). The HAADF intensity profile (inset, Figure III.32) clearly demonstrates no scattering density between the (Ti/Fe) S_2 layers, hence no Fe^{3+} cation migration. The selected-area

electron diffraction (SAED) of the fully-charged phase was also taken (Figure III.32c) which could again be successfully indexed with an $R\bar{3}m$ unit cell, in accordance with the SXRD pattern.

Finally, to assess the reversibility of Li-(de)intercalation, SXRD pattern of the fully-discharged sample was refined also. The Rietveld refinement is shown in Figure III.32d, and the structural parameters are gathered in the Appendix Table A2.5. The fully discharged phase is indeed very similar to the pristine phase ($V=196.896(2) \text{ \AA}^3$) with an average Ti–S bond length of $2.4825(3) \text{ \AA}$ and average S–S distance of $3.51(2) \text{ \AA}$, confirming the reversibility.

At this point it is interesting to verify whether S-dimerization occurs accompanying the anionic S^{2-}/S_2^{n-} redox. We plotted the variation of bond lengths upon Li-(de)intercalation in Figure III.33. As we observe, despite the decrease of S–S bond lengths in fully-charged phase, such S–S distances are far larger than the $(S-S)^{2-}$ bond length reported for TiS_3 (2.04 \AA) and FeS_2 (2.16 \AA), hence implying the onset of solely a partial S–S dimerization upon removal of Li from $Li_{1.13}Ti_{0.57}Fe_{0.3}S_2$. Although there is no doubt about the oxidation of S (which will be proved further via local-structure sensitive techniques in the later sections), it is evident that its extent is not enough to form S^- that would condense as $(S_2)^{2-}$. A simple charge balance (assuming one electron transfer in the $Fe^{2+/3+}$ process) suggests that the value of n in our compound is $\sim S^{1.65-}$, hence much smaller than S^- . This may explain that the oxidized sulfur in our Li-rich layered sulfide does not condense as in TiS_3 or pyrites FeS_2 . Another important distinction of these layered materials compared to pyrites is rooted in the nature of S–S bond, which are reported between two neighboring FeS_6 octahedra in FeS_2 .²⁸⁷ Similar S–S bonds or intra-octahedral S–S bond in $Li_{1.13}Ti_{0.57}Fe_{0.3}S_2$ would need significant rearrangement of the crystal structure of the compounds studied here. This is not observed experimentally as the layered structure persists.

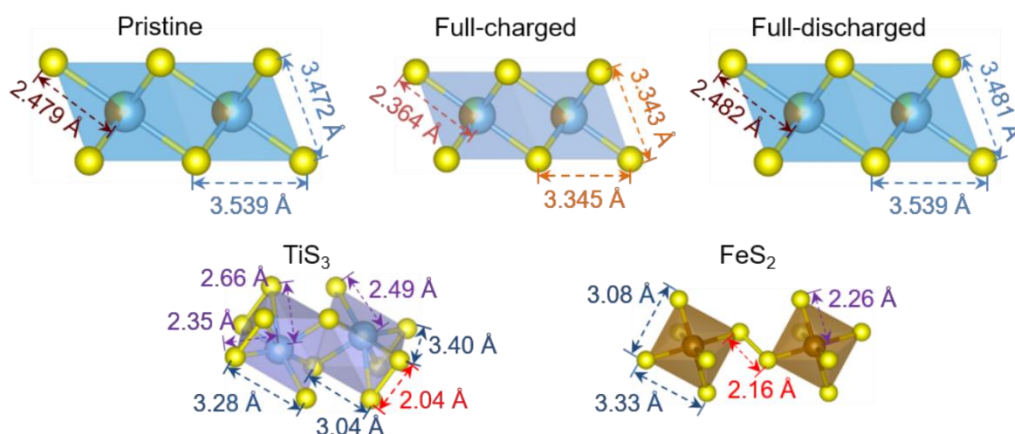


Figure III.33. The bond-lengths observed in the pristine, full-charged and full-discharged phase (as obtained from the Rietveld refinement of the corresponding SXRD patterns). Some typical bond-lengths in TiS_3 and FeS_2 are also given for comparison (adapted from Ref ²⁵⁷, and Ref ²⁸⁷).

III.3.2.6 Charge compensation mechanism

III.3.2.6.1 Cationic redox process

To identify the underlying redox mechanism which accounts for the high capacity obtained from the Li-rich sulfides, we performed *operando* Mössbauer spectroscopy^F using an in-house designed electrochemical cell²⁸⁸, to probe the cationic $\text{Fe}^{2+/3+}$ redox process. Spectra were collected while charging and discharging a $\text{Li}_{1.13}\text{Ti}_{0.57}\text{Fe}_{0.3}\text{S}_2/\text{Li}$ cell at a rate of C/70 (Figure III.34a). The Mössbauer spectra for pristine $\text{Li}_{1.13}\text{Ti}_{0.57}\text{Fe}_{0.3}\text{S}_2$, can neatly be fitted with four doublets (shown in the Appendix Table A2.6), and thus highlights the presence of a distribution of high-spin (HS) Fe^{2+} , as already encountered for FeS and various other Fe(II) -based sulfides.^{289,290} The necessity of four doublets is simply due to different local arrangements of disordered Ti/Li/Fe cations around a given Fe site (shown in Figure III.35).

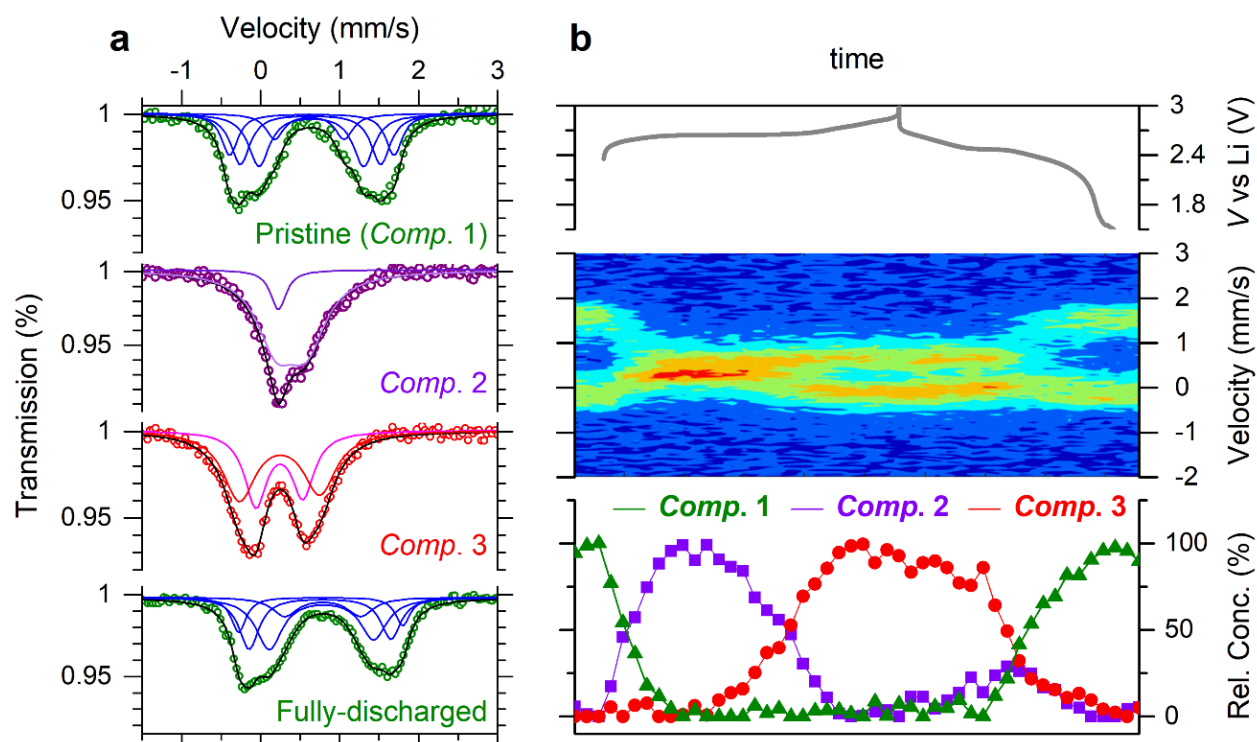


Figure III.34. *Operando* Mössbauer spectroscopy to identify the $\text{Fe}^{2+/3+}$ redox process in $\text{Li}_{1.13}\text{Ti}_{0.57}\text{Fe}_{0.3}\text{S}_2$. (a) Typical Mössbauer spectra and their deconvolution for the pristine (*comp. 1*), *comp. 2*, *comp. 3* (fully charged) and the fully-discharged product. (b) Contour plot of evolution of the Mössbauer spectra collected during *in situ* cycling of a $\text{Li}_{1.13}\text{Ti}_{0.57}\text{Fe}_{0.3}\text{S}_2/\text{Li}$ half-cell at a rate of C/70. For reference, the voltage profile is shown in the top panel. The lowest panel shows the evolution of the reconstructed components during the cycling.

^F Mössbauer studies were performed by Dr Moulay Tahar Sougrati, Institut Charles Gerhardt (Montpellier).

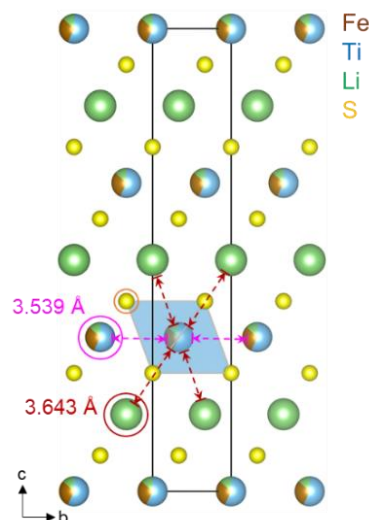


Figure III.35. Coordination of Fe atoms in $\text{Li}_{1.13}\text{Ti}_{0.57}\text{Fe}_{0.3}\text{S}_2$.

The evolution of the spectra obtained during in situ cycling is shown as a contour plot in Figure III.34b, with the spectra analyzed using principal component analysis (PCA), as described in Appendix Section A2.1 and the fitting parameters are summarized in Appendix Table A2.6. All measured spectra could be adequately fitted as linear combinations of three reconstructed spectral components. As expected, the first component (*Comp. 1*) is identical to the pristine material's spectrum. The *Comp. 2* can be fitted using at least two doublets (Figure III.34a). The major one (90%) has an isomer shift of 0.48 mm/s which stands between what is expected for HS Fe^{2+} and HS Fe^{3+} , alike what has been seen in Fe_3S_4 and FeV_2S_4 .²⁸⁹ The second doublet with a 10% contribution to the overall spectrum is indicative of the HS- Fe^{3+} signature, as seen in NaFeS_2 .²⁸⁹ Overall, the average oxidation state of *Comp. 2* is higher than Fe^{2+} but not fully reaching Fe^{3+} . Note that *Comp. 2* reaches its maximum around $x_{\text{Li}} = \sim 0.93$, just before the voltage plateau (P). This indicates an exchange of ~ 0.2 Li, that takes place in the sloppy profile (S), before the plateau and in agreement with the voltage window opening experiment (see the Appendix Figure A2.8). During the plateau, the *Comp. 2* converts progressively to the *Comp. 3* (fully-charged, 3 V), which can be fitted as low-spin Fe^{3+} state alike in the previous report²⁴⁶. On discharge, the evolution of the components is reversed, except for a much lower contribution from the *Comp. 2* (Figure III.34b). This is fully consistent with the path dependence observed above with XRD. Overall, these data indicate the progressive oxidation of Fe^{2+} to Fe^{3+} on charge and its full reduction back to Fe^{2+} on discharge.

Similarly, *operando* Mössbauer spectroscopy was performed for the $\text{LiTi}_{0.5}\text{Fe}_{0.5}\text{S}_2$ ($y = 0.5$) composition that contains more Fe, and the results are summarized in Figure III.36 with the fitting results in Appendix Table A2.7. The scenario is similar as before except the intermediate phase (*comp 2*, with mixed valence) that contains more HS- Fe^{2+} , since it is well fitted using 27% of HS- Fe^{2+} and 73% of $\text{Fe}^{2+}/\text{Fe}^{3+}$ environments and reaches its maximum around $x_{\text{Li}} = \sim 0.6$. Furthermore, the spectra were

collected over the 2nd cycle, which shows evolution of the spectra similar to the 1st cycle (shown in Appendix Figure A2.9), thus confirming the trend of the $\text{Fe}^{2+/3+}$ redox among the compositions.

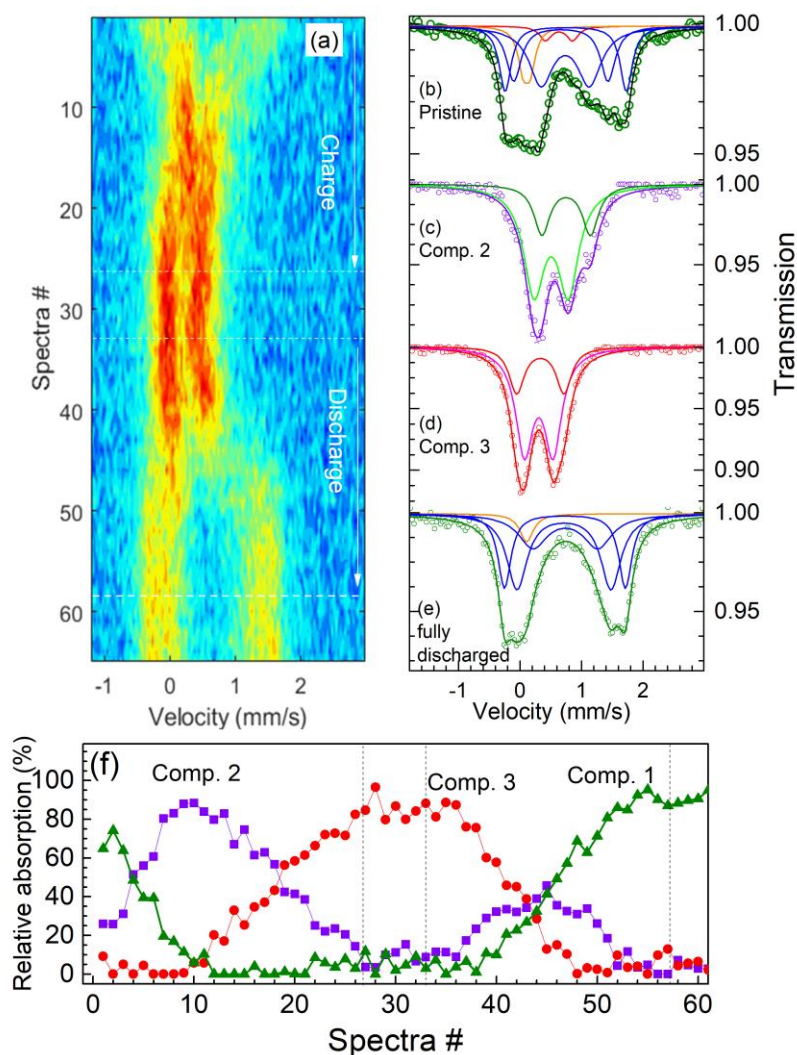


Figure III.36. Operando Mössbauer spectroscopy for the $\text{LiTi}_{0.5}\text{Fe}_{0.5}\text{S}_2$ ($y = 0.5$) sample. (a-e) Spectra map during the first cycle (a), typical fitted spectra for pristine (b), *comp 2* (c), *comp 3* (d), and fully discharged sample (e). (f) Evolution of the fitted components during the first cycle. The ranges delimited with dotted lines indicate a relaxation periods.

Furthermore, X-ray absorption near edge structure (XANES) spectroscopy was performed to confirm the above observation in $\text{Li}_{1.13}\text{Ti}_{0.57}\text{Fe}_{0.3}\text{S}_2$. See the Appendix Section A2.1 for details of the methods of XANES acquisition. The results of the Fe $L_{2,3}$ -edge TFY-XANES spectra are shown in Figure III.37b, with the spectra in TEY mode gathered in Appendix Figure A2.10. The spectra for the pristine material is similar to that of FeS confirming the presence of Fe^{2+} .^{291,292} It enlists two main peaks corresponding to $2p_{3/2} \rightarrow 3d$ (L_3) and $2p_{1/2} \rightarrow 3d$ (L_2) transitions. These peaks shift to higher energy upon charge indicating gradual conversion to Fe^{3+} . The position and shifts in energy observed in our Fe

$L_{2,3}$ -edge XAS data upon oxidation are consistent with previous literature of Fe^{2+} and Fe^{3+} sulfide species.²⁹³ After discharge, the Fe $L_{2,3}$ edge converts back to its initial phase.

Next we turn to the Ti atoms. To probe its redox, Ti $L_{2,3}$ -edge XANES spectra were also recorded for the aforementioned samples (Figure III.37c and Appendix Figure A2.12). The edge consists of four peaks attributed to the transitions $2p_{3/2} \rightarrow 3d(t_{2g})$, $2p_{3/2} \rightarrow 3d(e_g)$ (the L_3 edge) and $2p_{1/2} \rightarrow 3d(t_{2g})$, $2p_{1/2} \rightarrow 3d(e_g)$ (the L_2 edge). As expected, the spectrum for pristine $\text{Li}_{1.13}\text{Ti}_{0.57}\text{Fe}_{0.3}\text{S}_2$ is identical to that of Ti^{4+}S_2 (see Appendix Figure A2.12), confirming the formal oxidation state of Ti as $4+$.²⁴³ Moreover, no changes in the position of L_2 and L_3 peaks could be observed, irrespective of the sample state of charges (SoCs). Ti $L_{2,3}$ -edge electron energy loss spectroscopy (EELS) spectra were also recorded (shown in Appendix Figure A2.11) for the samples (further including a partially-charged sample) and they exhibit spectra similar to that of XANES. This indicates that the Ti^{4+} remains invariant throughout the charge/discharge cycle.

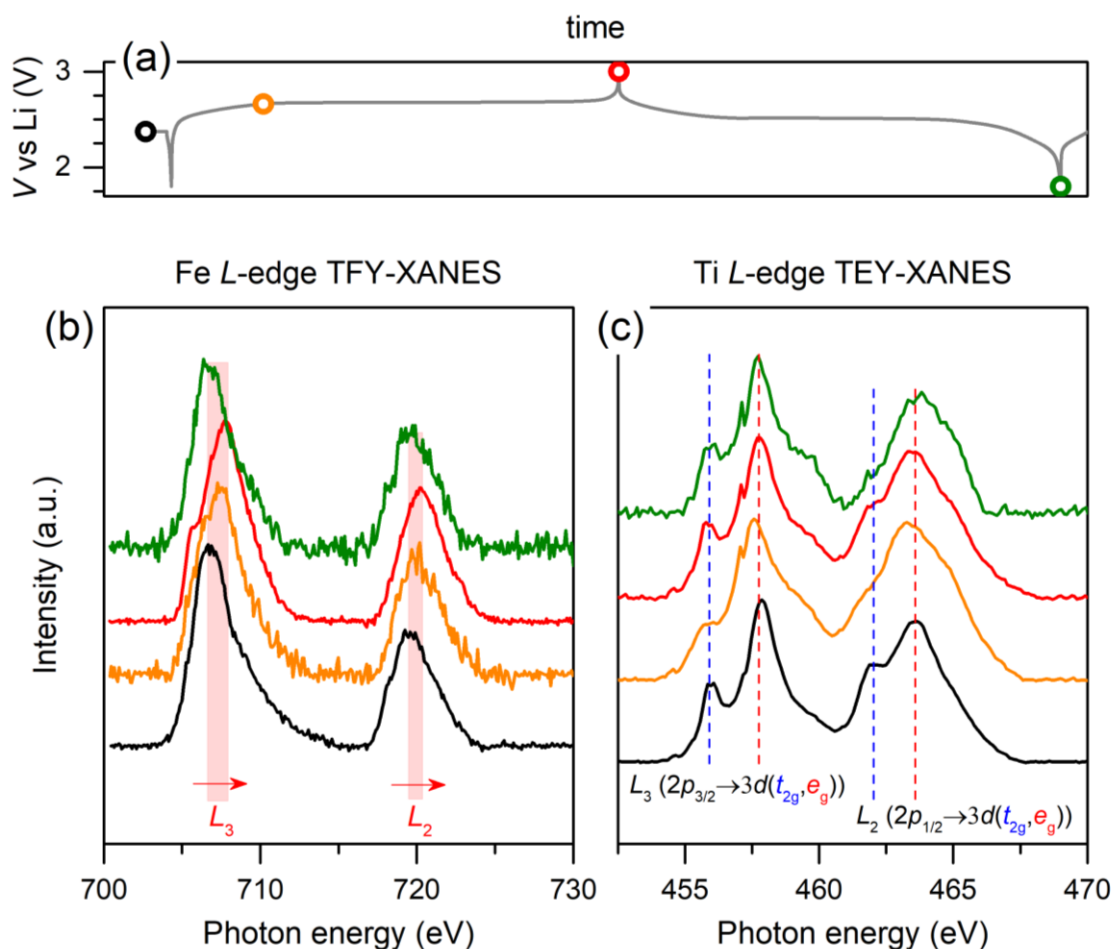


Figure III.37. Probing the cationic redox processes in $\text{Li}_{1.13}\text{Ti}_{0.57}\text{Fe}_{0.3}\text{S}_2$ by *ex situ* XAS. TFY-XANES spectra at the Fe $L_{2,3}$ -edge (b), and at the Ti $L_{2,3}$ -edge (c). A representative is shown in (a), to indicate the SoCs of the *ex situ* samples.

III.3.2.6.2 Anionic redox process

After probing the electrochemical participations of the cations, we move to assess the participations of the S ligand. For this, S *K*-edge TFY-XANES spectra were collected at various SoCs and they are reported in Figure III.37d. The XANES spectra collected in TEY mode are gathered in the Appendix, which are similar to the TFY spectra. The spectrum presents two main regions. The pre-edge feature, below 2471 eV, arises generally from unoccupied S *3p*/TM *3d* hybridized states. Their position and intensity depend on their occupancy, the relative contribution of S and TM, and their position with respect to the core level, thus being a general measure of covalence of the TM–S bond.²⁹⁴ Above this energy, the signals correspond to transitions to higher states, such as S *3p*/TM *4s*, *p* or those involving S *4p*, and the photoionization of S atoms, involving complete ejection of the core electron to the continuum. Therefore, the position of the absorption threshold is strongly dependent on the effective nuclear charge (Z_{eff}) on S,²⁹⁴ being a measure of redox transitions at the ligands. Note, the S *K*-edge XANES spectra of all as-synthesized samples of $\text{Li}_{1.33-2y/3}\text{Ti}_{0.67-y/3}\text{Fe}_y\text{S}_2$, $y = 0 - 0.5$, are similar, confirming identical S-states in all compositions, see Appendix Figure A2.13.

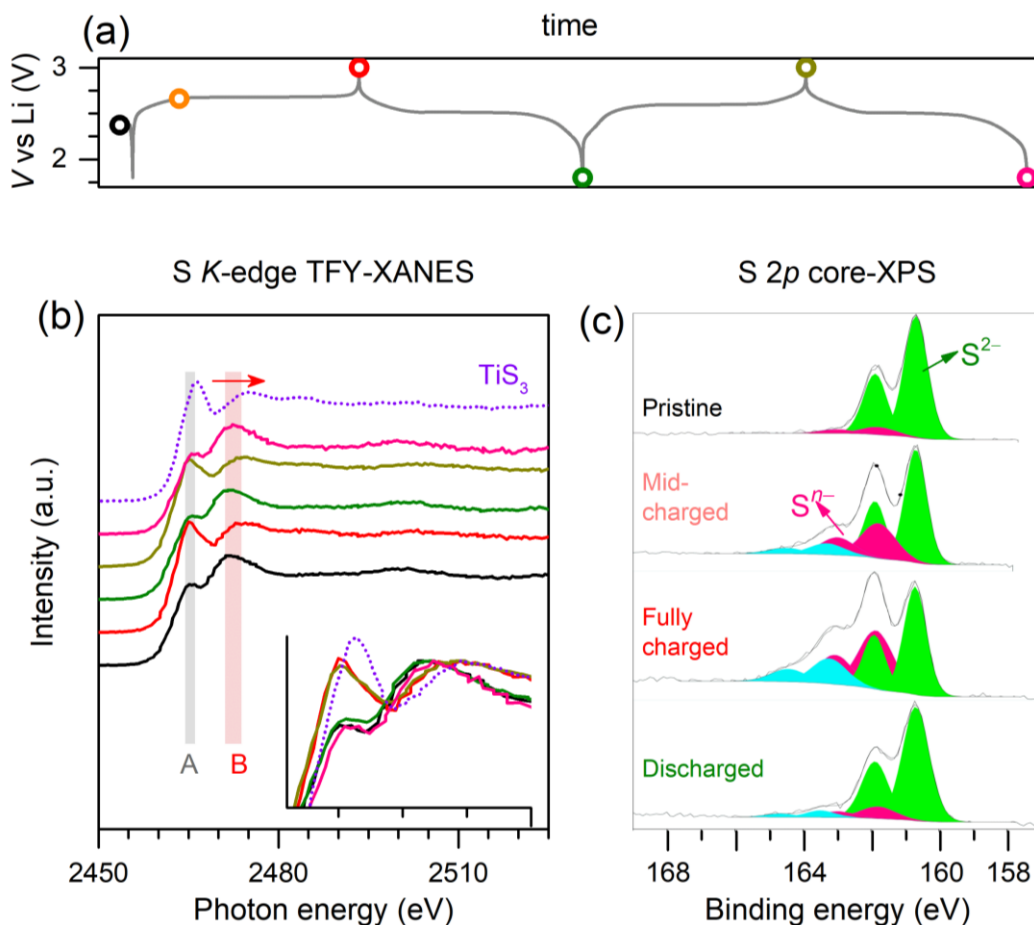


Figure III.38. Probing the anionic redox processes in $\text{Li}_{1.13}\text{Ti}_{0.57}\text{Fe}_{0.3}\text{S}_2$. S *K*-edge TFY-XANES spectra (b), and S *2p* core XPS spectra (c) of the *ex situ* samples. A representative is shown in (a), to indicate the SoCs of the *ex situ* samples. In (c), another extra doublet at a higher binding energy (163.3

- 164.5 eV, denoted as S^{m-}) was also observed, which probably originated from some surface deposited species.

Coming back to the $\text{Li}_{1.13}\text{Ti}_{0.57}\text{Fe}_{0.3}\text{S}_2$ phase, the TFY-XANES spectra at different state of charges (SoCs) are shown in Figure III.38 (with the TEY spectra in Appendix Figure A2.14). The spectra for pristine $\text{Li}_{1.13}\text{Ti}_{0.57}\text{Fe}_{0.3}\text{S}_2$ also consists in a weak pre-edge at ~ 2465 eV (denoted as **A**) and a broad edge (denoted as **B**) centered at ~ 2472 eV similar to what is observed in amorphous rocksalt Li_2TiS_3 and hence characteristic of S^{2-} .²⁸²

For the fully charged state ($\sim \text{Li}_{0.1}\text{Ti}_{0.57}\text{Fe}_{0.3}\text{S}_2$), the spectrum (red curve in Figure III.37d) undergoes remarkable changes with namely an increase in amplitude of the pre-edge **A** and a ~ 1.5 eV shift of the **B** edge towards higher energy, and bears resemblance to that of TiS_3 (dashed purple curve).²⁶⁸ Similarly, the opposite shift in the edge **B** is observed during re-lithiation, as was reported for TiS_3 , and VS_4 .^{250,256} The 1.2 eV shift in **B** is therefore a clear indication of the oxidation of S^{2-} into S^{n-} , $n < 2$. Similarly, the increase in intensity of pre-edge **A** is indicative of the increase in density of unoccupied states just above the Fermi level with an S character, in agreement with the expectation that the redox change is compensated by S $3p$ /Fe $3d$ electrons. The shift of the main absorption edge also suggests that this compensation, and the resulting states, have a significant S character. This unambiguously confirms the participation of S in the overall electrochemical activity of $\text{Li}_{1.13}\text{Ti}_{0.57}\text{Fe}_{0.3}\text{S}_2$ together with its reversibility since the S K -edge XANES spectra of the fully-discharged and pristine samples nearly superimpose (Figure III.37d).

To confirm the above observations S $2p$ core X-ray photoelectron spectroscopy (XPS) spectra were also taken and are shown in Figure III.37e. Clear variations of the spectra are observed upon charging-discharging the samples. The S $2p_{3/2-1/2}$ XPS core spectrum can be fitted with a single doublet (160.7 - 161.9 eV) attributable to S^{2-} for the pristine material, as in the TiS_2 reference.²⁹⁵ As the sample gets oxidized, the spectrum markedly changes, with namely the appearance of one extra doublet at higher binding energies (161.8 - 163.0 eV), which is indicative of the presence of oxidized S^{n-} ($n < 2$), in light of early previous studies on TiS_3 that is well-known to contain partially oxidized sulfur.^{255,295} On discharge, the XPS spectrum is almost restored to the pristine-like state, confirming the reversibility of the anionic redox process.

At this point, though the anionic participation is confirmed, question remains whether the S atoms fully dimerize upon oxidation. To check this point, *ex situ* electron energy loss spectroscopy (EELS) spectra at the S $L_{2,3}$ edge were collected and shown in Figure III.39. The spectra consist of a weak pre-edge and an intense broad edge feature that correspond to a series of transitions from the S $2p$ core levels to unoccupied states.²⁷⁷ The S $L_{2,3}$ edge for the pristine sample is similar to that of FeS indicating the predominance of S^{2-} state (Figure III.40).²⁷⁷ It remains nearly alike for the partially charged sample (at 2.66 V) with the exception of minor alterations that could be ascribed to a probable decrease of the Ti/Fe-S bond covalency. In contrast, for the fully-charged sample (at 3 V), the S $L_{2,3}$ rising-edge shifts by ~ 1.6 eV towards higher energies and this is indicative of a partial oxidation of S^{2-} .²⁹¹ However the S $L_{2,3}$ pre-edge does not show the typical peak splitting seen in pyrite- FeS_2 or elemental

S^0 (Figure S7b).²⁹² Lastly, it is worth mentioning that the initial shape as well as the energy of the rising-edge of the S - $L_{2,3}$ edge are fully recovered towards the end of the discharge, further indicative of the reversibility of the sulfur redox process.

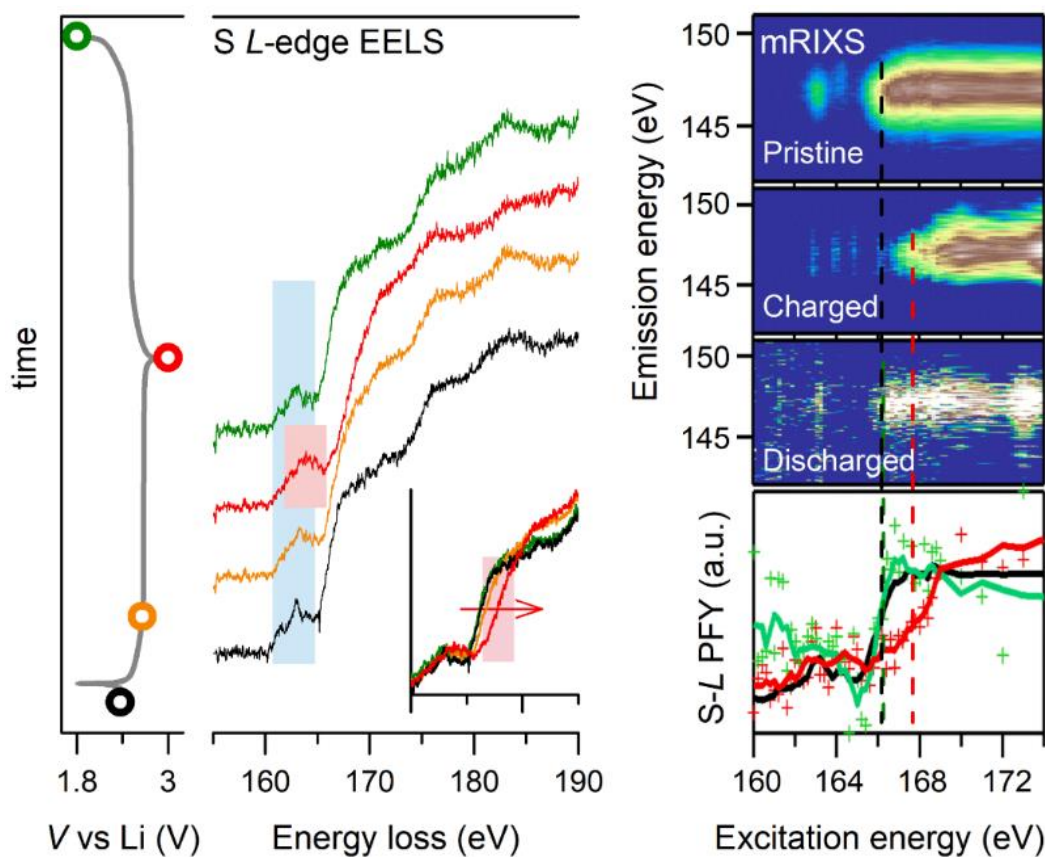


Figure III.39. Probing S L -edge to identify the S -redox processes. The EELS spectra of the S L -edge (middle panel), mRIXS of the S L -edge with integrated PFY spectra on the bottom (right panel). The voltage profile is shown in the left panel to indicate the *ex situ* samples.

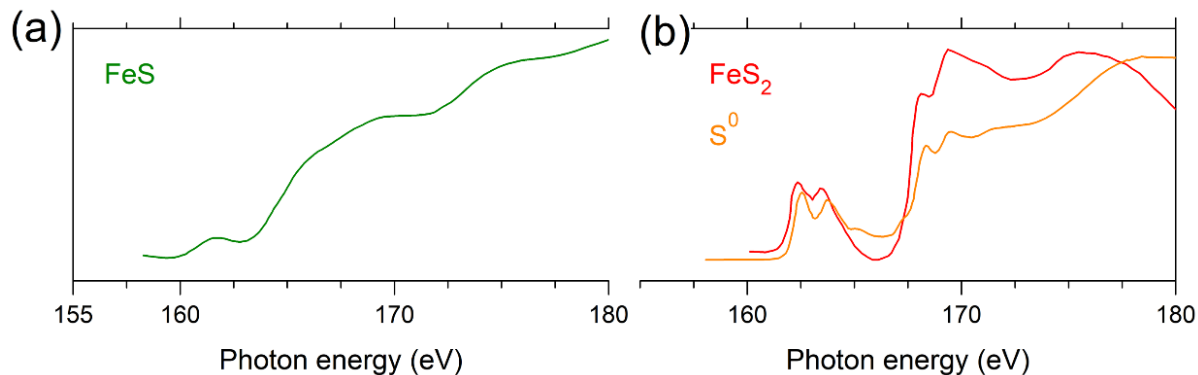


Figure III.40. S - $L_{2,3}$ edge EELS of FeS (a), and FeS_2 and elemental S (b). The data have been adopted from References^{277,292}.

To complement the EELS data that were collected locally on individual electrode particles, we further probed the S *L*-edge by soft X-ray absorption spectroscopy (sXAS) performed in fluorescence mode, which provides bulk-sensitive information about sulfur redox activity (see Appendix for details).^G Direct measurements of the electrodes on the S *L*-edge through conventional sXAS turned out to be challenging, because of interfering background signals from the carbon present in the electrodes which contributes an overwhelming background through 2nd order harmonic around 140 eV, right below the S-*L* signals around 160 eV (Appendix Figure A2.15a,b). We could successfully distinguish the S signals from the strong C background, by employing high-efficiency mapping of resonant inelastic X-ray scattering (mRIXS), see the Appendix Section A2.1 and Appendix Figure A2.15c for details. This advanced technique, which has emerged as a seminal technique for detecting oxygen redox,^{296–302} further resolves the emitted photon energy, called emission energy, after each sXAS excitation process.²⁹⁷ Figure III.39 displays these S-*L* mRIXS signals collected from the pristine, fully-charged, and fully-discharged electrodes. The integration of all the signals within the emission energy range (142 - 151 eV) provides the partial fluorescence yield (PFY) signals of the clean S-*L* sXAS, as summarized in the bottom panel. The pristine $\text{Li}_{1.13}\text{Ti}_{0.57}\text{Fe}_{0.3}\text{S}_2$ without carbon additive displays the strongest S-*L* features. The relatively sharp features in mRIXS at 163 and 164.1 eV excitation energies correspond well with the pre-edge peaks observed in EELS. The sharp features suggest these are dominated by the localized TM 3*d* character that is hybridized with S orbitals.²⁷⁷ At higher excitation energy, the continuous band-like feature corresponds to the intrinsic sulfur states hybridized with TM 4*s*/4*p* orbitals. It is clear that the leading edge of these sulfur band-like feature shifts towards high energy for over 1.2 eV in the full charged phase, in complete agreement with EELS and indicating the oxidation of sulfur states. Furthermore, the leading edge position completely recovers after discharge, suggesting a reversible redox reaction of the sulfur.

Overall, the characterizations at the S *L*-edge confirms the redox-participation of S ligands without fully dimerization of S atoms, in accordance with the crystal structure that was deduced for the fully-charged phase (Figure III.33).

III.3.3 Discussions

We have shown the feasibility of triggering electrochemical activity in Li_2TiS_3 (i.e., $\text{Li}_{1.33}\text{Ti}_{0.67}\text{S}_3$) by partially substituting Ti^{4+} belonging to the metal layer with suitable metal substituent TM. Alike the Li-rich layered oxides having *d*⁰ metals (Li_2TiO_3 , etc...), we showed the feasibility to trigger Li electrochemical activity in Li-rich layered sulfides having *d*⁰ metals by the injection of metal substituents. This does not come as a total surprise as such metal substitution modifies the *U* over Δ competition, so that it falls within the domain (lower Δ) to trigger reversible anionic redox activity as

^G sXAS and mRIXS were performed by Dr Wanli Yang and Dr Yang Ha (Lawrence Berkeley National Laboratory).

established from theoretical calculations (recall Section I.1.3).²⁷⁹ Nevertheless, the unsubstituted Li_2TiS_3 demands further scrutiny, as it possess sufficiently high conductivity and low optical bandgap (black in color), and furthermore due to the fact that its disordered rocksalt (space group $Fm\bar{3}m$) counterpart (i.e., Li_2TiS_3 prepared by ball-milling), is electrochemically active.^{282,283,303}

We studied in detail the effect of substitution of $\text{TM} = \text{Fe}^{2+}$, that can initiate the electrochemical activity in Li_2TiS_3 . The Fe^{2+} substituted phase, showing electrochemical activity due to cumulated cationic and anionic ($\text{S}^{2-}/\text{S}^{n-}$, $n < 2$) redox processes, were chosen to study as model materials for anionic redox. The anionic redox activity upon oxidation was spectroscopically confirmed in $\text{Li}_{1.13}\text{Ti}_{0.57}\text{Fe}_{0.3}\text{S}_2$ via clear energy shifts in the S $L_{2,3}$ -edge EELS and XANES spectra as well as the onset of a doublet signal in the S $2p_{3/2-1/2}$ XPS core spectra. Structure-wise on the other hand, our XRD and EELS evidence did not suggest the local formation of very short S–S dimers (like in pyrites). For comparing with oxides, let's recall that the XPS fingerprint of anionic redox activity in oxides was also the appearance of a new component at slightly higher binding energy (531.5 eV) in the O $1s$ XPS core spectra that we assigned to O^{n-} ($n < 2$).^{48,50,52} Interestingly, the binding energy of this component was independent of the structure and composition as seen in various Li-rich oxides that show anionic redox activity, with or without evidences of O–O shortening. This observation indicates that although XPS features have been widely used as the spectroscopic signature of the anionic redox activity in various materials, caution has to be exercised when interpreting XPS spectra.

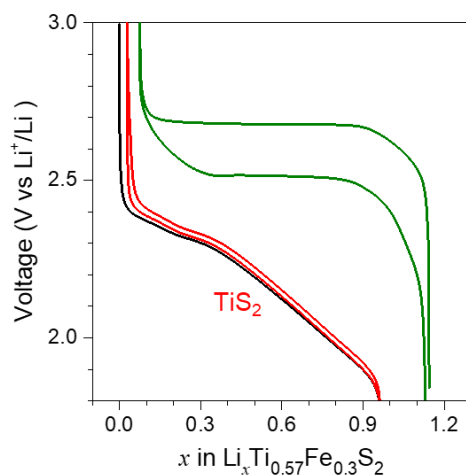


Figure III.41. Comparison of the voltage profiles of TiS_2 and $\text{Li}_{1.13}\text{Ti}_{0.57}\text{Fe}_{0.3}\text{S}_2$ (green curve).

Compared to Li-stoichiometric TiS_2 , the Li-rich sulfide phases offer higher voltage with availability of extracting more Li, as shown here for the $\text{Li}_{1.13}\text{Ti}_{0.57}\text{Fe}_{0.3}\text{S}_2$ (Figure III.41). Besides, we found that $\text{Li}_{1.13}\text{Ti}_{0.57}\text{Fe}_{0.3}\text{S}_2$ can deliver capacities as high as $245 \text{ mAh}\cdot\text{g}^{-1}$ with a near-zero irreversible capacity during the first cycle as compared to ~ 0.2 Li for Li-rich $3d$ metal-based oxides. This is consistent not only with the absence of cationic migration in the Li-rich sulfides, but also with less severe changes observed between the first charge and discharge profiles in $\text{Li}_{1.13}\text{Ti}_{0.57}\text{Fe}_{0.3}\text{S}_2$, as opposed to Li-rich NMCs that show a staircase charge curve drastically changing to a S-shaped discharge curve. Lastly, part of the initial irreversibility in oxides is associated to a small amount of oxygen release from

the surface, either directly as O₂ gas or indirectly by reacting with the electrolyte.^{23,304} This is quite unlikely to occur with S, which is a softer element as compared to O, therefore showing less reactivity and greater stability for the same degree of electrochemical oxidation.

III.4 Expanding the S-redox chemistry

So far we have shown the reversible electrochemical activity in Li-rich layered Li₂TiS₃ by partially substituting Ti⁴⁺ with suitable metal substituent TM = Fe²⁺. Its favourable electrochemical properties that positively contrasts with Li-rich oxides, raises the question about the electrochemical benefits in other Li/Na-rich sulfides, under similar testing protocol. To assess this point, we have extended our study to Li₂TiS₃ substituted by TM = Ti³⁺, Co²⁺, and also to Na₂TiS₃, that were reported elsewhere^{79,272,281} and briefly discussed below.

III.4.1 Ti³⁺-substituted Li₂TiS₃

Ti³⁺-substitution as a mean to electrochemically activate Li₂TiS₃, was explored by Flamarly-Mespoulie *et al* (Thesis, 2018).²⁷². They prepared nominal compositions of Li_{1.33-*y*/3}Ti⁴⁺_{0.67-2*y*/3}Ti³⁺_{*y*}S₂ (or can be regarded as the solid solution of Li₂Ti⁴⁺S₃ and LiTi³⁺S₂) and described its crystal structure and electrochemical properties in detail.

Hence, to study the practicability of anionic redox upon Ti³⁺-substitution, we have prepared the composition Li_{1.2}Ti_{0.8}S₂ (i.e., Li_{1.2}Ti⁴⁺_{0.4}Ti³⁺_{0.4}S₂, with *y* = 0.4). Details of the synthesis and characterization can be found in the Appendix Section A2.1 and Appendix Figure A2.16.

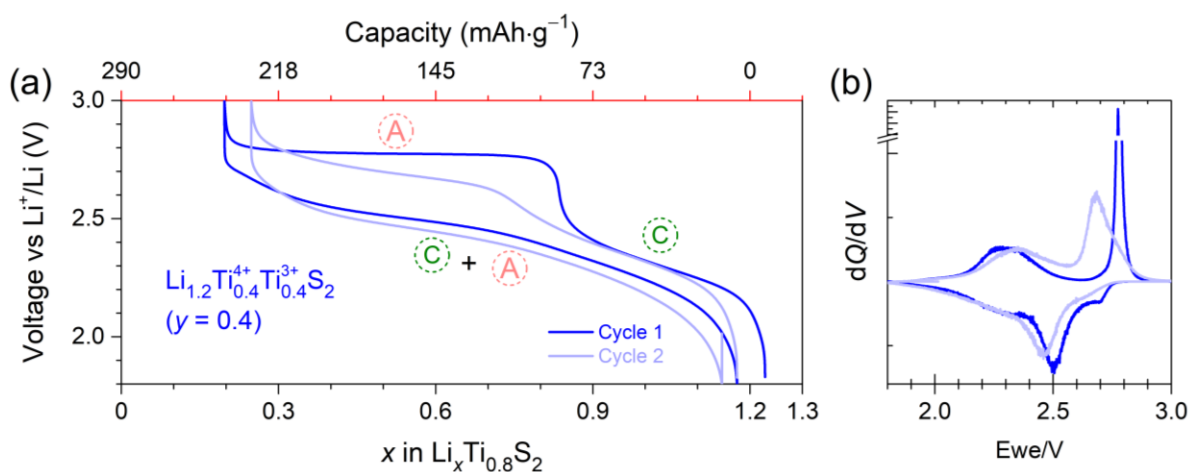


Figure III.42. Electrochemical behaviour of the Li_{1.2}Ti_{0.8}S₂ sample. (a) The voltage profile, and (b) the corresponding dQ/dV curves, of the composition. Cationic and anionic plateaus are indicated by C and A, on the figure.

The electrochemical performance, the composition is shown in Figure III.42, that shows a capacity of $\sim 235 \text{ mAh}\cdot\text{g}^{-1}$, leading to a specific energy of $\sim 560 \text{ Wh}\cdot\text{kg}^{-1}$. A staircase like charging profile was observed, which becomes S-shaped in discharge, alike the Li-rich NMC. The broad peak at

~ 2.3 V in the dQ/dV is from the $Ti^{3+/4+}$ cationic redox, whereas, the peak at higher voltage corresponds to the $S^{2-}/(S_2)^{n-}$ anionic redox. During discharge, the voltage profile changes its shape and an S-shaped curve is obtained comprising both cationic and anionic redox, which corresponds to the broad peak at 2.5 V in the dQ/dV curve.

III.4.2 Co^{2+} -substituted Li_2TiS_3

The electrochemical property of the $Li_{1.2}Ti_{0.6}Co_{0.2}S_2$ composition was reported by Li *et al* (2018).²⁸¹ We prepared the compositions of $Li_{1.33-2y/3}Ti_{0.67-y/3}Co^{2+}_yS_2$, with $y = 0.2$, and 0.3 for our studies. Detailed structural characterizations can be found in the Appendix Figure A2.17.

The electrochemical behaviour for both compositions are shown in Figure III.43. Note that, much lesser capacity (up to $190 \text{ mAh}\cdot\text{g}^{-1}$, with specific energy of $\sim 420 \text{ Wh}\cdot\text{kg}^{-1}$, for $y = 0.2$) could be obtained than the Fe-substituted samples. Furthermore, irrespective of Co-content, ~ 0.4 Li always remains inaccessible in the fully-oxidized samples. Interestingly, the voltage of dQ/dV peaks remains invariant amongst Co-substituted samples, in contrast to the Fe-substitution.

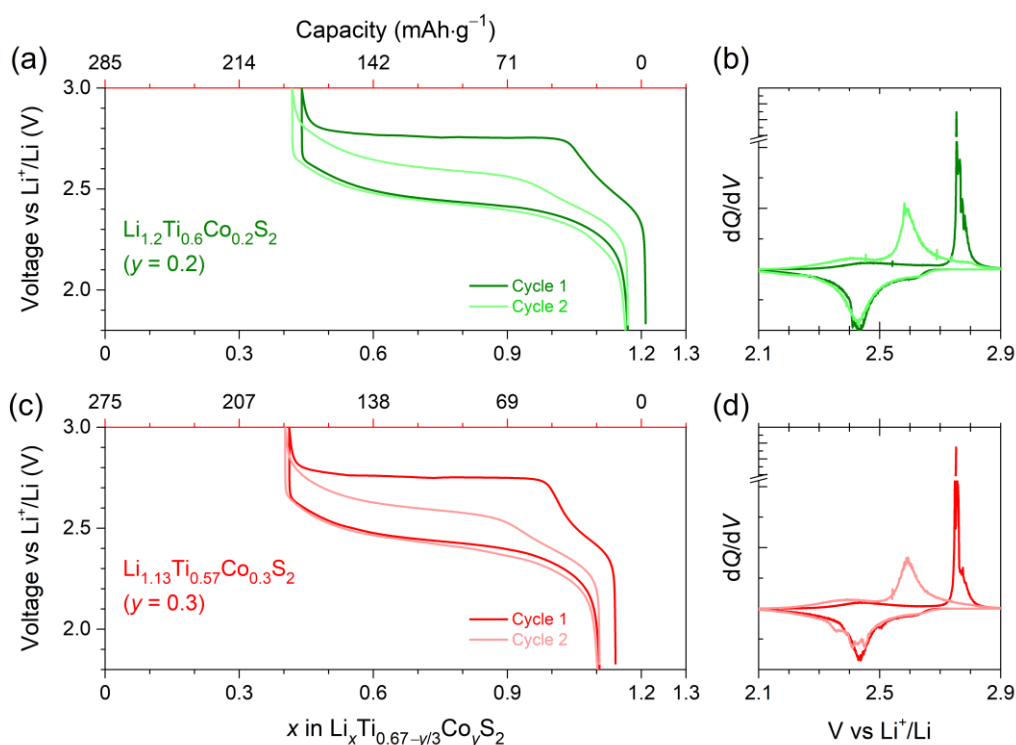


Figure III.43. Electrochemical activity of the $Li_{1.33-2y/3}Ti_{0.67-y/3}Co_yS_2$ samples. (a,c) Voltage profiles of the compositions obtained over cycling vs Li at C/20 for the first two cycles. The curves in lighter colors denote the second cycles. (b,d) the corresponding dQ/dV curves. Note that the y-axis break was provided to enlarge the peaks at 2nd cycle.

In short, electrochemical activity in Li_2TiS_3 can be activated via both Co^{2+} , and Ti^{3+} substitution, alike the Fe^{2+} substitution. Therefore, these phases are also chosen for our study relate to the practicability of S-redox.

III.4.3 Na_2TiS_3

In contrary to the Li_2TiS_3 , its Na-counterpart is shown to be redox-active, without any substitution.^{78,79} The Na_2TiS_3 (also written as $\text{Na}_{1.33}\text{Ti}_{0.67}\text{S}_2$) has a low temperature O3-polymorph and high temperature P2-polymorph.^{78,79} Amongst the two phases, only the voltage profile for O3- Na_2TiS_3 was reported, by Pele *et al.*, 2016 (in Na-half cell)⁷⁸, and by Nasu *et al.*, 2019 (in ASSB)⁷⁹. Thus, to grasp further into the anionic redox in sulfides, we decided to extend our studies to Na_2TiS_3 .

The O3 and P2 phases were synthesized slow-cooling and quenching, respectively (see methods in Appendix Section A2.1). Their structural characterizations can be found in Appendix Figure A2.19, Appendix Figure A2.20 and Appendix Figure A2.21. Their electrochemical performances were tested in Na-half cell, using 1 M NaPF_6 in PC as electrolyte. For the O3 phase, ~ 1.16 Na could be deintercalated in 1st charge, and there remains an irreversibility only ~ 0.1 Na in the 1st discharge and stable cycling occurs afterwards with a polarization of ~ 300 mV (Figure III.44a,b). Note that we obtained much higher capacity ($\sim 225 \text{ mAh}\cdot\text{g}^{-1}$) than the reported ($\sim 100 \text{ mAh}\cdot\text{g}^{-1}$)⁷⁸, which is most likely due to the electrolyte used (1 M NaPF_6 in TEGDME), see the Appendix Figure A2.22 for details.

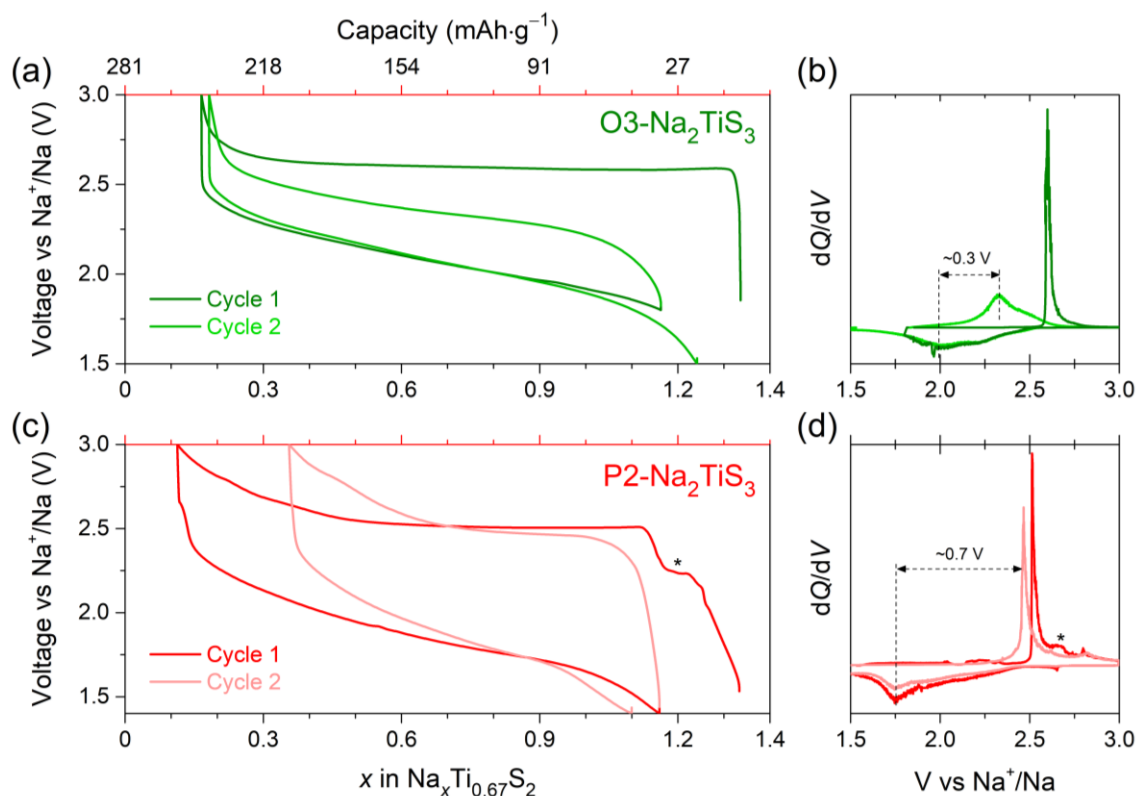


Figure III.44. Electrochemical behaviour of the O3- and P2- Na_2TiS_3 . (a) Voltage profile, and (b) corresponding dQ/dV curves of the O3- Na_2TiS_3 . (c) Voltage profile, and (b) corresponding dQ/dV curves of the P2- Na_2TiS_3 . The lines in lighter colors denote the 2nd cycle. For P2 phase, the plateau or dQ/dV peaks marked by *, are possibly from the impurity phase(s) as was detected in the XRD also.

For the P2 phase, the Na-(de)intercalation occurs at a lower voltage than the O3 phase (Figure III.44c,d). Up to ~ 1.2 Na could be extracted in the 1st cycle of the P2 phase, but in discharge it shows a

large irreversibility >0.2 Na, and also a larger polarization (~ 700 mV) than the O3 phase. For both O3- and P2- Na_2TiS_3 , only one dQ/dV peak is observed during charge-discharge, indicating a single redox process, which can be assigned to the $\text{S}^{2-}/\text{S}_2^{n-}$ ($n < 2$) anionic redox, as Ti^{4+} (d^0) is supposed to be redox-inactive.

To summarize this section, the Na_2TiS_3 also presents an interesting case of anionic redox in sulfides, which we will use next for our comparative studies.

III.5 Chapter Conclusions

Aiming to re-examine sulfide based cathode materials, we have studied various Li-stoichiometric and Li(Na)-rich sulfides. Li-stoichiometric TiS_2 possess lower energy density (~ 450 $\text{mAh}\cdot\text{g}^{-1}$), however with excellent reversibility and rate capability, while relying solely on usual cationic redox of the transition metal. To push the energy density higher, we scrutinized the practicability of anionic $\text{S}^{2-}/\text{S}^{n-}$ ($n < 2$) redox, encouraged by the recent paradigm of anionic $\text{O}^{2-}/(\text{O}_2)^{n-}$ redox in Li-rich oxides. The $\text{S}^{2-}/\text{S}^{n-}$ redox, based on intercalation chemistry was known either in ‘pseudo-layered’ TiS_3 , or in layered Li_2TiS_3 . In fact, the S-redox in $\text{LiTi}_{0.5}\text{Fe}_{0.5}\text{S}_2$ was predicted by Tarascon *et al* in 1983.²⁴⁶ We have revisited TiS_3 , to understand the structural and electrochemical implications of the anionic redox. However in TiS_3 , the structural irreversibility and sluggish kinetics of the $\text{S}^{2-}/\text{S}_2^{2-}$ redox leads to rapid capacity fading and high voltage hysteresis. On the other hand, Li_2TiS_3 is nearly electrochemically inactive, probably because of unfavourable band positioning (recall Figure III.22). Therefore we designed a new class of Li-rich layered sulfides, namely Fe^{2+} -substituted Li_2TiS_3 , and studied for their electrochemical behaviour as cathode materials. Within this series, the phase $\text{Li}_{1.13}\text{Ti}_{0.57}\text{Fe}_{0.3}\text{S}_2$ offers the largest reversible capacity (245 $\text{mAh}\cdot\text{g}^{-1}$) and we have shown that this capacity mainly originates from anionic $\text{S}^{2-}/\text{S}^{n-}$ ($n < 2$) redox, besides the cationic $\text{Fe}^{2+/3+}$ redox. Energy-wise, these Li-rich layered sulfide positive electrodes display a specific energy of ~ 600 $\text{Wh}\cdot\text{kg}^{-1}$ at the material-level while being composed of earth-abundant elements ($3d$ metals only). Furthermore, we extended our studies to Ti^{3+} , and Co^{2+} substituted Li_2TiS_3 , and Na_2TiS_3 , which are capable of undergoing reversible anionic redox.

The Li/Na-rich sulfide phases can serve as excellent ‘model’ electrodes to study the general properties of anionic redox chemistry, this is exactly what will be discussed in the next chapter, where we benchmark their performances against Li/Na-rich oxides.

Chapter IV

Practicability of Anionic redox in Li-rich sulfides[#]

[#]This chapter includes the following publication: Saha *et al.*, *Nature Energy* 2019.

IV.1 Chapter Introduction

In the previous chapter, we showed that redox activity in Li-rich layered sulfides can be triggered by suitable TM-substituents. More specifically, the $\text{Li}_{1.33-2y/3}\text{Ti}^{4+}_{0.67-y/3}\text{Fe}^{2+y}\text{S}_2$ family (with $\text{TM} = \text{Fe}^{2+}$) displays excellent reversibility of Li-(de)intercalation while involving anionic S-redox. Furthermore, we spotted that $\text{TM} = \text{Ti}^{3+}$, Co^{2+} substitution can equally trigger reversible redox activity in Li_2TiS_3 , whereas the Na_2TiS_3 is active without any substitution. At this stage, having evidenced the strong participation of anionic redox in the charge compensation mechanism in these Li-rich layered sulfides, the next legitimate question remains about the practicability of anionic redox in sulfides. Despite the promise of large capacity in Li-rich NMC oxide, certain practical issues, such as voltage fade, sluggish kinetics, large voltage hysteresis, and irreversible oxygen loss, have delayed the commercialization of Li-rich NMCs. Although the crucial role of oxygen redox towards these issues was clearly highlighted by detailed investigations on ‘practical’ Li-rich NMC and also for ‘model’ $\text{Li}_{1.33}\text{Ru}_{0.5}\text{Sn}_{0.17}\text{O}_2$ electrode, much remains to be understood prior to provide implementable solutions.^{37,49,278} Using these Li-rich sulfides as model compounds, we investigated whether these practical issues, still persist when oxygen is replaced by sulfur. Therefore in this chapter we will systematically assess the practical figures of merit in Li-rich sulfides starting with the voltage hysteresis issue.

IV.1.1 Voltage hysteresis

Let’s recall first that the Li-rich $\text{Li}_{1.13}\text{Ti}_{0.57}\text{Fe}_{0.3}\text{S}_2$ sulfide shows an overpotential of only ~100 mV during cycling at $C/5$ rate (with current density of $46 \text{ mA} \cdot \text{g}^{-1}$). To get further insight into the voltage hysteresis, we performed a galvanostatic intermittent titration technique (GITT) experiment (See Appendix for the method). For this, a rest of 30 mins was applied after each 30 mins of charge/discharge of the Li-half cell and the voltage was recorded. The GITT voltage profile of $\text{Li}_{1.13}\text{Ti}_{0.57}\text{Fe}_{0.3}\text{S}_2$ is shown in Figure IV.1a and it indicates that the voltage hysteresis almost disappears throughout the cycle (only ~30 mV gap remains after just 30 mins of relaxation), see Figure IV.1a. Furthermore a typical voltage profile during the relaxation is also shown (inset, Figure IV.1a), which shows that the voltage profile is almost stabilized within the small rest period of 30 min.

When compared with Li-rich oxides, this is a significantly better scenario than in Li-rich NMC ($\text{Li}_{1.2}\text{Ni}_{0.13}\text{Mn}_{0.54}\text{Co}_{0.13}\text{O}_2$), where a severe OCV hysteresis up to 270 mV has been reported and further shown to be associated with oxygen redox (Figure IV.1b).⁵⁰ It was shown before that by moving to $\text{Li}_2\text{Ru}_{0.75}\text{Sn}_{0.25}\text{O}_3$ ($4d$ metal-based), the voltage hysteresis was considerably mitigated but it could not be fully eliminated (Figure IV.2).⁴⁹ The performance of $\text{Li}_{1.13}\text{Ti}_{0.57}\text{Fe}_{0.3}\text{S}_2$ is also better than the ~100 mV OCV hysteresis in $\text{Li}_2\text{Ru}_{0.75}\text{Sn}_{0.25}\text{O}_3$ and approaches the favorable hysteresis-free situation observed for $5d$ metal-based $\beta\text{-Li}_2\text{IrO}_3$.^{49,52}

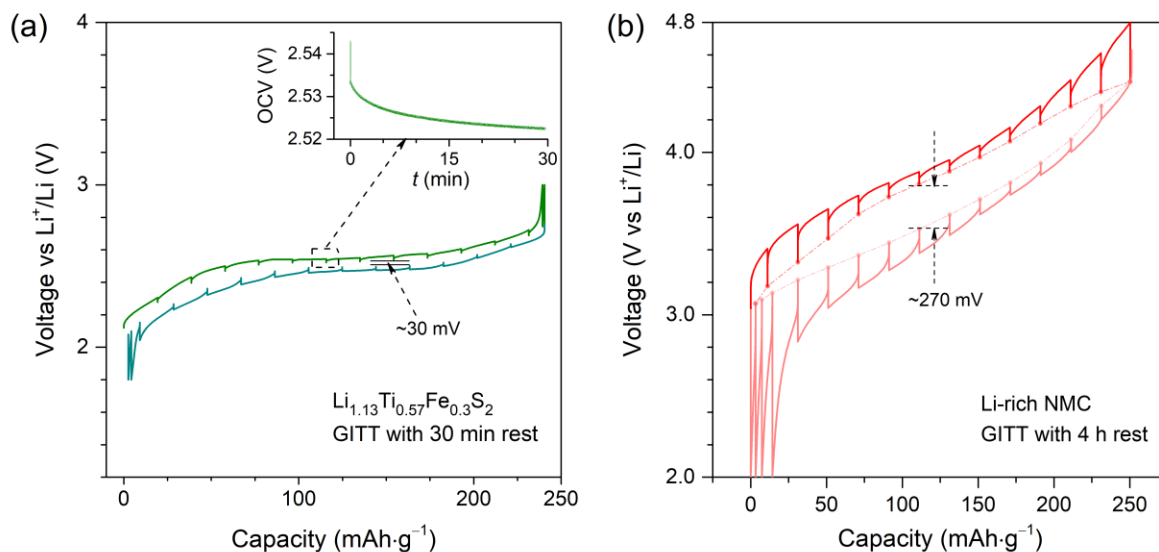


Figure IV.1. GITT Voltage profile of $\text{Li}_{1.13}\text{Ti}_{0.57}\text{Fe}_{0.3}\text{S}_2$ and Li-rich NMC in a three-electrode cell. (a) The voltage profile was recorded in the 8th cycle (once the voltage profile stabilizes after 7 cycles), at $C/5$ rate (i.e., current density of $46 \text{ mA}\cdot\text{g}^{-1}$) with 30 min rests for equilibration. Inset shows the OCV profile during the relaxation period after the indicated step. Sample was used as a self-standing electrode in three-electrode Swagelok type cell. (b) GITT Voltage profile of Li-rich NMC recorded in three-electrode Swagelok cell (in 4th cycle, with $40 \text{ mA}\cdot\text{g}^{-1}$ pulses and 4 h rests for equilibration).

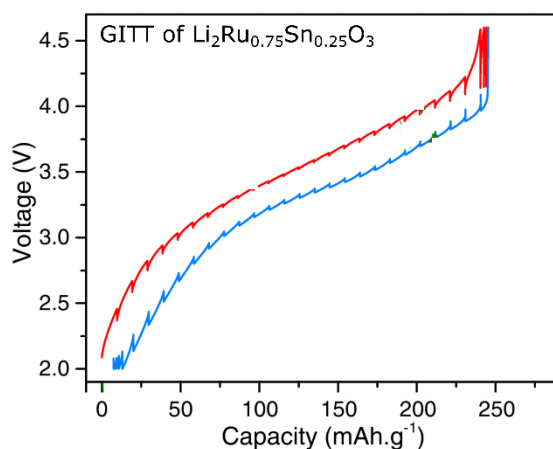


Figure IV.2. GITT Voltage profile of $\text{Li}_2\text{Ru}_{0.75}\text{Sn}_{0.25}\text{O}_3$ (LRSO). GITT was recorded with a $C/25$ pulse for 90 min, and 10 h rest (in the 2nd cycle). Note that even after 10 h rest, ~ 100 mV hysteresis still remains. Figure adapted from reference⁴⁹.

To further assess the hysteresis within the series, we performed GITT experiment on the $\text{LiTi}_{0.5}\text{Fe}_{0.5}\text{S}_2$ ($y = 0.5$) composition. The GITT was performed in a two-electrode Swagelok cell with the sample employed as powder and the voltage profile is gathered in Figure IV.3. To recall, the $\text{LiTi}_{0.5}\text{Fe}_{0.5}\text{S}_2$ composition has lesser amount of anionic $\text{S}^{2-}/(\text{S}_2)^{n-}$ redox, since it contains higher amount of Fe than in the $\text{Li}_{1.13}\text{Ti}_{0.57}\text{Fe}_{0.3}\text{S}_2$. For $\text{LiTi}_{0.5}\text{Fe}_{0.5}\text{S}_2$, only a small thermodynamic hysteresis of ~ 25 mV remains, with the voltage profile almost stabilized after 30 mins of relaxation.

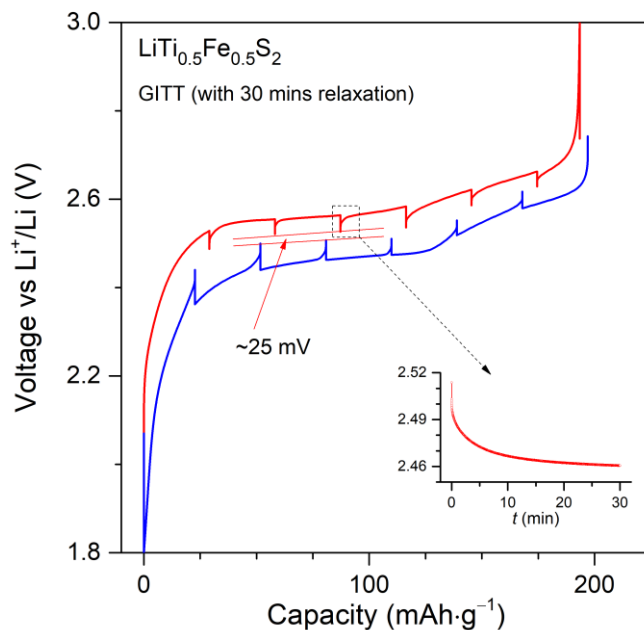


Figure IV.3. GITT Voltage profile of $\text{LiTi}_{0.5}\text{Fe}_{0.5}\text{S}_2$ ($y = 0.5$) in a two-electrode cell. The voltage profile was recorded once the voltage profile stabilizes after 7 cycles, at $C/5$ rate with 30 min rests for equilibration. Sample was used as powder in two-electrode Swagelok type cell.

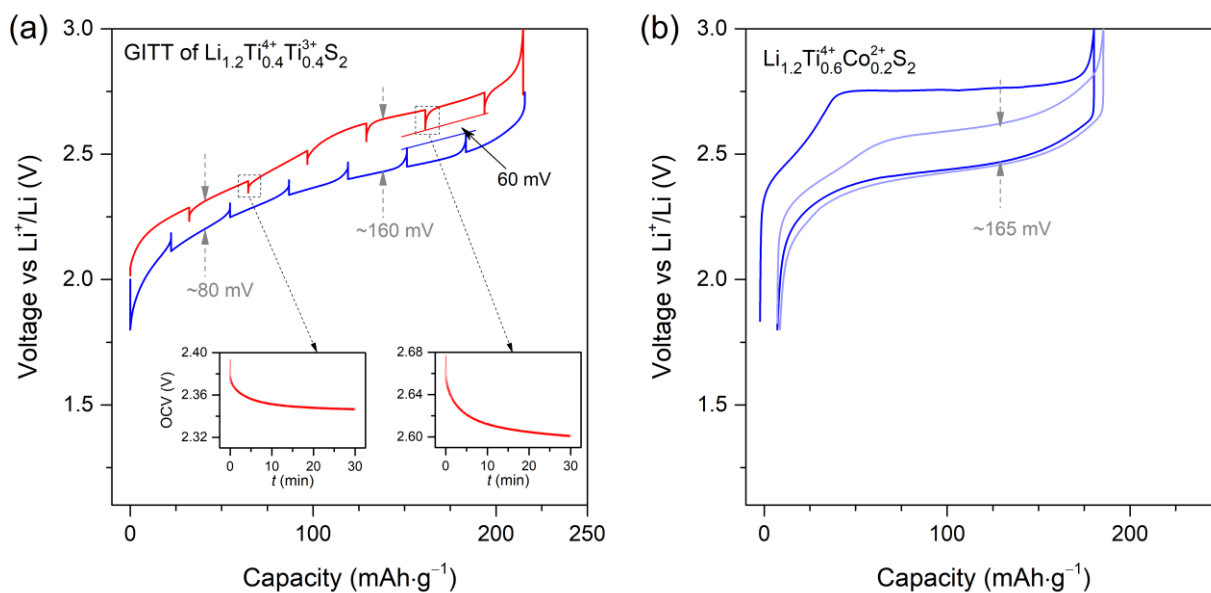


Figure IV.4. Voltage hysteresis in Ti^{3+} and Co^{2+} substituted Li_2TiS_3 . (a) Voltage profile of $\text{Li}_{1.2}\text{Ti}^{4+}_{0.4}\text{Ti}^{3+}_{0.4}\text{S}_2$ recorded with a GITT protocol. Experiment was performed with the sample as powder in a two-electrode Swagelok type cell in the 8th cycle, at $C/5$ rate with 30 min rests for equilibration. Inset shows the OCVs during the relaxations. (b) Voltage profile of $\text{Li}_{1.2}\text{Ti}^{4+}_{0.6}\text{Co}^{2+}_{0.2}\text{S}_2$ cycled at a rate of $C/20$.

To verify whether the low hysteresis is true for other Li-rich sulfides, we have studied the $\text{Li}_{1.2}\text{Ti}_{0.8}\text{S}_2$ phase (i.e., $\text{Li}_{1.2}\text{Ti}^{4+}_{0.4}\text{Ti}^{3+}_{0.4}\text{S}_2$) also. In $\text{Li}_{1.2}\text{Ti}_{0.8}\text{S}_2$, under normal cycling at C/5 rate, there remains voltage gaps of ~ 80 mV in the sloppy voltage region and ~ 160 mV in the high-voltage plateau region (Figure IV.4a). The GITT of the $\text{Li}_{1.2}\text{Ti}_{0.8}\text{S}_2$ is shown in Figure IV.4a. During the sloppy voltage region no hysteresis is observed after the relaxation (30 mins), whereas there remains a small thermodynamic hysteresis of ~ 60 mV in the high-voltage plateau region. Furthermore, the OCV stabilizes within few mins in the sloppy voltage region, but longer relaxation is needed for the 2nd plateau. This indicates that the small voltage hysteresis is due to the anionic $\text{S}^{2-}/\text{S}^{n-}$ ($n < 2$) redox. In short, small hysteresis is observed here, but much smaller compared to Li-rich oxides.^{49,50} Lastly, we turn to the $\text{Li}_{1.2}\text{Ti}_{0.6}\text{Co}_{0.2}\text{S}_2$ composition. GITT was not performed in this case, but we again observed a small overpotential of ~ 165 mV during cycling under normal condition (Figure IV.4b).

Overall, this observation clearly highlights that voltage hysteresis can be effectively mitigated by tuning the ligand, and not just by choosing appropriate transition metals (i.e., $4d / 5d$ based).

Next we asked the question whether the anionic redox has a path dependence, as in Li-rich oxides, for which the hysteresis was shown to be associated with the path difference during charge and discharge^{49,50,278}. This aspect was further studied by progressive opening of voltage-windows during charge in subsequent cycles and the voltage profiles are summarized in Figure IV.5. First, the charging voltage window is opened gradually in subsequent cycles (Figure IV.5a), however no increase in the hysteresis was noticed. Thus irrespective of the charge window, the discharge voltage is never lowered noticeably. This is reflected in the dQ/dV curves (Figure IV.5b), as all the oxidative capacity from charging even in the high voltage (denoted by red arrows), could be recovered by ~ 2.48 V peak upon reduction (see the blue arrow). Next, the voltage window was opened gradually during discharge from 100% SoC (3 V) and the results are summarized in Figure IV.5c. It is clear that the charging voltage is always maintained irrespective of the discharge window. The corresponding dQ/dV curves (Figure IV.5d) also reveal that all the capacity obtained from discharge (blue arrows) are recovered by the 2.55 V peak during charge (red arrow) without creating any new peaks.

This is drastically different from Li-rich NMC, where charging beyond 4.1 V leads to a noticeable hysteresis that lowers the discharge potential around mid-SoCs (Figure IV.6a). The corresponding dQ/dV curves show that the oxidative capacity above 4.1V is only fully recovered on reduction up to significantly low potential (below 3.6 V), see Figure IV.6b.⁵⁰ Similar scenario was observed in $4d$ metal-based $\text{Li}_2\text{Ru}_{0.75}\text{Sn}_{0.25}\text{O}_3$ (LRSO).⁴⁹ Thus, in $\text{Li}_{1.2}\text{Ti}_{0.8}\text{S}_2$ no hysteresis loop is observed, letting us to conclude that anionic redox in $\text{Li}_{1.2}\text{Ti}_{0.8}\text{S}_2$ is not path dependent.

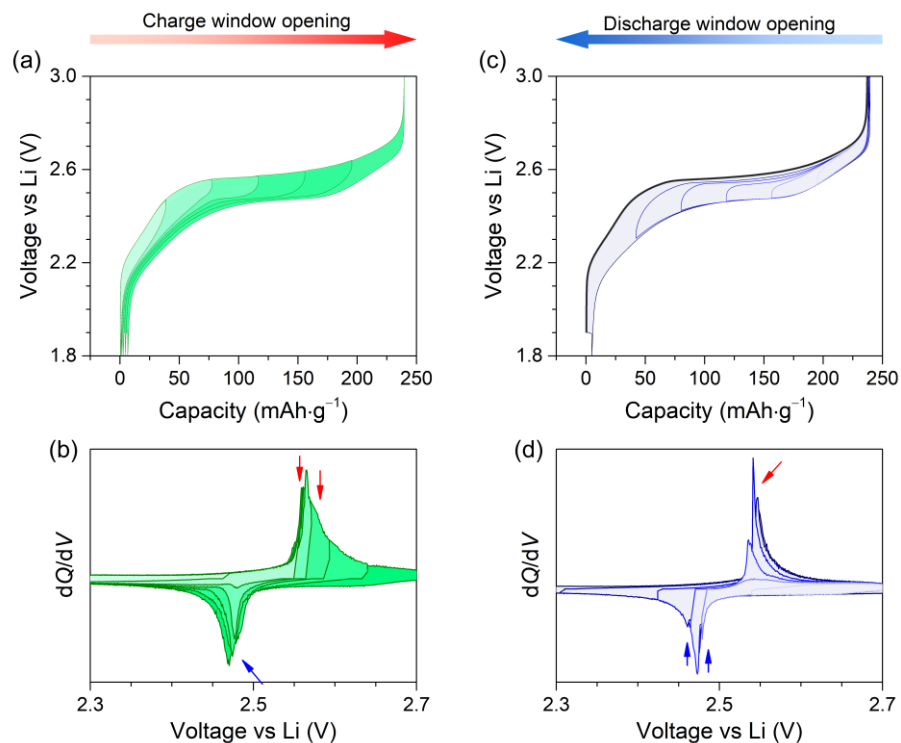


Figure IV.5. Probing the hysteresis of $\text{Li}_{1.13}\text{Ti}_{0.57}\text{Fe}_{0.3}\text{S}_2$ by voltage window opening experiment. (a) Voltage profiles with corresponding dQ/dV curves (b) during charge opening. (c) Voltage profiles with corresponding dQ/dV curves (d) during discharge opening.

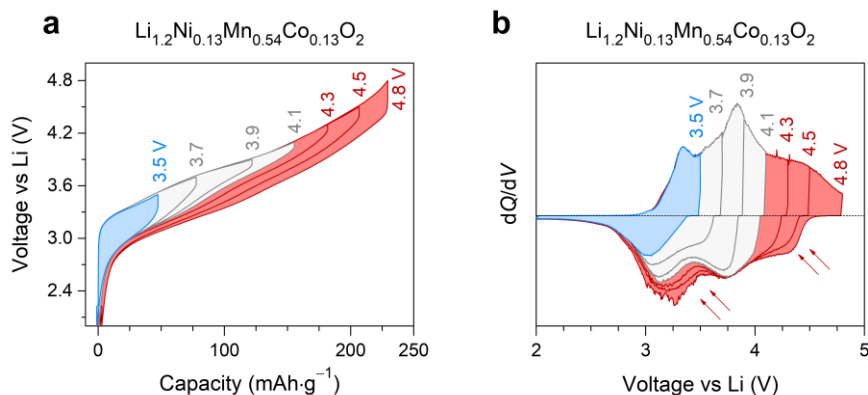


Figure IV.6. Anionic redox in Li-rich NMC. (a) Voltage profiles and (b) corresponding dQ/dV curves of $\text{Li}_{1.2}\text{Ni}_{0.13}\text{Mn}_{0.54}\text{Co}_{0.13}\text{O}_2$ (Li-rich NMC), obtained as the charge window is opened stepwise from 2.0 to 4.8 V. In (b), the arrows indicate the splitting of the capacities obtained by charging above ~ 4.1 V.⁵⁰

Again we performed similar voltage window opening experiments for the $\text{Li}_{1.2}\text{Ti}_{0.4}\text{Ti}_{0.4}\text{S}_2$. During the charging window opening (Figure IV.7a and Appendix Figure A3.4), hysteresis was not increased in the sloppy voltage region. However, in the high-voltage plateau, the polarization increases slightly compared to 1st plateau, but deeper oxidation does not lead to a noticeable increase in the hysteresis. Thus irrespective of the charge window, the discharge voltage is never lowered noticeably.

This is reflected in the dQ/dV curves (Figure IV.7b), as all the oxidative capacity from charging even in the high voltage, could be recovered by ~ 2.45 V peak upon reduction (see the red arrows). Next, the voltage window was opened gradually during discharge from 100% SoC (3 V) and the results are summarized in Figure IV.7c. It is clear that the charging voltage is almost maintained irrespective of the discharge window. The corresponding dQ/dV curves also reveal that all the capacity obtained from discharge are recovered by the 2.35 V and 2.65 V peaks without creating any new peaks (Figure IV.7d).

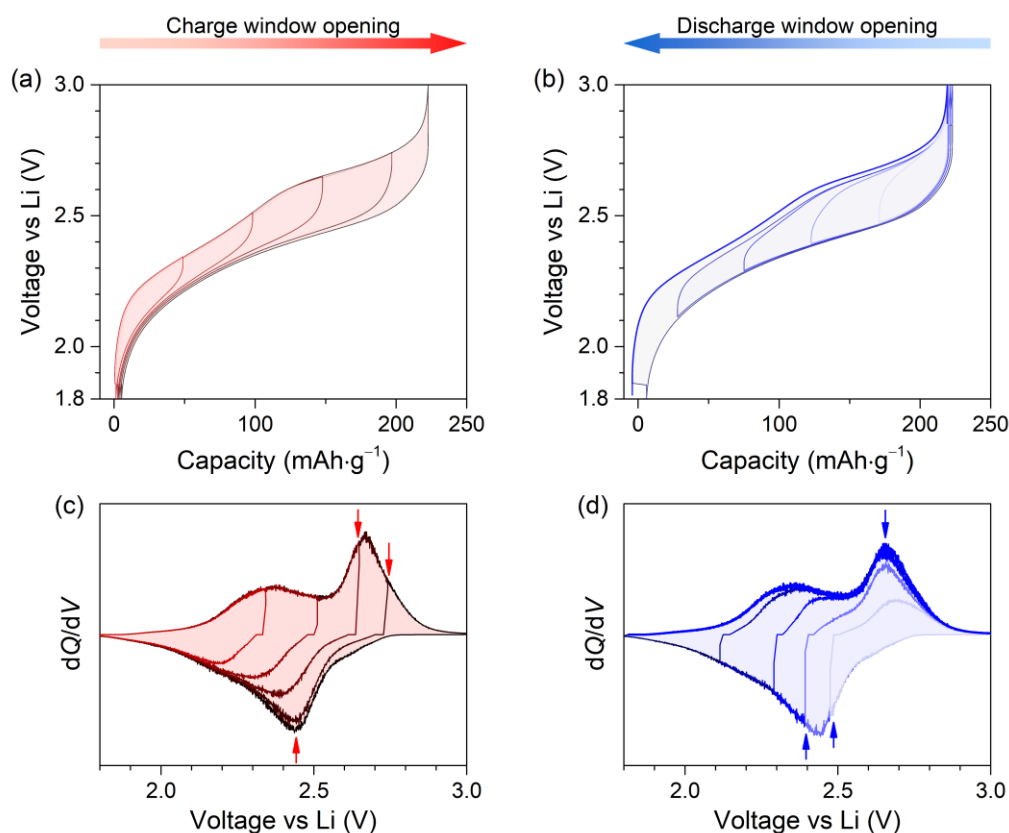


Figure IV.7. Probing the hysteresis of $\text{Li}_{1.2}\text{Ti}^{+0.4}\text{Ti}^{3+0.4}\text{S}_2$ by voltage window opening experiment. (a) Voltage profiles and (b) corresponding dQ/dV curves during charge opening and (c) Voltage profiles and (d) corresponding dQ/dV curves during discharge opening.

Overall, since the anionic redox in Li-rich sulfides have the same dQ/dV peak in either charge-discharge (i.e., symmetrically between charge and discharge). This indicates the absence of any path dependence or hysteresis loop, and explains the very small voltage hysteresis observed.

IV.1.2 Electrochemical Kinetics

The low voltage hysteresis observed above could be related to fast interfacial and / or bulk Li diffusion kinetics. Concerning the kinetics, it was shown previously how oxygen redox displays sluggish kinetics in the Li-rich oxides.^{49,50} Hence, to check whether the kinetics in Li-rich sulfides is fast or sluggish, we first deduced cell resistance from the voltage drop during the first 10 s of the relaxation

steps of the GITT experiment. As showed for $\text{Li}_{1.13}\text{Ti}_{0.57}\text{Fe}_{0.3}\text{S}_2$, the electrochemical resistance remains quite low throughout the whole cycle (Figure IV.8), in contrast to the Li-rich NMC, for which the resistance is significantly larger at all SoCs with additionally an increase at low and high SoCs, the regions involving oxygen redox.⁵⁰

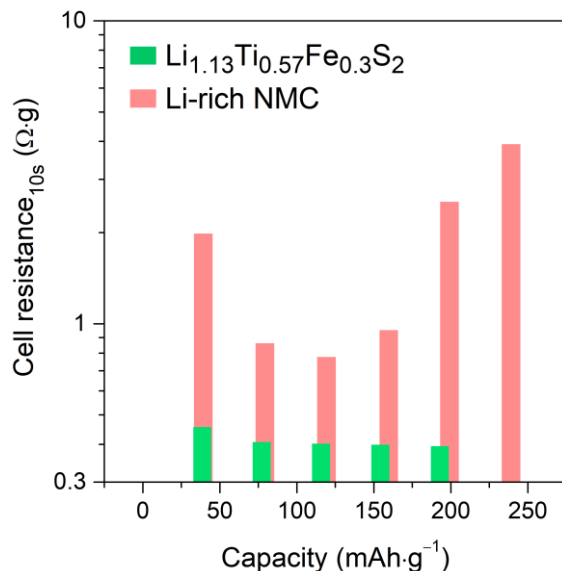


Figure IV.8. Cell's electrochemical resistance as a function of SoC. The resistance (during charging) was estimated by Ohm's law from the voltage drop in first 10 s of rest from GITT experiment in a two-electrode cell (shown in the Appendix).

The kinetics can be better assessed from the evolution of charge-transfer resistance (R_{ct} , i.e., the resistance associated to the Li^+ transfer process at electrolyte / electrode interface) at different SoCs. For Li-rich oxides, the R_{ct} is shown to increase drastically in the anionic redox regime, compared to the cationic redox regime (Appendix Figure A3.2).^{37,50} Therefore, to access the R_{ct} in our Li-rich sulfides, we performed electrochemical impedance spectra (EIS) in Swagelok type cell in a two-electrode configuration. A typical Nyquist plot of the EIS is shown in Figure IV.9. The spectra consists a depressed semicircle followed by a rising tail could be fitted with an equivalent circuit $R_0(R_{HF}/Q_{HF})(R_{MF}/Q_{MF})W_{LF}$, where R , Q , and W represent the resistances, constant phase elements, and Warburg element. The resistance R_0 corresponds to the resistance from electrolyte and electrical contacts of the cell configuration. The high-frequency (HF) semicircle (at ~ 300 Hz) comprises the contributions for interphase contacts, surface film, etc. The mid-frequency (MF) arc, at the onset of the rising tail (at ~ 1 Hz), enlists the charge-transfer resistance (R_{ct}), and followed by low-frequency (LF) Warburg tail that comprises the resistance of Li-diffusion into the electrode.

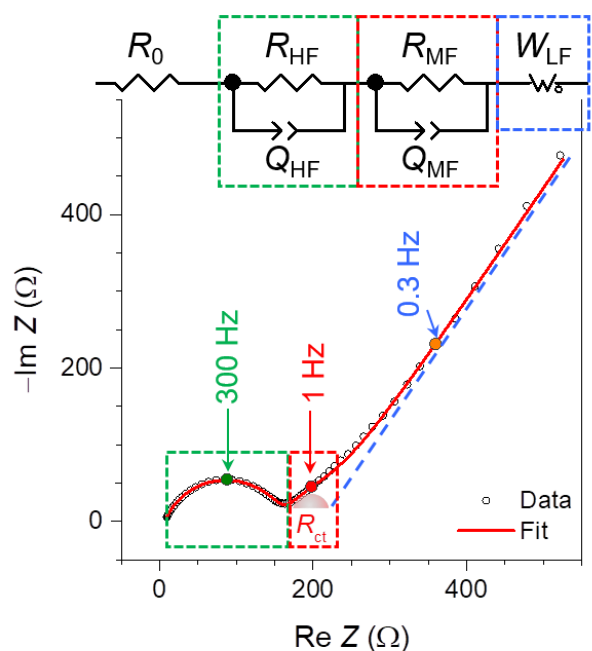


Figure IV.9. Typical Nyquist plot of EIS of $\text{Li}_{1.13}\text{Ti}_{0.57}\text{Fe}_{0.3}\text{S}_2$ in Li-half cell. THE EIS was collected at full-discharged state after first cycle. The sample was used as a self-standing electrode. Observed data points are shown by black circles and fitting of the data are indicated by red line. The equivalent circuit used is shown above. The deconvoluted MF semicircle (corresponding to the R_{ct}) and LF Warburg tail is illustrated by red semicircle and blue dotted line, respectively.

Therefore, we collected electrochemical impedance spectra (EIS) at different SoCs for $\text{Li}_{1.13}\text{Ti}_{0.57}\text{Fe}_{0.3}\text{S}_2$, specifically after each relaxation step during the GITT experiment (shown in the Appendix Figure A3.1) and the evolution of the EIS Nyquist plots is shown in Figure IV.10a,b. Note that the semicircle for the charge-transfer resistance, located in the mid-frequency regime of the spectra (characteristic frequency around ~ 1 Hz), remains barely distinguishable, indicating very small and nearly constant R_{ct} throughout the cycle, irrespective of whether it is cationic or anionic redox regime.

Similarly, EIS spectra were collected for $\text{LiTi}_{0.5}\text{Fe}_{0.5}\text{S}_2$ ($y = 0.5$) composition also after the relaxation step during the GITT experiment (shown in Figure IV.3) and the evolution of the EIS Nyquist plots is shown in Figure IV.10c,d. The EIS Nyquist plots are similar to the $\text{Li}_{1.13}\text{Ti}_{0.57}\text{Fe}_{0.3}\text{S}_2$ composition (except lower impedance in HF region because of cell-configuration and amount of Li anode). For this composition also, the semicircle for the charge-transfer resistance (R_{ct}) remains barely distinguishable, indicating very small R_{ct} throughout the cycle. Similarly low R_{ct} at all SoCs was confirmed for the $\text{Li}_{1.2}\text{Ti}^{4+}_{0.4}\text{Ti}^{3+}_{0.4}\text{S}_2$, from the evolution of EIS spectra (shown in the Appendix Figure A3.3).

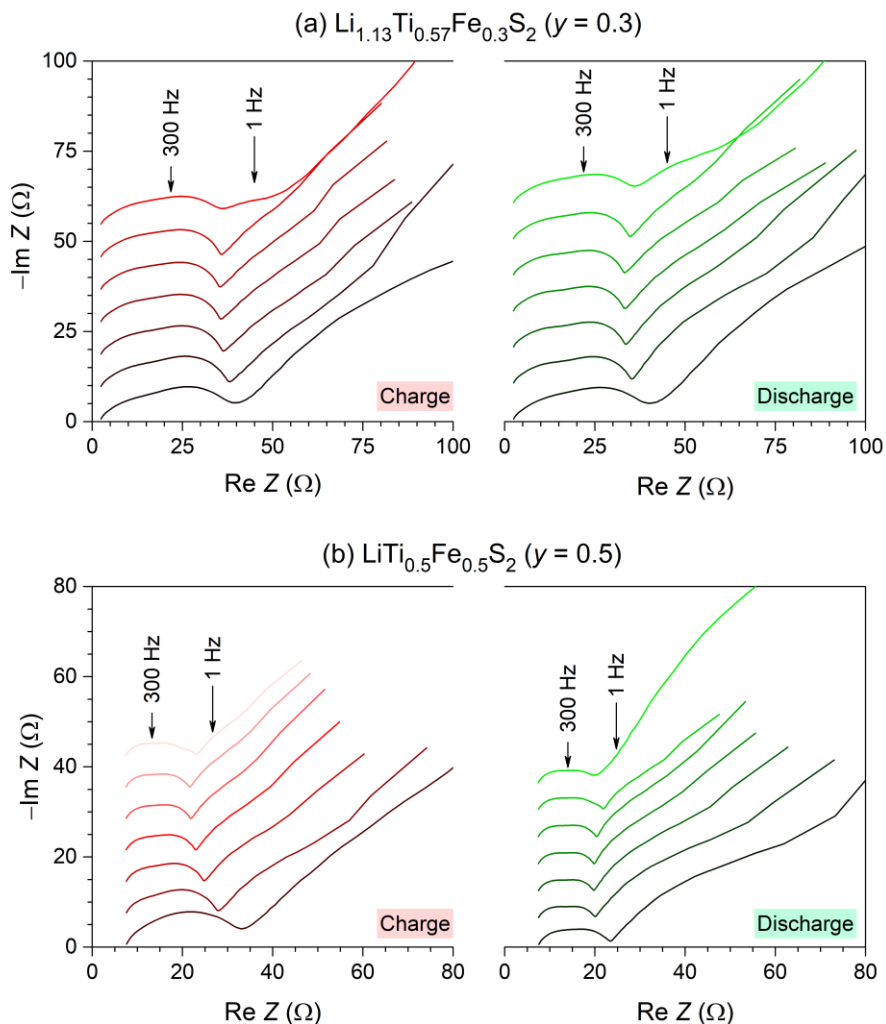


Figure IV.10. Nyquist plots of EIS recorded after each relaxation in GITT. EIS was recorded for $\text{Li}_{1.13}\text{Ti}_{0.57}\text{Fe}_{0.3}\text{S}_2$ (a), and $\text{LiTi}_{0.5}\text{Fe}_{0.5}\text{S}_2$ (b) during charge and discharge. Experiment was done in a two-electrode Swagelok cell and the sample was used as powder (hand-ground with 20 wt% Csp).

Overall, anionic redox in Li-rich sulfides is fast and no impedance build-up occurs upon cycling, which is positively reflected into the voltage hysteresis. This is quite contrary to Li-rich oxides where the resistance builds up drastically with deeper oxidation of oxygen (shown in Appendix Figure A3.2).^{37,50} This clearly highlights the positive attribute of Li-rich sulfides concerning kinetics.

IV.1.3 Voltage fade

Lastly, regarding the critical issue of voltage fade, we found that it still afflicts Li-rich sulfides (Figure IV.11). However, the voltage fade exists in much lower extent, as shown in Figure IV.12. The voltage fade for $\text{Li}_{1.13}\text{Ti}_{0.57}\text{Fe}_{0.3}\text{S}_2$ can be divided in two regimes, starting first with a well-pronounced decrease from 2nd cycle to the 7th (a drop of ~35 mV) followed by a stabilization afterwards to reach an overall drop of ~50 mV after 64 cycles (the maximum we have cycled), see Figure IV.12. This again

positively contrasts with Li-rich NMC that shows a nearly continuous voltage fade upon cycling with an accumulated drop of ~ 150 mV after 60 cycles (Figure IV.12).

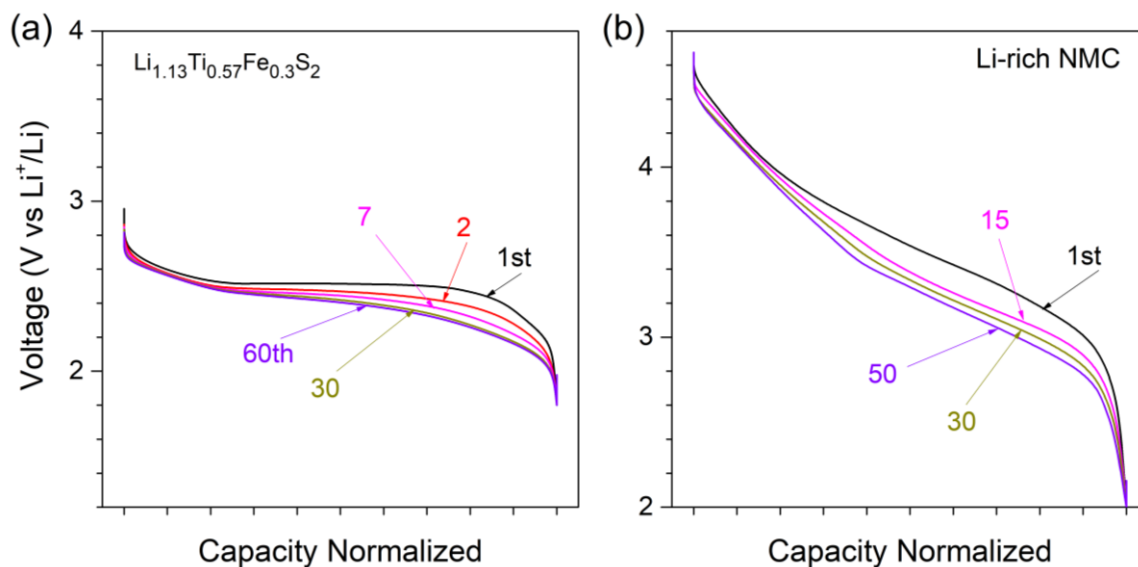


Figure IV.11. Discharge profiles of $\text{Li}_{1.13}\text{Ti}_{0.57}\text{Fe}_{0.3}\text{S}_2$ over long cycling to show the voltage fade. The sample was cycled as powder in Swagelok type cells with sample as powder, at $C/2.5$ rate. Note that the voltage profile almost stabilizes after the 7th cycle.

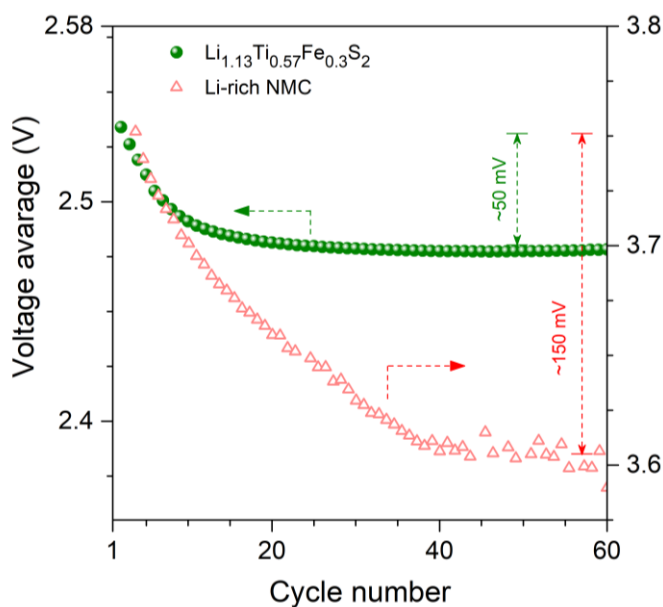


Figure IV.12. Average voltage during long cycling of $\text{Li}_{1.13}\text{Ti}_{0.57}\text{Fe}_{0.3}\text{S}_2$ and Li-rich NMC in Li-half cells. In each cycle, the average voltage is defined as the mean of the average charge and discharge voltages that and was calculated by dividing the energy with the capacity obtained. Data for Li-rich NMC is taken from reference³⁰⁵.

Furthermore, we calculated the voltage fade for the Co^{2+} and Ti^{3+} substituted Li_2TiS_3 . Both the compositions behave similarly to the Fe-substituted phase and only a small voltage fade is observed (Figure IV.13).

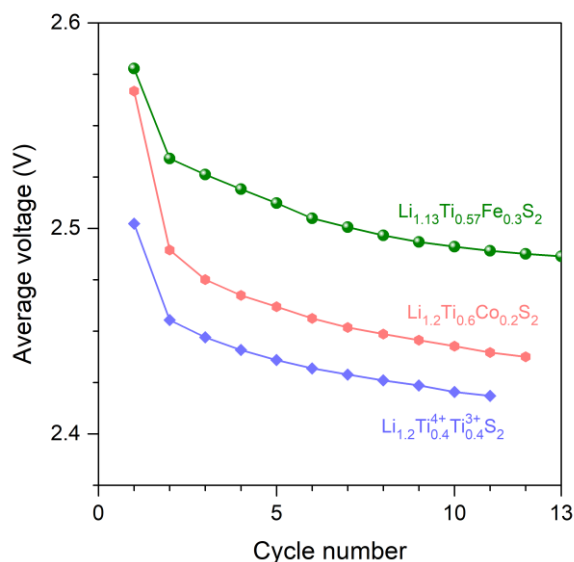


Figure IV.13. Average voltage of Li-rich sulfides in Li-half cells. In each cycle, the average voltage is defined as the mean of the average charge and discharge voltages that was calculated by dividing the energy with the capacity obtained. Samples were cycled in Swagelok type cells, with samples as powders.

In short, anionic redox promotes voltage fade Li-rich sulfides, but not to the extent that was observed for Li-rich oxides.

IV.1.4 Na_2TiS_3

At this point we move to the Na-rich sulfide Na_2TiS_3 (i.e., $\text{Na}_{1.33}\text{Ti}_{0.67}\text{S}_2$), in order to verify whether the positive attribute of anionic redox in sulfides is maintained for Na-(de)intercalation also.

For the O3- Na_2TiS_3 , stable cycling occurs with a polarization of ~ 300 mV (Figure IV.14). In contrast, the P2- Na_2TiS_3 shows a large polarization of ~ 700 mV. Hence, we choose the O3- Na_2TiS_3 phase for comparison with the $\text{Na}_{0.67}[\text{Mg}_{0.28}\text{Mn}_{0.72}\text{O}_2]$ oxide and shown in Figure IV.14. It is clear that the hysteresis in Na_2TiS_3 (~ 0.3 V) is much smaller than the same observed for $\text{Na}_{0.67}\text{Mg}_{0.28}\text{Mn}_{0.72}\text{O}_2$ (~ 1.2 V), or recently reported P2- $\text{Na}_{0.67}\text{Zn}_{0.22}\text{Mn}_{0.78}\text{O}_2$.⁶⁷ Therefore, the $\text{S}^{2-}/\text{S}_2^{n-}$ anionic redox possess much lesser hysteresis than the anionic $\text{O}^{2-}/\text{O}_2^{n-}$ anionic redox in Na-cathode materials. Note that this value of hysteresis is comparable to that of cationic redox, e.g., in $\text{NaNi}_{0.5}\text{Mn}_{0.5}\text{O}_2$ (~ 0.15 V),³⁰⁶ etc., and approaches the state-of-art hysteresis-free situation observed in $\text{Na}_3\text{V}_2(\text{PO}_4)_2\text{F}_3$ (NVPF).³⁰⁷

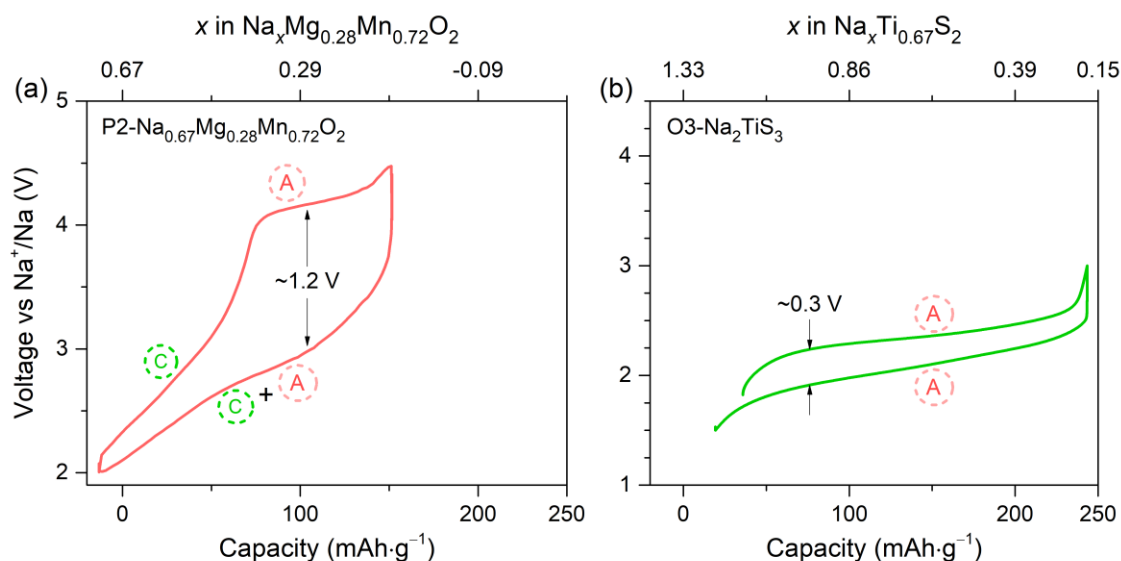


Figure IV.14. The voltage profiles in 2nd cycle of (a) $\text{Na}_{0.67}[\text{Mg}_{0.28}\text{Mn}_{0.72}\text{O}_2]$, and (b) $\text{O3-Na}_2\text{TiS}_3$. In (a) cationic $\text{Mn}^{3+/4+}$ redox is indicated by C and anionic $\text{O}^{2-}/\text{O}_2^{n-}$ by A, and in (b) by anionic $\text{S}^{2-}/\text{S}_2^{n-}$ is indicated by A. Cycling rate of $10 \text{ mAh}\cdot\text{g}^{-1}$ was used. Data for (a) is taken from Reference⁴⁴.

Next, to check the capacity fade, we plotted the capacity retention of the O3 and P2 phases in Figure IV.15. The O3- Na_2TiS_3 , in the 1st cycle, shows a discharge capacity of $>240 \text{ mAh}\cdot\text{g}^{-1}$, leading to a decent discharge energy density of $\sim 450 \text{ Wh}\cdot\text{kg}^{-1}$ (at material level). Furthermore, the phase shows a decent capacity retention, as shown in the cycling of first few cycles, even though the cycling condition was not optimized. Initially it shows slight capacity decay, but the capacity stabilizes at $\sim 180 \text{ mAh}\cdot\text{g}^{-1}$ after first 10 cycles. The P2- Na_2TiS_3 , despite having similar capacity in 1st cycle alike the O3-phase, exhibits rapid capacity fading. Nevertheless, the energy density (at material level) obtained for O3- Na_2TiS_3 is comparable to NVPF ($\sim 500 \text{ mAh}\cdot\text{g}^{-1}$).³⁰⁸

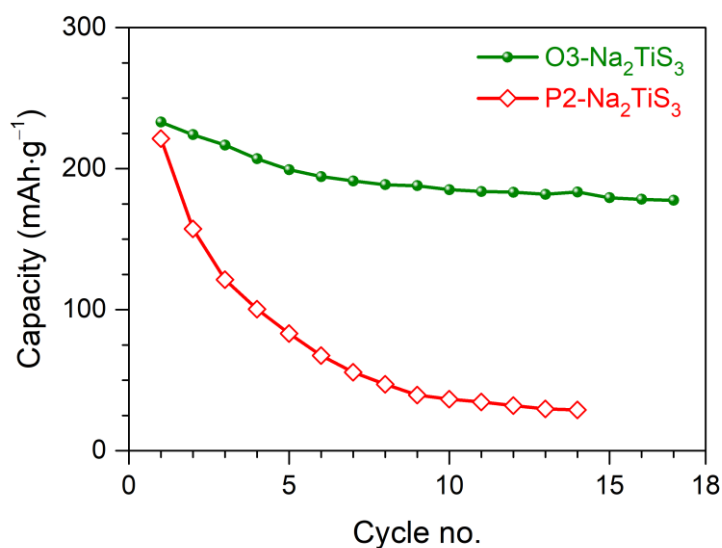


Figure IV.15. Capacity retentions of the O3- and P2- Na_2TiS_3 . The samples (hand-ground with 20 wt% Csp) were cycled as powder in Swagelok cells without further optimization.

Lastly, to check the voltage fade, we compared the average voltage decay of Na_2TiS_3 and the results are summarized in Figure IV.16. Clearly amongst the phases, the O3- Na_2TiS_3 presents higher voltage and smaller fading in discharge voltage (~ 85 mV in first 18 cycles), than the P2-phase that shows rapid voltage decay (~ 150 mV in first 14 cycles).

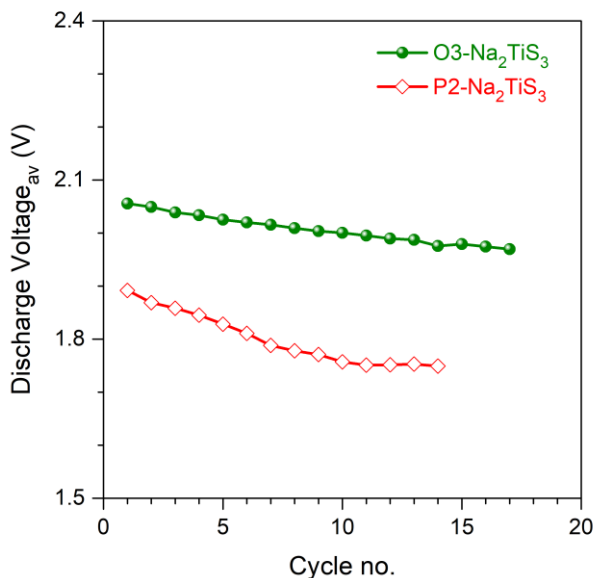


Figure IV.16. Average discharge voltages obtained in O3- and P2- Na_2TiS_3 over first few cycles. Average voltage here is defined by the ratio of energy density and the capacity obtained in each cycle.

Overall, amongst O3- and P2- Na_2TiS_3 , the O3-phase offers better electrochemical performance. This is probably because the O3-phase, being thermodynamically stable, is more robust against Na-(de)insertion, whereas the kinetically stabilized P2-phase is less sustainable to structural evolution upon Na-(de)insertion. Furthermore, the O3- Na_2TiS_3 phase demonstrate excellent reversibility of anionic $\text{S}^{2-}/(\text{S}_2)^{n-}$ redox in Na-cathode materials, with much lesser voltage hysteresis than the same in oxides, with small voltage and capacity fading. Further improvement here can be performed by fabricating Na-full cell (to avoid side reactions with Na metal anode) and also probably by partial metal-substitution in Na_2TiS_3 , as shown for Li_2TiS_3 in this thesis.

IV.2 Chapter Conclusions

In summary, we have assessed the practical aspects of anionic redox in Li-rich layered sulfides, namely $\text{Fe}^{2+}/\text{Co}^{2+}/\text{Ti}^{3+}$ substituted Li_2TiS_3 , and Na_2TiS_3 , via detailed electrochemical analysis. When benchmarked against Li-rich NMCs, these phases present several positive attributes such as (i) very small overall voltage fade (as low as ~ 50 mV for $\text{Li}_{1.13}\text{Ti}_{0.57}\text{Fe}_{0.3}\text{S}_2$ even after 60 cycles) and (ii) low voltage hysteresis (~ 30 mV for $\text{Li}_{1.13}\text{Ti}_{0.57}\text{Fe}_{0.3}\text{S}_2$), along with fast kinetics, as compared to Li-rich NMC showing a voltage fade of 150 mV and a hysteresis of 300 mV besides sluggish kinetics. Similar positive

attribution was observed for Na_2TiS_3 , that shows low overpotential and decent energy density, compared to the oxides.

Overall, moving from oxygen to sulfur as the ligand turns out to be a correct strategy to partially mitigate the practical bottlenecks of anionic redox. However, we need to keep in mind that this comes at the expense of the overall energy density compared to Li-rich oxides, because of lower potential and higher molecular weight of sulfur. The energy density of $\text{Li}_{1.13}\text{Ti}_{0.57}\text{Fe}_{0.3}\text{S}_2$ is compared with Li-stoichiometric and Li-rich NMC in Figure IV.17. The $\text{Li}_{1.13}\text{Ti}_{0.57}\text{Fe}_{0.3}\text{S}_2$ offers an energy density at par with LiCoO_2 , which may not be attractive as this is much lower than the $\sim 1000 \text{ Wh}\cdot\text{kg}^{-1}$ obtained for Li-rich NMC and $>700 \text{ mAh}\cdot\text{g}^{-1}$ for today's commercialized NMC cathodes. Nevertheless, we believe that they could serve as excellent 'model' electrodes to study the general properties of anionic redox chemistry, especially via the realization of S-based solid-state batteries that can enable playing with temperature as an extra dimension. Both low hysteresis and structural integrity upon Li (de)intercalation are promising assets to design next-generation cathodes provided we can overcome the energy density penalty pertaining to the use of sulfur as a ligand. A compromise could consist in combining the energy advantage of oxygen redox with the practicability of sulfur redox by preparing 3d-metal-based oxysulfides, if they are made possible to synthesize ever.

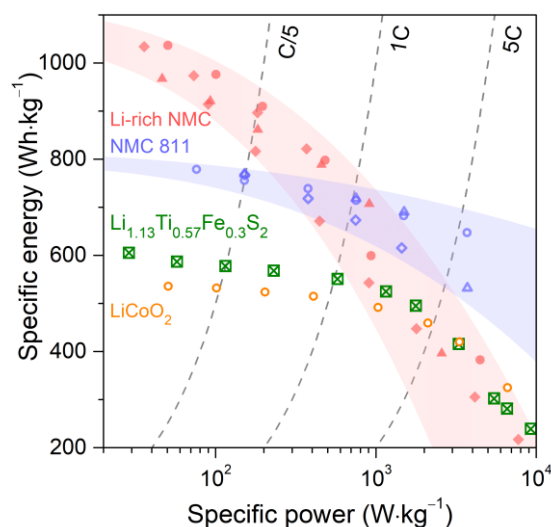


Figure IV.17. Ragone plots of $\text{Li}_{1.13}\text{Ti}_{0.57}\text{Fe}_{0.3}\text{S}_2$. The sample was cycled as a self-standing electrode to minimize the Li-diffusion limitation inside the active material. Li-rich NMC, Li-stoichiometric NMC 811 ($\text{LiNi}_{0.8}\text{Mn}_{0.1}\text{Co}_{0.1}\text{O}_2$), and LiCoO_2 are also included for comparison. Only values at material-level are considered and values for the NMC-811 and the Li-rich NMC are adapted from Reference³⁷.

Interestingly, these sulfide based cathode materials can be good candidates for the all-solid-state batteries (ASSBs) with sulfide solid-state electrolytes, due to interfacial compatibility between sulfide-base electrodes and electrolyte materials. Hence, we decided to use the $\text{Li}_{1.13}\text{Ti}_{0.57}\text{Fe}_{0.3}\text{S}_2$ as positive electrode in ASSB as will be presented in the next chapter.

Chapter V

Application of Sulfide-based Cathode materials in All-Solid-State Batteries[#]

[#]Part of this chapter includes the following publication: Marchini and Saha *et al.*, manuscript under preparation.

V.1 Chapter Introduction

Tremendous attention has been recently focused on all-solid-state-batteries (ASSB), to increase the safety and energy density of Li-ion batteries. This has been unveiled by the discovery of thiophosphate based solid electrolyte (SEs) $\text{Li}_{10}\text{GeP}_2\text{S}_{12}$ by Kanno and colleagues,¹²⁷ that offer an ionic conductivity ($12 \text{ mS}\cdot\text{cm}^{-1}$) comparable to the liquid electrolytes. In spite of this advance, the practical development of ASSBs remains an issue, mostly because of the difficulties to master the interfaces in ASSBs. Current Li-ion batteries relies on layered oxides such as LiCoO_2 (LCO), and $\text{LiNi}_{1-x-y}\text{Mn}_y\text{Co}_x\text{O}_2$ (NMCs), etc., as cathode materials because of their high performance.^{27,30} For sulfide electrolyte based ASSBs using layered oxides as positive electrodes, the oxide-sulfide interface remains problematic, because of the formation of resistive decomposition layer and / or Li-depleted layer (i.e., the space-charge layer) at the interface (Figure V.1a).^{193,198,233,309,310} This leads to highly resistive cathode electrolyte interface (CEI) when oxide cathode materials are used with sulfide electrolytes and is detrimental for the ASSB performance.^{193,198,233,309,311,312} This interfacial resistance could be partially mitigated by coating the cathode materials with a buffer redox-inactive (electronically insulating, but ionically conducting) layer of ZrO_2 , LiNbO_3 , $\text{LiNb}_{0.5}\text{Ta}_{0.5}\text{O}_3$ or $\text{Li}_2\text{O}\text{-ZrO}_2$ etc., which effectively shields the chemical reactivity and high electrode potential of the oxides (Figure V.1b).^{193,200-202}

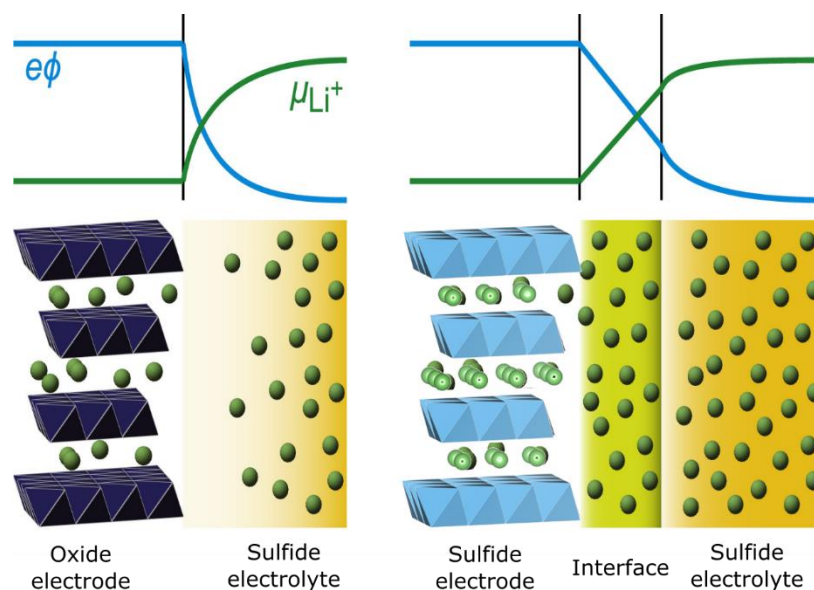


Figure V.1. Schematic diagram of cathode/sulfide electrolyte interfaces with oxide or sulfide cathode. Figure adapted from reference³¹³. The μ_{Li^+} is the chemical potential of Li ion, and $e\phi$ is its electrostatic energy (e is elementary charge and ϕ is local electrostatic potential). The μ_{Li^+} in the bulk of sulfide electrolytes is relatively high, because of Li ions weakly bonded to the anionic framework. High ϕ at the surface of oxide cathode materials lowers the μ_{Li^+} at the interface, leading to decrease of Li ion concentration.³¹³

Herein, we wanted to explore the performance of sulfide-based cathode materials in ASSB to alleviate the interfacial incompatibility with sulfide SEs. Indeed sulfide based positive electrodes, such as TiS_2 , TiS_3 , etc., have been shown for small interfacial resistances and good performances in ASSB

with sulfide SEs.^{283,314–316} Furthermore, as sulfide SEs are electrochemically instable at high voltage, sulfide cathode materials with moderate voltage (2 - 3 V) can be helpful by limiting the cell potential. Therefore, we decided to utilize high-capacity Li-rich sulfide cathode material $\text{Li}_{1.13}\text{Ti}_{0.57}\text{Fe}_{0.3}\text{S}_2$ (LTFS) that has been reported in Chapter 3.

V.2 Designing a cell for ASSB assembly

In order to fabricate an ASSB, we first started building a suitable testing setup in lab. This was the beginning of a long journey in collaboration with Daniel Alves Dalla Corte. This task is quite challenging, and expensive as well, as a setup for ASSB must fulfill the following basic criteria:

- (1) An insulating body to contain the ASSB.
- (2) Strong body that can withstand with high pressure needed to fabricate (typically up to ~380 MPa) and cycle (at ~70 MPa) the ASSB.^{127,157,193,198,317–319}
- (3) Cycling in air-tight cell (i.e., in inert atmosphere).
- (4) Additional capabilities such as controlling/monitoring temperature and pressure.

A simple testing setup was designed and fabricated by other people and engineers in our lab-Florencia Marchini, Marc Duchardt, Daniel Alves Dalla Corte, and Thomas Dargon (Figure V.2). It consists of a core made of PEEK (polyether ether ketone) polymer, that is very tough, and rigid polymer and that can bear high mechanical and tensile strength. Furthermore, it is stable up to high temperature (260 °C) while showing no water absorption.

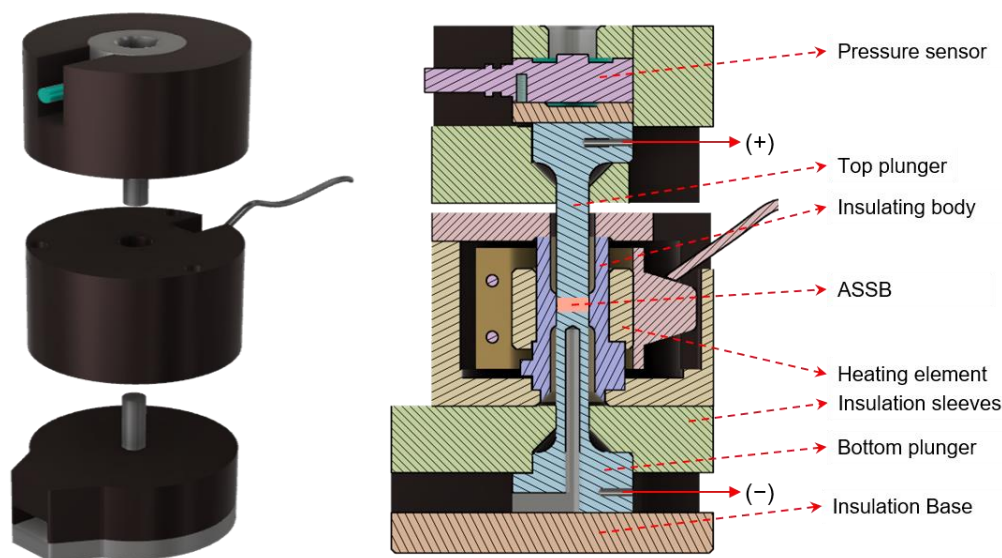


Figure V.2. A picture of the ASSB setup fully designed and assembled at lab, that was used in this study. Further details can be found at <https://sphere-energy.eu>.

Hardened steel plungers were used to apply pressure, having a diameter of 8 mm. Moreover, the setup includes the capability of applying temperature (up to 200 °C) and pressure (up to 4 tons·cm⁻²)

that can be controlled independently. Lastly, to cycle in inert atmosphere, the whole ASSB assembling and cycling was done inside an Ar-filled glovebox.

V.3 Protocol to fabricate ASSB in the setup

Using the cell previously described the ASSB was assembled by cold-pressing the cathode, solid electrolyte and anode materials, layer by layer, using a hydraulic press. A schematic of the ASSB stack (8 mm in diameter) is shown in Figure V.3. First the solid electrolyte powder ($\sim 30 - 40$ mg, corresponding to a thickness of $\sim 40 - 60$ μm) was pressed inside the ASSB setup for 5 mins with a uniaxial pressure of $4 \text{ tons}\cdot\text{cm}^{-2}$. Then the cathode composite powder ($\sim 5 - 10$ mg) was pressed on the solid electrolyte layer, with a uniaxial pressure of $4 \text{ tons}\cdot\text{cm}^{-2}$ for 1 min. The cathode composite was prepared by mixing cathode material and solid electrolyte powders in 70 : 30 weight-ratio and hand-grinding them for 5 mins in an agate mortar. Note that, we avoided conductive carbon-additive Csp in the cathode composite, because of its detrimental effect on the electrolyte.^{309,320–322} Then a piece of indium (In) foil was placed on the other side of the electrolyte and pressed with $1 \text{ tons}\cdot\text{cm}^{-2}$ for 1 min, that acts as an anode. The In/InLi_x alloy-anode has a constant potential of 0.6 V vs. Li/Li⁺. At this point Li-metal anode was not used, to avoid dendrites issue and side reactions.^{309,323,324} The process was performed inside an Ar-filled glovebox. Thus the three-layer ASSB was obtained and was cycled with a uniaxial pressure of $1 \text{ tons}\cdot\text{cm}^{-2}$ using the pressure frame of the ASSB setup.

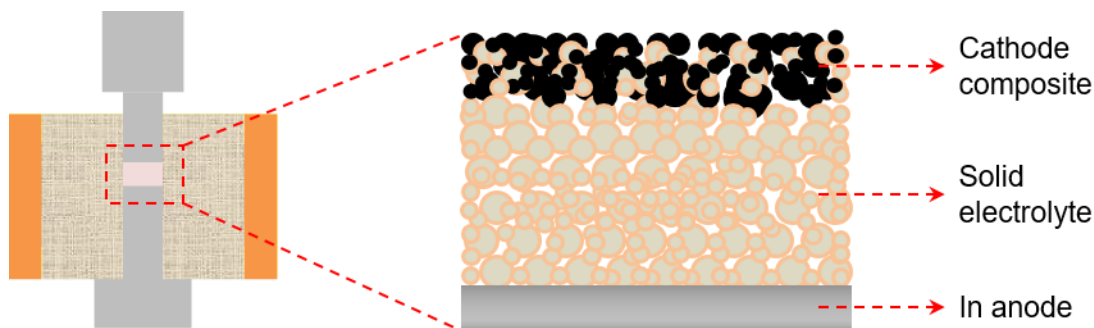


Figure V.3. Schematics of the three-layer ASSB.

V.4 Solid electrolytes used for ASSB

A prerequisite prior to start working on ASSB, is to select suitable solid electrolytes. Toward this end, we have chosen to work with sulfide-based solid electrolytes. We did not consider the oxide-based solid electrolytes that were explored in the Chapter 2, because of their low ionic conductivity. Nevertheless, oxide solid electrolytes in general are challenging to use in ASSBs, because of their processing difficulties as discussed in the Introduction Section. Generally, oxide solid electrolytes

require sintering at high pressure and temperature to form intimate inter-particle contacts. In contrary, the sulfide solid electrolytes possess higher ionic conductivity than oxides while being easy to use in ASSBs with RT processing.¹⁵⁴ In this regards, we decided to work with $\text{Li}_2\text{S-P}_2\text{S}_5$ glass (denoted as g-LPS) and crystalline $\beta\text{-Li}_3\text{PS}_4$ (denoted as LPS) according to the literature reports.^{151,154,177,325,326}

The $\text{Li}_2\text{S-P}_2\text{S}_5$ glass (g-LPS) electrolyte used here was synthesized by mechanochemical synthesis (low-energy ball milling) following literature reported procedure.^{151,325} Among g-LPS compositions, the 75· Li_2S -25· P_2S_5 (in molar ratio) presents the highest Li-conductivity, hence this composition was chosen in this thesis. Required amount of Li_2S (99.9%, Alfa Aesar) and P_2S_5 (98%, ACROS Organics) powder were first mixed homogenously by hand grinding for 10 mins in agate mortar. The mixture was transferred to an air-tight zirconia jar (500 ml) with zirconia balls (10 mm diameter, 12 balls) and closed. Then it was ball milled in a planetary ball mill (Frisch Pulverisette 7) for 30 h at 510 rpm. A rest of 10 mins was given after each 15 mins of milling. The resulting g-LPS was collected and hand-grinded again prior to use in ASSB. The as-synthesized g-LPS shows an ionic conductivity of $\sim 0.1 \text{ mS}\cdot\text{cm}^{-1}$ at RT (Figure V.4a). Whole process was done inside an Ar-filled glovebox, except the ball-milling, to avoid air exposure.

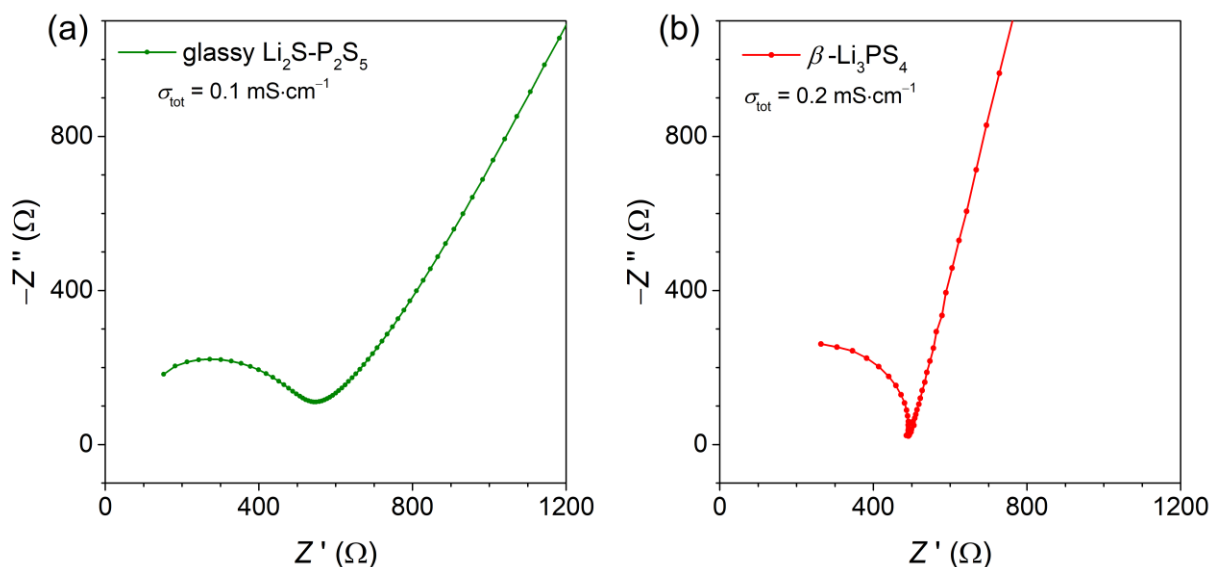


Figure V.4. EIS spectra of the glassy 75· Li_2S -25· P_2S_5 (g-LPS) and $\beta\text{-Li}_3\text{PS}_4$ (LPS) solid electrolyte. See the Appendix for details of the measurement protocol. The EIS was collected on sample-pellets, with 25 mV bias in the frequency range of 0.5 MHz - 1 Hz.

The $\beta\text{-Li}_3\text{PS}_4$ solid electrolyte was prepared (courtesy to Dr. Florencia Marchini) via a facile solvent-based route reported elsewhere.^{177,326} Required amount of Li_2S and P_2S_5 were thoroughly mixed using mortar and pestle, dispersed in anhydrous tetrahydrofuran (THF, 99.9%, Sigma Aldrich), and followed by stirring for 2 days. The white precipitate was recovered, washed with THF, and then dried in vacuum. Finally, the as-prepared powder was heated at 140 °C under vacuum. Whole synthesis was carried out in an Ar-filled glovebox. The synthesized nanoporous $\beta\text{-Li}_3\text{PS}_4$ shows an ionic conductivity

of $\sim 0.2 \text{ mS}\cdot\text{cm}^{-1}$ at RT (Figure V.4b). The purity of the $\beta\text{-Li}_3\text{PS}_4$ was further confirmed from the Rietveld refinement of its synchrotron XRD pattern (Figure V.5).

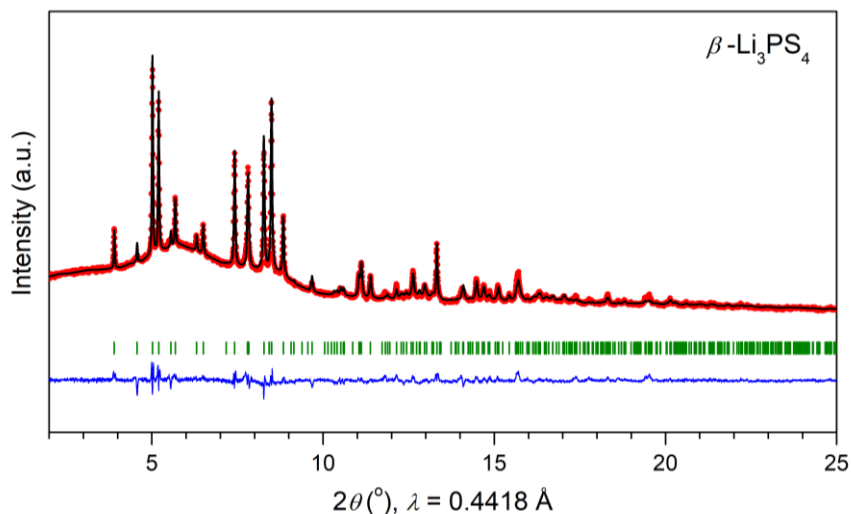


Figure V.5. Rietveld refinement of the SXRD pattern of the as-synthesized $\beta\text{-Li}_3\text{PS}_4$ SE. The red circles, black continuous line, blue line, and green tick bars represent the observed, calculated, and difference patterns, and Bragg positions, respectively. The SXRD pattern was refined in $Pnma$ space group with unit cell parameters $a = 12.97721(27) \text{ \AA}$, $b = 8.03258(20) \text{ \AA}$, $c = 6.12629(13) \text{ \AA}$, and $V = 638.608(25) \text{ \AA}^3$, in agreement with the reported structural model.¹⁴³

Since spontaneous chemical reactivity of sulfide-based SEs remains an issue in ASSBs,³²⁷ we first checked the chemical compatibility of $\beta\text{-Li}_3\text{PS}_4$ with the Li-rich sulfide $\text{Li}_{1.13}\text{Ti}_{0.57}\text{Fe}_{0.3}\text{S}_2$ (LTFS). For this purpose, we have collected SXRD pattern after annealing the cathode composite at 200°C for 2 days. Even after the heat treatment, the SXRD pattern did not show any trace of impurity phase (Figure V.6), thus ruling out any chemical reaction between them.

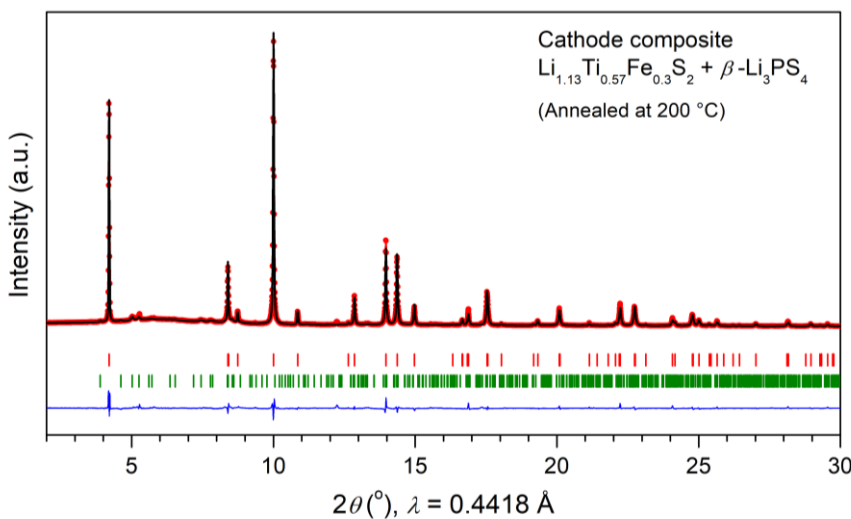


Figure V.6. Rietveld refinement of the SXRD pattern of the cathode composite. The red circles, black continuous line, blue line, and tick bars represent the observed, calculated, and difference patterns, and Bragg positions, respectively. The red and green tick bars represent the Bragg positions of LTFS

and β -Li₃PS₄, respectively. For LTFS, the previously obtained structural model in $R\bar{3}m$ space group (see Chapter III) was used and the refinement returns $a = b = 3.53393(1)$ Å, $c = 18.06313(14)$ Å, and $V = 195.362(2)$ Å³. The β -Li₃PS₄ returns a unit cell (space group $Pnma$) with $a = 13.02691(37)$ Å, $b = 7.97269(23)$ Å, $c = 6.04383(14)$ Å, and $V = 627.710(31)$ Å³.

Furthermore, in absence of conductive additives, the electronic percolation in cathode composites are provided only through interconnected cathode particles.^{309,320} Hence, it is crucial to have a good electronic conductivity of the LTFS cathode material and indeed we observed a high electronic conductivity of $3 \cdot 10^{-2}$ S·cm⁻¹ in LTFS (deduced from DC polarization measurement, details in the Appendix Figure A4.1). We also measured the electronic conductivity of the cathode composite (LTFS + β -Li₃PS₄) and found an electronic conductivity of $5 \cdot 10^{-3}$ S·cm⁻¹ (Figure V.7), which is sufficiently high to be used in ASSB.²³³

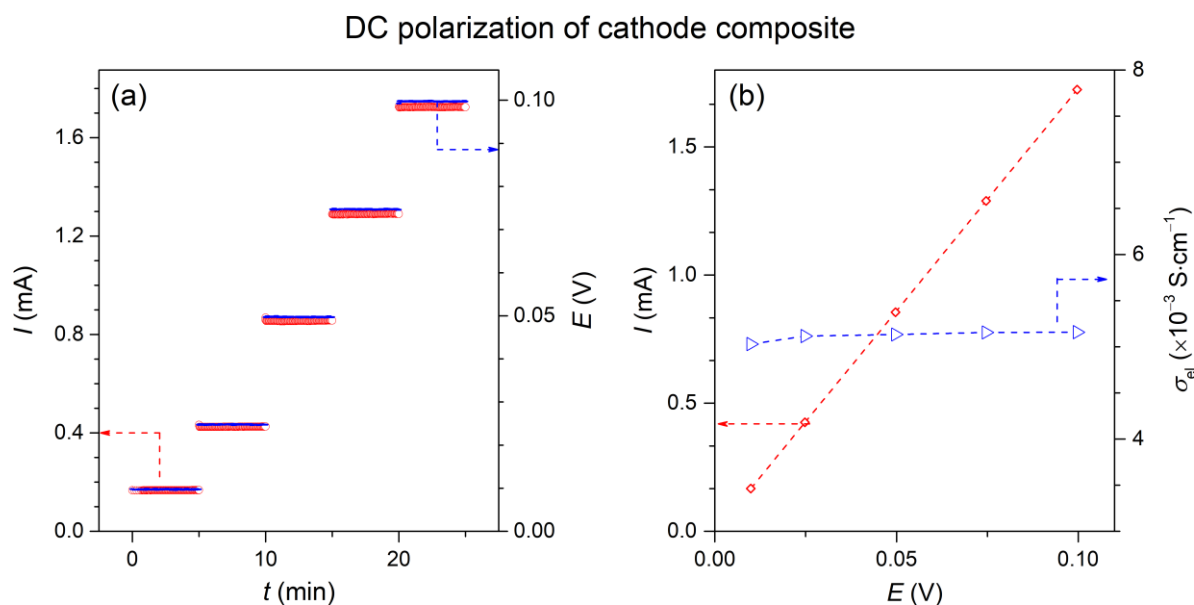


Figure V.7. DC polarization plots of LTFS-LPS cathode composite. (a) The steady state current (I , in left axis) obtained by applying DC voltages (E , in right axis) to the sample pellet (thickness of 1.5 mm) placed between two steel electrodes. (b) Variation of I with E , which was used to deduce the resistance (by Ohm's law). The electronic conductivity (σ_{ei}) was calculated from the resistance, according to the formulae $\sigma = (d/A) \cdot (1/R)$ and plotted in right axis.

V.5 Cycling results of ASSBs

Oxide cathode materials, such as, LiCoO₂, LiNi_{0.8}Mn_{0.1}Co_{0.1}O₂, etc., could be cycled, as reported in literature, but show rapid capacity fading due to reactivity (at the surface) with the sulfide solid electrolytes (β -Li₃PS₄, LGPS, etc.) when they are not surface-coated,^{193,198,309} hence our attempt to cycle sulfide-based cathode materials in ASSB. The Li_{1.13}Ti_{0.57}Fe_{0.3}S₂ (LTFS), the best composition amongst the Li-rich sulfides (see Chapter 3) was chosen for the studies. The performance of the LTFS with g-LPS and β -Li₃PS₄ as SEs in ASSB are summarized below.

V.5.1 Cycling with glassy LPS SE

The ASSB using $\text{Li}_{1.13}\text{Ti}_{0.57}\text{Fe}_{0.3}\text{S}_2$ (LTFS) as cathode material in ASSB using $\text{Li}_2\text{S}-\text{P}_2\text{S}_5$ glass (with 75 : 25 molar-ratio) as solid electrolyte and indium as anode was cycled within the potential range of 1.8 – 3.6 V vs Li^+/Li at a rate of $C/30$. The voltage profile is shown in Figure V.8.

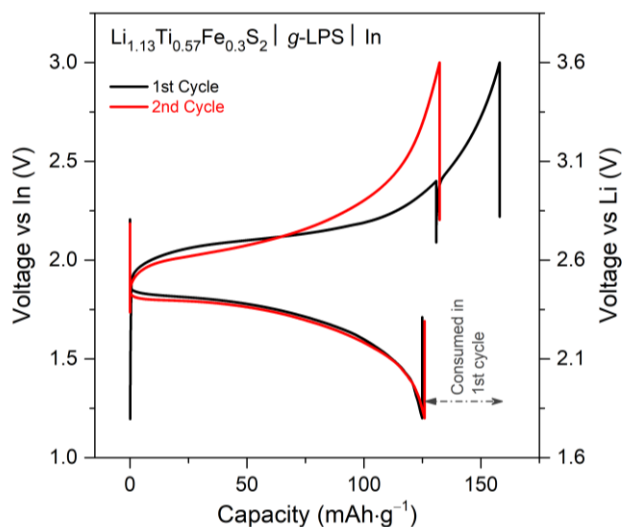


Figure V.8. Voltage profile of $\text{Li}_{1.13}\text{Ti}_{0.57}\text{Fe}_{0.3}\text{S}_2$ (LTFS) cycled in ASSB at RT. 75- Li_2S -25- P_2S_5 glass (*g*-LPS) was used as solid electrolyte and In metal was used as anode. Cycling rate of $C/30$ was used.

A discharge capacity of $\sim 125 \text{ mAh}\cdot\text{g}^{-1}$ was obtained. However, the 1st discharge delivers less capacity than the 1st charge, implying some Li was consumed in the 1st cycle, probably by interfacial reactions.^{193,194} This irreversibility was not observed after the 1st cycle (Figure V.9). An overpotential of $\sim 400 \text{ mV}$ could be observed in the ASSB (Figure V.9).

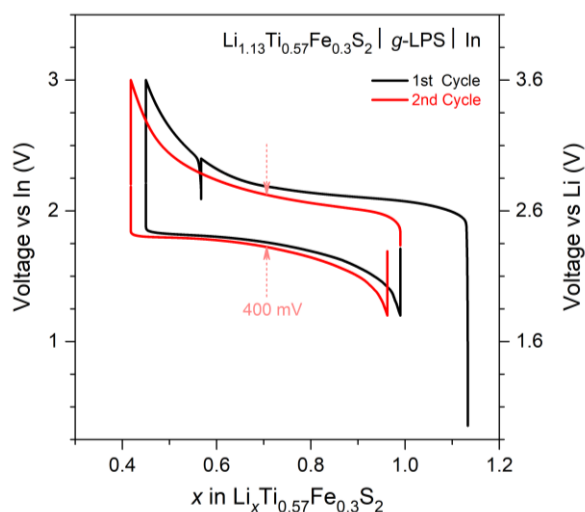


Figure V.9. Polarization in charge-discharge of $\text{Li}_{1.13}\text{Ti}_{0.57}\text{Fe}_{0.3}\text{S}_2 | \text{g-LPS} | \text{In}$ ASSB. The ASSB was cycled at $C/30$ rate. Note that in the first charge, the voltage drop at $x = \sim 0.5$ is due to a relaxation (at OCV) of 20 mins.

V.5.2 ASSB with β -Li₃PS₄ SE

Next we have replaced g-LPS by β -Li₃PS₄ (LPS) as solid electrolyte and used a cathode composite comprised of LTFS and LPS (in 70:30 wt%). The ASSB was then cycled between 1.8 - 3 V (courtesy of *Florenzia Marchini*) and the voltage profile is shown in Figure V.10. Cycling of the ASSB with higher voltage cut off (up to 4.2 V vs Li) can be found in the Appendix Figure A4.2. Using β -Li₃PS₄, more capacity could be obtained (discharge capacity $\sim 150 \text{ mAh}\cdot\text{g}^{-1}$). Interestingly, a polarization $\sim 200 \text{ mV}$ (in 2nd cycle) was observed, which is smaller than the value observed in the g-LPS ASSB (Figure V.9). This improvement became possible probably due to better interfacial compatibility or SEI formation with the β -Li₃PS₄ as solid electrolyte. Furthermore, we observed improvement of the overpotential at higher temperature, as a consequence of the increased ionic conductivity of the β -Li₃PS₄ SE at higher temperature.

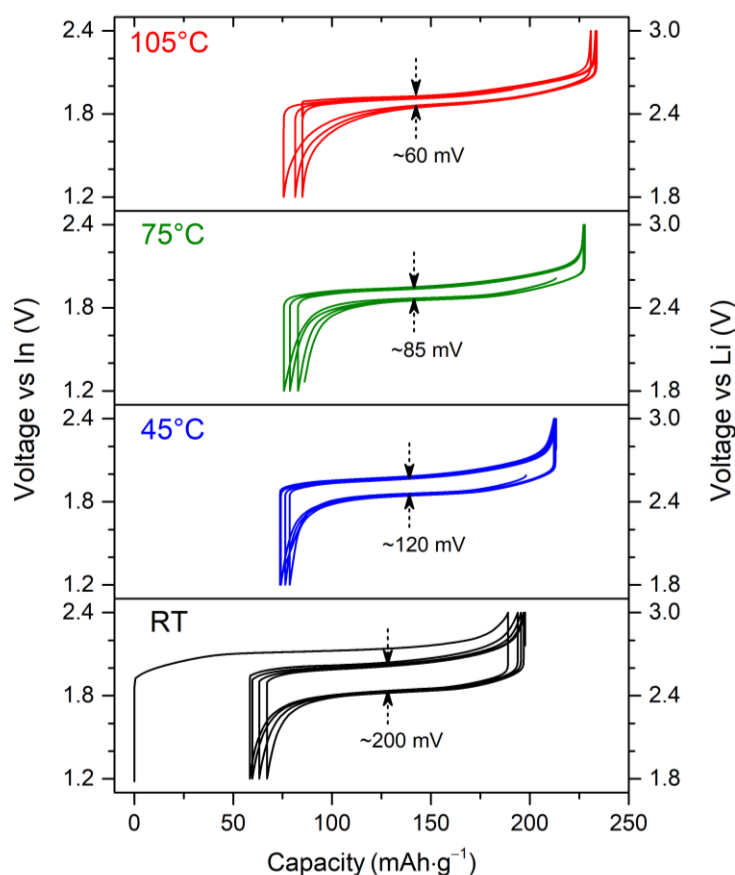


Figure V.10. Voltage profile of $\text{Li}_{1.13}\text{Ti}_{0.57}\text{Fe}_{0.3}\text{S}_2$ cycled in ASSB at RT using β -Li₃PS₄ as solid electrolyte. The temperatures of cycling are indicated on the plot. The temperature were increased in for the same cell, in subsequent cycles. In metal was used as anode. Cycling rate of C/30 was used. ASSB: courtesy of *Florenzia Marchini*.

V.5.3 EIS study of the ASSB

To further grasp insights into the interfacial compatibility in the ASSB, we collected *in situ* electrochemical impedance spectra (EIS) of the $\text{Li}_{1.13}\text{Ti}_{0.57}\text{Fe}_{0.3}\text{S}_2 \mid \text{g-LPS} \mid \text{In}$ cell at full-charged and full-discharged states. The EIS was recorded in two-electrode cell configuration, with 25 mV bias in the frequency range of 0.5 MHz - 1 Hz (Figure V.11a). All spectra consists a semicircle at high frequencies (HF, >14 kHz) and a very small, almost non-visible semicircle at mid frequency region (MF, 14 kHz - 100 Hz), followed by Warburg tail at low frequencies (LF, <100 Hz). Interestingly, slight increase was observed only until the 1st charge, whereas no significant increase of the impedance was observed 1st charge onwards.

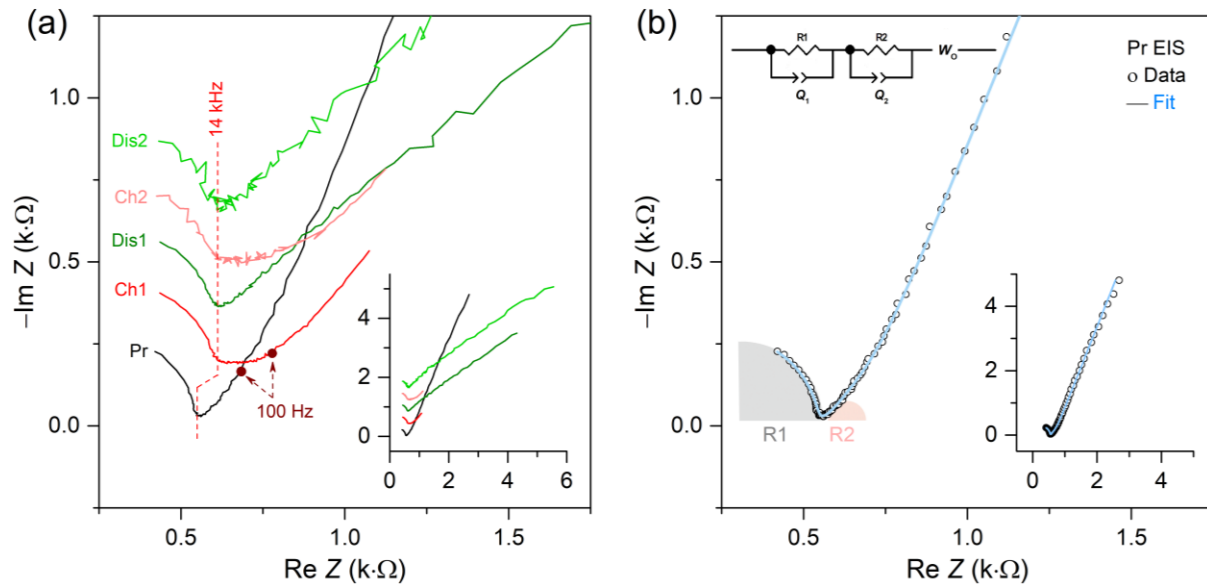


Figure V.11. EIS characterization of the $\text{Li}_{1.13}\text{Ti}_{0.57}\text{Fe}_{0.3}\text{S}_2 \mid \text{g-LPS} \mid \text{In}$ ASSB. (a) EIS spectra (enlarged) of the ASSB collected at various SoCs during the first two cycle. The abbreviations Pr, Ch, and Dis stands for pristine, full-charged, and full-discharged, respectively. Inset shows the whole spectra. (b) Fitting of the EIS for the pristine state. Inset shows the whole spectra. The equivalent circuit used for fitting is also shown in top left corner.

The EIS for the pristine state (before cycling) was fitted with an equivalent circuit model $(R_1//Q_1)(R_2//Q_2)W_0$, where R and Q represent the resistance and constant phase element, respectively, and W_0 is the Warburg resistance. The fitting is shown in Figure V.11b. The HF semicircle (R1) corresponds mainly to the total ionic conductivity of the solid electrolyte (R_{SE} , capacitance $C \approx 800$ pF). Importantly, the MF semicircle (R2), which comprises the interfaces between solid electrolyte and cathode ($R_{\text{SE-cathode}}$), is negligible (barely visible). Note that a well-separated semicircle (typically >200 Ω) was often reported when oxide cathode materials (LiCoO_2 , $\text{LiNi}_{0.8}\text{Mn}_{0.1}\text{Co}_{0.1}\text{O}_2$, etc.) were cycled with sulfide electrolytes.^{193,198} This finding suggests that sulfide based cathode $\text{Li}_{1.13}\text{Ti}_{0.57}\text{Fe}_{0.3}\text{S}_2$ forms stable interface with the $\text{Li}_2\text{S-P}_2\text{S}_5$ sulfide glass. This imply that no coating is necessary for the $\text{Li}_{1.13}\text{Ti}_{0.57}\text{Fe}_{0.3}\text{S}_2$, whereas expensive $\text{LiNb}_{0.5}\text{Ta}_{0.5}\text{O}_3$ or $\text{Li}_2\text{O-ZrO}_2$ coating is usually required for oxide

cathode materials (e.g., LiCoO_2 , $\text{LiNi}_{0.8}\text{Co}_{0.15}\text{Al}_{0.05}\text{O}_2$, etc.) to decrease the interfacial resistance (to $>40 \Omega$).^{193,200}

V.6 Chapter Conclusions

In summary, the sulfide-based $\text{Li}_{1.13}\text{Ti}_{0.57}\text{Fe}_{0.3}\text{S}_2$ (Li-rich sulfide) was successfully cycled in all-solid-state batteries and we found it is chemically/electrochemically compatible with the sulfide-based solid electrolytes. Moreover, its excellent electronic conductivity contributes positively to the cycling performance. However, we observed a large irreversibility in the 1st cycle which is probably originated from the Li-loss in SEI formation at the In-anode. To alleviate this Li-loss, further investigations are being pursued to cycle with Li anode. Lastly, through this study we showed sulfides could regain interest in ASSBs that use Li metal as negative electrode. Hence we are going back to the early time of Li-metal batteries, when sulfides were stellar. Whatever, whether sulfides can replace oxides as positive electrode in ASSBs remains to be proved.

Chapter VI

General Conclusions

In this thesis, two main axes were simultaneously pursued. The first one is related to the all-solid-state battery (ASSB) that are supposed to improve the safety and performance of Li-ion batteries. Over the last few years, ASSBs have emerged as a topic of intense research, and furthermore, with immense push from industries, especially EV makers. However, this task is indeed very challenging, and on the practical level, it still remains to be demonstrated. The second one has dealt with the anionic redox, which improves the energy density of cathode materials. Although anionic redox have equally been explored, from both application and fundamental point of view, numerous questions regarding its practicability remains to be addressed. This is what we have done in this thesis work was carried out and the findings are summarized below.

In the framework of the ASSBs, we first focused to develop new oxide-based solid electrolytes (SEs), and explored new phases in the $\text{Li}/(\text{Na})_2\text{O}-\text{ZnO}-\text{P}_2\text{O}_7$ phase diagram. We investigated the $\text{Li}_6\text{Zn}(\text{P}_2\text{O}_7)_2$ and $\text{Li}_4\text{Zn}(\text{PO}_4)_2/\text{Na}_4\text{Zn}(\text{PO}_4)_2$ phases, that undergo an order-disorder phase transition(s) with temperature. Much higher Li/Na conductivity (and lower activation energy) could be obtained for the high-temperature phases (HTPs) due to disorder. To correlate this increment, we solved the crystal structures by combination of SXRD and NPD studies, we found for the HTPs, the structural backbones consisting of $\text{P}_2\text{O}_7/\text{PO}_4$ groups remains invariant, whereas the mobile Li sublattice becomes disordered and cation-mixed (with Zn). Furthermore, the BVEL calculations for $\text{Li}_6\text{Zn}(\text{P}_2\text{O}_7)_2 / \text{Li}_4\text{Zn}(\text{PO}_4)_2$ indicate, that the conduction mechanism, which is 2-D in the ordered low-temperature phase (LTP) becomes 3-D in the HTP. Having characterized the phase and determined the conductivity transitions, a challenge was to stabilize the HTPs at RT.

We perused this question via hypervalent substitution. We have showed that the HTPs can be stabilized by partially substituting the Zn^{2+} by M^{3+} , thus creating ‘inherently’ disordered phases that are stable at RT. Such an effort was failed for $\text{Li}_6\text{Zn}(\text{P}_2\text{O}_7)_2$, however it was successful for $\text{Li}_4\text{Zn}(\text{PO}_4)_2/\text{Na}_4\text{Zn}(\text{PO}_4)_2$. The newly designed $\beta\text{-Li}_{4-x}\text{Zn}^{2+}_{1-x}\text{Ga}^{3+}_x(\text{PO}_4)_2$ and $\beta\text{-Na}_{4-x}\text{Zn}^{2+}_{1-x}\text{M}^{3+}_x(\text{PO}_4)_2$ ($\text{M} = \text{Ga}, \text{Al}$) phases are stable at RT while crystallizing with the HTP structure. Furthermore we showed that, by conventional ball-milling the disordered $\beta\text{-Li}_4\text{Zn}(\text{PO}_4)_2$ phase could be stabilized.

Such study can guide as a ‘model’ to design new efficient SEs, especially by extending to its sulfide-counterparts.³²⁸ However, despite such exploration of rich crystal chemistry and materials engineering, the ionic conductivities obtained ($< 10^{-10} \text{ S}\cdot\text{cm}^{-1}$) for these new phases at RT were too low to be implemented in functional all-solid-state batteries (ASSBs). Hence, we decided to use previously reported sulfide-based SEs, namely amorphous $\text{Li}_2\text{S}-\text{P}_2\text{S}_5$ glass and crystalline $\beta\text{-Li}_3\text{PS}_4$, for their sufficiently high Li-conductivities ($\sim 10^{-4} \text{ S}\cdot\text{cm}^{-1}$), and capability of RT processing, for practical ASSB fabrication. At this point, we took a different strategy to tackle the interfacial incompatibility of sulfide SEs with oxide cathode materials. Specifically, we decided to design Li-rich sulfide cathode materials with higher capacity, capitalizing the benefit of anionic redox.

We started with revisiting the well-known $\text{S}_2^{2-}/\text{S}^{2-}$ redox in ‘pseudo-layered’ TiS_3 . Interestingly, we identified a subtle discrepancy in the reported structural model (by Furuseth *et al*, 1975²⁵⁷) of TiS_3 . Our structural model supports its structure alike the ‘ ZrSe_3 -type variant’, where S atoms form ‘isosceles

triangles' around the Ti atoms, as was shown by Guilmeau *et al*, 2014.²⁵⁸ Whatever, TiS_3 shows a rapid capacity fading upon Li-(de)intercalation with large hysteresis, due to unsustainable structural rearrangement during S–S bond breaking/reformation.

Towards this end, we decided to design Li-rich layered sulfides that undergo sulfur redox without involving complete S–S dimerization. We have chosen Li_2TiS_3 for this purpose; however, was found to be nearly electrochemically inactive. To initiate the reversible redox activity we demonstrated the benefit of partial substitution with proper transition metal (TM). We showed that with $\text{TM} = \text{Fe}^{2+}$, we can initiate reversible redox activity. Along this line, we have synthesized the Li-rich layered $\text{Li}_{1.33-2y/3}\text{Ti}^{4+}_{0.67-y/3}\text{Fe}^{2+y}\text{S}_2$ family that shows reversible redox activity. We have isolated the composition $\text{Li}_{1.13}\text{Ti}_{0.57}\text{Fe}_{0.3}\text{S}_2$ ($y = 0.3$) that was shown to have a specific energy of $600 \text{ Wh}\cdot\text{kg}^{-1}$ (which compares favorably with LiCoO_2). Detailed charge-compensation mechanism was investigated indicating the presence of Fe^{3+} and S^{n-} ($n < 2$) in the fully-charged phase, thus demonstrating simultaneous cationic and anionic redox.

Next, inspired by this reversibility of the anionic $\text{S}^{2-}/\text{S}^{n-}$ ($n < 1$) redox, we have benchmarked the Li-rich sulfides against the Li-rich NMC oxides. The anionic $\text{O}^{2-}/\text{O}^{n-}$ ($n < 2$) redox has emerged as a new paradigm to design high-energy Li-rich oxide cathode materials (e.g., Li-rich NMC), however with several practical drawbacks, such as large voltage hysteresis, voltage fade, sluggish kinetics, etc. In contrarily, our Li-rich sulfide $\text{Li}_{1.13}\text{Ti}_{0.57}\text{Fe}_{0.3}\text{S}_2$ shows (i) a voltage hysteresis as low as $\sim 30 \text{ mV}$ under OCV condition, (ii) small voltage fade ($\sim 50 \text{ mV}$ in 60 cycles), along with fast electrochemical kinetics. Furthermore, we extended our study to $\text{Ti}^{3+}/\text{Co}^{2+}$ substituted Li_2TiS_3 and Na_2TiS_3 that also highlight the positive attributions of S-redox. However, we need to keep in mind that this comes with a price of energy density, because of lower voltage in sulfides. The best compromise would consists in designing oxysulfides-based Li-rich cathode materials, which could be an attractive direction for future.^{329–334}

Having designed the Li-rich sulfides, we proceed to assemble full ASSB using $\text{Li}_{1.13}\text{Ti}_{0.57}\text{Fe}_{0.3}\text{S}_2$ as positive electrode. We assembled the $\text{Li}_{1.13}\text{Ti}_{0.57}\text{Fe}_{0.3}\text{S}_2 \mid \text{SE} \mid$ In ASSBs, with glassy $\text{Li}_2\text{S-P}_2\text{S}_5$ and $\beta\text{-Li}_3\text{PS}_4$ as SEs, that demonstrate excellent cyclability. Such performance could be attributed to the high electronic conductivity ($>10^{-2} \text{ S}\cdot\text{cm}^{-1}$) of $\text{Li}_{1.13}\text{Ti}_{0.57}\text{Fe}_{0.3}\text{S}_2$ and its small interfacial resistance. Thus, use of Li-rich sulfide based cathode materials could be beneficial to tackle that interfacial challenge and low electrochemical stability window of sulfide SEs in ASSBs. Will sulfide replace the oxides remains an open question. Interfaces are obviously more friendly with sulfides, but their use could be hindered because of their moisture-sensitivity and unwanted H_2S gas release.

Appendix

A1 Supporting Information for Chapter II

A1.1 Methods

Material Synthesis. $\text{Li}_6\text{Zn}(\text{P}_2\text{O}_7)_2$ sample was prepared by following classical solid state synthesis. Li_2CO_3 (Sigma Aldrich, 99%), ZnO (Sigma Aldrich, 99%), and $\text{NH}_4\text{H}_2\text{PO}_4$ (Alfa Aesar, 98%) were used as precursors. Required amounts of precursors were mixed homogeneously by ball-milling for 20 mins with stainless-steel balls in a stainless-steel vial using SPEX-8000M mixer-miller and pressed into a pellet subsequently. The pellet was heated on an alumina boat for 36 hours at 700 °C in air after a ramp of 3 °C/min, followed by quenching in air. The pellet was grinded again and pelletized, followed by subsequent annealing at 300 °C for 12 hours in air to obtain the pure $\alpha\text{-Li}_6\text{Zn}(\text{P}_2\text{O}_7)_2$ of the compound.

To prepare samples of $\text{Li}_4\text{Zn}(\text{PO}_4)_2$ and $\text{Li}_4\text{Zn}_{1-x}\text{Ga}_x(\text{PO}_4)_2$ stoichiometric amounts of Li_2CO_3 , ZnO , $\text{NH}_4\text{H}_2\text{PO}_4$ and Ga_2O_3 (Alfa Aesar, 99.99%) were used as precursors.

Na_2CO_3 (Sigma Aldrich, 99.95%), ZnO , $\text{NH}_4\text{H}_2\text{PO}_4$, and Al_2O_3 (Sigma Aldrich, 99%)/ Ga_2O_3 / In_2O_3 (Sigma Aldrich, 99.99%), were used as precursors to prepare samples of $\text{Na}_4\text{Zn}(\text{PO}_4)_2$ and $\text{Na}_4\text{Zn}_{1-x}\text{M}_x(\text{PO}_4)_2$ (M= Al, Ga, and In).

In case of $\text{Li}_4\text{Zn}_{1-x}\text{Ga}_x(\text{PO}_4)_2$, different pellets were heated in alumina boats for 36 hours at 800 °C after a ramp of 1 °C/min, followed by quenching in air. For $\text{Na}_4\text{Zn}(\text{PO}_4)_2$ and $\text{Na}_4\text{Zn}_{1-x}\text{M}_x(\text{PO}_4)_2$ (M= Al, Ga, and In), pellets were heated in alumina boats for 24 hours at 700 °C after a ramp of 1 °C/min, followed by quenching or cooling slowly (1 °C/min) to room- temperature (RT), as indicated in the chapter.

For the high-energy ball-milling synthesis of the $\beta\text{-Li}_4\text{Zn}(\text{PO}_4)_2$, the as-prepared α -phase of the samples was continuously milled for 2 hrs using balls-to-powder weight ratio of 40.

Structural Characterizations. Powder X-ray diffraction (XRD) patterns were recorded in Bragg–Brentano geometry using a Bruker D8 Advance diffractometer equipped with a $\text{Cu K}\alpha$ X-ray source ($\lambda_1 = 1.54056 \text{ \AA}$, $\lambda_2 = 1.54439 \text{ \AA}$) and a LynxEye detector. Evolution of XRD patterns of the samples with temperature were monitored *in situ* in the same diffractometer equipped with an Anton Paar HTK 1200N furnace to control the temperature. A ramping rate of 2 °C/min was applied.

Complementary synchrotron X-ray powder diffraction (SXRD) and neutron powder diffraction (NPD) data were also obtained for more accurate characterization. Temperature-driven structural transitions were monitored *in situ* in the MSPD beamline at the ALBA synchrotron beamline (Barcelona, Spain) equipped with a hot-air blower to control the temperature. All SXRD data were collected in transmission mode with $\lambda = 0.4948 \text{ \AA}$, placing the powder in a sealed quartz capillary with a diameter of 0.5 mm and a ramping rate of 5 °C/min was applied for the temperature-driven experiment.

In addition, some SXRD patterns at RT were also collected at the 11-BM beamline of the Advanced Photon Source (APS), Argonne National Laboratory, in transmission mode with $\lambda = 0.4127$ Å, with the powder sealed in a kapton capillary of 0.7 mm diameter. Complementary high-resolution NPD patterns were collected with the HRPT instrument at SINQ-PSI (Villigen, Switzerland). The sample powder was placed in a vanadium container of 8 mm diameter to record the NPD patterns in transmission mode with a neutron wavelength of 1.494 Å.

All patterns were refined using the Rietveld method,²⁰⁸ or by Le Bail fitting³³⁵, as implemented in the FullProf program³³⁶.

All crystal structures in this thesis are drawn using the program VESTA^{337,338}.

DSC measurements. Differential scanning calorimetry (DSC) measurements were done in air using a STA 449C Netzsch apparatus at a rate of 10 °C/min or at a rate mentioned otherwise.

TEM studies. The samples for selected area electron diffraction (SAED) were prepared by depositing the sample onto holey carbon grids by drop-casting a sample-ethanol suspension. Electron diffraction patterns were collected with a FEI Tecnai G2 electron microscope operated at 200 kV.

Bond Valence Energy Landscape maps (BVEL) Analysis. Bond Valence Energy Landscape maps (BVEL) were generated according to the method developed by Adams,³³⁹ using the program BondSTR as implemented in the FullProf Suite³³⁶.

The ‘bond valence modeling’ is a simple theoretical tool, which gives a necessary first approximation for the mechanism of lithium diffusion pathways.³⁴⁰ Generally, ion transport from one Li equilibrium site to the other one follows a pathway, along which the valence mismatch $\Delta V = |V - V_{\text{nom}}|$ between the bond valence V and the nominal valence V_{nom} remains as small as possible. Following Pauling’s rule (1929), the total bond valence sum V of cation M^+ can be expressed as,

$$V = \sum_X S_{M^+-X}$$

Here the individual bond valences S_{M^+-X} are calculated using the bond lengths R_{M^+-X} between cation M^+ and the adjacent anions X :

$$S_{M^+-X} = \exp\left(\frac{R_0 - R_{M^+-X}}{b}\right)$$

The bond valence parameters R_0 and b are deduced from a large number of crystalline compounds containing the same $M^+ - X$ pairs, but having different coordination number and bond length distributions. In all these different compounds, a monovalent cation M^+ should have a bond

valence sum (BVS) close to $V_{\text{ideal}} = 1$. Hence for crystalline compounds, the process of the ion M^+ transport from one equilibrium site to another should follow the channel which requires the lowest valence mismatch $\Delta V = |V - V_{\text{nom}}|$, which in turn corresponds to the energetically most favored pathway. Thus in principle, the activation energy E_a should be directly related to ΔV . However, this model based on valence V still does not include all interactions other than the $M^+ - X$ interaction. Hence, in 2011, Adams *et al* proposed BV-based force-field approach by introducing the interaction energies. In this method, the Li ions are assumed to move within a framework composed of immobile anions and other cations. Thus, the interaction between a dummy Li ion in the space and the ions surrounding it are empirically evaluated by the summation of the attraction between Li^+ and anions described by Morse-type potential and the repulsion between Li^+ and cations expressed by Coulombic potential follows,

$$E(\text{Li})_{\text{Morse}} = D_0 [\{\exp [\alpha(R_{\text{min}} - R)] - 1\}^2 - 1]$$

$$E(\text{Li} - A)_{\text{Coulomb}} = \frac{q_{\text{Li}} \cdot q_A}{R_{\text{Li}-A}} \operatorname{erfc} \left(\frac{R_{\text{Li}-A}}{\rho_{\text{Li}-A}} \right)$$

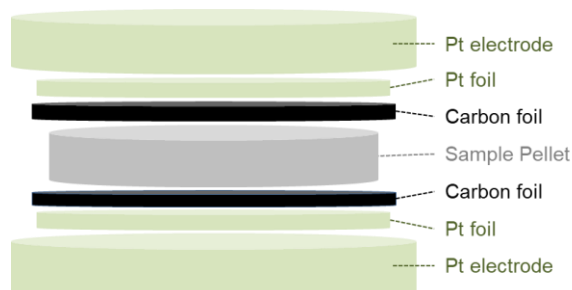
Where D_0 , α , and R_{min} are Morse potentials determine from large amount of stable compounds, q and R refer to the charge and Li-A distance respectively. The summation of above two terms on grids of points with a small resolution (e.g., a unit cell divided into 100s smaller subcell) builds the maps of the total potential energy $E(\text{Li})$ of the unit cell. The region enclosed by the isosurfaces of constant $E(\text{Li})$ are considered as the space where Li^+ can move through and the threshold value of $E(\text{Li})$ to form a continuous pathway is estimated as the Li^+ migration energy barrier.

However the $E(\text{Li})$ does not necessarily give the real E_a of a compound, as in real systems lot of other complex interactions exist which this model cannot take into account. Hence, in this thesis, the percolation energy above the minimum, $E(\text{Li})$ obtained is only used qualitatively and the isosurfaces is used to predict possible Li conduction channel. For the BVEL maps, calculations of Li/Na conduction paths were done after the removal of pre-existing Li/Na in the unit cell and also after removing Zn and Ga ions located at mixed Li sites. Anionic neighbors up to 8 Å were considered.

Electrochemical Impedance Spectroscopy (EIS). EIS was used to determine the Li-ion conductivity of the samples. The AC impedance measurements were made using a Bio-Logic MTZ-35 impedance analyzer equipped with a HTF-1100 furnace. To perform the measurements, pellets of ~8 mm diameter and ~1.5 mm thickness were obtained by cold-pressing using a uniaxial pressure of ~5 bars in a hydraulic press and were densified by sintering at 600 °C for 6 hours following a heating rate of 1 °C/min and then quenched to RT and reannealed at 300°C to obtain the pure α - $\text{Li}_6\text{Zn}(\text{P}_2\text{O}_7)_2$ phase. In case of $\text{Li}_4\text{Zn}_{1-x}\text{Ga}_x(\text{PO}_4)_2$ and $\text{Na}_4\text{Zn}_{1-x}\text{M}_x(\text{PO}_4)_2$, pellets of ~8 mm diameter and ~1.5 mm thickness were obtained by cold-pressing using a uniaxial pressure of ~5 bars in a hydraulic press and were densified by sintering at 700 °C for 6 hours while heated and cooled at a rate of 1 °C/min. In exceptional case of low-temperature sintering, that was applied to the pellet of ball-milled β - $\text{Li}_4\text{Zn}(\text{PO}_4)_2$ or γ - $\text{Na}_4\text{Zn}(\text{PO}_4)_2$, pellets were sintered at 200 °C for 4 days. The sintered pellet was found to have a density

of ~75 – 80 % with respect to the crystallographic densities; hence, our reported conductivity values were not corrected by the pellet porosities.

The AC impedance measurements were performed using platinum (Pt) blocking electrodes, by applying a sinusoidal signal of 500 mV amplitude over a frequency range of 10 MHz to 1 Hz. A thin foil of carbon was placed between the Pt electrode and the pellet in order to improve the electrode contact, as shown as in Appendix Figure A1.1.

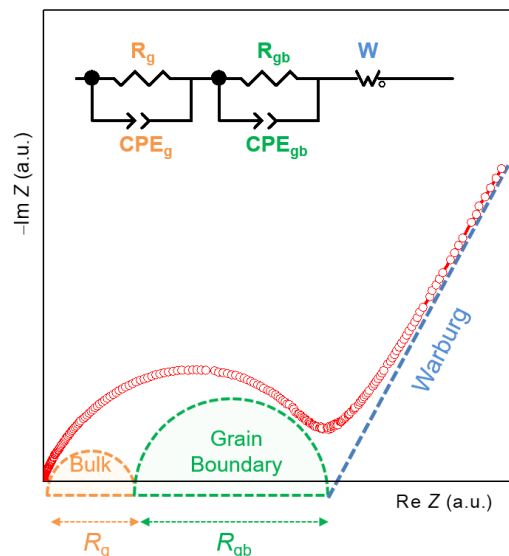


Appendix Figure A1.1. Schematics of the AC impedance measurement procedure.

The measurements were carried out in the temperature range of 50 - 650 °C (or mentioned otherwise) with an accuracy of ± 1 °C and were soaked for 15 mins at each measurement temperature prior triggering each sweep of frequency dependent impedance measurement at the temperature.

Analysis of EIS. The Appendix Figure A1.2 shows a typical Nyquist impedance plot of a sintered pellet. Each spectra recorded shows a depressed semicircle at high frequencies followed by a Warburg spike at lower frequency region. The low frequency spike represents the impedance response due to the blocking of mobile Li ions at the electrode interface with Pt blocking electrode and it confirms that the ac conductivity is ionic in nature. The total ionic conductivity (σ_{tot}) can be obtained from the value of intercept of the extrapolated low frequency spike with the real axis. However, we have explored the impedance spectra further by examining the semicircle at high frequency, which is too depressed to be accounted by the inhomogeneities of the sample-electrode interfaces and hence needs to deconvolute to different contributions. The impedance response of polycrystalline materials are expected to be composed of contributions from grains and grain boundaries (see Appendix Figure A1.2). Hence, we decoupled the spectra by fitting the complex impedance plot to an equivalent circuit model $(R_g CPE_g)(R_{gb} CPE_{gb})W_O$, where R and CPE represent the resistance and constant phase element (CPE) associated with the grains (g) or grain boundaries (gb) of the sample respectively and W_O is the Warburg resistance. The contributions were assigned to either bulk/grains (σ_g) or grain boundaries (σ_{gb}) based on their associated capacitances (C), calculated according to the following formulae³⁴¹,

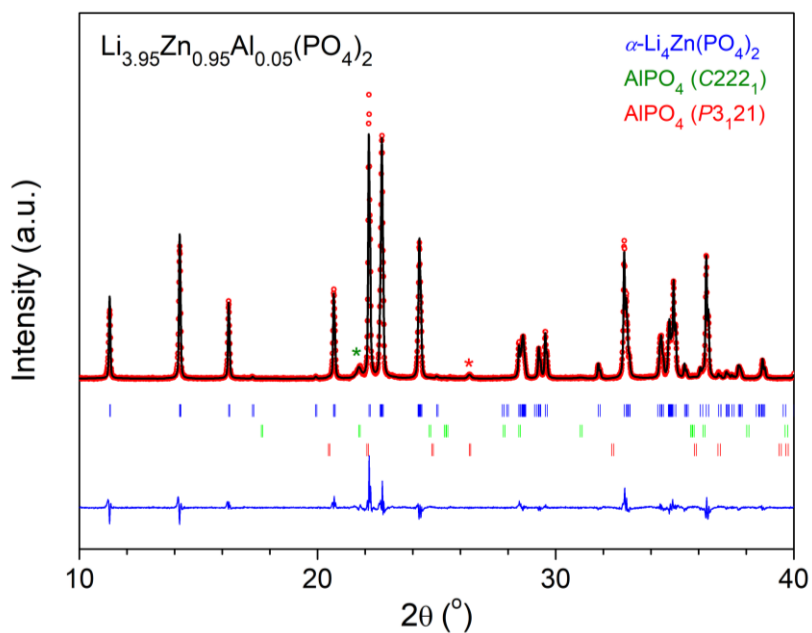
$$C = R^{\frac{1-n}{n}} \cdot Q^{\frac{1}{n}}$$



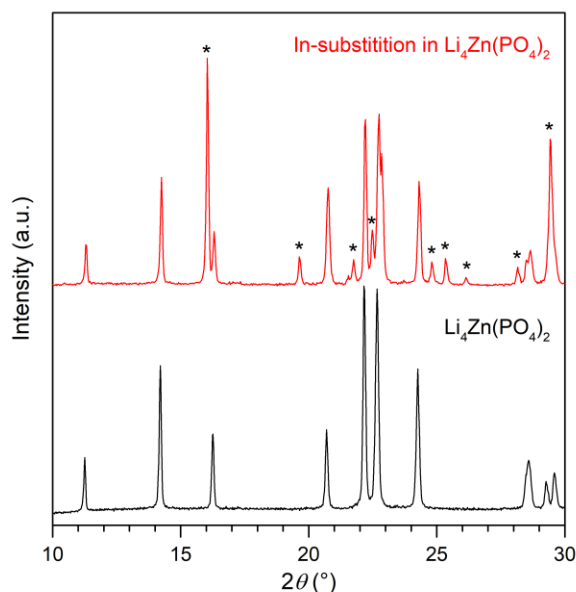
Appendix Figure A1.2. Typical Nyquist impedance plot of a sintered pellet and its interpretation. For visualization, the contributions from bulk (grain), grain boundary and Warburg resistances are shown by dashed semicircles or line. Inset shows the equivalent circuit that was used to fit the Nyquist plot.

Here Q is the pre-factor of the CPE, and n its exponent. Typically, the capacitances were calculated to be $\sim 10^{-12} - 10^{-11}$ F for grains or $\sim 10^{-11} - 10^{-10}$ F for grain boundaries.^{216,342} This assignment was confirmed by calculating the relaxation frequency (f_r) which generally appears at the apex of the deconvoluted arcs and is always higher for grains response than that of the grain boundaries.^{216,342} The conductivities were calculated from the resistances according to the formulae, $\sigma = (d/A) \cdot (1/R)$, where d and A are the thickness and the area of the pellet measured, respectively.

A1.2 Supporting Figures

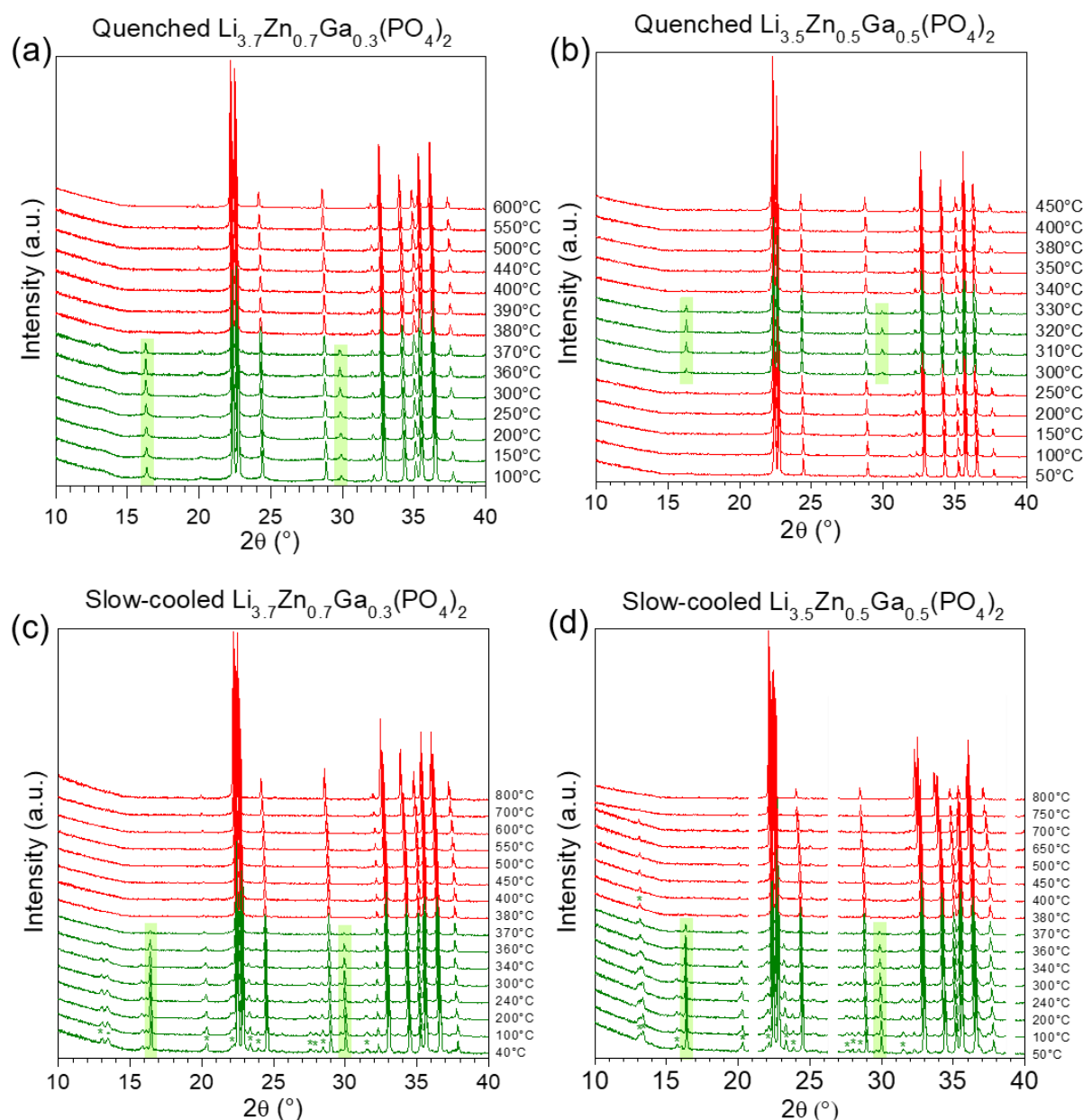


Appendix Figure A1.3. Rietveld refinement of the as-synthesized sample when a nominal composition of Li_{3.95}Zn_{0.95}Al_{0.05}(PO₄)₂ was tried to synthesize. As evident, the sample consists a mixture of α -Li₄Zn(PO₄)₂ and AlPO₄. The red circles, black continuous line, and blue line represent the observed, calculated, and difference patterns, respectively. The blue, green and red tick bars indicates the Bragg positions of α -Li₄Zn(PO₄)₂, AlPO₄ (space group C222₁) and AlPO₄ (space group P3₁21).

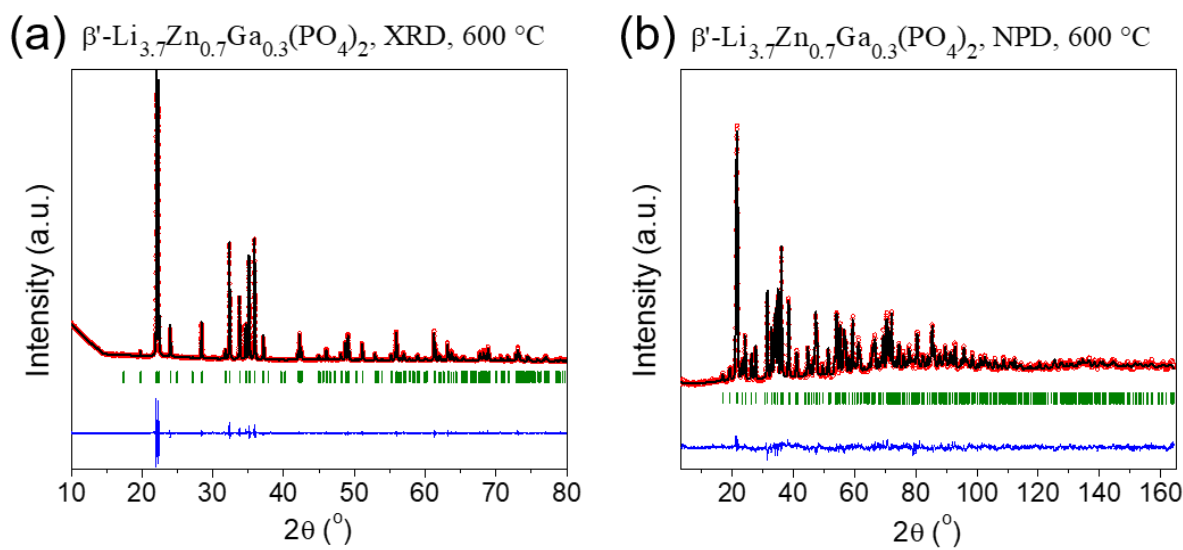


Appendix Figure A1.4. XRD pattern of as-synthesized sample when a nominal composition of Li_{4-x}Zn_{1-x}In_x(PO₄)₂ with $x_{\text{In}} = 0.3$ was tried to synthesize. The unidentified impurity phases are

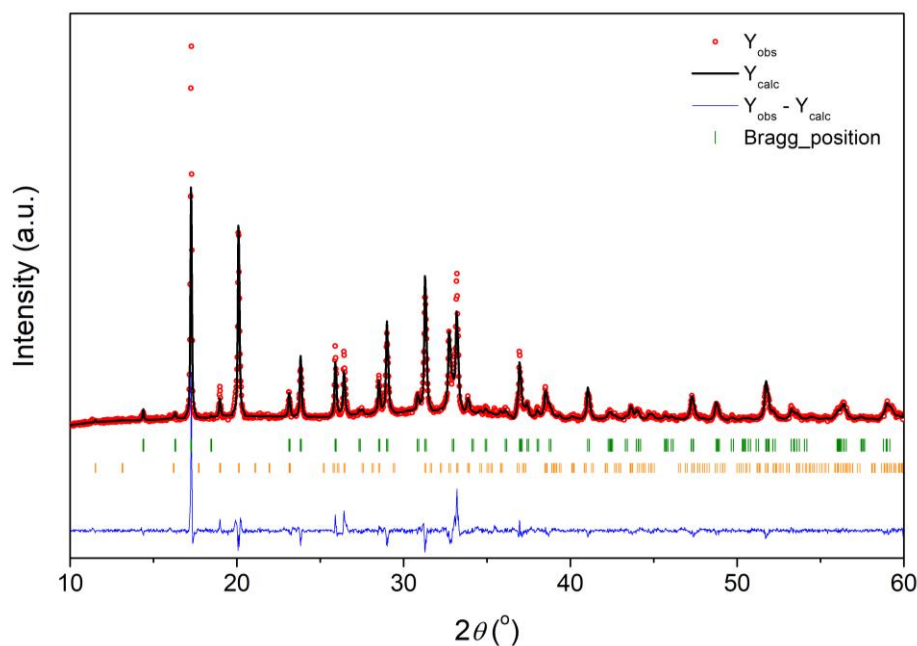
indicated by *. Note that similar impurity peaks were also observed when $x_{\text{In}} = 0.1$ was tried to synthesize.



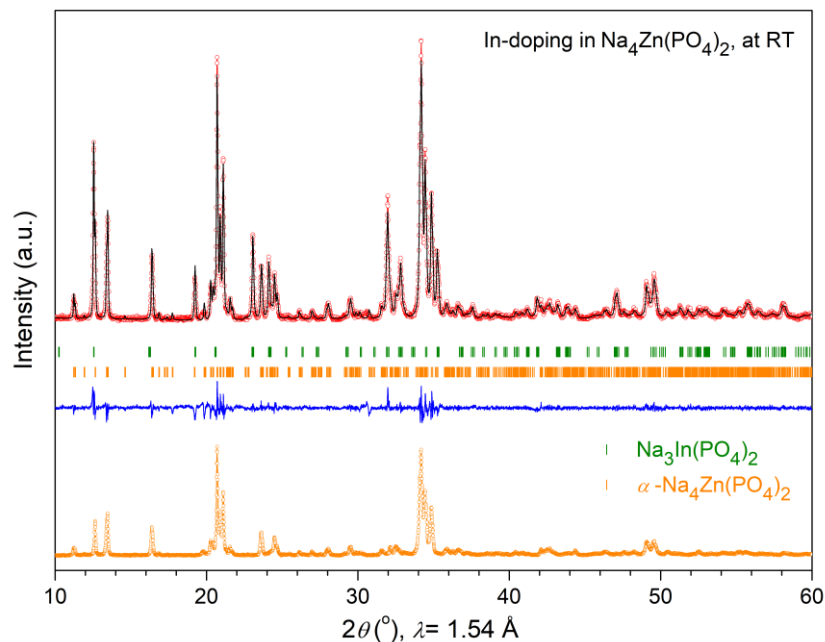
Appendix Figure A1.5. Evolution of XRD patterns of Ga-substituted samples with temperature. (a) quenched $\text{Li}_{3.7}\text{Zn}_{0.7}\text{Ga}_{0.3}(\text{PO}_4)_2$, (b) quenched $\text{Li}_{3.5}\text{Zn}_{0.5}\text{Ga}_{0.5}(\text{PO}_4)_2$, (c) slow-cooled $\text{Li}_{3.7}\text{Zn}_{0.7}\text{Ga}_{0.3}(\text{PO}_4)_2$ and (d) slow-cooled $\text{Li}_{3.5}\text{Zn}_{0.5}\text{Ga}_{0.5}(\text{PO}_4)_2$. The patterns colored in green and red corresponds to the β' - and β - polymorphs, respectively, and the peaks that disappear for the β - phase has been indicated by green backgrounds. The samples was found to transform into the β - phase at 380 °C, as witnessed by the disappearance of the (011) and (013) peaks, except the quenched β - $\text{Li}_{3.5}\text{Zn}_{0.5}\text{Ga}_{0.5}(\text{PO}_4)_2$, upon heating it transforms to the β' structure at 300 °C before transforming back to β at 340°C. Note that the slow-cooled phases contain some additional superstructure peaks (indicated by *).



Appendix Figure A1.6. Rietveld refinement of the XRD (a), and NPD (b) patterns of β' - $\text{Li}_{3.7}\text{Zn}_{0.7}\text{Ga}_{0.3}(\text{PO}_4)_2$ at 600 °C. The red circles, black continuous line, blue line and green tick bars represent the observed, calculated, and difference patterns, and Bragg positions, respectively.

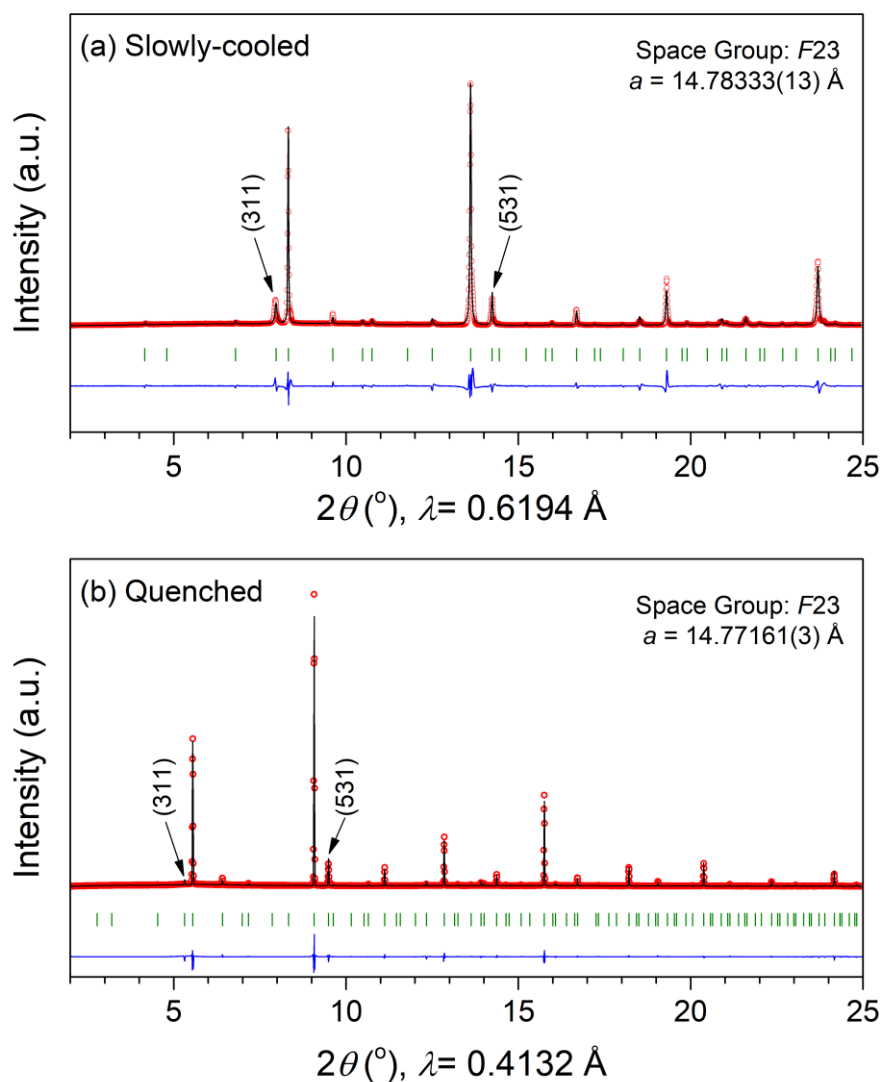


Appendix Figure A1.7. Rietveld refinement of the XRD pattern of the as-synthesized end-product when a nominal composition of $\text{Na}_6\text{Zn}(\text{P}_2\text{O}_7)_2$ was targeted to synthesize. A two-phase refinement was performed against the structural model of $\text{Na}_2\text{Zn}_2(\text{P}_2\text{O}_7)_2$ (green tick bars) and $\text{Na}_4(\text{P}_2\text{O}_7)_2$ (orange tick bars). The end product always found to a mixture of $\text{Na}_2\text{Zn}_2(\text{P}_2\text{O}_7)_2$ (47 weight%) and $\text{Na}_4(\text{P}_2\text{O}_7)_2$ (53 weight%). The end product always found to a mixture of $\text{Na}_2\text{Zn}_2(\text{P}_2\text{O}_7)_2$ (47 weight%) and $\text{Na}_4(\text{P}_2\text{O}_7)_2$ (53 weight%). The red circles, black continuous line, blue line and green/orange tick bars represent the observed, calculated, and difference patterns, and Bragg positions, respectively. Note that, the phase $\text{Na}_6\text{Zn}(\text{P}_2\text{O}_7)_2$ was never reported in literature.

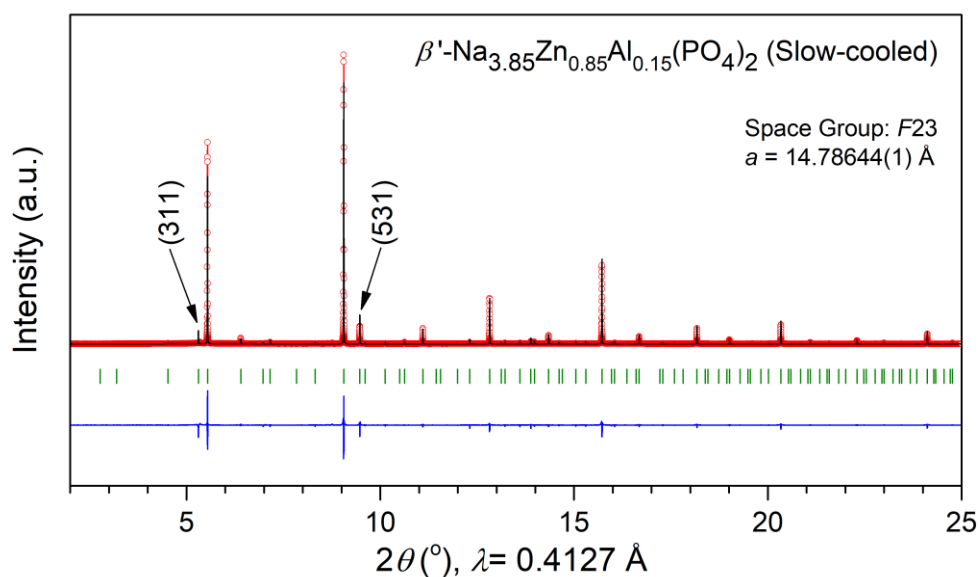


Appendix Figure A1.8. The Rietveld refinement of the XRD pattern (red circles) of the as-synthesized product (slow-cooled) when a nominal composition of $\text{Na}_{3.85}\text{Zn}_{0.85}\text{In}_{0.15}(\text{PO}_4)_2$ was tried to synthesize. The black, and blue lines, and tick bars represent the calculated, and difference patterns, and Bragg positions, respectively. For the $\alpha\text{-Na}_4\text{Zn}(\text{PO}_4)_2$, Le Bail refinement was performed. For reference, the XRD pattern of the $\alpha\text{-Na}_4\text{Zn}(\text{PO}_4)_2$ is also included (orange pattern).

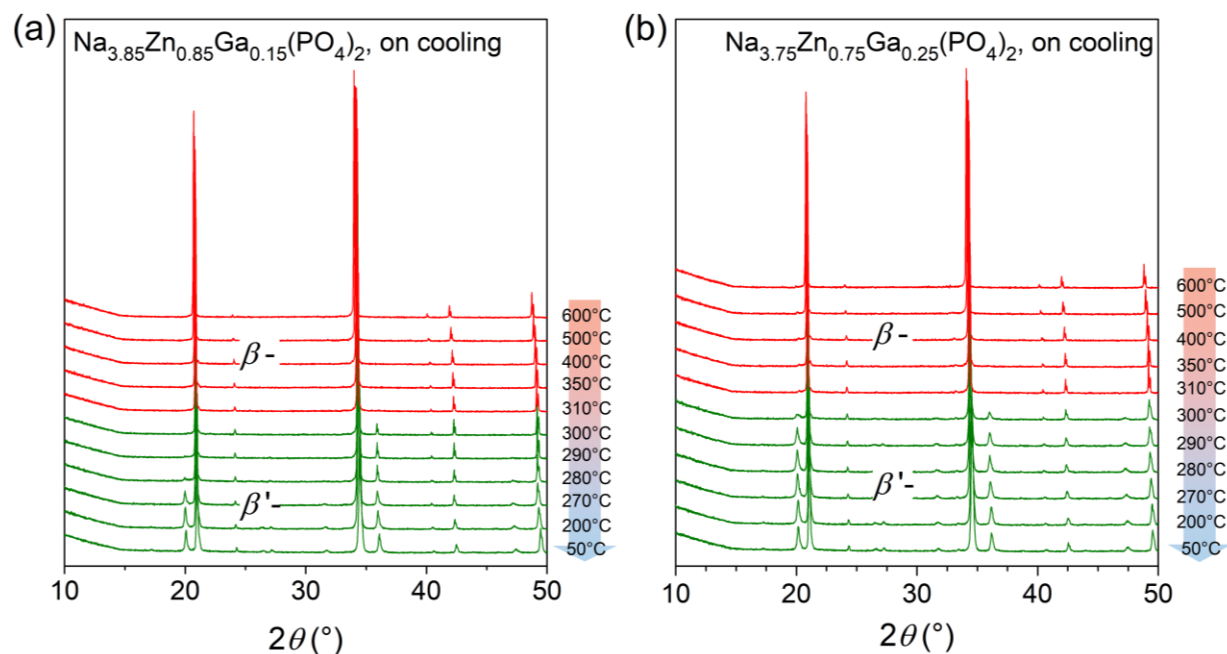
SXRD of β - $\text{Na}_{3.85}\text{Zn}_{0.85}\text{Ga}_{0.15}(\text{PO}_4)_2$, at RT



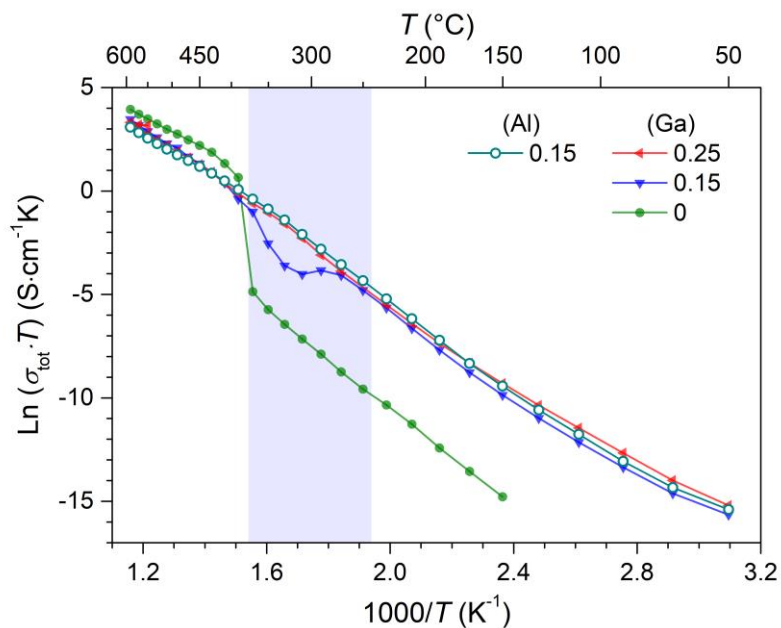
Appendix Figure A1.9. Le Bail refinement of the SXRD patterns of the β - $\text{Na}_{3.85}\text{Zn}_{0.85}\text{Ga}_{0.15}(\text{PO}_4)_2$, $x_{\text{Ga}} = 0.15$ sample synthesized by cooling slowly (a), and quenching (b). Some characteristic peaks for the β -phase are indicated on the figure. The black, and blue lines, and tick bars represent the calculated, and difference patterns, and Bragg positions, respectively.



Appendix Figure A1.10. Le Bail refinement of the SXRD patterns of the β - $\text{Na}_{3.85}\text{Zn}_{0.85}\text{Al}_{0.15}(\text{PO}_4)_2$, $x_{\text{Al}} = 0.15$ sample synthesized by cooling slowly. The black, and blue lines, and tick bars represent the calculated, and difference patterns, and Bragg positions, respectively.



Appendix Figure A1.11. Evolution of XRD patterns of as-synthesized $\text{Na}_{4-x}\text{Zn}_{1-x}\text{Ga}_x(\text{PO}_4)_2$ samples (prepared by slow-cooling) with temperature upon cooling, for $x_{\text{Ga}} = 0.15$ (a), and $x_{\text{Ga}} = 0.25$ (b). The corresponding temperatures are indicated at the right side of the XRD patterns.



Appendix Figure A1.12. Arrhenius plot of total ionic conductivity of the $\text{Na}_{4-x}\text{Zn}_{1-x}\text{M}_x(\text{PO}_4)_2$ samples synthesized by slow cooling. The values of x for $\text{M} = \text{Ga}$, and Al , are indicated in the legends (by filled, and hollow symbols, respectively).

A1.3 Supporting Tables

Appendix Table A1.1. Structural Parameters for $\alpha\text{-Li}_6\text{Zn}(\text{P}_2\text{O}_7)_2$, deduced from the Rietveld refinement of the NPD. Isotropic temperature factors (B_{iso}) were constraint to be equal for a same chemical species.^a

$\alpha\text{-Li}_6\text{Zn}(\text{P}_2\text{O}_7)_2$, at RT							
space group: $C 2/c$							
$a = 25.66942(10) \text{ \AA}$, $b = 10.25856(4) \text{ \AA}$, $c = 9.10213(3) \text{ \AA}$, $\beta = 104.7074(3)^\circ$							
$V = 2313.0(1) \text{ \AA}^3$, $Z = 8$							
atom	site	x	y	z	$B_{\text{iso}} (\text{\AA}^2)$	occ.	BVS
Zn	8f	0.18337(9)	0.4266(2)	0.4387(3)	2.05(5)	1	1.842(19)
P1	8f	0.19763(18)	0.3036(4)	0.1283(5)	0.27(3)	1	5.159(61)
O11	8f	0.2545(3)	0.2542(6)	0.2282(8)	0.72(3)	1	2.194(32)
O12	8f	0.2116(3)	0.4081(7)	0.0320(8)	0.72(3)	1	2.114(37)
O13	8f	0.1695(3)	0.1884(7)	0.0445(8)	0.72(3)	1	2.073(37)
O14	8f	0.1631(3)	0.3638(7)	0.2255(9)	0.72(3)	1	1.946(37)
P2	8f	0.44386(16)	0.0784(4)	0.1524(5)	0.27(3)	1	5.193(60)
O21	8f	0.4518(3)	0.1461(6)	0.0168(8)	0.72(3)	1	2.031(40)

O22	4e	0	0.5179(10)	0.25	0.72(3)	1	2.023(21)
O23	8f	0.0880(3)	0.4567(7)	0.3883(8)	0.72(3)	1	2.039(36)
O24	8f	0.4226(3)	0.1672(7)	0.2580(9)	0.72(3)	1	1.866(39)
P3	8f	0.29985(19)	0.3226(4)	0.3533(5)	0.27(3)	1	5.092(61)
O31	8f	0.2264(3)	0.1016(7)	0.5410(8)	0.72(3)	1	1.786(36)
O32	8f	0.3360(3)	0.2117(7)	0.4367(8)	0.72(3)	1	1.932(31)
O33	8f	0.3316(3)	0.4037(8)	0.2727(7)	0.72(3)	1	2.207(43)
P4	8f	0.05528(16)	0.0818(4)	0.3449(5)	0.27(3)	1	4.926(56)
O41	8f	0.0778(3)	0.1437(7)	0.2223(8)	0.72(3)	1	2.101(41)
O42	8f	0.0393(3)	0.1768(7)	0.4525(8)	0.72(3)	1	2.017(42)
O43	8f	0.4151(3)	0.4620(7)	0.0791(8)	0.72(3)	1	1.933(35)
O44	4e	0	0.0128(9)	0.25	0.72(3)	1	1.961(21)
Li1	8f	0.0281(7)	0.1790(16)	0.0191(19)	-0.15(12)	1	1.009(29)
Li2	8f	0.0831(7)	0.3376(16)	0.1998(19)	-0.15(12)	1	0.907(23)
Li3	8f	0.5831(7)	0.1760(18)	0.0368(18)	-0.15(12)	1	1.065(28)
Li4	8f	0.3730(7)	0.5606(17)	0.3677(19)	-0.15(12)	1	1.062(28)
Li5	8f	0.3835(7)	0.3229(17)	0.1719(19)	-0.15(12)	1	0.987(26)
Li6	8f	0.2049(6)	0.0607(17)	-0.0635(19)	-0.15(12)	1	0.988(24)

^a The relatively large B_{iso} for Zn (2.05 \AA^2), while the B_{iso} for the Li atoms (refined with the constraint that they are all equal) are slightly negative (-0.15 \AA^2). As Li^+ and Zn^{2+} are similar in size, this could indicate a possible mixing between those atoms. Preliminary refinements using Li/Zn mixing indicate that this possible mixing would involve less than 2% of Zn on the Li sites. However, due to the complexity of the structure with six independent Li sites, we did not push further this quantification.

Appendix Table A1.2. Structural Parameters for $\zeta\text{-Li}_6\text{Zn}(\text{P}_2\text{O}_7)_2$, deduced from the Rietveld refinement of the NPD recorded at 600 °C. Isotropic temperature factors (B_{iso}) were constraint to be equal for a same chemical species.

$\zeta\text{-Li}_6\text{Zn}(\text{P}_2\text{O}_7)_2$, at 600 °C							
space group: $C 2/c$							
$a = 13.24574(6) \text{ \AA}$, $b = 5.19764(2) \text{ \AA}$, $c = 8.92388(4) \text{ \AA}$, $\beta = 105.1842(4)^\circ$							
$V = 592.8(2) \text{ \AA}^3$, $Z = 2$							
atom	site	x	y	z	$B_{\text{iso}} (\text{\AA}^2)$	occ.	BVS
P	8f	0.3921(2)	0.6545(5)	0.1418(4)	2.10(5)	1	5.241(55)
O1	8f	0.3385(5)	0.3970(14)	0.0868(8)	4.44(10)	1	1.833(30)
O2	4e	0.5	0.5538(14)	0.25	4.44(10)	1	2.155(14)

O3	8f	0.4115(5)	0.8063(13)	0.0136(8)	4.44(10)	1	2.064(35)
O4	8f	0.3381(6)	0.7934(13)	0.2446(9)	4.44(10)	1	2.290(41)
Li1/Zn1	8f	0.0969(6)	0.3587(18)	0.0311(11)	9.3(4)	0.852(3)/ 0.148(3)	0.964(17)/ 1.834(33)
Li2/Zn2	8f	0.2277(12)	0.652(4)	0.3082(16)	17.2(8)	0.898(3)/ 0.102(3)	0.843(27)/ 1.706(51)

Appendix Table A1.3. Structural Parameters for α -Li₄Zn(PO₄)₂, deduced from the Rietveld refinement of the NPD at RT. Isotropic temperature factors (B_{iso}) were constraint to be equal for a same chemical species.

α -Li ₄ Zn(PO ₄) ₂ , RT							
Space group $P 2_1/c$							
$a = 8.11990(16) \text{ \AA}$, $b = 10.24192(13) \text{ \AA}$, $c = 8.10549(15) \text{ \AA}$, $\beta = 104.8589(9)^\circ$							
$V = 651.538(2) \text{ \AA}^3$, $Z = 4$							
atom	site	x	y	z	B_{iso}	Occ.	
Zn1	4e	0.5938(8)	0.1567(7)	0.0933(8)	0.72(9)	1	
P1	4e	0.2125(6)	0.4079(4)	0.4726(7)	0.30(4)	1	
P2	4e	0.2706(7)	0.5916(4)	0.0353(7)	0.30(4)	1	
O1	4e	0.1628(7)	0.1505(6)	0.1313(6)	0.535(17)	1	
O2	4e	0.0620(7)	0.3992(4)	0.3115(7)	0.535(17)	1	
O3	4e	0.3614(6)	0.3328(6)	0.4378(6)	0.535(17)	1	
O4	4e	0.2518(6)	0.5549(4)	0.5046(6)	0.535(17)	1	
O5	4e	0.1230(6)	0.6536(6)	0.0888(7)	0.535(17)	1	
O6	4e	0.5688(6)	0.1017(4)	0.3127(7)	0.535(17)	1	
O7	4e	0.6926(6)	0.3308(6)	0.1152(6)	0.535(17)	1	
O8	4e	0.2249(6)	0.0465(4)	0.4769(6)	0.535(17)	1	
Li1	4e	0.3484(20)	0.1466(17)	0.341(2)	0.39(10)	1	
Li2	4e	0.1164(19)	0.3395(18)	0.1121(19)	0.39(10)	1	
Li3	4e	0.0203(19)	0.0738(9)	0.269(2)	0.39(10)	1	
Li4	4e	0.150(2)	0.8355(16)	0.157(2)	0.39(10)	1	

Appendix Table A1.4. Structural Parameters for β -Li₄Zn(PO₄)₂, deduced from the combined Rietveld refinement of the XRD and NPD recorded at 600 °C. Isotropic temperature factors (B_{iso}) were constraint to be equal for a same chemical species.

β -Li ₄ Zn(PO ₄) ₂ , high temperature form						
Space group $Pnm\bar{a}$						
$a = 10.2974(4) \text{ \AA}$, $b = 6.5021(3) \text{ \AA}$, $c = 5.0011(2) \text{ \AA}$,						
$V = 334.85(2) \text{ \AA}^3$, $Z = 2$						
atom	site	x	y	z	B_{iso}	Occ.
P1	4c	0.40840(15)	3/4	0.8105(3)	1.87(7)	1
O1	8d	0.3415(2)	0.5553(3)	0.7009(5)	2.77(7)	1
O2	4c	0.5522(2)	3/4	0.7330(6)	2.55(9)	1
O4	4c	0.6039(3)	1/4	0.8808(5)	2.63(9)	1
Li1/Zn1	8d	0.1546(2)	0.4995(3)	0.8074(4)	3.10(8)	0.75/0.25
Li3	4c	0.9207(17)	1/4	0.780(4)	4.45(8)	0.5

Appendix Table A1.5. Structural Parameters for β' -Li_{3.7}Zn_{0.7}Ga_{0.3}(PO₄)₂ deduced from the combined Rietveld refinement of the XRD and NPD patterns recorded at RT.

β' -Li _{3.7} Zn _{0.7} Ga _{0.3} (PO ₄) ₂ , RT						
Space group $P2_12_12_1$						
$a = 4.9391(2) \text{ \AA}$, $b = 6.4803(3) \text{ \AA}$, $c = 10.1468(5) \text{ \AA}$,						
$V = 324.77(3) \text{ \AA}^3$, $Z = 2$						
atom	site	x	y	z	B_{iso}	Occupancy
P	4a	0.1879(4)	0.0077(6)	0.3419(2)	0.92(5)	1
O1	4a	0.3045(11)	0.1887(7)	0.4158(4)	1.23(3)	1
O2	4a	0.2705(6)	0.0131(8)	0.1959(2)	1.23(3)	1
O3	4a	0.7091(11)	0.2999(8)	0.0953(4)	1.23(3)	1
O4	4a	0.1229(5)	0.4896(8)	0.1434(3)	1.23(3)	1
Li1/Ga1	4a	0.1826(15)	0.246(16)	0.5784(5)	0.97(8)	0.85/0.15
Li2/Zn2	4a	0.3092(8)	0.2531(9)	0.1032(3)	0.97(8)	0.65/0.35
Li3	4a	0.231(6)	0.532(6)	0.822(3)	2.1(7)	0.35

Appendix Table A1.6. Structural Parameters for β -Li_{3.7}Zn_{0.7}Ga_{0.3}(PO₄)₂ deduced from the combined Rietveld refinement of the XRD and NPD patterns recorded at 600 °C.

β -Li _{3.7} Zn _{0.7} Ga _{0.3} (PO ₄) ₂ , 600 °C						
Space group: <i>Pnma</i>						
$a = 10.20903(3) \text{ \AA}$, $b = 6.57170(2) \text{ \AA}$, $c = 4.996639(16) \text{ \AA}$,						
$V = 333.66(6) \text{ \AA}^3$, $Z = 2$						
atom	site	x	y	z	B_{iso}	Occupancy
P1	4c	0.40749(13)	0.75	0.8135(3)	2.01(6)	1
O1	8d	0.34021(19)	0.5588(2)	0.6975(4)	2.99(5)	1
O2	4c	0.5519(2)	0.75	0.7386(5)	2.99(5)	1
O4	4c	0.6100(2)	0.25	0.8821(4)	2.99(5)	1
Li1/Zn1/Ga1	8d	0.15404(19)	0.5003(2)	0.8062(4)	3.34(8)	0.750/0.175/0.075
Li3	4c	0.922(3)	0.25	0.781(6)	7.4(9)	0.35

Appendix Table A1.7. Structural Parameters for β -Li_{3.5}Zn_{0.5}Ga_{0.5}(PO₄)₂ deduced from the combined Rietveld refinement of the XRD and NPD patterns recorded at RT.

β -Li _{3.5} Zn _{0.5} Ga _{0.5} (PO ₄) ₂ , RT						
Space group <i>Pnma</i>						
$a = 10.08925(3) \text{ \AA}$, $b = 6.51080(2) \text{ \AA}$, $c = 4.935878(15) \text{ \AA}$,						
$V = 324.162(0.054) \text{ \AA}^3$, $Z = 2$						
atom	site	x	y	z	B_{iso}	Occupancy
P1	4c	0.40726(18)	0.75	0.8106(4)	1.16(7)	1
O1	8d	0.3384(3)	0.5511(3)	0.6966(5)	1.89(5)	1
O2	4c	0.5531(3)	0.75	0.7319(7)	1.89(5)	1
O4	4c	0.6072(3)	0.25	0.8766(6)	1.89(5)	1
Li1/Zn1/Ga1	8d	0.1589(2)	0.5013(3)	0.8123(4)	1.37(8)	0.75/0.125/0.125
Li3	4c	0.940(3)	0.25	0.900(7)	1.37(8)	0.5

Appendix Table A1.8. Structural Parameters for the γ -Na₄Zn(PO₄)₂, deduced from the Rietveld refinement of the SXRD Pattern.

γ -Na ₄ Zn(PO ₄) ₂ , at 500 °C						
Space group: $Fm\bar{3}m$						
$a = 7.46901(4) \text{ \AA}$, $V = 416.667(4) \text{ \AA}^3$						
atom	site	x	y	z	Occ.	$B_{\text{iso}} (\text{\AA}^2)$
P	4a	0	0	0	1	4.63(8)
O1	96k	-0.0646(5)	-0.0646(5)	0.1802(7)	0.167	5.9(3)
Na1/Zn1	8c	0.25	0.25	0.25	0.75/0.25	6.52(9)
Na2	4b	0.5	0.5	0.5	0.5	7.8(3)

Appendix Table A1.9. Structural Parameters for the β -Na₄Zn(PO₄)₂, deduced from the combined Rietveld refinement of the SXRD and NPD patterns.^a

β -Na ₄ Zn(PO ₄) ₂ , at RT						
Space group: $F23$						
$a = 14.786037(10) \text{ \AA}$, $V = 3232.626(4) \text{ \AA}^3$ (from SXRD)						
$a = 14.77614(14) \text{ \AA}$, $V = 3226.136(1) \text{ \AA}^3$ (from NPD)						
atom	site	x	y	z	Occ.	$B_{\text{iso}} (\text{\AA}^2)$
P1	4a	0	0	0	1	2.00(2)
P2	24g	0.25	0.25	-0.0011(3)	1	2.00(2)
P3	4b	0.5	0.5	0.5	1	2.00(2)
Na1/Zn1	16e	0.1255(2)	0.1255(2)	0.1255(2)	0.75/0.25	3.35(3)
Na2/Zn2	16e	0.3723(3)	0.3723(3)	0.3723(3)	0.75/0.25	3.35(3)
Na3/Zn3	16e	0.3731(3)	0.3731(3)	0.8731(3)	0.75/0.25	3.35(3)
Na4/Zn4	16e	0.1264(2)	0.1264(2)	0.6264(2)	0.75/0.25	3.35(3)
Na5	4d	0.25	0.25	0.75	0.5	2.92(7)
Na6	4c	0.25	0.25	0.25	0.5	2.92(7)
Na7	24f	0.2548(15)	0	0	0.5	2.92(7)
O1	48h	0.0043(14)	0.0468(11)	0.9099(6)	0.333	6.7(3)

O2	48h	0.3352(3)	0.2508(6)	-0.0557(4)	1	5.798(5)
O3	48h	0.7548(8)	0.3316(4)	0.9453(5)	1	11.924(7)
O4	48h	0.0942(3)	0.9742(11)	0.5307(10)	0.333	3.1(3)

^aIsotropic temperature factors (B_{iso}) were constrained to be equal for the chemical species in same sites.

A2 Supporting information for Chapter III

A2.1 Methods

Synthesis. $\text{Li}_{1.33-2y/3}\text{Ti}_{0.67-y/3}\text{Fe}_y\text{S}_2$ samples were prepared by solid-state reaction of stoichiometric amounts of Li_2S (Alfa Aesar, 99.9%), TiS_2 (Sigma Aldrich, 99.9%) and FeS (Alfa Aesar, 99%). Homogeneously mixed and hand-grinded precursor powders were filled in quartz tubes in an Ar-filled glovebox followed by sealing the tubes under vacuum ($\sim 10^{-5}$ mbar). The sealed tubes were subsequently annealed at 750 °C for 36 h followed by quenching in water. TiS_3 , was prepared similarly, by reacting TiS_2 and elemental S (15 wt% extra), in a vacuum sealed quartz tube at 550 °C, followed by cooling slowly.

The $\text{Li}_{1.2}\text{Ti}_{0.8}\text{S}_2$ ($\text{Li}_{1.33-y/3}\text{Ti}_{0.67-2y/3}\text{Ti}^{3+}_y\text{S}_2$ with $y = 0.4$) was synthesized similarly, by controlling the stoichiometry and by reacting stoichiometric amount of Li_2S , and TiS_2 in a vacuum-sealed quartz tube at 750 °C.

Nominal compositions of $\text{Li}_{1.33-2y/3}\text{Ti}_{0.67-y/3}\text{Co}^{2+}_y\text{S}_2$, with $y = 0.2$, and 0.3, were prepared by reacting Li_2S , TiS_2 and CoS (Alfa Aesar, 99.5%).

The Na_2TiS_3 was prepared by prepared via solid-state synthesis, by reacting Na_2S (Sigma Aldrich), and TiS_2 in stoichiometric amounts in vacuum-sealed quartz tubes at 750 °C for 36 h, followed by either cooling to RT at 1 °C/min (for O3 phase) or quenching in water (for P2 phase).

The as-prepared samples were collected inside a glovebox and hand-grinded prior to further use. In the whole process, air contact was avoided and subsequent processing was done in an Ar-filled glovebox.

Structural Characterizations. Synchrotron X-ray powder diffraction (SXRD) patterns were collected at the 11-BM beamline of the Advanced Photon Source (APS), Argonne National Laboratory. All SXRD data were collected in transmission mode with $\lambda = 0.4127$ Å, with the powder sealed in a quartz capillary of 0.7 mm diameter. *Operando* X-ray powder diffraction (XRD) was performed in an airtight electrochemical cell equipped with a Be window. XRD patterns were recorded in reflection

mode in Bragg–Brentano geometry using a Bruker D8 Advance diffractometer equipped with a Cu-K α X-ray source ($\lambda_1 = 1.54056 \text{ \AA}$, $\lambda_2 = 1.54439 \text{ \AA}$) and a LynxEye detector.

High-resolution neutron diffraction was performed for the TiS₃ sample on the D1B powder diffractometer (Institut Laue-Langevin) with a wavelength $\lambda = 1.286 \text{ \AA}$. The neutron diffraction of the Li_{1.13}Ti_{0.57}Fe_{0.3}S₂ sample was performed on the HRPT instrument at SINQ-PSI (Villigen, Switzerland) with a wavelength $\lambda = 1.494 \text{ \AA}$. In both instances, the sample powders were placed in a vanadium container of 8 mm diameter to record the NPD patterns in transmission mode.

The refinements of the XRD or NPD patterns were done using the Rietveld method²⁰⁸ as implemented in the FullProf program³³⁶. For some cases, Le Bail refinement was also performed³³⁵ in the FullProf program. All crystal structures are drawn using the program VESTA^{337,338}.

Electrochemical characterizations. All samples were cycled in galvanostatic mode in Li half-cells assembled in Swagelok-type cells. The cathode materials were mixed with 20 wt% conductive carbon Super-P by hand-grinding for 5 min in an agate mortar and pestle prior to cycling. LP30 (1M LiPF₆ in ethylene carbonate/dimethyl carbonate in 1:1 weight ratio) was used as the electrolyte and was soaked in a Whatman GF/D borosilicate glass fiber membrane that was used as separator. Typical loadings of 10 mg·cm⁻² of active materials were used and metallic Li was used as the negative electrode. The cells were assembled in an Ar-filled glovebox and were cycled at a C/20 rate between 1.8 V and 3 V if not specified otherwise. To check whether Li-vacancy exists in the pristine samples, fresh cells or all compositions were cycled starting with discharge. The cells showed negligible Li-intercalation in those discharges, thus confirming the absence of Li-vacancies.

The electrochemical performances of the Na₂TiS₃ (mixed and hand-ground with 20 wt% Csp) were tested in Na-half cells, where 1 M NaPF₆ in PC was used as electrolyte.

Charged/discharged samples from the Swagelok cells were recovered for *ex situ* characterizations by disassembling the cells inside glovebox, rinsed thoroughly with anhydrous DMC and dried under vacuum.

Mössbauer spectroscopy. Room-temperature ⁵⁷Fe Mössbauer spectra were recorded in transmission geometry in the constant acceleration mode and with a ⁵⁷Co(Rh) source with a nominal activity of 370 MBq. The velocity scale ($\pm 4 \text{ mms}^{-1}$) was calibrated at RT with α -Fe foil. The *in situ* cell was prepared with 32 mg·cm⁻² of active material mixed with 8 mg of carbon black. The hyperfine parameters IS (isomer shift) and QS (quadrupole splitting) were determined by fitting Lorentzian lines to the experimental data. The isomer shifts values are calculated with respect to that of α -Fe standard at RT.

The whole Mössbauer dataset was analyzed using a chemometric approach including Principal component Analysis (PCA) followed by Multivariate Curve Resolution - Alternate Least Squares

(MCR-ALS) approach.^{343–345} PCA is a tool, which extracts the maximum amount of useful information from a large data set by considering each spectrum as a vector in a multidimensional space. The “principal components” are the independent (orthogonal) vectors necessary to describe the whole set of spectra, but these components are only orthogonal mathematic functions, not real Mössbauer spectra. The MCR-ALS method is then needed to reconstruct the real components. The fitting was then performed on these reconstructed spectral components with least square conventional Mössbauer methods. Details on this fitting approach can be found in the *Reference*³⁴⁶.

TEM studies. The sample was prepared in an Ar-filled glove box by crushing the crystals in a mortar in DMC and depositing drops of the suspension onto holey carbon grids. The samples were transported to the transmission electron microscope (TEM) column while completely avoiding contact with air. High angle annular dark field scanning transmission electron microscopy (HAADF-STEM) images and Energy loss spectra (EELS) spectra were obtained with a FEI Titan G3 electron microscope operated at 120 kV and equipped with a monochromator and a Gatan Enfium ER spectrometer. Energy resolution measured by full width at half maximum of the zero loss peak is 0.15 eV.

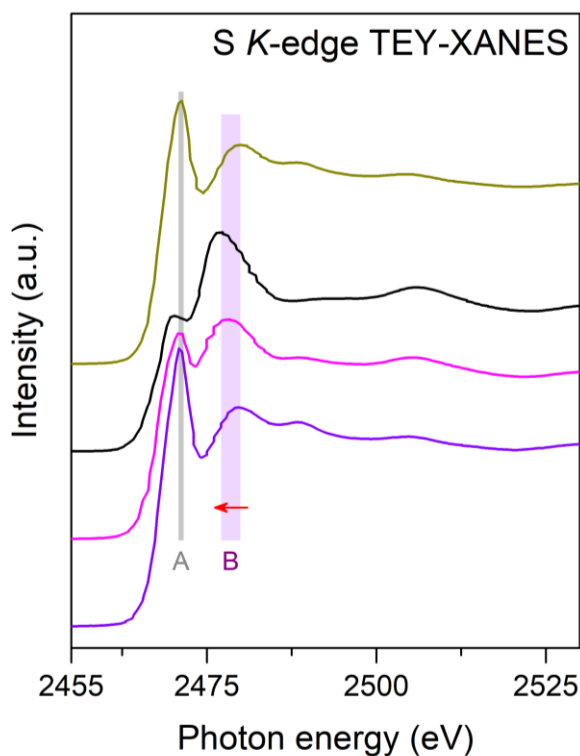
X-ray absorption spectroscopy (XAS). S K-edge, Fe L-edge and Ti L-edge X-ray absorption near edge spectroscopy (XANES) measurements were performed at 4-ID-C beamline of APS at Argonne National Laboratory. Spectra were recorded simultaneously under both the total electron yield (TEY) mode from the sample photocurrent at $\sim 10^{-9}$ Torr and total fluorescence yield (TFY) mode using a silicon drift diode detector at a spectral resolution of ~ 0.2 eV, with a 2 s dwell time. The energy scales of the spectra were calibrated with the references of Mo metal, Fe metal and SrTiO₃ measured simultaneously, for S, Fe and Ti edges, respectively.

sXAS and mRIXS. Soft X-ray absorption spectroscopy (sXAS) and mapping of resonant inelastic X-ray scattering (mRIXS) experiments were performed in the iRIXS endstation of beamline 8.0.1 at the Advanced Light Source (ALS) of Lawrence Berkeley National Laboratory.³⁴⁷ The pristine powder and cycled electrodes were mounted in high purity Ar glove box and transferred into the experimental vacuum chamber through a home-made kit to avoid any air exposure. The experimental energy resolution of sXAS is better than 0.1 eV without considering the intrinsic core hole broadening (~ 0.2 eV). The energy resolution along the emission energy in mRIXS is about 0.2 eV,³⁴⁷ which is sufficient for separating the intrinsic S-L signals from the strong C-K (2nd order) background that are different for about 10 eV. The X-ray exposure area on the samples were kept moving throughout the mRIXS experiments to avoid irradiation damage.

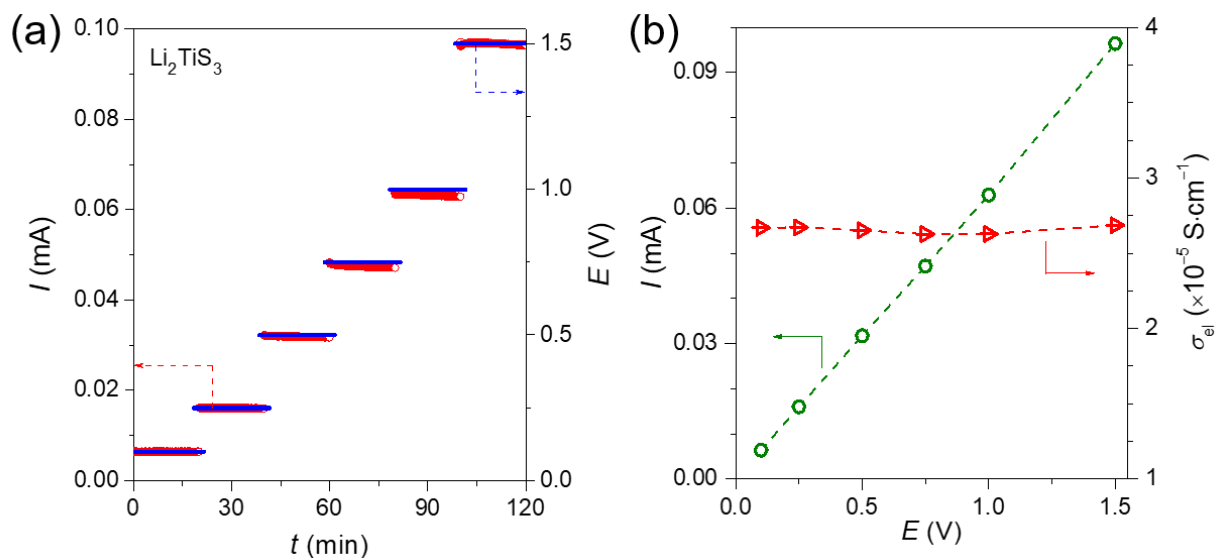
X-ray photoemission spectroscopy (XPS). XPS spectra were collected on a sample (analyzed area = $300 \times 700 \mu\text{m}^2$) with a Kratos Axis Ultra spectrometer, using focused monochromatic

Al K α radiation ($h\nu = 1.4866$ keV). The pressure in the analysis chamber was around 5×10^{-9} mbar. The binding energy scale was calibrated using the C 1s peak at 285.0 eV from the invariably present hydrocarbon contamination (for the pristine sample), and using the S $^{2-}$ position of the S 2p $_{3/2}$ at 160.7 eV for a better accuracy (for the other cycled samples). Peaks were recorded with constant pass energy of 20 eV. Core peaks were analyzed using a nonlinear Shirley-type background.³⁴⁸ The peak positions and areas were optimized by a weighted least-squares fitting method using 70 % Gaussian, 30 % Lorentzian line shapes. Quantification was performed on the basis of Scofield's relative sensitivity factors.³⁴⁹

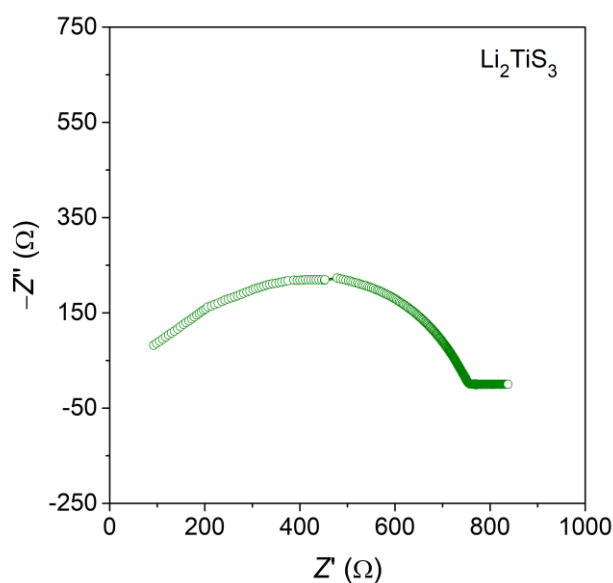
A2.2 Supporting Figures.



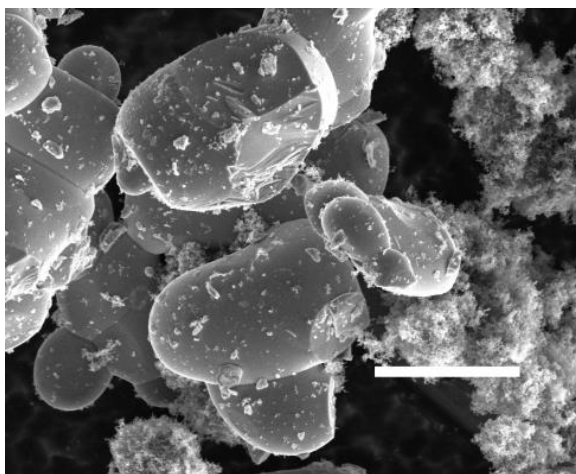
Appendix Figure A2.1. S K-edge TEY-XANES spectra collected for the *ex situ* TiS $_3$ samples. For color codes refer to Figure III.17. Note that the spectra are similar to the XANES collected in TFY mode.



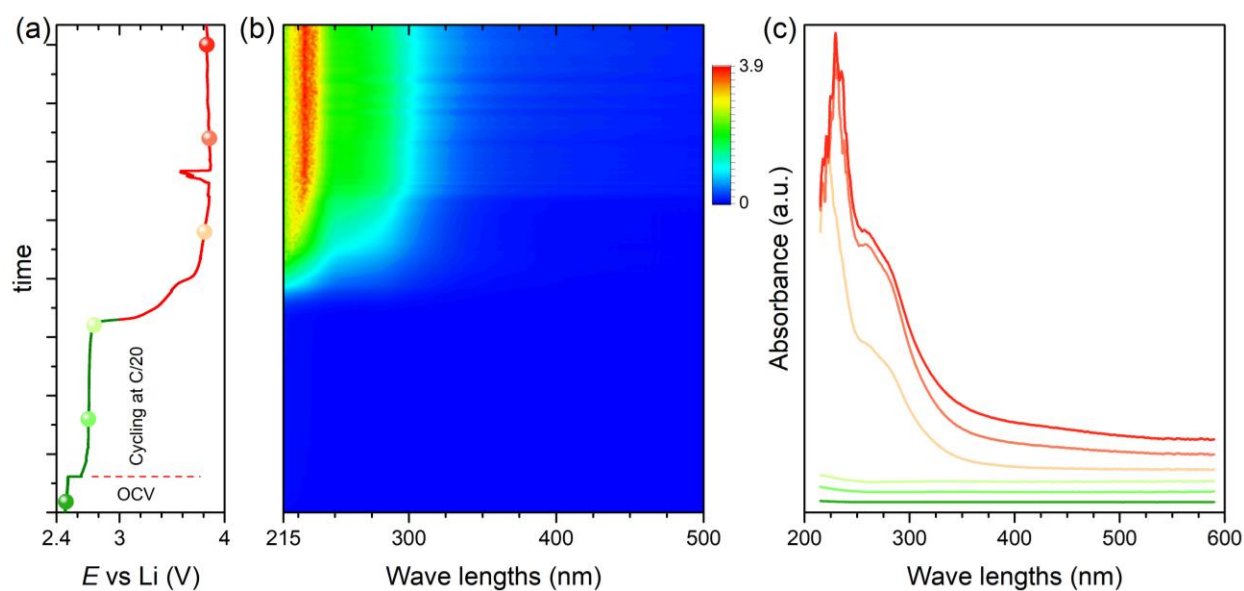
Appendix Figure A2.2. DC polarization plots of Li_2TiS_3 pellet. (a) The steady state current (I , in left axis) obtained by applying DC voltages (E , in right axis) to the sample pellet placed between two steel electrodes. (b) Variation of I with E , which was used to deduce the resistance (by Ohm's law). The electronic conductivity (in right axis) was calculated from the resistance, according to the formulae $\sigma = (d/A) \cdot (1/R)$. Indeed, the Li_2TiS_3 possess a good electronic conductivity of $\sim 2.7 \cdot 10^{-5} \text{ S}\cdot\text{cm}^{-1}$.



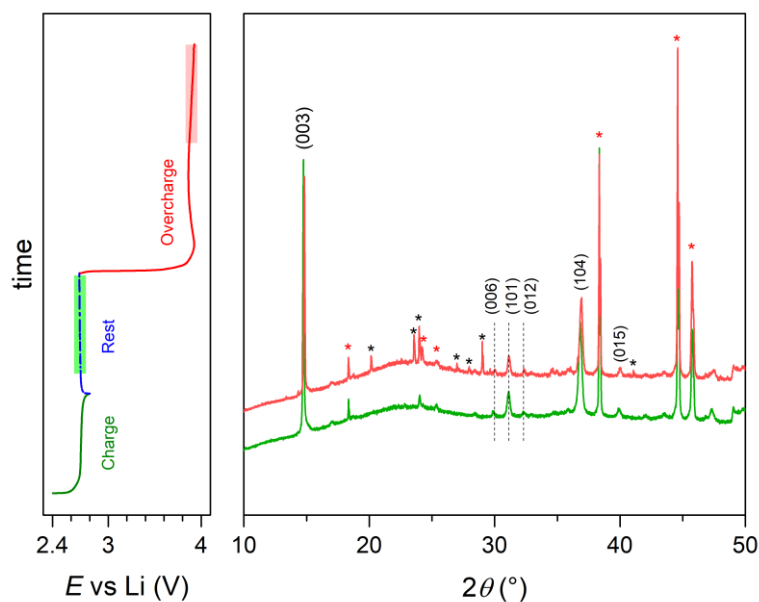
Appendix Figure A2.3. Nyquist EIS plot of Li_2TiS_3 pellet. The Li_2TiS_3 shows an ionic conductivity of $\sim 5.5 \cdot 10^{-4} \text{ S}\cdot\text{cm}^{-1}$. For the methods of the EIS acquisition and interpretation, see the Supporting information for Chapter 2.



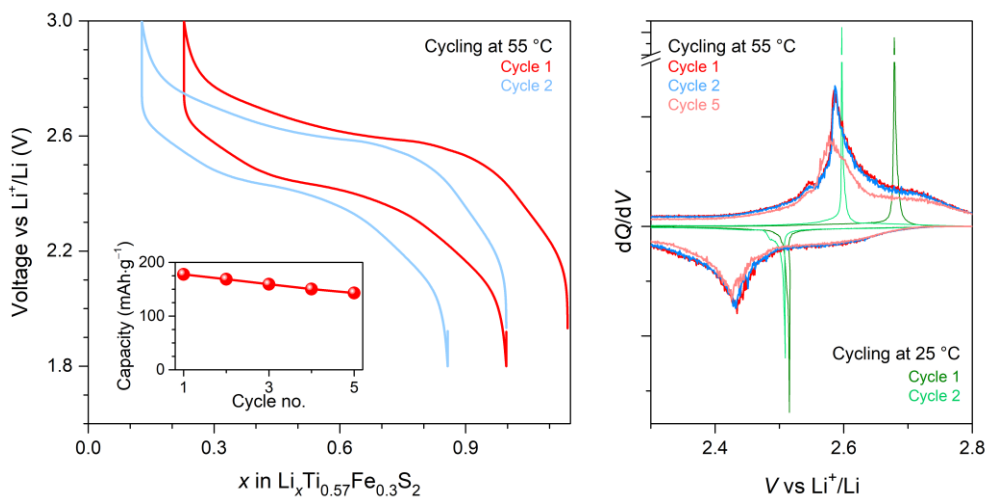
Appendix Figure A2.4. Scanning electron microscopy (SEM) image of $\text{Li}_{1.13}\text{Ti}_{0.57}\text{Fe}_{0.3}\text{S}_2$ (after hand-grinding with Csp). The whitish region corresponds to the amorphous Csp. Scale is indicated by the white bar (10 μm).



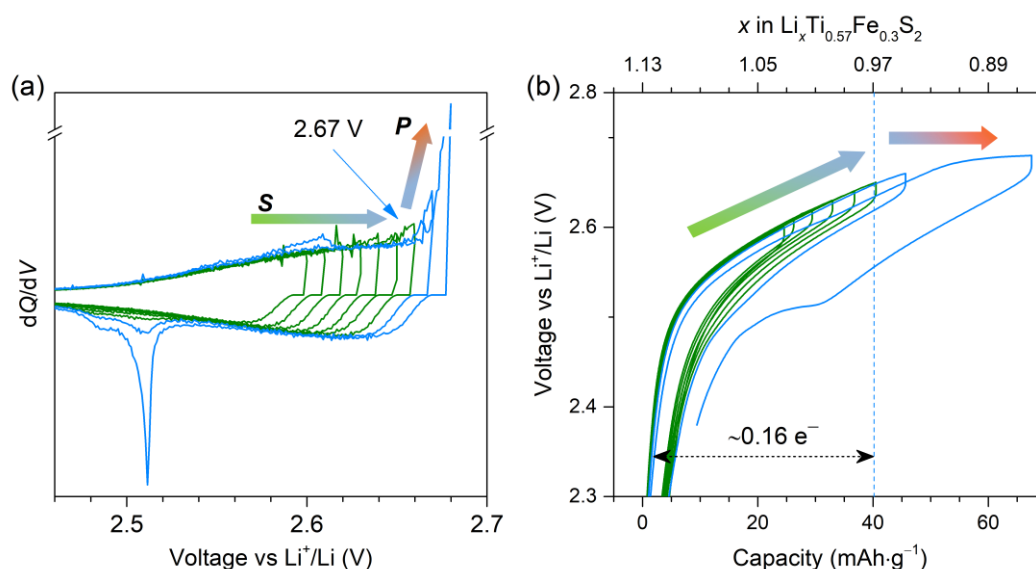
Appendix Figure A2.5. Operando UV-Vis spectroscopy experiment of $\text{Li}_{1.13}\text{Ti}_{0.57}\text{Fe}_{0.3}\text{S}_2 \mid \text{LP30} \mid \text{Li}$ cell. (a) Voltage profile of the cell when charged up to 4 V. (b) Contour plot of the evolution of UV-Vis spectra of the electrolyte with time. The absorbance is plotted in color scale and cycling time in the Y-axis. (c) Representative UV-Vis spectra at the points indicated in (a). For the UV-Vis spectra, the starting spectra before cycling was taken as the blank spectra. It is clear that when the cell was cycled up to 3 V (green curve in (a)), the spectra do not show any trace of dissolved species. In contrast, the spectra drastically change when charged to >3 V (red curve in (a)) indicating the presence of copious amount of dissolved species. However, the position of the absorption peaks is rather reminiscent of alkyl carbonates than polysulfides.³⁰⁷ Hence, electrolyte decomposition might occur in presence of aggressive S_2^{n-} species within the electrode material. See reference³⁰⁷ for the experimental details. Note that, when we cycled the $\text{Li}_{1.13}\text{Ti}_{0.57}\text{Fe}_{0.3}\text{S}_2$ in all-solid-state-battery, we found a stability up to >4.2 V, which will be shown in the Appendix Figure A4.2.



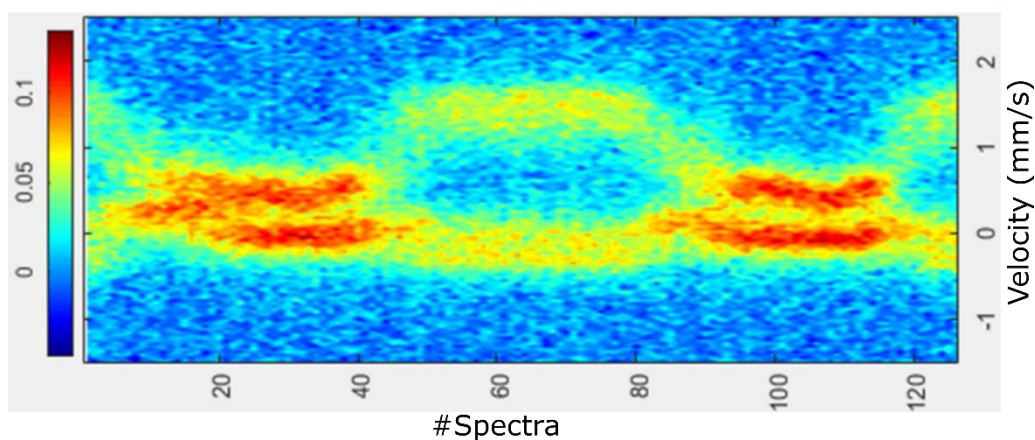
Appendix Figure A2.6. Operando XRD for the cycling of $\text{Li}_{1.13}\text{Ti}_{0.57}\text{Fe}_{0.3}\text{S}_2$ up to high voltage. The left panel shows the charging profile at a rate of $C/10$, up to 2.8 V (green line) followed by a rest (blue line) and again charging up to 4 V (red line). The right panel shows the XRD patterns of the $\text{Li}_{1.13}\text{Ti}_{0.57}\text{Fe}_{0.3}\text{S}_2$ collected during the time indicated in left panel. Some peaks marked by * (red stars) are from the window of our XRD measurement cell. New peaks corresponding to unidentified second phases appear in the XRD patterns when charged to high voltage (indicated by *), implying a partial decomposition of the electrode. Since electrolyte decomposition (shown above, Appendix Figure A2.5) is catalyzed by the electrode material, it can be deteriorated itself.



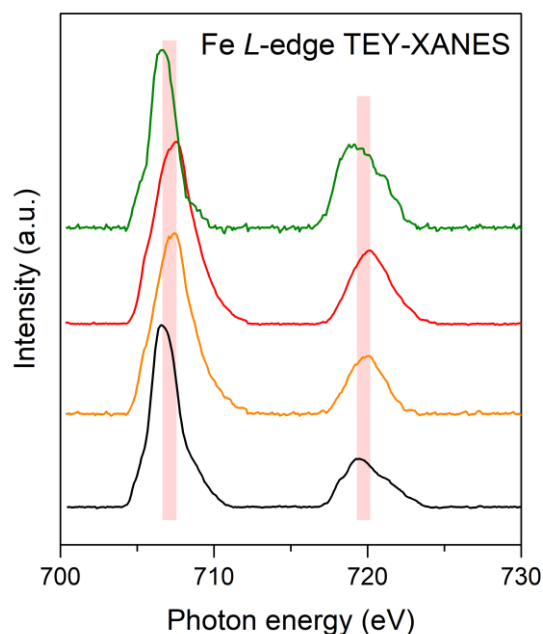
Appendix Figure A2.7. Electrochemical behaviour of $\text{Li}_{1.13}\text{Ti}_{0.57}\text{Fe}_{0.3}\text{S}_2$ phase at 55 °C. (a) Voltage profile in first 2 cycles. Inset shows capacity over first 5 cycles. (b) The dQ/dV curves corresponding to the first 2 cycles. For comparison, the dQ/dV curves for cycling at RT are also shown (in green curves). The sample powder (hand-ground with 20 wt% Csp) were cycled in Swagelok type cells at a rate of $C/20$ inside a constant-temperature furnace. Overall, the material loses its capacity rapidly at 55 °C.



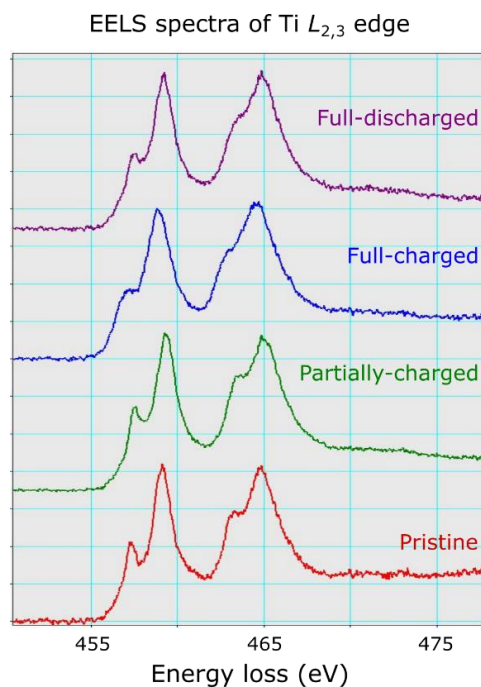
Appendix Figure A2.8. Voltage window opening experiment of $\text{Li}_{1.13}\text{Ti}_{0.57}\text{Fe}_{0.3}\text{S}_2$ in sloppy redox regime. The dQ/dV curves (a), and the corresponding charge-discharge profiles (b) are shown. Thus, the cationic contribution, which was assumed to be manifested in the slope (S), involving the $\text{Fe}^{2+/3+}$ redox, can be decoupled from the presumed anionic plateau (P). For this purpose, the upper cut-off voltage was gradually increased in subsequent cycle by 0.5 V during charging. The dQ/dV curves reveals that initially charging leads to sloppy dQ/dV curves (green curves). Only after charging above ~ 2.67 V, the intense dQ/dV peaks appear (in charge and discharge, blue curves), which can be regarded as the initiation of the anionic process. The corresponding voltage profiles indicate only a capacity of ~ 40 $\text{mAh}\cdot\text{g}^{-1}$ is obtained from solely cationic redox (i.e., before the blue lines appear) which corresponds to $\sim 0.16 e^-$ transfer. This gives a hint that the $\text{Fe}^{2+/3+}$ redox (capable of $0.3 e^-$ transfer) does not complete prior to the anionic redox.



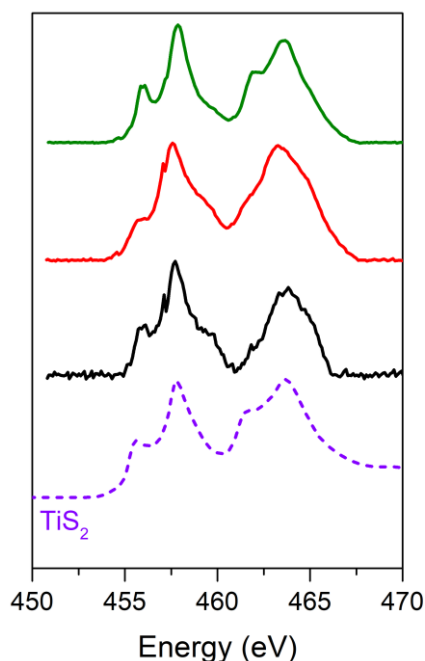
Appendix Figure A2.9. Spectra map of operando Mössbauer spectroscopy of the $\text{LiTi}_{0.5}\text{Fe}_{0.5}\text{S}_2$ sample over first two cycles. The map consists 1st cycle (spectra# 0 - 50), followed by a relaxation and 2nd cycle (spectra# 75 onward).



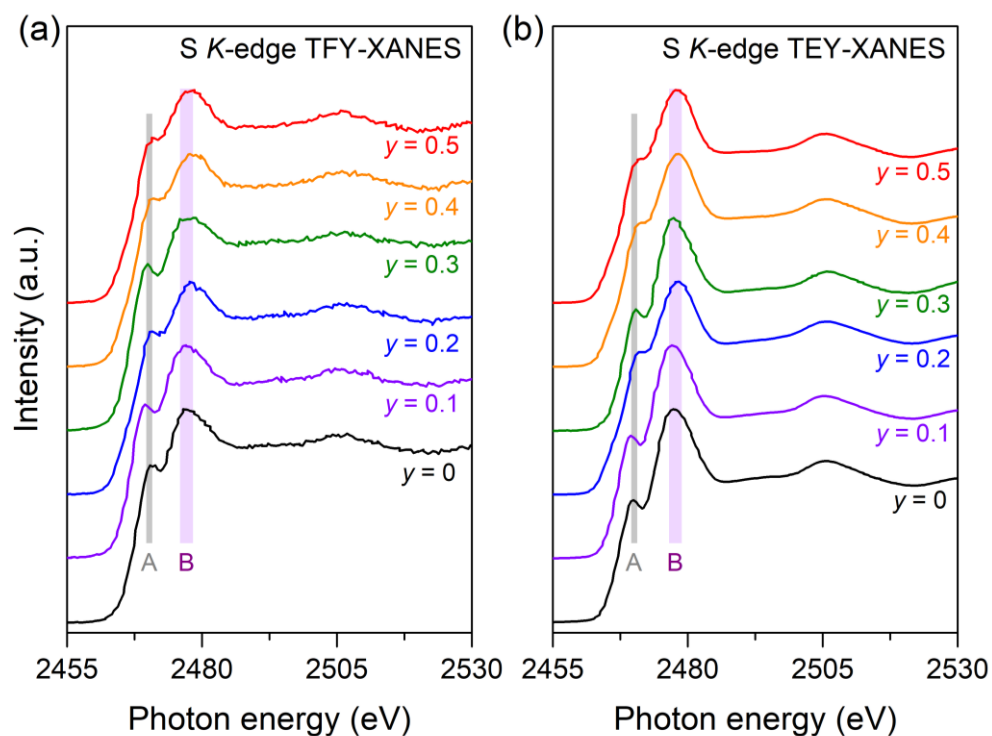
Appendix Figure A2.10. The Fe $L_{2,3}$ -edge XANES spectra collected in TEY mode of the *ex situ* $\text{Li}_{1.13}\text{Ti}_{0.57}\text{Fe}_{0.3}\text{S}_2$ samples. For color codes refer to Figure III.37b. Note that the TFY-XANES shows the bulk Fe was still oxidized during the mid-charge to the full charge, while TFY-XANES indicate the surface Fe remained constant after the mid charge, showing different reactivity of Fe in the surface. Hence, precaution should be taken while interpreting XAS data and more bulk sensitive TFY data are always better.



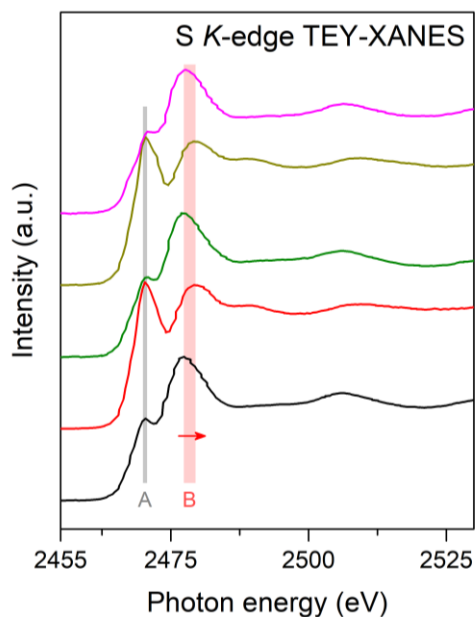
Appendix Figure A2.11. EELS spectra of the Ti $L_{2,3}$ edge collected for the *ex situ* $\text{Li}_{1.13}\text{Ti}_{0.57}\text{Fe}_{0.3}\text{S}_2$ samples. The partially-charged sample was charged to 2.66 V (corresponding to ~ 0.15 Li deintercalation).



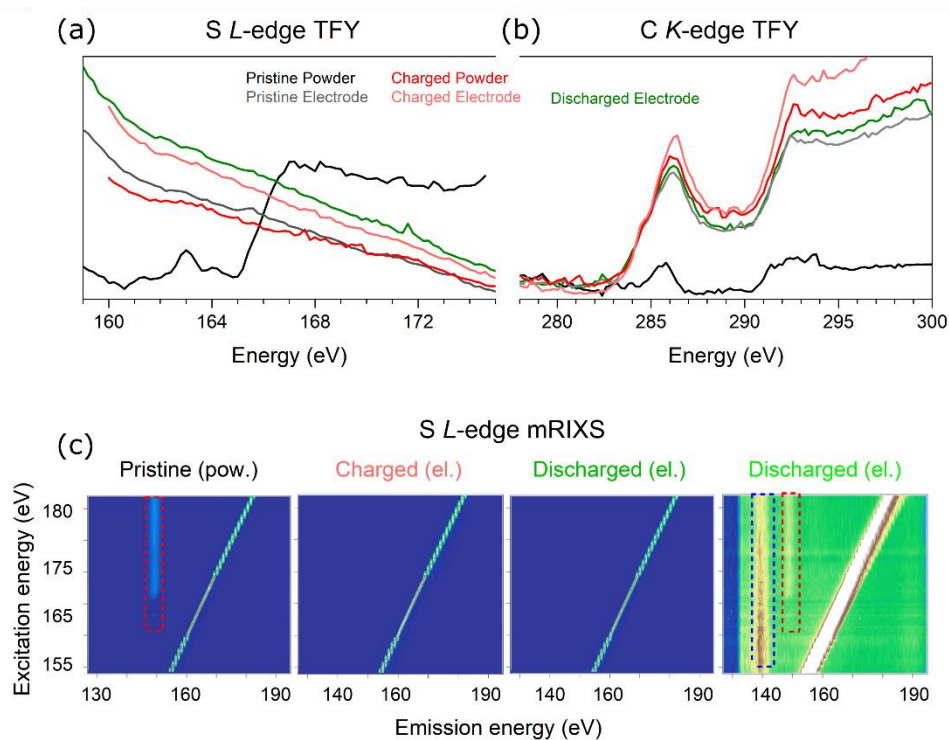
Appendix Figure A2.12. Ti $L_{2,3}$ -edge TEY-XANES of the pristine, full-charged and full-discharge $\text{Li}_{1.13}\text{Ti}_{0.57}\text{Fe}_{0.3}\text{S}_2$ samples are compared with TiS_2 . The spectra for TiS_2 is adopted from Reference²⁴³.



Appendix Figure A2.13. S K-edge XANES spectra collected for the *ex situ* $\text{Li}_{1.33-2y/3}\text{Ti}_{0.67-y/3}\text{Fe}_y\text{S}_2$ samples with $y = 0 - 0.5$. Both TFY (a) and TEY (b) spectra are shown.

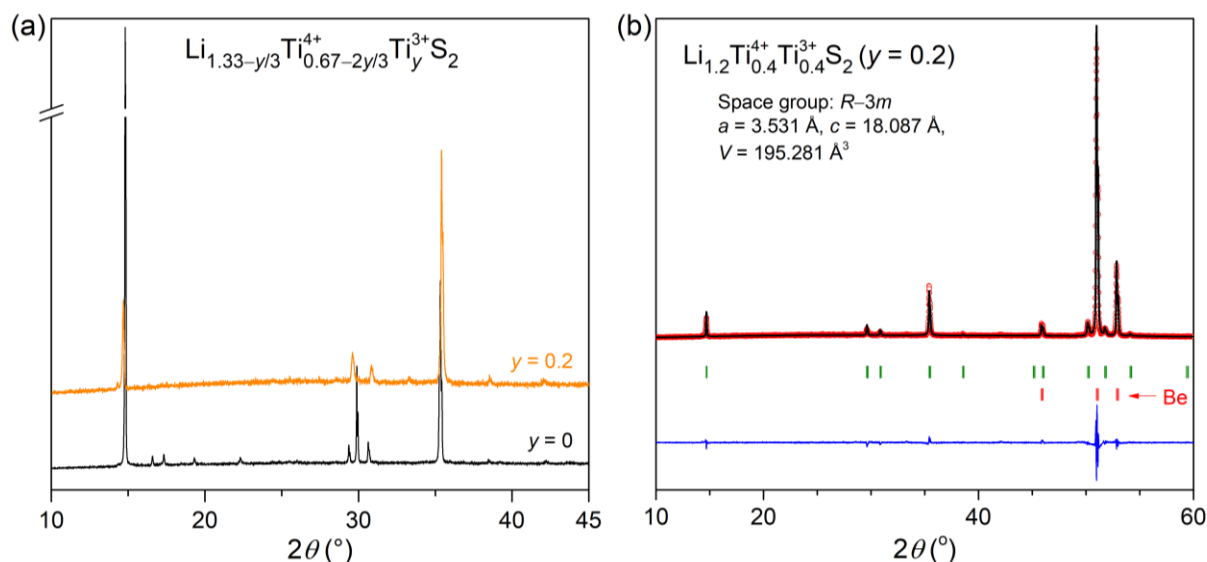


Appendix Figure A2.14. S K-edge TEY-XANES spectra collected for the *ex situ* $\text{Li}_{1.13}\text{Ti}_{0.57}\text{Fe}_{0.3}\text{S}_2$ samples. For color codes refer to Figure III.37d. Note that the spectra are similar to the XANES collected in TFY mode.

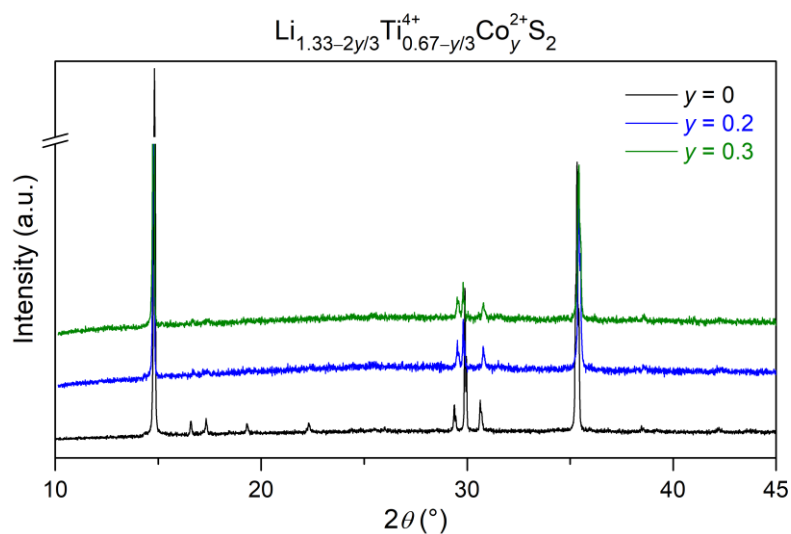


Appendix Figure A2.15. Details of sXAS and mRIXS of the *ex situ* $\text{Li}_{1.13}\text{Ti}_{0.57}\text{Fe}_{0.3}\text{S}_2$ samples. (a-b) Conventional sXAS of S-L (a) and C-K (b) of the pristine powder and cycled electrodes. The dominating background slope in the S-L sXAS range and strong C-K signals can be seen easily for the cycled samples except for the pristine powder sample that is not mixed with conductive carbon. (c) S L-

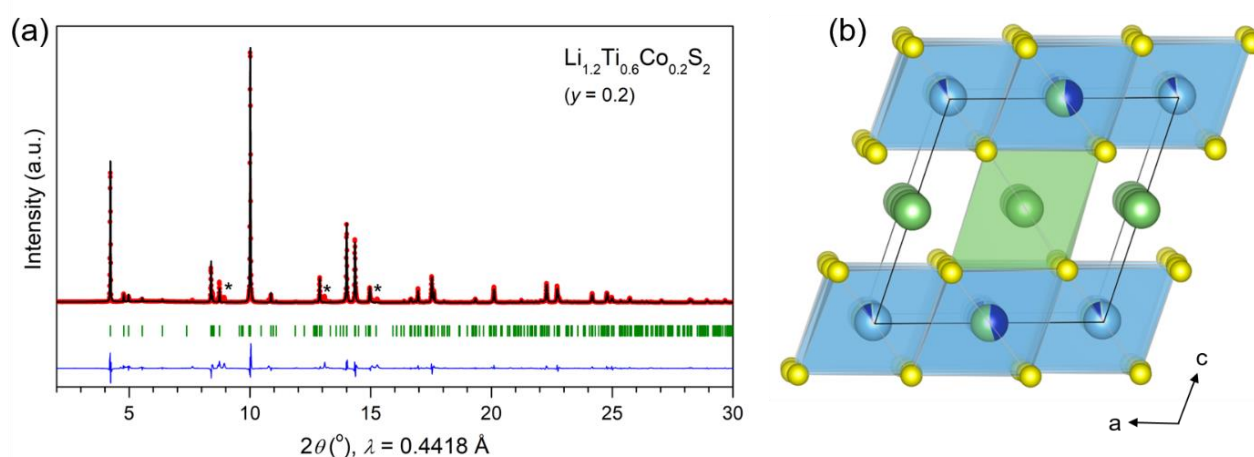
edge mRIXS results of the pristine powder, fully-charged electrode, and full-discharged electrode and full-discharged electrode (but with a different color scale to emphasize the weak-signals). The strongest line feature in all the maps is from the elastic peak, i.e., the same energy of the outgoing fluorescence photons (emission energy, horizontal axis) and the incident photons (excitation energy, vertical axis). The mRIXS is collected at each excitation energy that is used for X-ray absorption spectroscopy,³⁵⁰ but provides the information of the emission energy of the fluorescence photons.²⁹⁷ Only the pristine powder without strong carbon background directly displays signals of S-L (red rectangle in 1st panel). However, the weak signals, as brought up in the 4th panel, display clearly the S-L (red rectangle in 4th panel) signals sitting on the strong C-K (2nd order) background. Fortunately, the S-L and C-K (2nd order) signals are separated for 10 eV in emission energies, which could be easily separated apart in our mRIXS experiments with 0.2 eV resolution. The intrinsic S-L signals at 142-151 eV are extracted from these maps and shown in Figure III.39 for analysis on the sulfur states upon electrochemical cycling. Intensity integrations along emission energies generate the partial fluorescence yield (PFY) spectra that is essentially the same as sXAS but with S-L signals extracted from the strong carbon signal background.



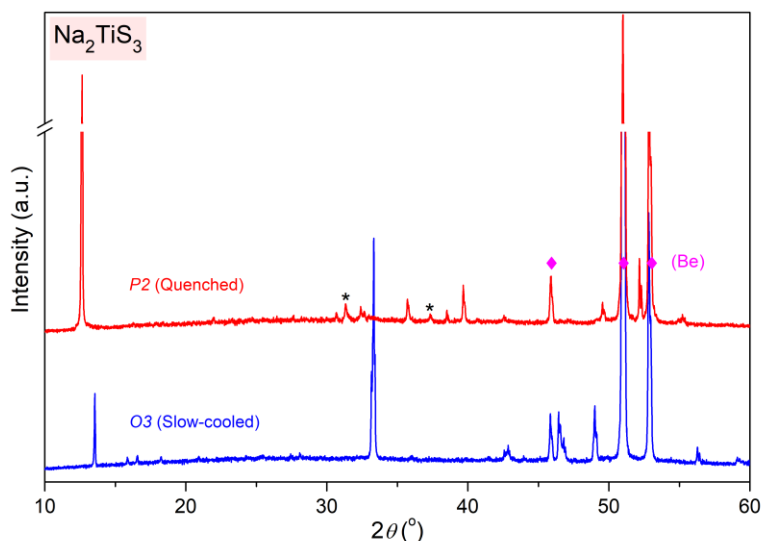
Appendix Figure A2.16. XRD pattern and refinement of the $\text{Li}_{1.2}\text{Ti}_{0.4}\text{Ti}_{0.4}\text{S}_2$ sample. (a) The XRD pattern is compared with $\text{Li}_{1.33}\text{Ti}_{0.67}\text{S}_2$ (Li_2TiS_3). (b) Le Bail refinement of the XRD pattern. The red circles, black continuous line, blue line, and tick bars represent the observed, calculated, and difference patterns, and Bragg positions, respectively. For $\text{Li}_{1.2}\text{Ti}_{0.8}\text{S}_2$ also we did not observe the superstructure peaks. Hence, the XRD pattern could be fitted in a hexagonal $R\bar{3}m$ description. The XRD pattern could be fitted to a unit cell with $a = 3.53091(19)$ Å, $c = 18.08659(3)$ Å, and $V = 195.281(9)$ Å³.



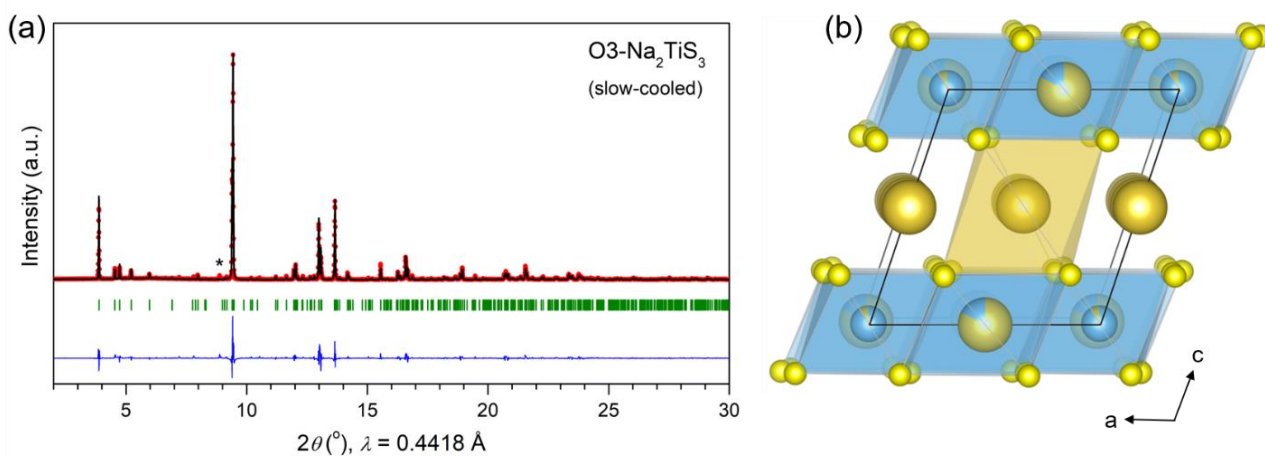
Appendix Figure A2.17. XRD patterns of the as-synthesized $\text{Li}_{1.33-2y/3}\text{Ti}_{0.67-y/3}^{4+}\text{Co}_y^{2+}\text{S}_2$ samples.



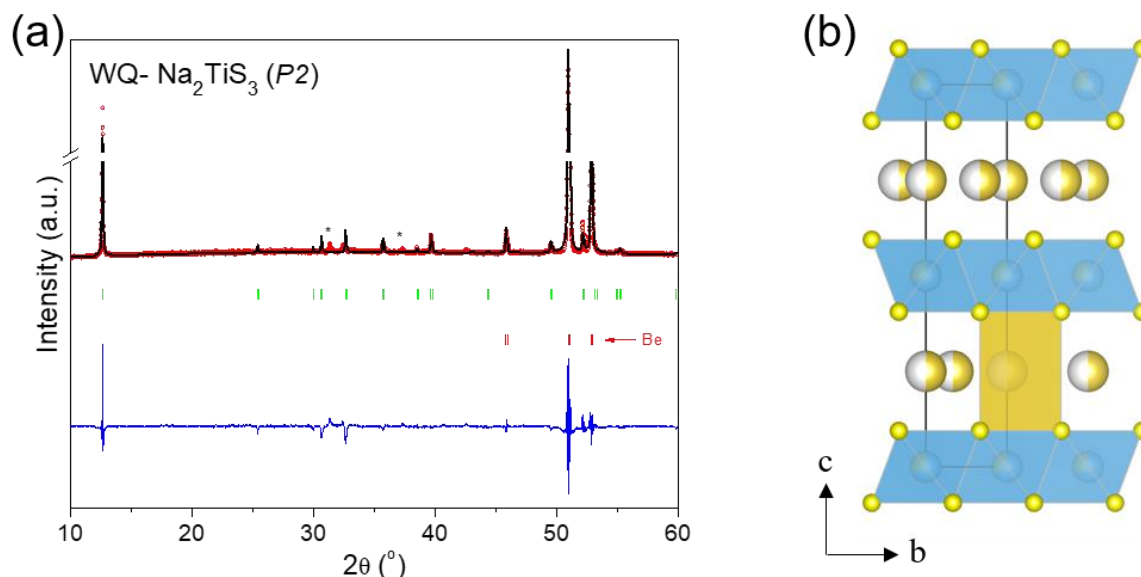
Appendix Figure A2.18. Crystal structure of $\text{Li}_{1.2}\text{Ti}_{0.6}\text{Co}_{0.2}\text{S}_2$ sample from the SXRD pattern. (a) Rietveld refinement of the SXRD pattern. The peaks denoted by * are from some minor impurity. The red circles, black continuous line, blue line, and tick bars represent the observed, calculated, and difference patterns, and Bragg positions, respectively. (b) The corresponding crystal structure. Li, Ti, Co, and S atoms are shown in green, light blue, deep blue, and yellow colors, respectively. The SXRD pattern could be fitted in a monoclinic $C2/m$ unit cell with $a = 6.13150(7) \text{ \AA}$, $b = 10.59888(12) \text{ \AA}$, $c = 6.33265(7) \text{ \AA}$, $\beta = 108.8386(11)^\circ$, and $V = 389.495(7) \text{ \AA}^3$ (Appendix Table A2.8). Note that this unit cell corresponds to a 1.4% decrease in unit cell volume compared to the Li_2TiS_3 . Thus incorporation of Co into the lattice has been confirmed.



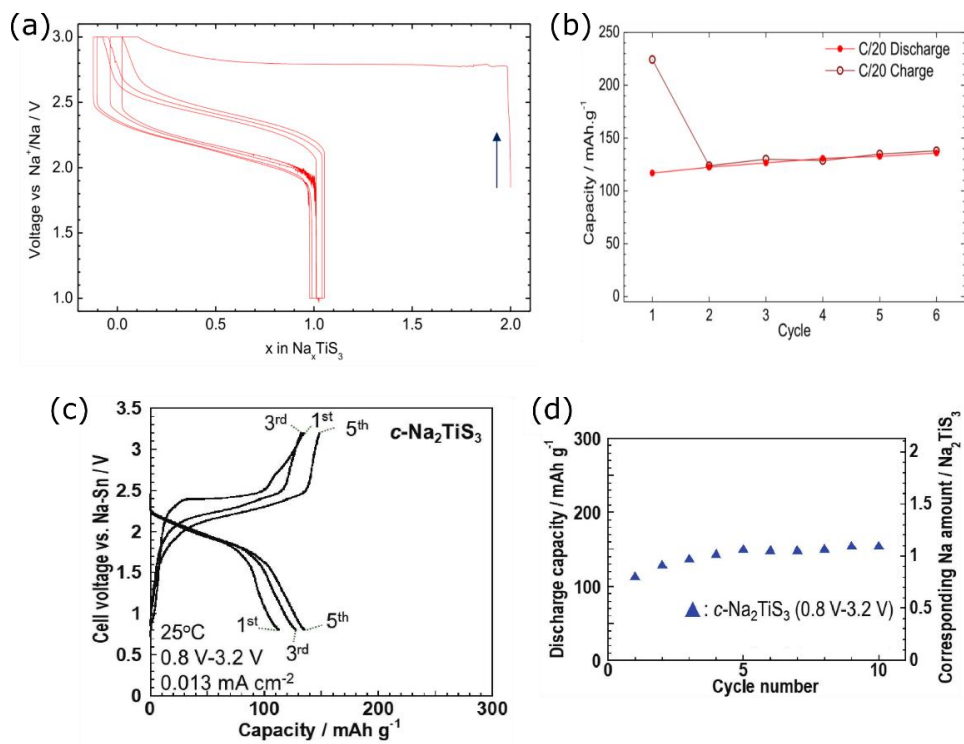
Appendix Figure A2.19. XRD pattern of the as-synthesized Na_2TiS_3 , prepared by quenching (P2), or slow-cooling (O1). Peaks marked by * are from some minor impurity and marked by \blacklozenge are from the Be-window of the XRD measurement cell. For the O3- Na_2TiS_3 , the superstructure peaks were observed, confirming its honeycomb ordering. For the P2- Na_2TiS_3 , the XRD pattern is different from the O3, hence indicating a different crystal structure.



Appendix Figure A2.20. Crystal structure of O3- Na_2TiS_3 sample from the SXR D pattern. Rietveld refinement of the SXR D pattern. The peaks denoted by * are from some minor impurity. The red circles, black continuous line, blue line, and tick bars represent the observed, calculated, and difference patterns, and Bragg positions, respectively. (b) The corresponding crystal structure. Na, Ti, and S atoms are shown in golden, blue, and yellow colors, respectively. To refine the XRD pattern of the O3- Na_2TiS_3 , the structural model of Li_2TiS_3 was adapted and Li was replaced by Na. The structural model (gathered in Appendix Table A2.9) could index the SXR D pattern in $C2/m$ space group with a unit cell of $a = 6.42880(6)$ Å, $b = 11.16169(11)$ Å, $c = 6.88911(7)$ Å, and $\beta = 108.5724(5)^\circ$, leading to $V = 468.593(8)$ Å³. The corresponding crystal structure shows that the Na in Na-layer occupies octahedral position. Note that this unit cell corresponds to 18.6% increase in unit cell volume compared to the Li_2TiS_3 . Although the thermodynamically stable phase of Na_2TiS_3 is O3, this kind of stacking is not common for Na-cathode materials, as only observed for Na_2IrO_3 , to our best knowledge.⁷⁴



Appendix Figure A2.21. Structural characterization of P2- Na_2TiS_3 by refining XRD patterns. (a) Le Bail refinement of the XRD pattern of the P2- Na_2TiS_3 , and (b) crystal structure. In (a), the red circles, black continuous line, blue line, and tick bars represent the observed, calculated, and difference patterns, and Bragg positions, respectively. The peaks for beryllium (Be, red tick bars) are from the Be window of the XRD measurement cell. Na, Ti, and S atoms are shown in golden, blue, and yellow colors, respectively. The P2 phase is mostly observed in Na-cathode materials. To index the XRD pattern of the kinetically stable P2-phase of Na_2TiS_3 , the structural model of P-type NaTiS_2 was adopted. The modified structural model could index the SXRD pattern in space group $P6_3/mmc$ with a unit cell of $a = b = 3.44403(8)$ Å, and $c = 14.00732(1)$ Å, leading to $V = 143.886(3)$ Å³. The unit cell obtained is shown in which Na occupies prismatic (*P*) sites in the Na-layer, which share edges with MS_6 octahedra of the metal layers.



Appendix Figure A2.22. Reported electrochemical behaviour of the O3-Na₂TiS₃. (a-b) Voltage profile (a), and capacity (b), reported by Pele *et al* (2016)⁷⁸. They used 1 M NaPF₆ in TEGDME (tetra ethylene glycol dimethyl ether) as electrolyte (in Na-half cell). (c-d) Voltage profile, and capacity (b), reported by Nasu *et al* (2019)⁷⁹. They cycled the phase vs Na₁₅Sn₄ anode in ASSB, using Na₃PS₄ glass-ceramics as solid electrolyte. Figures are adapted from references^{78,79}. Note that only a capacity of ~110 mAh·g⁻¹ was observed which is much less than what we found in Na-half cell, probably because of the electrolyte used.

A2.3 Supporting Tables

Appendix Table A2.1. Structural parameters for the TiS₃ powder-sample obtained from Rietveld refinement of the NPD pattern.

TiS ₃						
Space group: <i>P2</i> ₁ / <i>m</i>						
$a = 4.9667(3) \text{ \AA}$, $b = 3.40157(10) \text{ \AA}$, $c = 8.8008(4) \text{ \AA}$, $\beta = 97.485(7)^\circ$, $V = 147.419(11) \text{ \AA}^3$						
atom	site	x	y	z	Occ.	<i>B</i> (Å ²)
Ti1	2e	0.7887(12)	0.25	0.65638(6)	1	0.96(8)
S1	2e	0.2610(15)	0.25	0.54997(7)	1	1.01(8)
S2	2e	0.3824(14)	0.25	0.1714(6)	1	0.83(10)
S3	2e	-0.0279(13)	0.25	0.18302(6)	1	0.71(11)

Appendix Table A2.2. Structural parameters for the Li-rich layered Li_2TiS_3 sample obtained from Rietveld refinement of the SXRD pattern.

Li_2TiS_3 (i.e., $\text{Li}_{1.33}\text{Ti}_{0.67}\text{S}_2$)						
Space group: $C2/m$						
$a = 6.17277(1) \text{ \AA}$, $b = 10.69513(1) \text{ \AA}$, $c = 6.33252(1) \text{ \AA}$, $\beta = 109.1311(7)^\circ$, $V = 394.974(1) \text{ \AA}^3$						
atom	site	x	y	z	Occ.	$B (\text{\AA}^2)$
S1	4i	0.24373(2)	0	0.23748(16)	1	0.981(9)
S2	8j	0.25057(12)	0.32522(8)	0.23240(11)	1	0.981(9)
Ti1/Li1	4g	0	0.16751(8)	0	0.914(5)/0.086(5)	0.856(14)
Ti2/Li2	2b	0	0.5	0	0.172(5)/0.828(5)	4.866(197)
Li3	2c	0	0	0.5	1	2.693(117)
Li4	4h	0	0.32050(82)	0.5	1	2.693(117)
Goodness of fit: $\chi^2 = 4.36$, $R_{\text{wp}} = 1.56\%$, $R_{\text{B}} = 1.32\%$						
$(\chi^2, R_{\text{wp}}$, and R_{B} denote the reduced chi-square, weighted profile factor, and Bragg R -factor respectively)						

Appendix Table A2.3. Structural parameters for the $\text{Li}_{1.13}\text{Ti}_{0.57}\text{Fe}_{0.3}\text{S}_2$ sample obtained from Rietveld refinement of the SXRD pattern.

$\text{Li}_{1.13}\text{Ti}_{0.57}\text{Fe}_{0.3}\text{S}_2$ ($y = 0.3$)						
Space group: $R\bar{3}m$						
$a = 3.53987(2) \text{ \AA}$, $c = 18.09676(2) \text{ \AA}$, $V = 196.384(2) \text{ \AA}^3$						
atom	site	x	y	z	Occ.	$B (\text{\AA}^2)$
Li1	3b	0	0	0.5	1	3.170(106)
Ti/Fe/Li2	3a	0	0	0	0.567/0.3/0.133	1.447(9)
S1	6c	0	0	0.25578(2)	1	0.870(7)
Goodness of fit: $\chi^2 = 3.02$, $R_{\text{wp}} = 1.22$, $R_{\text{B}} = 0.389$						

Appendix Table A2.4. Structural parameters for the fully charged $\sim\text{Li}_{0.1}\text{Ti}_{0.57}\text{Fe}_{0.3}\text{S}_2$ sample obtained from Rietveld refinement of SXRD pattern.

$\sim\text{Li}_{0.1}\text{Ti}_{0.57}\text{Fe}_{0.3}\text{S}_2$, Charged to 3 V Space group: $R\bar{3}m$ $a = 3.34546(6) \text{ \AA}$, $c = 17.78031(31) \text{ \AA}$, $V = 172.338(6) \text{ \AA}^3$						
atom	site	x	y	z	Occ.	$B (\text{Å}^2)$
S1	6c	0	0	0.25659(9)	1	5.857(78)
Ti/Fe/Li2	3a	0	0	0	0.567/0.3/0.1	4.007(74)
Goodness of fit: $\chi^2 = 0.88$, $R_{\text{wp}} = 0.948$, $R_{\text{B}} = 1.39$						

Appendix Table A2.5. Structural parameters for the discharged $\text{Li}_{1.13}\text{Ti}_{0.57}\text{Fe}_{0.3}\text{S}_2$ sample obtained from Rietveld refinement of SXRD pattern.

$\text{Li}_{1.13}\text{Ti}_{0.57}\text{Fe}_{0.3}\text{S}_2$, discharged to 1.8 V Space group: $R\bar{3}m$ $a = 3.53951(2) \text{ \AA}$, $c = 18.14764(3) \text{ \AA}$, $V = 196.896(2) \text{ \AA}^3$						
atom	site	x	y	z	Occ.	$B (\text{Å}^2)$
Li1	3b	0	0	0.5	1	3.180(104)
Ti/Fe/Li2	3a	0	0	0	0.567/0.3/0.133	1.650(11)
S1	6c	0	0	0.25569(2)	1	0.950(6)
Goodness of fit: $\chi^2 = 3.44$, $R_{\text{wp}} = 1.06 \%$, $R_{\text{B}} = 0.633 \%$						

Appendix Table A2.6. The isomer shift (IS), the quadrupole splitting (QS), the line width (LW), and the absorption (abs) parameters from the fitting of the Mössbauer spectra obtained during in situ cycling of the $\text{Li}_{1.13}\text{Ti}_{0.57}\text{Fe}_{0.3}\text{S}_2/\text{Li}$ half-cell. The isomer shifts are relative to α -Fe standard at RT.

Spectrum	Doublet	IS (mm/s)	QS (mm/s)	LW (mm/s)	Abs. (%)	Assignment
Comp. 1 (Pristine)	1	0.75	2.08	0.25	21	HS-Fe ²⁺
	2	0.73	1.77	0.29	31	HS-Fe ²⁺
	3	0.74	1.32	0.32	34	HS-Fe ²⁺
	4	0.72	0.87	0.27	14	HS-Fe ²⁺
Comp. 2	1	0.32	0	0.24	10	HS-Fe ³⁺
	2	0.48	0.39	0.59	90	Fe ²⁺ /Fe ³⁺
Comp. 3 (Fully charged)	1	0.34	0.60	0.34	42	LS-Fe ³⁺
	2	0.30	1.02	0.50	58	LS-Fe ³⁺
Fully- discharged	1	0.76	2.08	0.23	15	HS-Fe ²⁺
	2	0.75	1.80	0.31	30	HS-Fe ²⁺
	3	0.77	1.32	0.40	40	HS-Fe ²⁺
	4	0.79	0.95	0.39	15	HS-Fe ²⁺

Appendix Table A2.7. Fitted Mössbauer parameters of the pristine and cycled $\text{LiTi}_{0.5}\text{Fe}_{0.5}\text{S}_2$ powder. IS, QS, LW, Abs are the isomer shift, the quadrupole splitting, the line width and absorption respectively. Isomer shift is given relative to α -Fe standard at RT.

Spectrum	Doublet	IS (mm/s)	QS (mm/s)	LW (mm/s)	Abs. (%)	Assignment
Pristine (<i>comp</i> 1)	1	0.74	1.97	0.24	21	HS-Fe ²⁺
	2	0.67	1.53	0.29	22	HS-Fe ²⁺
	3	0.96	1.31	0.24	6	HS-Fe ²⁺
	4	0.74	0.79	0.47	36	HS-Fe ²⁺
	5	0.63	0.44	0.23	10	HS-Fe ²⁺
	6	0.21	0.11	0.20	5	~ tetra-Fe ³⁺

Comp 2	1	0.50	0.56	0.41	73	HS-Fe ²⁺ /Fe ³⁺
	2	0.75	0.79	0.31	27	HS-Fe ²⁺
Comp 3	1	0.31	0.47	0.34	72	HS-Fe ³⁺
	2	0.33	0.77	0.30	28	HS-Fe ³⁺
Discharged	1	0.73	1.97	0.26	27	HS-Fe ²⁺
	2	0.72	1.53	0.40	42	HS-Fe ²⁺
	3	0.74	1.05	0.56	26	HS-Fe ²⁺
	5	0.11	0	0.27	5	-

Note that the tetra-Fe³⁺ in the pristine spectra indicates some minor impurities.

Appendix Table A2.8. Structural parameters for the Li_{1.2}Ti_{0.6}Co_{0.2}S₂ sample obtained from Rietveld refinement of the SXRD pattern.

Li _{1.2} Ti _{0.6} Co _{0.2} S ₂ ($y = 0.2$)						
Space group: <i>C2/m</i>						
$a = 6.13150(7) \text{ \AA}$, $b = 10.59888(12) \text{ \AA}$, $c = 6.33265(7) \text{ \AA}$, $\beta = 108.8386(11)^\circ$, $V = 389.495(7) \text{ \AA}^3$						
atom	site	x	y	z	Occ.	$B (\text{\AA}^2)$
S1	4i	0.2363(11)	0	0.2327(10)	1	0.83(2)
S2	8j	0.2483(9)	0.3265(4)	0.2323(5)	1	0.83(2)
Ti1/Co1/Li1	4g	0	0.1683(4)	0	0.894(3)/0.081(3)/0.006(3)	1.92(11)
Ti2/Co2/Li2	2b	0	0.5	0	0.013(3)/0.437(3)/0.587(3)	1.4(3)
Li3	2c	0	0	0.5	1	0.4(4)
Li4	4h	0	0.300(2)	0.5	1	0.4(4)

Appendix Table A2.9. Structural parameters for the O3-Na₂TiS₃ sample obtained from Rietveld refinement of the SXRD pattern.

O3-Na₂TiS₃ (i.e., Na _{1.33} Ti _{0.67} S ₂)						
Space group: <i>C2/m</i>						
$a = 6.42880(6) \text{ \AA}$, $b = 11.16169(11) \text{ \AA}$, $c = 6.88911(7) \text{ \AA}$, $\beta = 108.5724(5)^\circ$, $V = 468.593(8) \text{ \AA}^3$						
atom	site	x	y	z	Occ.	$B (\text{\AA}^2)$
S1	4i	0.2043(7)	0	0.2120(7)	1	1.27(4)
S2	8j	0.2561(5)	0.3168(3)	0.2120(4)	1	1.27(4)
Ti1/Na1	4g	0	0.1690(3)	0	0.911(2)/0.089(2)	1.19(8)
Ti2/Na2	2b	0	0.5	0	0.177(2)/0.823(2)	1.5(2)
Na3	2c	0	0	0.5	1	1.75(9)
Na4	4h	0	0.3408(6)	0.5	1	1.75(9)

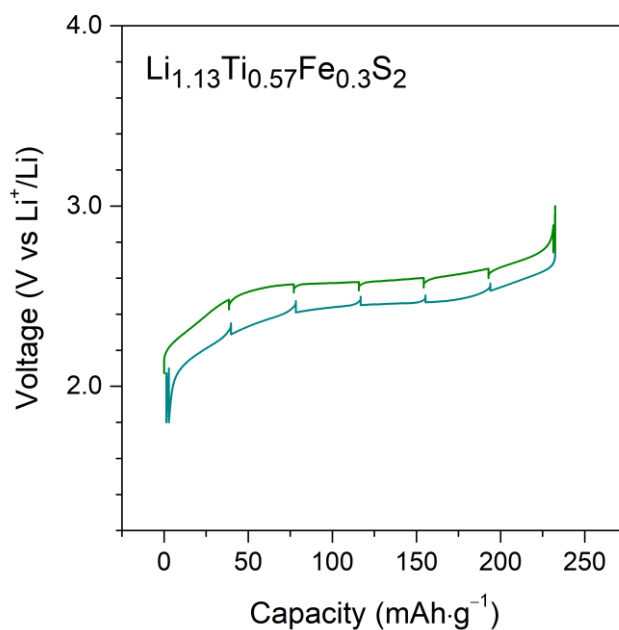
A3 Supporting Information for Chapter IV

A3.1 Methods

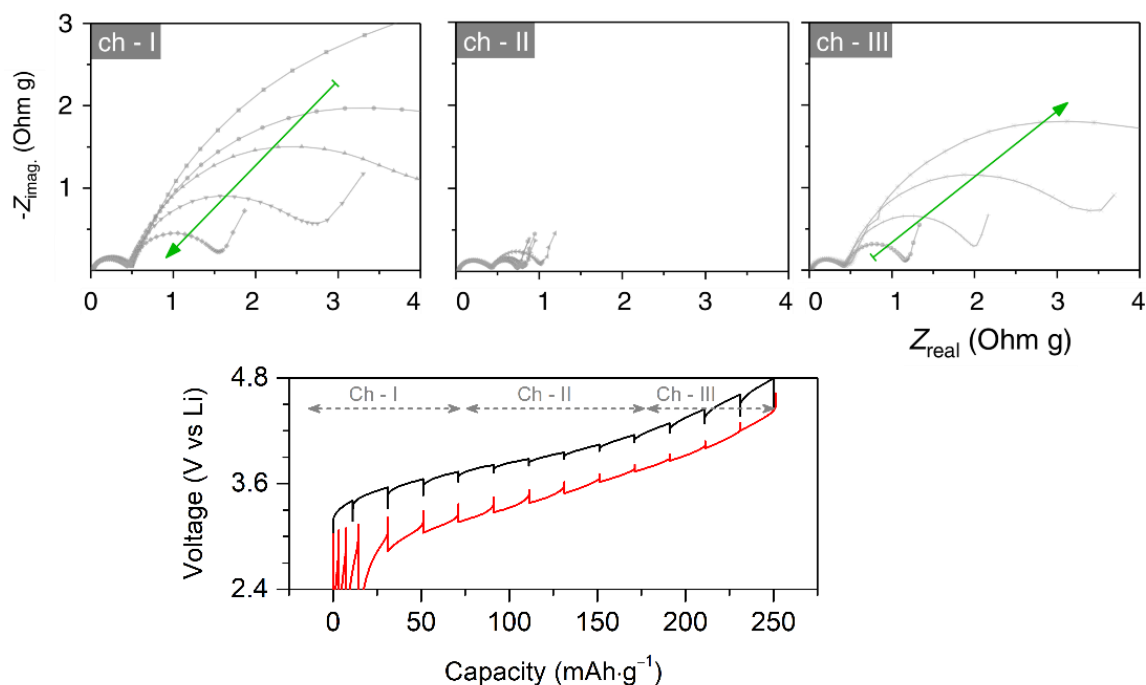
All electrochemical tests were performed similar to the way described in previous chapter. In case the samples were used as self-standing electrodes, they were prepared by mixing the sample with polytetrafluoroethylene (PTFE) polymer and conductive carbon Csp (in 75 : 5 : 20 wt%), with a sample loading of $\sim 4 \text{ mg}\cdot\text{cm}^{-2}$.

GITT experiments were performed in two or three electrode (as specified in the text) Swagelok type cells, after 7 cycles (the first cycle at C/20 and the next six at C/5) so that the voltage profiles are stabilized. All electrochemical cycling and EIS measurements (in 10 mHz - 200 kHz frequency range applying a 10 mV sinusoidal wave) were performed with BioLogic potentiostats.

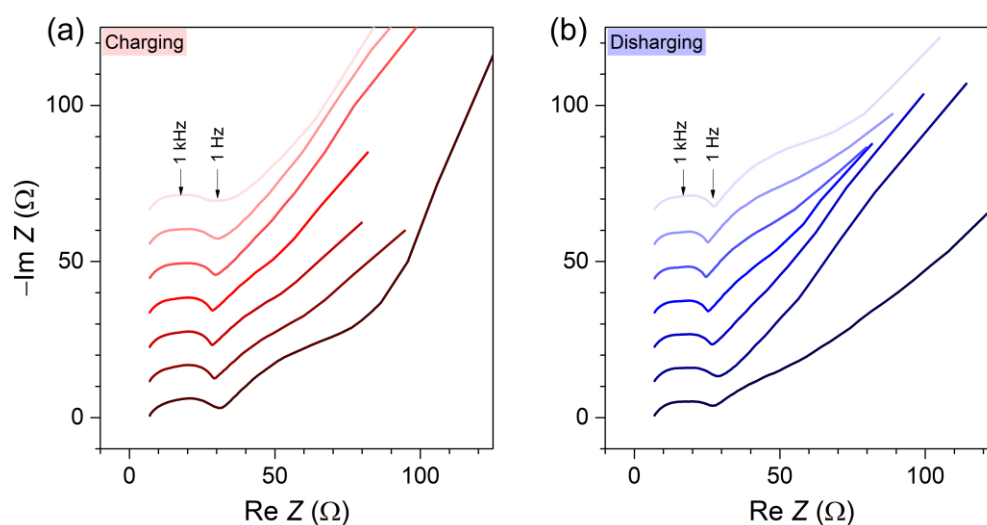
A3.2 Supporting Figures



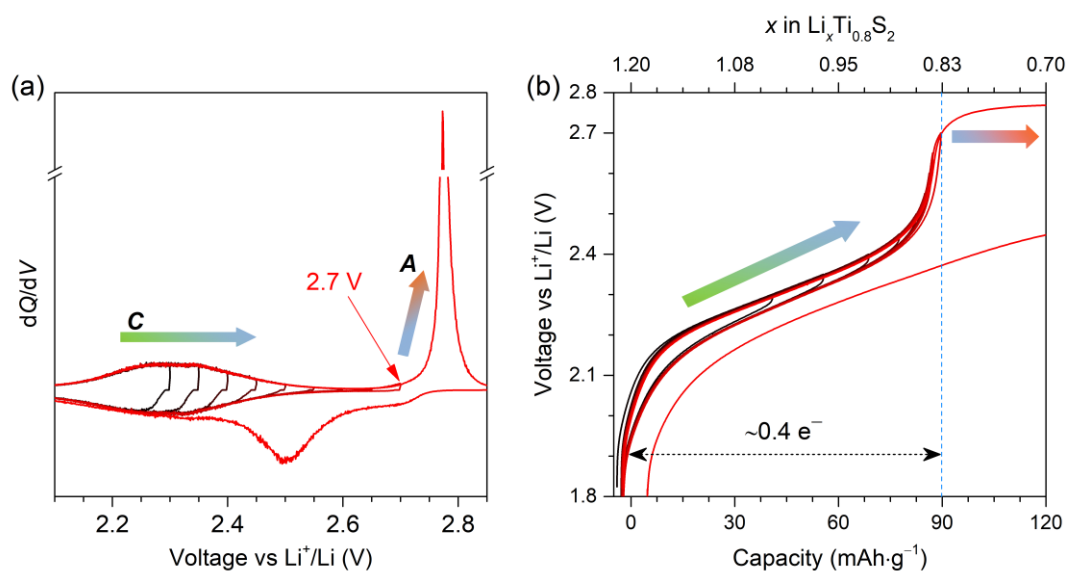
Appendix Figure A3.1. Li-rich layered sulfide as a model material to study the practicability of anionic redox. (a) Voltage profile of $\text{Li}_{1.13}\text{Ti}_{0.57}\text{Fe}_{0.3}\text{S}_2$ in a two-electrode cell in the 8th cycle, recorded with a GITT protocol (C/5 rate with 30 min rests for equilibration).



Appendix Figure A3.2. The evolutions of EIS Nyquist plots of Li-rich NMC during charge. EIS were taken at each step after the GITT relaxation steps (shown in lower panel). For convenience, the charge profile was divided into three regions, and note that the semicircle corresponding to the R_{ct} increases drastically in Ch - I and III, which involves oxygen redox. The GITT was recorded in the 4th charge-discharge cycle, in a three-electrode cell, using $40 \text{ mA}\cdot\text{g}^{-1}$ pulses with 4h rests for equilibration. Figure adapted from Assat *et al*⁵⁰.



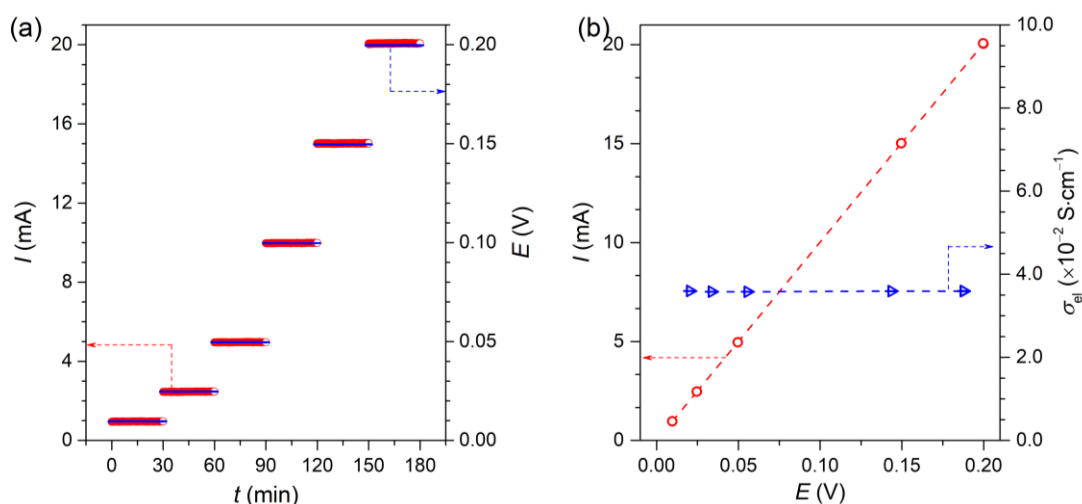
Appendix Figure A3.3. Evolution of Nyquist EIS plots of $\text{Li}_{1.2}\text{Ti}_{0.8}\text{S}_2$ at different SoCs. The EIS spectra were recorded in the relaxation steps during GITT experiment. Experiment was done in a two-electrode Swagelok cell and the sample was used as powder (hand-ground with 20 wt% Csp).



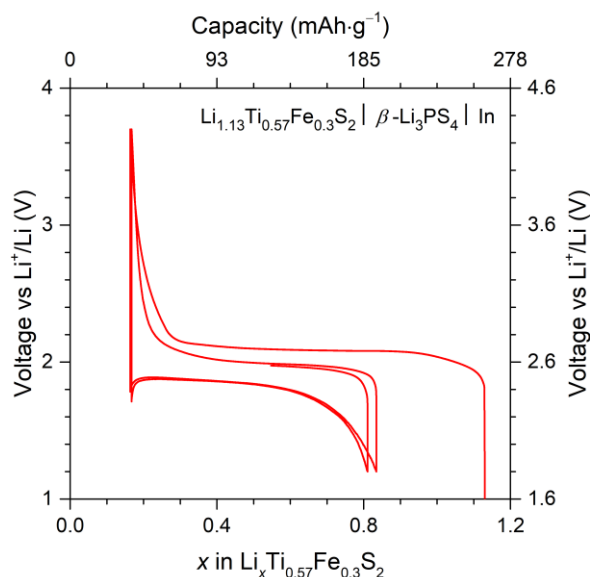
Appendix Figure A3.4. Voltage window opening experiment of the $\text{Li}_{1.2}\text{Ti}_{0.8}\text{S}_2$. In a fresh Li-halfcell of $\text{Li}_{1.2}\text{Ti}_{0.8}\text{S}_2$, the upper voltage cut-off was increased by 0.05 V in subsequent cycles. (a) The dQ/dV curves, and, (b) the voltage profiles, of the cycling. In the dQ/dV curves, the gradual opening (in subsequent cycles) of broad peak corresponding to the 1st plateau (marked by c) is shown. As soon as the voltage was opened >2.7 V, the intense dQ/dV peak corresponding to the 2nd plateau appeared. The charge-discharge profile shows that a capacity $\sim 90 \text{ mAh}\cdot\text{g}^{-1}$ is obtained before the 2nd dQ/dV peak appears. This capacity corresponds to exchange of 0.4 Li, thus indicating most likely the oxidation of 0.4 Ti^{3+} .

A4 Supporting Information for Chapter V

A4.1 Supporting Figures



Appendix Figure A4.1. DC polarization plots of $\text{Li}_{1.13}\text{Ti}_{0.57}\text{Fe}_{0.3}\text{S}_2$ (LTFS) sample. (a) The steady state current (I , in left axis) obtained by applying DC voltages (E , in right axis) to the sample pellet placed between two steel electrodes. (b) Variation of I with E , which was used to deduce the resistance (by Ohm's law). The electronic conductivity (in right axis) was calculated from the resistance, according to the formulae $\sigma = (d/A) \cdot (1/R)$. Indeed, the $\text{Li}_{1.13}\text{Ti}_{0.57}\text{Fe}_{0.3}\text{S}_2$ (LTFS) possess a very high electronic conductivity of $\sim 3.5 \cdot 10^{-2} \text{ S}\cdot\text{cm}^{-1}$.



Appendix Figure A4.2. Voltage profile of $\text{Li}_{1.13}\text{Ti}_{0.57}\text{Fe}_{0.3}\text{S}_2$ cycled in ASSB at RT using increased upper cutoff voltage ($> 4.2 \text{ V}$ vs Li). Cycling rate was C/30. ASSB: courtesy of *Florenzia Marchini*. Note that such a larger electrochemical stability window was not feasible for $\text{Li}_{1.13}\text{Ti}_{0.57}\text{Fe}_{0.3}\text{S}_2$ in liquid electrolyte (recall Fig), because of electrolyte decomposition at higher voltage due to the presence of aggressive $(\text{S}_2)^{n-}$ ($n < 2$) species in the electrode.

List of Figures

Figure I.1. Schematic configuration of Li-metal and Li-ion batteries.....	7
Figure I.2. Comparison of band positions and voltage profiles in LiMS_2 sulfides and LiMO_2 oxides.	8
Figure I.3. Improving the specific capacity of layered oxides cathode materials.	9
Figure I.4. Illustrating cationic and anionic redox.	10
Figure I.5. Voltage profiles of some Li-rich oxides.	11
Figure I.6. Schematic band diagrams that governs the anionic redox.....	12
Figure I.7. Moving from Li-rich layered oxides to sulfides.	13
Figure I.8. Reported pictures of LIBs causing fire in electronic devices and vehicles.	14
Figure I.9. Battery technologies using solid electrolyte.	15
Figure I.10. Minimum thickness required for a SE to match the resistance of liquid electrolytes.	16
Figure I.11. Heat content (left y-axis) and ionic conductivity (right y-axis) of PbF_2	17
Figure I.12. Development of solid electrolytes towards superionic conductivity.	18
Figure I.13. Simplified schematics illustration of ionic conduction process in liquid (a) and solid (b) electrolytes. ^{126,165}	22
Figure I.14. Illustration of Li-conduction in $\text{Li}_{10}\text{GeP}_2\text{S}_{12}$ (LGPS).	23
Figure I.15. Ionic conductivity of $\text{Li}_{4-3x}\text{Al}_x\text{SiO}_4$	24
Figure I.16. Crystal structures of LLZO. O atoms are not shown.....	25
Figure I.17. Ionic conductivity of Li_3PS_4	25
Figure I.18. Enhancement of ionic conductivity by moving from oxides to sulfides.	26
Figure I.19. Structural and configurational features of superionic conductors.	27
Figure I.20. Comparison of advantages/disadvantages between oxide and sulfide solid electrolytes.	28
Figure I.21. Electrochemical stability and decomposition of solid electrolytes.....	28
Figure I.22. RT sinterability of sulfide SEs.	29
Figure I.23. Performances of ASSBs with different sulfide SEs.	30
Figure II.1. Phase diagram of the Li(Na)-Zn-P-O System.	34
Figure II.2. Probing temperature-dependent structural modifications by DSC and SXRD.	36
Figure II.3. Evolution of the SXRD patterns during cooling of the $\text{Li}_6\text{Zn}(\text{P}_2\text{O}_7)_2$ sample.	37
Figure II.4. Combined Rietveld refinement of the XRD (a) and NPD patterns (b) of $\alpha\text{-Li}_6\text{Zn}(\text{P}_2\text{O}_7)_2$	38
Figure II.5. Rietveld refinement of the XRD and NPD patterns of $\zeta\text{-Li}_6\text{Zn}(\text{P}_2\text{O}_7)_2$, recorded at 600 °C.	39

Figure II.6. Crystal structure of the polymorphs of $\text{Li}_6\text{Zn}(\text{P}_2\text{O}_7)_2$.	40
Figure II.7. AC impedance spectra of the $\text{Li}_6\text{Zn}(\text{P}_2\text{O}_7)_2$.	41
Figure II.8. Arrhenius plot of Ionic Conductivity of the $\text{Li}_6\text{Zn}(\text{P}_2\text{O}_7)_2$ sample.	42
Figure II.9. AC impedance spectra of $\alpha\text{-Li}_6\text{Zn}(\text{P}_2\text{O}_7)_2$ recorded at high temperatures.	43
Figure II.10. BVEL map of (a) $\alpha\text{-Li}_6\text{Zn}(\text{P}_2\text{O}_7)_2$ and (b) $\zeta\text{-Li}_6\text{Zn}(\text{P}_2\text{O}_7)_2$ at the percolation energies.	44
Figure II.11. Rietveld refinement of the XRD and NPD patterns of $\alpha\text{-Li}_4\text{Zn}(\text{PO}_4)_2$, measured at RT.	45
Figure II.12. Crystal structure of $\alpha\text{-Li}_4\text{Zn}(\text{PO}_4)_2$. (a) along 101 , (b) along [001].	46
Figure II.13. Probing temperature-dependent structural modifications of $\text{Li}_4\text{Zn}(\text{PO}_4)_2$ by DSC and XRD.	47
Figure II.14. Evolution of XRD patterns of $\text{Li}_4\text{Zn}(\text{PO}_4)_2$ with temperature during cooling.	47
Figure II.15. Rietveld refinement of the XRD and NPD patterns of $\beta\text{-Li}_4\text{Zn}(\text{PO}_4)_2$, measured at 600°C.	48
Figure II.16. Crystal structure of (a) $\alpha\text{-Li}_4\text{Zn}(\text{PO}_4)_2$, (b) $\beta\text{-Li}_4\text{Zn}(\text{PO}_4)_2$ and (c) $\beta'\text{-Li}_{3.7}\text{Zn}_{0.7}\text{Ga}_{0.3}(\text{PO}_4)_2$.	49
Figure II.17. Rietveld refinement of the XRD pattern of the ball-milled $\beta\text{-Li}_4\text{Zn}(\text{PO}_4)_2$ sample, measured at RT.	49
Figure II.18. SXRD patterns of the $\text{Li}_{4-x}\text{Zn}_{1-x}\text{Ga}_x(\text{PO}_4)_2$ samples.	50
Figure II.19. XRD patterns of the $\text{Li}_{4-x}\text{Zn}_{1-x}\text{Ga}_x(\text{PO}_4)_2$ samples.	51
Figure II.20. Rietveld refinement of (a) XRD, and (b) NPD patterns of $\beta'\text{-Li}_{3.7}\text{Zn}_{0.7}\text{Ga}_{0.3}(\text{PO}_4)_2$, measured at RT.	52
Figure II.21. Rietveld refinement of the RT XRD (a), and NPD (b) patterns of $\beta\text{-Li}_{3.5}\text{Zn}_{0.5}\text{Ga}_{0.5}(\text{PO}_4)_2$.	52
Figure II.22. Crystal structure of $\beta\text{-Li}_{3.5}\text{Zn}_{0.5}\text{Ga}_{0.5}(\text{PO}_4)_2$ at RT.	53
Figure II.23. DSC curves and simplified temperature-composition phase diagram of $\text{Li}_{4-x}\text{Zn}_{1-x}\text{Ga}_x(\text{PO}_4)_2$ samples.	54
Figure II.24. Ionic conductivities of the $\text{Li}_4\text{Zn}(\text{PO}_4)_2$ sample.	55
Figure II.25. Arrhenius plot ionic conductivity of $\text{Li}_{4-x}\text{Zn}_{1-x}\text{Ga}_x(\text{PO}_4)_2$ samples.	56
Figure II.26. DC polarization of $\beta'\text{-Li}_{3.7}\text{Zn}_{0.7}\text{Ga}_{0.3}(\text{PO}_4)_2$ sample.	58
Figure II.27. BVEL of (a) $\alpha\text{-Li}_4\text{Zn}(\text{PO}_4)_2$, (b) $\beta\text{-Li}_4\text{Zn}(\text{PO}_4)_2$ and (c) $\beta'\text{-Li}_{3.7}\text{Zn}_{0.7}\text{Ga}_{0.3}(\text{PO}_4)_2$ at the percolation energies.	58
Figure II.28. BVEL of $\beta\text{-Li}_{3.5}\text{Zn}_{0.5}\text{Ga}_{0.5}(\text{PO}_4)_2$, at the percolation energies.	59
Figure II.29. Variation of ionic conductivity and broadening of XRD peak with concentration of Li vacancy.	60
Figure II.30. FESEM images of the cross-section of the sintered pellets.	60
Figure II.31. Evolution of as-synthesized $\text{Na}_4\text{Zn}(\text{PO}_4)_2$ with temperature.	62
Figure II.32. Rietveld refinement of the SXRD pattern of $\gamma\text{-Na}_4\text{Zn}(\text{PO}_4)_2$ recorded at 500 °C.	64
Figure II.33. Combined Rietveld refinement of the SXRD (a), and NPD (b) patterns of $\beta\text{-Na}_4\text{Zn}(\text{PO}_4)_2$ recorded at RT.	64

Figure II.34. Crystal structures of the γ - $\text{Na}_4\text{Zn}(\text{PO}_4)_2$ (a), and β - $\text{Na}_4\text{Zn}(\text{PO}_4)_2$ (b).	65
Figure II.35. Le Bail refinement of the SXRD pattern (a) and the NPD pattern (b) of α - $\text{Na}_4\text{Zn}(\text{PO}_4)_2$	66
Figure II.36. XRD patterns of the $\text{Na}_{4-x}\text{Zn}_{1-x}\text{Ga}_x(\text{PO}_4)_2$ synthesized by quenching.	67
Figure II.37. XRD patterns of the $\text{Na}_{4-x}\text{Zn}_{1-x}\text{M}_x(\text{PO}_4)_2$ synthesized by slow cooling for M = Ga (a) and Al (b). ..	67
Figure II.38. Le Bail refinement of the SXRD pattern of slow-cooled β - $\text{Na}_{3.85}\text{Zn}_{0.85}\text{Ga}_{0.15}(\text{PO}_4)_2$ sample.	68
Figure II.39. Evolution of XRD patterns of as-synthesized $\text{Na}_{4-x}\text{Zn}_{1-x}\text{Ga}_x(\text{PO}_4)_2$ samples (prepared by slow-cooling) with temperature upon heating (at 1 °C/min), for $x_{\text{Ga}} = 0.15$ (a), and $x_{\text{Ga}} = 0.25$ (b).	69
Figure II.40. Arrhenius plot of total ionic conductivity of the $\text{Na}_4\text{Zn}(\text{PO}_4)_2$ samples.	70
Figure II.41. Arrhenius plot of total ionic conductivity of the $\text{Na}_{4-x}\text{Zn}_{1-x}\text{Ga}_x(\text{PO}_4)_2$ samples synthesized by slow cooling.	71
Figure II.42. Strategy to design new ionic conductors.	73
Figure III.1. Voltage profiles of TiS_2 , LiCoO_2 , and $\text{Li}_{1.2}\text{Ni}_{0.13}\text{Mn}_{0.54}\text{Co}_{0.13}\text{O}_2$ (Li-rich NMC).	76
Figure III.2. Reported crystal structure of TiS_3	77
Figure III.3. Picture of the as-synthesized TiS_3	78
Figure III.4. SEM images of the pristine TiS_3 powders.	79
Figure III.5. Rietveld refinement of the SXRD pattern of the pristine TiS_3 powder.	80
Figure III.6. Rietveld refinement of the NPD pattern of the pristine TiS_3 powder collected at D1b.	80
Figure III.7. The crystal structure of as-synthesized TiS_3	81
Figure III.8. HAADF-STEM image of TiS_3 single crystal showing the atomic arrangement.	82
Figure III.9. Charge-discharge profile of TiS_3 in the 1st cycle.	83
Figure III.10. Operando XRD of TiS_3	84
Figure III.11. HRTEM images of Li_2TiS_3 single crystals.	85
Figure III.12. SEM images of the <i>ex situ</i> Li_2TiS_3 (discharged TiS_3) powder.	85
Figure III.13. Le Bail refinement of <i>ex situ</i> Li_2TiS_3 powder.	86
Figure III.14. HAADF-STEM image of $\text{Li}_{-0.2}\text{TiS}_3$ after 1st cycle.	86
Figure III.15. S 2p and Ti 2p core XPS spectra of the cycled TiS_3 samples.	87
Figure III.16. EELS spectra of the S $L_{2,3}$ and Ti $L_{2,3}$ edge of the cycled TiS_3 samples.	88
Figure III.17. S K-edge TFY-XANES spectra collected for TiS_3 and LiTiS_3 , (mid-discharged), Li_2TiS_3 (full-discharged), and $\text{Li}_{-0.2}\text{TiS}_3$ (fully-charged) samples.	89
Figure III.18. Charge-discharge profile of TiS_3 over first 25 cycles.	90
Figure III.19. Voltage profile of TiS_3 recorded with a GITT protocol.	91
Figure III.20. Crystal structure of Li_2TiS_3 from Rietveld refinement of the SXRD pattern.	92

Figure III.21. The electrochemical performance of Li_2TiS_3 .	93
Figure III.22. Fe-substitution in Li_2TiS_3 . Schematic band structure of $\text{Li}_{1.33}\text{Ti}_{0.67}\text{S}_2$ (i.e., Li_2TiS_3 , in left), and its Fe^{2+} substituted derivative (in right).	94
Figure III.23. Structural behavior of the $\text{Li}_{1.33-2y/3}\text{Ti}_{0.67-y/3}\text{Fe}_y\text{S}_2$ series.	95
Figure III.24. Structural characterization of the $\text{Li}_{1.13}\text{Ti}_{0.57}\text{Fe}_{0.3}\text{S}_2$ ($y = 0.3$) sample.	96
Figure III.25. Comparing the crystal structures of $\text{Li}_{1.13}\text{Ti}_{0.57}\text{Fe}_{0.3}\text{S}_2$ (a) and Li-rich NMC (b).	97
Figure III.26. Electrochemical behavior of $\text{Li}_{1.33-2y/3}\text{Ti}_{0.67-y/3}\text{Fe}_y\text{S}_2$.	98
Figure III.27. Capacity and dQ/dV of $\text{Li}_{1.33-2y/3}\text{Ti}_{0.67-y/3}\text{Fe}_y\text{S}_2$.	99
Figure III.28. More details of the electrochemical properties of $\text{Li}_{1.13}\text{Ti}_{0.57}\text{Fe}_{0.3}\text{S}_2$ ($y = 0.3$).	99
Figure III.29. Cycling $\text{Li}_{1.13}\text{Ti}_{0.57}\text{Fe}_{0.3}\text{S}_2$ in a broader voltage range.	100
Figure III.30. Probing the Li (de)intercalation in <i>operando</i> .	102
Figure III.31. 2nd cycle of the <i>in situ</i> cycling of $\text{Li}/\text{Li}_{1.13}\text{Ti}_{0.57}\text{Fe}_{0.3}\text{S}_2$ half-cell.	103
Figure III.32. Structural characterization of $\text{Li}_{1.13}\text{Ti}_{0.57}\text{Fe}_{0.3}\text{S}_2$ after Li (de)intercalation.	104
Figure III.33. The bond-lengths observed in the pristine, full-charged and full-discharged phase (as obtained from the Rietveld refinement of the corresponding SXRD patterns).	105
Figure III.34. <i>Operando</i> Mössbauer spectroscopy to identify the $\text{Fe}^{2+/3+}$ redox process in $\text{Li}_{1.13}\text{Ti}_{0.57}\text{Fe}_{0.3}\text{S}_2$.	106
Figure III.35. Coordination of Fe atoms in $\text{Li}_{1.13}\text{Ti}_{0.57}\text{Fe}_{0.3}\text{S}_2$.	107
Figure III.36. <i>Operando</i> Mössbauer spectroscopy for the $\text{LiTi}_{0.5}\text{Fe}_{0.5}\text{S}_2$ ($y = 0.5$) sample.	108
Figure III.37. Probing the cationic redox processes in $\text{Li}_{1.13}\text{Ti}_{0.57}\text{Fe}_{0.3}\text{S}_2$ by <i>ex situ</i> XAS.	109
Figure III.38. Probing the anionic redox processes in $\text{Li}_{1.13}\text{Ti}_{0.57}\text{Fe}_{0.3}\text{S}_2$.	110
Figure III.39. Probing S <i>L</i> -edge to identify the S-redox processes.	112
Figure III.40. S- $L_{2,3}$ edge EELS of FeS (a), and FeS_2 and elemental S (b).	112
Figure III.41. Comparison of the voltage profiles of TiS_2 and $\text{Li}_{1.13}\text{Ti}_{0.57}\text{Fe}_{0.3}\text{S}_2$ (green curve).	114
Figure III.42. Electrochemical behaviour of the $\text{Li}_{1.2}\text{Ti}_{0.8}\text{S}_2$ sample.	115
Figure III.43. Electrochemical activity of the $\text{Li}_{1.33-2y/3}\text{Ti}_{0.67-y/3}\text{Co}_y\text{S}_2$ samples.	116
Figure III.44. Electrochemical behaviour of the O3- and P2- Na_2TiS_3 .	117
Figure IV.1. GITT Voltage profile of $\text{Li}_{1.13}\text{Ti}_{0.57}\text{Fe}_{0.3}\text{S}_2$ and Li-rich NMC in a three-electrode cell.	121
Figure IV.2. GITT Voltage profile of $\text{Li}_2\text{Ru}_{0.75}\text{Sn}_{0.25}\text{O}_3$ (LRSO).	121
Figure IV.3. GITT Voltage profile of $\text{LiTi}_{0.5}\text{Fe}_{0.5}\text{S}_2$ ($y = 0.5$) in a two-electrode cell.	122
Figure IV.4. Voltage hysteresis in Ti^{3+} and Co^{2+} substituted Li_2TiS_3 .	122
Figure IV.5. Probing the hysteresis of $\text{Li}_{1.13}\text{Ti}_{0.57}\text{Fe}_{0.3}\text{S}_2$ by voltage window opening experiment.	124
Figure IV.6. Anionic redox in Li-rich NMC.	124

Figure IV.7. Probing the hysteresis of $\text{Li}_{1.2}\text{Ti}^{4+}_{0.4}\text{Ti}^{3+}_{0.4}\text{S}_2$ by voltage window opening experiment.	125
Figure IV.8. Cell's electrochemical resistance as a function of SoC.	126
Figure IV.9. Typical Nyquist plot of EIS of $\text{Li}_{1.13}\text{Ti}_{0.57}\text{Fe}_{0.3}\text{S}_2$ in Li-half cell.	127
Figure IV.10. Nyquist plots of EIS recorded after each relaxation in GITT.	128
Figure IV.11. Discharge profiles of $\text{Li}_{1.13}\text{Ti}_{0.57}\text{Fe}_{0.3}\text{S}_2$ over long cycling to show the voltage fade.	129
Figure IV.12. Average voltage during long cycling of $\text{Li}_{1.13}\text{Ti}_{0.57}\text{Fe}_{0.3}\text{S}_2$ and Li-rich NMC in Li-half cells.	129
Figure IV.13. Average voltage of Li-rich sulfides in Li-half cells.	130
Figure IV.14. The voltage profiles in 2nd cycle of (a) $\text{Na}_{0.67}[\text{Mg}_{0.28}\text{Mn}_{0.72}\text{O}_2]$, and (b) O3- Na_2TiS_3	131
Figure IV.15. Capacity retentions of the O3- and P2- Na_2TiS_3	131
Figure IV.16. Average discharge voltages obtained in O3- and P2- Na_2TiS_3 over first few cycles.	132
Figure IV.17. Ragone plots of $\text{Li}_{1.13}\text{Ti}_{0.57}\text{Fe}_{0.3}\text{S}_2$	133
Figure V.1. Schematic diagram of cathode/sulfide electrolyte interfaces with oxide or sulfide cathode.	136
Figure V.2. A picture of the ASSB setup fully designed and assembled at lab, that was used in this study.	137
Figure V.3. Schematics of the three-layer ASSB.	138
Figure V.4. EIS spectra of the glassy $75\cdot\text{Li}_2\text{S}\cdot 25\cdot\text{P}_2\text{S}_5$ (g-LPS) and $\beta\text{-Li}_3\text{PS}_4$ (LPS) solid electrolyte.	139
Figure V.5. Rietveld refinement of the SXRD pattern of the as-synthesized $\beta\text{-Li}_3\text{PS}_4$ SE.	140
Figure V.6. Rietveld refinement of the SXRD pattern of the cathode composite.	140
Figure V.7. DC polarization plots of LTFS-LPS cathode composite.	141
Figure V.8. Voltage profile of $\text{Li}_{1.13}\text{Ti}_{0.57}\text{Fe}_{0.3}\text{S}_2$ (LTFS) cycled in ASSB at RT.	142
Figure V.9. Polarization in charge-discharge of $\text{Li}_{1.13}\text{Ti}_{0.57}\text{Fe}_{0.3}\text{S}_2 \text{g-LPS} \text{In}$ ASSB.	142
Figure V.10. Voltage profile of $\text{Li}_{1.13}\text{Ti}_{0.57}\text{Fe}_{0.3}\text{S}_2$ cycled in ASSB at RT using $\beta\text{-Li}_3\text{PS}_4$ as solid electrolyte.	143
Figure V.11. EIS characterization of the $\text{Li}_{1.13}\text{Ti}_{0.57}\text{Fe}_{0.3}\text{S}_2 \text{g-LPS} \text{In}$ ASSB.	144
Appendix Figure A1.1. Schematics of the AC impedance measurement procedure.	A-5
Appendix Figure A1.2. Typical Nyquist impedance plot of a sintered pellet and its interpretation.	A-6
Appendix Figure A1.3. Rietveld refinement of the as-synthesized sample when a nominal composition of $\text{Li}_{3.95}\text{Zn}_{0.95}\text{Al}_{0.05}(\text{PO}_4)_2$ was tried to synthesize.	A-7
Appendix Figure A1.4. XRD pattern of as-synthesized sample when a nominal composition of $\text{Li}_{4-x}\text{Zn}_{1-x}\text{In}_x(\text{PO}_4)_2$ with $x_{\text{In}} = 0.3$ was tried to synthesize.	A-7
Appendix Figure A1.5. Evolution of XRD patterns of Ga-substituted samples with temperature.	A-8
Appendix Figure A1.6. Rietveld refinement of the XRD (a), and NPD (b) patterns of $\beta^2\text{-Li}_{3.7}\text{Zn}_{0.7}\text{Ga}_{0.3}(\text{PO}_4)_2$ at 600 °C.	A-9

Appendix Figure A1.7. Rietveld refinement of the XRD pattern of the as-synthesized end-product when a nominal composition of $\text{Na}_6\text{Zn}(\text{P}_2\text{O}_7)_2$ was targeted to synthesize.....	A-9
Appendix Figure A1.8. The Rietveld refinement of the XRD pattern (red circles) of the as-synthesized product (slow-cooled) when a nominal composition of $\text{Na}_{3.85}\text{Zn}_{0.85}\text{In}_{0.15}(\text{PO}_4)_2$ was tried to synthesize.	A-10
Appendix Figure A1.9. Le Bail refinement of the SXRD patterns of the $\beta\text{-Na}_{3.85}\text{Zn}_{0.85}\text{Ga}_{0.15}(\text{PO}_4)_2$, $x_{\text{Ga}} = 0.15$ sample synthesized by cooling slowly (a), and quenching (b).....	A-11
Appendix Figure A1.10. Le Bail refinement of the SXRD patterns of the $\beta\text{-Na}_{3.85}\text{Zn}_{0.85}\text{Al}_{0.15}(\text{PO}_4)_2$, $x_{\text{Al}} = 0.15$ sample synthesized by cooling slowly.....	A-12
Appendix Figure A1.11. Evolution of XRD patterns of as-synthesized $\text{Na}_{4-x}\text{Zn}_{1-x}\text{Ga}_x(\text{PO}_4)_2$ samples (prepared by slow-cooling) with temperature upon cooling, for $x_{\text{Ga}} = 0.15$ (a), and $x_{\text{Ga}} = 0.25$ (b).....	A-12
Appendix Figure A1.12. Arrhenius plot of total ionic conductivity of the $\text{Na}_{4-x}\text{Zn}_{1-x}\text{M}_x(\text{PO}_4)_2$ samples synthesized by slow cooling.....	A-13
Appendix Figure A2.1. S <i>K</i> -edge TEY-XANES spectra collected for the <i>ex situ</i> TiS_3 samples.	A-22
Appendix Figure A2.2. DC polarization plots of Li_2TiS_3 pellet.	A-23
Appendix Figure A2.3. Nyquist EIS plot of Li_2TiS_3 pellet.....	A-23
Appendix Figure A2.4. Scanning electron microscopy (SEM) image of $\text{Li}_{1.13}\text{Ti}_{0.57}\text{Fe}_{0.3}\text{S}_2$ (after hand-grinding with Csp).	A-24
Appendix Figure A2.5. <i>Operando</i> UV-Vis spectroscopy experiment of $\text{Li}_{1.13}\text{Ti}_{0.57}\text{Fe}_{0.3}\text{S}_2$ LP30 Li cell.	A-24
Appendix Figure A2.6. <i>Operando</i> XRD for the cycling of $\text{Li}_{1.13}\text{Ti}_{0.57}\text{Fe}_{0.3}\text{S}_2$ up to high voltage.....	A-25
Appendix Figure A2.7. Electrochemical behaviour of $\text{Li}_{1.13}\text{Ti}_{0.57}\text{Fe}_{0.3}\text{S}_2$ phase at 55 °C.....	A-25
Appendix Figure A2.8. Voltage window opening experiment of $\text{Li}_{1.13}\text{Ti}_{0.57}\text{Fe}_{0.3}\text{S}_2$ in sloppy redox regime. ...	A-26
Appendix Figure A2.9. Spectra map of operando Mössbauer spectroscopy of the $\text{LiTi}_{0.5}\text{Fe}_{0.5}\text{S}_2$ sample over first two cycles.	A-26
Appendix Figure A2.10. The Fe $L_{2,3}$ -edge XANES spectra collected in TEY mode of the <i>ex situ</i> $\text{Li}_{1.13}\text{Ti}_{0.57}\text{Fe}_{0.3}\text{S}_2$ samples.	A-27
Appendix Figure A2.11. EELS spectra of the Ti $L_{2,3}$ edge collected for the <i>ex situ</i> $\text{Li}_{1.13}\text{Ti}_{0.57}\text{Fe}_{0.3}\text{S}_2$ samples.....	A-27
Appendix Figure A2.12. Ti $L_{2,3}$ -edge TEY-XANES of the pristine, full-charged and full-discharge $\text{Li}_{1.13}\text{Ti}_{0.57}\text{Fe}_{0.3}\text{S}_2$ samples are compared with TiS_2	A-28
Appendix Figure A2.13. S <i>K</i> -edge XANES spectra collected for the <i>ex situ</i> $\text{Li}_{1.33-2y/3}\text{Ti}_{0.67-y/3}\text{Fe}_y\text{S}_2$ samples with $y = 0 - 0.5$	A-28
Appendix Figure A2.14. S <i>K</i> -edge TEY-XANES spectra collected for the <i>ex situ</i> $\text{Li}_{1.13}\text{Ti}_{0.57}\text{Fe}_{0.3}\text{S}_2$ samples.	A-29
Appendix Figure A2.15. Details of sXAS and mRIXS of the <i>ex situ</i> $\text{Li}_{1.13}\text{Ti}_{0.57}\text{Fe}_{0.3}\text{S}_2$ samples.	A-29
Appendix Figure A2.16. XRD pattern and refinement of the $\text{Li}_{1.2}\text{Ti}^{4+}_{0.4}\text{Ti}^{3+}_{0.4}\text{S}_2$ sample.	A-30

Appendix Figure A2.17. XRD patterns of the as-synthesized $\text{Li}_{1.33-2y/3}\text{Ti}^{4+}_{0.67-y/3}\text{Co}^{2+}_y\text{S}_2$ samples.	A-31
Appendix Figure A2.18. Crystal structure of $\text{Li}_{1.2}\text{Ti}_{0.6}\text{Co}_{0.2}\text{S}_2$ sample from the SXRD pattern.....	A-31
Appendix Figure A2.19. XRD pattern of the as-synthesized Na_2TiS_3 , prepared by quenching (P2), or slow-cooling (O1).....	A-32
Appendix Figure A2.20. Crystal structure of O3- Na_2TiS_3 sample from the SXRD pattern.	A-32
Appendix Figure A2.21. Structural characterization of P2- Na_2TiS_3 by refining XRD patterns.	A-33
Appendix Figure A2.22. Reported electrochemical behaviour of the O3- Na_2TiS_3	A-34
Appendix Figure A3.1. Li-rich layered sulfide as a model material to study the practicability of anionic redox. A-40	
Appendix Figure A3.2. The evolutions of EIS Nyquist plots of Li-rich NMC during charge.	A-41
Appendix Figure A3.3. Evolution of Nyquist EIS plots of $\text{Li}_{1.2}\text{Ti}_{0.8}\text{S}_2$ at different SoCs.	A-41
Appendix Figure A3.4. Voltage window opening experiment of the $\text{Li}_{1.2}\text{Ti}_{0.8}\text{S}_2$	A-42
Appendix Figure A4.1. DC polarization plots of $\text{Li}_{1.13}\text{Ti}_{0.57}\text{Fe}_{0.3}\text{S}_2$ (LTFS) sample.	A-43
Appendix Figure A4.2. Voltage profile of $\text{Li}_{1.13}\text{Ti}_{0.57}\text{Fe}_{0.3}\text{S}_2$ cycled in ASSB at RT using increased upper cutoff voltage (> 4.2 V vs Li).....	A-43

List of Tables

Table I.1. Different classes of oxide-based solid electrolytes (crystalline). ^a	19
Table I.2. Different classes of sulfide-based solid electrolytes.	20
Table 3. Ionic conductivities of the $\text{Li}_{4-x}\text{Zn}_{1-x}\text{Ga}_x(\text{PO}_4)_2$ samples at RT obtained by extrapolation of the Arrhenius plot and at 200 °C and their activation energies (E_a).	57
Table 4. Ionic conductivities and activation energies of the $\text{Na}_{4-x}\text{Zn}_{1-x}\text{M}_x(\text{PO}_4)_2$ samples (M = Ga, Al).	71
Appendix Table A1.1. Structural Parameters for $\alpha\text{-Li}_6\text{Zn}(\text{P}_2\text{O}_7)_2$, deduced from the Rietveld refinement of the NPD.	A-13
Appendix Table A1.2. Structural Parameters for $\zeta\text{-Li}_6\text{Zn}(\text{P}_2\text{O}_7)_2$, deduced from the Rietveld refinement of the NPD recorded at 600°C.	A-14
Appendix Table A1.3. Structural Parameters for $\alpha\text{-Li}_4\text{Zn}(\text{PO}_4)_2$, deduced from the Rietveld refinement of the NPD at RT.	A-15
Appendix Table A1.4. Structural Parameters for $\beta\text{-Li}_4\text{Zn}(\text{PO}_4)_2$, deduced from the combined Rietveld refinement of the XRD and NPD recorded at 600 °C.	A-16
Appendix Table A1.5. Structural Parameters for $\beta'\text{-Li}_{3.7}\text{Zn}_{0.7}\text{Ga}_{0.3}(\text{PO}_4)_2$ deduced from the combined Rietveld refinement of the XRD and NPD patterns recorded at RT.....	A-16
Appendix Table A1.6. Structural Parameters for $\beta\text{-Li}_{3.7}\text{Zn}_{0.7}\text{Ga}_{0.3}(\text{PO}_4)_2$ deduced from the combined Rietveld refinement of the XRD and NPD patterns recorded at 600 °C.	A-17
Appendix Table A1.7. Structural Parameters for $\beta\text{-Li}_{3.5}\text{Zn}_{0.5}\text{Ga}_{0.5}(\text{PO}_4)_2$ deduced from the combined Rietveld refinement of the XRD and NPD patterns recorded at RT.....	A-17
Appendix Table A1.8. Structural Parameters for the $\gamma\text{-Na}_4\text{Zn}(\text{PO}_4)_2$, deduced from the Rietveld refinement of the SXRD Pattern.	A-18
Appendix Table A1.9. Structural Parameters for the $\beta\text{-Na}_4\text{Zn}(\text{PO}_4)_2$, deduced from the combined Rietveld refinement of the SXRD and NPD patterns. ^a	A-18
Appendix Table A2.1. Structural parameters for the TiS_3 powder-sample obtained from Rietveld refinement of the NPD pattern.	A-34
Appendix Table A2.2. Structural parameters for the Li-rich layered Li_2TiS_3 sample obtained from Rietveld refinement of the SXRD pattern.	A-35
Appendix Table A2.3. Structural parameters for the $\text{Li}_{1.13}\text{Ti}_{0.57}\text{Fe}_{0.3}\text{S}_2$ sample obtained from Rietveld refinement of the SXRD pattern.....	A-35

Appendix Table A2.4. Structural parameters for the fully charged $\sim\text{Li}_{0.1}\text{Ti}_{0.57}\text{Fe}_{0.3}\text{S}_2$ sample obtained from Rietveld refinement of SXRD pattern.	A-36
Appendix Table A2.5. Structural parameters for the discharged $\text{Li}_{1.13}\text{Ti}_{0.57}\text{Fe}_{0.3}\text{S}_2$ sample obtained from Rietveld refinement of SXRD pattern.	A-36
Appendix Table A2.6. The isomer shift (IS), the quadrupole splitting (QS), the line width (LW), and the absorption (abs) parameters from the fitting of the Mössbauer spectra obtained during in situ cycling of the $\text{Li}_{1.13}\text{Ti}_{0.57}\text{Fe}_{0.3}\text{S}_2/\text{Li}$ half-cell.	A-37
Appendix Table A2.7. Fitted Mössbauer parameters of the pristine and cycled $\text{LiTi}_{0.5}\text{Fe}_{0.5}\text{S}_2$ powder. IS, QS, LW, Abs are the isomer shift, the quadrupole splitting, the line width and absorption respectively. Isomer shift is given relative to α -Fe standard at RT.	A-37
Appendix Table A2.8. Structural parameters for the $\text{Li}_{1.2}\text{Ti}_{0.6}\text{Co}_{0.2}\text{S}_2$ sample obtained from Rietveld refinement of the SXRD pattern.	A-38
Appendix Table A2.9. Structural parameters for the O3- Na_2TiS_3 sample obtained from Rietveld refinement of the SXRD pattern.	A-39

List of Publications

This thesis includes the following articles:

1) **Sujoy Saha**, Gwenaëlle Rouse, François Fauth, Vladimir Pomjakushin, and Jean-Marie Tarascon; Influence of Temperature-Driven Polymorphism and Disorder on Ionic Conductivity in $\text{Li}_6\text{Zn}(\text{P}_2\text{O}_7)_2$. *Inorg. Chem.* 58, 1774–1781 (2019).

<http://pubs.acs.org/doi/10.1021/acs.inorgchem.8b01800>

2) **Sujoy Saha**, Gwenaëlle Rouse, Ignacio Blazquez Alcover, Matthieu Courty, Daniel Alves Dalla Corte, and Jean-Marie Tarascon; Polymorphism in $\text{Li}_4\text{Zn}(\text{PO}_4)_2$ and Stabilization of its Structural Disorder to Improve Ionic Conductivity. *Chem. Mater.* 30, 1379–1390 (2018).

<http://pubs.acs.org/doi/10.1021/acs.chemmater.7b05139>

3) **Sujoy Saha**, Gaurav Assat, Moulay Tahar Sougrati, Dominique Foix, Haifeng Li, Jean Vergnet, Soma Turi, Yang Ha, Wanli Yang, Jordi Cabana, Gwenaëlle Rouse, Artem M. Abakumov & Jean-Marie Tarascon; Exploring the bottlenecks of anionic redox in Li-rich layered sulfides. *Nat. Energy* 4, 977–987 (2019).

<http://dx.doi.org/10.1038/s41560-019-0493-0>

4) **Sujoy Saha et al.**, Improvement of Ionic Conductivity in $\text{Na}_{4-x}\text{Zn}_{1-x}\text{M}_x(\text{PO}_4)_2$ (M= Ga, Al) driven by a structural transition, *Manuscript in preparation*.

5) Florencia Marchini and **Sujoy Saha et al.**, A Li-rich layered sulfide as cathode active material in all-solid-state Li-metal batteries, *Manuscript submitted*.

References

1. International Energy Outlook 2019. (2019). Available at: www.eia.gov/ieo.
2. Abdi, H., Mohammadi-ivatloo, B., Javadi, S., Khodaei, A. R. & Dehnavi, E. Energy Storage Systems. in *Distributed Generation Systems* 333–368 (Elsevier, 2017). doi:10.1016/B978-0-12-804208-3.00007-8
3. Tarascon, J.-M. & Armand, M. Issues and challenges facing rechargeable lithium batteries. *Nature* **414**, 359–367 (2001).
4. Larcher, D. & Tarascon, J.-M. Towards greener and more sustainable batteries for electrical energy storage. *Nat. Chem.* **7**, 19–29 (2015).
5. Goodenough, J. B. & Park, K. S. The Li-ion rechargeable battery: A perspective. *J. Am. Chem. Soc.* **135**, 1167–1176 (2013).
6. Painter, D. S. Oil and Geopolitics: The Oil Crises of the 1970s and the Cold War. *Hist. Soc. Res. / Hist. Sozialforsch.* **39**, 186–208 (2014).
7. Kurzweil, P. Lithium Battery Energy Storage. in *Electrochemical Energy Storage for Renewable Sources and Grid Balancing* (eds. Moseley, P. T. & Garche, J. B. T.-E. E. S. for R. S. and G. B.) 269–307 (Elsevier, 2015). doi:10.1016/B978-0-444-62616-5.00016-4
8. Goodenough, J. B. How we made the Li-ion rechargeable battery. *Nat. Electron.* **1**, 204 (2018).
9. Whittingham, M. S. Electrical Energy Storage and Intercalation Chemistry. *Science (80-.)*. **192**, 1126–1127 (1976).
10. Whittingham, M. S. Chemistry of intercalation compounds: Metal guests in chalcogenide hosts. *Prog. Solid State Chem.* **12**, 41–99 (1978).
11. Whittingham, M. S. The Role of Ternary Phases in Cathode Reactions. *J. Electrochem. Soc.* **123**, 315 (1976).
12. Whittingham, M. S. Lithium batteries and cathode materials. *Chem. Rev.* **104**, 4271–4301 (2004).
13. Blomgren, G. E. The Development and Future of Lithium Ion Batteries. *J. Electrochem. Soc.* **164**, A5019–A5025 (2017).
14. J.B. Goodenough, K. Mizushima, P. J. W. Patent EP17400B1. (1979).
15. MIZUSHIMA, K., JONES, P., WISEMAN, P. & GOODENOUGH, J. Li_xCoO_2 ($0 < x \leq 1$): A new cathode material for batteries of high energy density. *Solid State Ionics* **3–4**, 171–174 (1981).
16. Yazami, R. & Touzain, P. A reversible graphite-lithium negative electrode for electrochemical generators. *J. Power Sources* **9**, 365–371 (1983).
17. Oberlin, A., Endo, M. & Koyama, T. Filamentous growth of carbon through benzene decomposition. *J. Cryst. Growth* **32**, 335–349 (1976).
18. Akira Yoshino, Kenichi Sanechika, T. N. Secondary battery, US patent 4668595A. (1986).
19. Yoshino, A. Development of the Lithium-Ion Battery and Recent Technological Trends. in *Lithium-Ion Batteries* (ed. Pistoia, G. B. T.-L.-I. B.) 1–20 (Elsevier, 2014). doi:10.1016/B978-0-444-59513-3.00001-7
20. Yoshino, A. The Birth of the Lithium-Ion Battery. *Angew. Chemie Int. Ed.* **51**, 5798–5800 (2012).
21. Manthiram, A. An Outlook on Lithium Ion Battery Technology. *ACS Cent. Sci.* **3**, 1063–1069 (2017).

22. Goodenough, J. B. & Kim, Y. Challenges for rechargeable Li batteries. *Chem. Mater.* **22**, 587–603 (2010).
23. Luo, K. *et al.* Charge-compensation in 3d-transition-metal-oxide intercalation cathodes through the generation of localized electron holes on oxygen. *Nat. Chem.* **8**, 684–691 (2016).
24. Goodenough, J. B. & Kim, Y. Locating redox couples in the layered sulfides with application to $\text{Cu}[\text{Cr}_2]\text{S}_4$. *J. Solid State Chem.* **182**, 2904–2911 (2009).
25. Yano, A., Shikano, M., Ueda, A., Sakaebe, H. & Ogumi, Z. LiCoO₂ Degradation Behavior in the High-Voltage Phase Transition Region and Improved Reversibility with Surface Coating. *J. Electrochem. Soc.* **164**, A6116–A6122 (2017).
26. Zhang, J.-N. *et al.* Trace doping of multiple elements enables stable battery cycling of LiCoO₂ at 4.6 V. *Nat. Energy* (2019). doi:10.1038/s41560-019-0409-z
27. Rozier, P. & Tarascon, J. M. Review—Li-Rich Layered Oxide Cathodes for Next-Generation Li-Ion Batteries: Chances and Challenges. *J. Electrochem. Soc.* **162**, A2490–A2499 (2015).
28. Ohzuku, T. & Makimura, Y. Layered Lithium Insertion Material of $\text{LiNi}_{1/2}\text{Mn}_{1/2}\text{O}_2$: A Possible Alternative to LiCoO₂ for Advanced Lithium-Ion Batteries. *Chem. Lett.* **30**, 744–745 (2001).
29. Lu, Z., MacNeil, D. D. & Dahn, J. R. Layered Cathode Materials $\text{Li}[\text{Ni}_{x/3}\text{Li}_{(1/3-2x/3)}\text{Mn}_{(2/3-x/3)}]\text{O}_2$ for Lithium-Ion Batteries. *Electrochem. Solid-State Lett.* **4**, A191 (2001).
30. Noh, H.-J., Youn, S., Yoon, C. S. & Sun, Y.-K. Comparison of the structural and electrochemical properties of layered $\text{Li}[\text{Ni}_x\text{Co}_y\text{Mn}_z]\text{O}_2$ ($x = 1/3, 0.5, 0.6, 0.7, 0.8$ and 0.85) cathode material for lithium-ion batteries. *J. Power Sources* **233**, 121–130 (2013).
31. Robert, R., Villevieille, C. & Novák, P. Enhancement of the high potential specific charge in layered electrode materials for lithium-ion batteries. *J. Mater. Chem. A* **2**, 8589 (2014).
32. Schmuck, R., Wagner, R., Hörpel, G., Placke, T. & Winter, M. Performance and cost of materials for lithium-based rechargeable automotive batteries. *Nat. Energy* **3**, 267–278 (2018).
33. Lu, Z. & Dahn, J. R. Understanding the Anomalous Capacity of $\text{Li}/\text{Li}[\text{Ni}_{x/3}\text{Li}_{(1/3-2x/3)}\text{Mn}_{(2/3-x/3)}]\text{O}_2$ Cells Using In Situ X-Ray Diffraction and Electrochemical Studies. *J. Electrochem. Soc.* **149**, A815 (2002).
34. Lu, Z., Beaulieu, L. Y., Donaberger, R. A., Thomas, C. L. & Dahn, J. R. Synthesis, Structure, and Electrochemical Behavior of $\text{Li}[\text{Ni}_x\text{Li}_{(1/3-2x/3)}\text{Mn}_{(2/3-x/3)}]\text{O}_2$. *J. Electrochem. Soc.* **149**, A778–A791 (2002).
35. Jiang, J. & Dahn, J. R. Insignificant impact of designed oxygen release from high capacity $\text{Li}[(\text{Ni}_{1/2}\text{Mn}_{1/2})_x\text{Co}_y(\text{Li}_{1/3}\text{Mn}_{2/3})_{1/3}]\text{O}_2$ ($x+y=2/3$) positive electrodes during the cycling of Li-ion cells. *Electrochim. Acta* **51**, 3413–3416 (2006).
36. Thackeray, M. M. *et al.* Li₂MnO₃-stabilized LiMO₂ (M = Mn, Ni, Co) electrodes for lithium-ion batteries. *J. Mater. Chem.* **17**, 3112 (2007).
37. Assat, G. & Tarascon, J. M. Fundamental understanding and practical challenges of anionic redox activity in Li-ion batteries. *Nat. Energy* **3**, 373–386 (2018).
38. Koga, H. *et al.* Reversible Oxygen Participation to the Redox Processes Revealed for $\text{Li}_{1.20}\text{Mn}_{0.54}\text{Co}_{0.13}\text{Ni}_{0.13}\text{O}_2$. *J. Electrochem. Soc.* **160**, A786–A792 (2013).
39. Yabuuchi, N. Solid-state Redox Reaction of Oxide Ions for Rechargeable Batteries. *Chem. Lett.*

- 46**, 412–422 (2017).
40. Seo, D.-H. *et al.* The structural and chemical origin of the oxygen redox activity in layered and cation-disordered Li-excess cathode materials. *Nat. Chem.* **8**, 692–697 (2016).
 41. Saubanère, M., McCalla, E., Tarascon, J.-M. & Doublet, M.-L. The intriguing question of anionic redox in high-energy density cathodes for Li-ion batteries. *Energy Environ. Sci.* **9**, 984–991 (2016).
 42. Okubo, M. & Yamada, A. Molecular Orbital Principles of Oxygen-Redox Battery Electrodes. *ACS Appl. Mater. Interfaces* **9**, 36463–36472 (2017).
 43. Yabuuchi, N. *et al.* Origin of stabilization and destabilization in solid-state redox reaction of oxide ions for lithium-ion batteries. *Nat. Commun.* **7**, 13814 (2016).
 44. Maitra, U. *et al.* Oxygen redox chemistry without excess alkali-metal ions in Na_{2/3}[Mg_{0.28}Mn_{0.72}]O₂. *Nat. Chem.* **10**, 288–295 (2018).
 45. Mortemard de Boisse, B. *et al.* Highly Reversible Oxygen-Redox Chemistry at 4.1 V in Na_{4/7-x}[□_{1/7}Mn_{6/7}]O₂ (□: Mn Vacancy). *Adv. Energy Mater.* **8**, 1800409 (2018).
 46. Li, W., Song, B. & Manthiram, A. High-voltage positive electrode materials for lithium-ion batteries. *Chem. Soc. Rev* **3006**, 3006 (2017).
 47. Li, B. & Xia, D. Anionic Redox in Rechargeable Lithium Batteries. *Adv. Mater.* **29**, 1701054 (2017).
 48. Sathiya, M. *et al.* Reversible anionic redox chemistry in high-capacity layered-oxide electrodes. *Nat. Mater.* **12**, 827–835 (2013).
 49. Assat, G., Delacourt, C., Corte, D. A. D. & Tarascon, J.-M. Editors' Choice—Practical Assessment of Anionic Redox in Li-Rich Layered Oxide Cathodes: A Mixed Blessing for High Energy Li-Ion Batteries. *J. Electrochem. Soc.* **163**, A2965–A2976 (2016).
 50. Assat, G. *et al.* Fundamental interplay between anionic/cationic redox governing the kinetics and thermodynamics of lithium-rich cathodes. *Nat. Commun.* **8**, 2219 (2017).
 51. McCalla, E. *et al.* Visualization of O-O peroxo-like dimers in high-capacity layered oxides for Li-ion batteries. *Science (80-.)*. **350**, 1516 LP – 1521 (2015).
 52. Pearce, P. E. *et al.* Evidence for anionic redox activity in a tridimensional-ordered Li-rich positive electrode β-Li₂IrO₃. *Nat. Mater.* **16**, 580–586 (2017).
 53. Pearce, P. *et al.* Anionic and Cationic Redox Processes in β-Li₂IrO₃ and Their Structural Implications on Electrochemical Cycling in Li-Ion Cell. *ChemRxiv* (2019). doi:10.26434/CHEMRXIV.10028603.V1
 54. Perez, A. J. *et al.* Approaching the limits of cationic and anionic electrochemical activity with the Li-rich layered rocksalt Li₃IrO₄. *Nat. Energy* **2**, 954–962 (2017).
 55. House, R. A. *et al.* Lithium manganese oxyfluoride as a new cathode material exhibiting oxygen redox. *Energy Environ. Sci.* **11**, 926 (2018).
 56. Lee, J. *et al.* Reversible Mn²⁺/Mn⁴⁺ double redox in lithium-excess cathode materials. *Nature* **556**, 185–190 (2018).
 57. Nowack, E., Schwarzenbach, D. & Hahn, T. Charge densities in CoS₂ and NiS₂ (pyrite structure). *Acta Crystallogr. Sect. B Struct. Sci.* **47**, 650–659 (1991).
 58. Poizot, P., Laruelle, S., Grugeon, S. & Tarascon, J.-M. Rationalization of the Low-Potential Reactivity of 3d-Metal-Based Inorganic Compounds toward Li. *J. Electrochem. Soc.* **149**, A1212

- (2002).
59. Yan, J. M., Huang, H. Z., Zhang, J., Liu, Z. J. & Yang, Y. A study of novel anode material CoS₂ for lithium ion battery. *J. Power Sources* **146**, 264–269 (2005).
 60. Grayfer, E. D., Pazhetnov, E. M., Kozlova, M. N., Artemkina, S. B. & Fedorov, V. E. Anionic Redox Chemistry in Polysulfide Electrode Materials for Rechargeable Batteries. *ChemSusChem* **10**, 4805–4811 (2017).
 61. Zheng, L. *et al.* Na₂MnO₃ as cathode materials for Na ion batteries: From first-principles investigations. *Solid State Ionics* **320**, 210–214 (2018).
 62. Gao, X. *et al.* Electronic Properties, Phase Transformation, and Anionic Redox of Monoclinic Na₂MnO₃ Cathode Material for Sodium-Ion Batteries: First-Principle Calculations. *ChemElectroChem* **6**, 3987–3993 (2019).
 63. Kataoka, R., Kitta, M., Ozaki, H., Takeichi, N. & Kiyobayashi, T. Spinel manganese oxide: A high capacity positive electrode material for the sodium ion battery. *Electrochim. Acta* **212**, 458–464 (2016).
 64. Van Nghia, N., Ou, P.-W. & Hung, I.-M. Synthesis and Electrochemical Properties of Sodium Manganese-based Oxide Cathode Material for Sodium-ion Batteries. *Electrochim. Acta* **161**, 63–71 (2015).
 65. Nghia, N. Van, Ou, P.-W. & Hung, I.-M. Synthesis and electrochemical performances of layered NaLi_{0.2}Ni_{0.2}Mn_{0.6}O₂ cathode for sodium-ion batteries. *Ceram. Int.* **41**, 10199–10207 (2015).
 66. Yabuuchi, N. *et al.* A new electrode material for rechargeable sodium batteries: P2-type Na_{2/3}[Mg_{0.28}Mn_{0.72}]O₂ with anomalously high reversible capacity. *J. Mater. Chem. A* **2**, 16851–16855 (2014).
 67. Bai, X. *et al.* Anionic Redox Activity in a Newly Zn-Doped Sodium Layered Oxide P2-Na_{2/3}Mn_{1-y}Zn_yO₂ (0 < y < 0.23). *Adv. Energy Mater.* **8**, 1802379 (2018).
 68. Yabuuchi, N. *et al.* New O2/P2-type Li-Excess Layered Manganese Oxides as Promising Multi-Functional Electrode Materials for Rechargeable Li/Na Batteries. *Adv. Energy Mater.* **4**, 1301453 (2014).
 69. Cheng, C. *et al.* Elucidation of anionic and cationic redox reactions in a prototype sodium layered oxide cathode. *ACS Appl. Mater. Interfaces* **acsami.9b13013** (2019). doi:10.1021/acsami.9b13013
 70. Shadike, Z. *et al.* Antisite occupation induced single anionic redox chemistry and structural stabilization of layered sodium chromium sulfide. *Nat. Commun.* **8**, 566 (2017).
 71. Wang, T. *et al.* Anionic redox reaction in layered NaCr_{2/3}Ti_{1/3}S₂ through electron holes formation and dimerization of S–S. *Nat. Commun.* **10**, 4458 (2019).
 72. Tamaru, M., Wang, X., Okubo, M. & Yamada, A. Layered Na₂RuO₃ as a cathode material for Na-ion batteries. *Electrochem. commun.* **33**, 23–26 (2013).
 73. Mortemard de Boisse, B. *et al.* Intermediate honeycomb ordering to trigger oxygen redox chemistry in layered battery electrode. *Nat. Commun.* **7**, 11397 (2016).
 74. Perez, A. J. *et al.* Strong Oxygen Participation in the Redox Governing the Structural and Electrochemical Properties of Na-Rich Layered Oxide Na₂IrO₃. *Chem. Mater.* **28**, 8278–8288 (2016).
 75. Pearce, P. E. *et al.* β-Na_{1.7}IrO₃: A Tridimensional Na-Ion Insertion Material with a Redox

- Active Oxygen Network. *Chem. Mater.* **30**, 3285–3293 (2018).
76. Rozier, P. *et al.* Anionic redox chemistry in Na-rich $\text{Na}_2\text{Ru}_{1-y}\text{Sn}_y\text{O}_3$ positive electrode material for Na-ion batteries. *Electrochem. commun.* **53**, 29–32 (2015).
77. Zhang, X. *et al.* Manganese-Based Na-Rich Materials Boost Anionic Redox in High-Performance Layered Cathodes for Sodium-Ion Batteries. *Adv. Mater.* **31**, 1807770 (2019).
78. Pele, V. Nouveaux matériaux d'électrodes pour microbatteries au sodium, Université de Bordeaux. (2016).
79. Nasu, A., Otoyama, M., Sakuda, A., Hayashi, A. & Tatsumisago, M. Amorphous Na_2TiS_3 as an Active Material for All-solid-state Sodium Batteries. *Chem. Lett* **48**, 288–290 (2019).
80. Xu, K. Nonaqueous Liquid Electrolytes for Lithium-Based Rechargeable Batteries. *Chem. Rev.* **104**, 4303–4418 (2004).
81. Lagadec, M. F., Zahn, R. & Wood, V. Characterization and performance evaluation of lithium-ion battery separators. *Nat. Energy* **4**, 16–25 (2019).
82. Galushkin, N. E., Yazvinskaya, N. N. & Galushkin, D. N. Mechanism of Thermal Runaway in Lithium-Ion Cells. *J. Electrochem. Soc.* **165**, A1303–A1308 (2018).
83. Feng, X. *et al.* Key Characteristics for Thermal Runaway of Li-ion Batteries. *Energy Procedia* **158**, 4684–4689 (2019).
84. Golubkov, A. W. *et al.* Thermal runaway of large automotive Li-ion batteries. *RSC Adv.* **8**, 40172–40186 (2018).
85. Dell's Exploding Computer and Other Image Problems - The New York Times, published on 10/07/2006. Available at: <https://www.nytimes.com/2006/07/10/technology/10dell.html>. (Accessed: 16th October 2019)
86. Blaze on Boeing 787 Dreamliner at Heathrow 'triggered by trapped battery wires' report reveals - Mirror Online; published on 19/08/2015. Available at: <https://www.mirror.co.uk/news/uk-news/blaze-boeing-787-dreamliner-heathrow-6277905>. (Accessed: 16th October 2019)
87. Tesla Model S catches on fire in France during test drive; published on 15/08/2016. Available at: <https://www.teslarati.com/tesla-model-s-fire-france-test-drive/>. (Accessed: 16th October 2019)
88. Why Are Samsung's Galaxy Note 7 Phones Exploding?; published on 4/09/2016. Available at: <https://www.forbes.com/sites/jvchamary/2016/09/04/samsung-note7-battery/#1480a13337ca>. (Accessed: 16th October 2019)
89. Gallagher, S. Boeing's Dreamliner Batteries "Inherently Unsafe"—And Yours May be Too, <https://arstechnica.com/information-technology/2013/01/boeings-dreamliner-batteries-inherently-unsafe-and-yours-may-be-too/>, (accessed July 29, 2017). *Ars Tech* (2013).
90. Meier, F. & Woodyard, C. Feds review third Tesla fire as shares fall again, <https://www.usatoday.com/story/money/cars/2013/11/07/third-fire-in-tesla-model-s-reported/3465717/> (accessed July 29, 2017). *USA Today* (2016).
91. Oh, G., Hirayama, M., Kwon, O., Suzuki, K. & Kanno, R. Bulk-Type All Solid-State Batteries with 5 V Class $\text{LiNi}_{0.5}\text{Mn}_{1.5}\text{O}_4$ Cathode and $\text{Li}_{10}\text{GeP}_2\text{S}_{12}$ Solid Electrolyte. *Chem. Mater.* **28**, 2634–2640 (2016).
92. Han, X. *et al.* Negating interfacial impedance in garnet-based solid-state Li metal batteries. *Nat. Mater.* **16**, 572–579 (2017).

93. Li, J., Ma, C., Chi, M., Liang, C. & Dudney, N. J. Solid electrolyte: The key for high-voltage lithium batteries. *Adv. Energy Mater.* **5**, 1–6 (2015).
94. Manthiram, A., Yu, X. & Wang, S. Lithium battery chemistries enabled by solid-state electrolytes. *Nat. Rev. Mater.* **2**, 1–16 (2017).
95. Research Progress: Next Generation Secondary Batteries | TOYOTA MOTOR CORPORATION GLOBAL WEBSITE. Available at: http://www.toyota.com.cn/innovation/environmental_technology/next_generation_secondary_batteries.html. (Accessed: 16th October 2019)
96. Zeier, W. G. & Janek, J. A solid future for battery development. *Nat. Energy* **1**, 16141 (2016).
97. Yung-Fang Yu Yao & Kummer, J. T. Ion exchange properties of and rates of ionic diffusion in beta-alumina. *J. Inorg. Nucl. Chem.* **29**, 2453–2475 (1967).
98. Lu, X., Lemmon, J. P., Sprenkle, V. & Yang, Z. Sodium-beta alumina batteries: Status and challenges. *JOM* **62**, 31–36 (2010).
99. Dunn, B., Kamath, H. & Tarascon, J.-M. Electrical Energy Storage for the Grid: A Battery of Choices. *Science* (80-.). **334**, 928–935 (2011).
100. Dudney, N. J. Solid-state thin-film rechargeable batteries. *Mater. Sci. Eng. B* **116**, 245–249 (2005).
101. BATES, J. Electrical properties of amorphous lithium electrolyte thin films. *Solid State Ionics* **53–56**, 647–654 (1992).
102. Bates, J. Thin-film lithium and lithium-ion batteries. *Solid State Ionics* **135**, 33–45 (2000).
103. Sudworth, J. The sodium/nickel chloride (ZEBRA) battery. *J. Power Sources* **100**, 149–163 (2001).
104. Bates, J. B. *et al.* Fabrication and characterization of amorphous lithium electrolyte thin films and rechargeable thin-film batteries. *J. Power Sources* **43**, 103–110 (1993).
105. Samson, A. J., Hofstetter, K., Bag, S. & Thangadurai, V. A bird’s-eye view of Li-stuffed garnet-type Li₇La₃Zr₂O₁₂ ceramic electrolytes for advanced all-solid-state Li batteries. *Energy Environ. Sci.* 1–502 (2019). doi:10.1039/C9EE01548E
106. Garbayo, I. *et al.* Glass-Type Polyamorphism in Li-Garnet Thin Film Solid State Battery Conductors. *Adv. Energy Mater.* **8**, 1702265 (2018).
107. Faraday, M. Experimental Researches in Electricity, third series. *Philos. Trans. R. Soc. London* **123**, 23–54 (1833).
108. Funke, K. Solid State Ionics: from Michael Faraday to green energy—the European dimension. *Sci. Technol. Adv. Mater.* **14**, 043502 (2013).
109. E. Masdupuy. No Title. *Ann. Chim. Paris Ser. 13* 527 (1957).
110. Goodenough, J. B., Hong, H. -P., Kafalas, J. A. & J. Goodenough, H. P. H. and J. K. Fast Na⁺-ion transport in skeleton structures. *Mater. Res. Bull.* **11**, 203–220 (1976).
111. SUBRAMANIAN, M., SUBRAMANIAN, R. & CLEARFIELD, A. Lithium ion conductors in the system AB(IV)₂(PO₄)₃ (B = Ti, Zr and Hf). *Solid State Ionics* **18–19**, 562–569 (1986).
112. Aono, H., Sugimoto, E., Sadaoka, Y., Imanaka, N. & Adachi, G. Y. Ionic Conductivity of Solid Electrolytes Based on Lithium Titanium Phosphate. *J. Electrochem. Soc.* **137**, 1023–1027 (1990).

113. Kennedy, J. H. & Yang, Y. Glass-forming region and structure in $\text{SiS}_2\text{-Li}_2\text{S-LiX}$ ($X = \text{Br, I}$). *J. Solid State Chem.* **69**, 252–257 (1987).
114. KENNEDY, J., SAHAMI, S., SHEA, S. & ZHANG, Z. Preparation and conductivity measurements of $\text{SiS}_2\text{-Li}_2\text{S}$ glasses doped with LiBr and LiCl . *Solid State Ionics* **18–19**, 368–371 (1986).
115. Kennedy, J. H. Further Characterization of $\text{SiS}_2\text{-Li}_2\text{S}$ Glasses Doped with Lithium Halide. *J. Electrochem. Soc.* **135**, 859 (1988).
116. Mercier, R., Malugani, J.-P., Fahys, B. & Robert, G. Superionic conduction in $\text{Li}_2\text{S-P}_2\text{S}_5\text{-LiI}$ glasses. *Solid State Ionics* **5**, 663–666 (1981).
117. JONES, S., AKRIDGE, J. & SHOKOOHI, F. Thin film rechargeable Li batteries. *Solid State Ionics* **69**, 357–368 (1994).
118. Kanehori, K., Matsumoto, K., Miyauchi, K. & Kudo, T. Thin film solid electrolyte and its application to secondary lithium cell. *Solid State Ionics* **9–10**, 1445–1448 (1983).
119. Inaguma, Y. *et al.* High ionic conductivity in lithium lanthanum titanate. *Solid State Commun.* **86**, 689–693 (1993).
120. Hong, H. Y. P. Crystal structure and ionic conductivity of $\text{Li}_{14}\text{Zn}(\text{GeO}_4)_4$ and other new Li^+ superionic conductors. *Mater. Res. Bull.* **13**, 117–124 (1978).
121. TACHEZ, M., MALUGANI, J., MERCIER, R. & ROBERT, G. Ionic conductivity of and phase transition in lithium thiophosphate Li_3PS_4 . *Solid State Ionics* **14**, 181–185 (1984).
122. Xu, X., Wen, Z., Yang, X. & Chen, L. Dense nanostructured solid electrolyte with high Li-ion conductivity by spark plasma sintering technique. *Mater. Res. Bull.* **43**, 2334–2341 (2008).
123. Murugan, R., Thangadurai, V. & Weppner, W. Fast lithium ion conduction in garnet-type $\text{Li}_7\text{La}_3\text{Zr}_2\text{O}_{12}$. *Angew. Chemie - Int. Ed.* **46**, 7778–7781 (2007).
124. Harada, Y., Ishigaki, T., Kawai, H. & Kuwano, J. Lithium ion conductivity of polycrystalline perovskite $\text{La}_{0.672x}\text{Li}_{3x}\text{TiO}_3$ with ordered and disordered arrangements of the A-site ions. *Solid State Ionics* **108**, 407–413 (1998).
125. Bachman, J. C. *et al.* Inorganic Solid-State Electrolytes for Lithium Batteries: Mechanisms and Properties Governing Ion Conduction. *Chem. Rev.* **116**, 140–162 (2016).
126. Kanno, R. & Murayama, M. Lithium Ionic Conductor Thio-LISICON: The $\text{Li}_2\text{S-GeS}_2\text{-P}_2\text{S}_5$ System. *J. Electrochem. Soc.* **148**, A742 (2001).
127. Kamaya, N. *et al.* A lithium superionic conductor. *Nat. Mater.* **10**, 682–6 (2011).
128. Liu, Z. *et al.* Anomalous High Ionic Conductivity of Nanoporous $\beta\text{-Li}_3\text{PS}_4$. *J. Am. Chem. Soc.* **135**, 975–978 (2013).
129. Zhang, Z. *et al.* New horizons for inorganic solid state ion conductors. *Energy Environ. Sci.* **11**, 1945–1976 (2018).
130. Thangadurai, V., Narayanan, S. & Pinzaru, D. Garnet-type solid-state fast Li ion conductors for Li batteries: critical review. *Chem. Soc. Rev.* **43**, 4714–27 (2014).
131. YAMANE, H. *et al.* Crystal structure of a superionic conductor, $\text{Li}_7\text{P}_3\text{S}_{11}$. *Solid State Ionics* **178**, 1163–1167 (2007).
132. Xie, H., Goodenough, J. B. & Li, Y. $\text{Li}_{1.2}\text{Zr}_{1.9}\text{Ca}_{0.1}(\text{PO}_4)_3$, a room-temperature Li-ion solid electrolyte. *J. Power Sources* **196**, 7760–7762 (2011).

133. Monchak, M. *et al.* Lithium Diffusion Pathway in $\text{Li}_{1.3}\text{Al}_{0.3}\text{Ti}_{1.7}(\text{PO}_4)_3$ (LATP) Superionic Conductor. *Inorg. Chem.* **55**, 2941–2945 (2016).
134. Liu, Q. *et al.* Safe LAGP-based all solid-state Li metal batteries with plastic super-conductive interlayer enabled by In-situ solidification. *Energy Storage Mater.* (2019). doi:10.1016/j.ensm.2019.09.023
135. Ma, C. *et al.* Atomic-scale origin of the large grain-boundary resistance in perovskite Li-ion-conducting solid electrolytes. *Energy Environ. Sci.* **7**, 1638 (2014).
136. Hu, Y.-W. Ionic Conductivity of Lithium Orthosilicate-Lithium Phosphate Solid Solutions. *J. Electrochem. Soc.* **124**, 1240 (1977).
137. Hong, H. -P. Crystal structure and ionic conductivity of $\text{Li}_{14}\text{Zn}(\text{GeO}_4)_4$ and other new Li^+ superionic conductors. *Mater. Res. Bull.* **13**, 117–124 (1978).
138. Deng, Y. *et al.* Structural and Mechanistic Insights into Fast Lithium-Ion Conduction in Li_4SiO_4 - Li_3PO_4 Solid Electrolytes. *J. Am. Chem. Soc.* **137**, 9136–45 (2015).
139. TATSUMISAGO, M. *et al.* Electrical and mechanical properties of glass and glass-ceramic electrolytes in the system Li_3BO_3 – Li_2SO_4 . *J. Ceram. Soc. Japan* **125**, 433–437 (2017).
140. Tatsumisago, M., Takano, R., Tadanaga, K. & Hayashi, A. Preparation of Li_3BO_3 - Li_2SO_4 glass-ceramic electrolytes for all-oxide lithium batteries. *J. Power Sources* **270**, 603–607 (2014).
141. Abbate, M. *et al.* Controlled-valence properties of $\text{La}_{1-x}\text{Sr}_x\text{FeO}_3$ and $\text{La}_{1-x}\text{Sr}_x\text{MnO}_3$ studied by soft-x-ray absorption spectroscopy. *Phys. Rev. B* **46**, 4511–4519 (1992).
142. Kalita, D. J., Lee, S. H., Lee, K. S., Ko, D. H. & Yoon, Y. S. Ionic conductivity properties of amorphous Li - La - Zr - O solid electrolyte for thin film batteries. *Solid State Ionics* **229**, 14–19 (2012).
143. Homma, K. *et al.* Crystal structure and phase transitions of the lithium ionic conductor Li_3PS_4 . *Solid State Ionics* **182**, 53–58 (2011).
144. Kuhn, A. *et al.* A new ultrafast superionic Li-conductor: ion dynamics in $\text{Li}_{11}\text{Si}_2\text{PS}_{12}$ and comparison with other tetragonal LGPS-type electrolytes. *Phys. Chem. Chem. Phys.* **16**, 14669–14674 (2014).
145. Bron, P. *et al.* $\text{Li}_{10}\text{SnP}_2\text{S}_{12}$: An Affordable Lithium Superionic Conductor. *J. Am. Chem. Soc.* **135**, 15694–15697 (2013).
146. Deiseroth, H.-J. *et al.* $\text{Li}_6\text{PS}_5\text{X}$: A Class of Crystalline Li-Rich Solids With an Unusually High Li^+ Mobility. *Angew. Chemie Int. Ed.* **47**, 755–758 (2008).
147. Deiseroth, H. *et al.* Li_7PS_6 and $\text{Li}_6\text{PS}_5\text{X}$ (X: Cl, Br, I): Possible Three-dimensional Diffusion Pathways for Lithium Ions and Temperature Dependence of the Ionic Conductivity by Impedance Measurements. *Z. Anorg. Allg. Chem.* **637**, 1287–1294 (2011).
148. Adeli, P. *et al.* Boosting Solid-State Diffusivity and Conductivity in Lithium Superionic Argyrodites by Halide Substitution. *Angew. Chemie Int. Ed.* **58**, 8681–8686 (2019).
149. Seino, Y., Ota, T., Takada, K., Hayashi, A. & Tatsumisago, M. A sulphide lithium super ion conductor is superior to liquid ion conductors for use in rechargeable batteries. *Energy Environ. Sci.* **7**, 627–631 (2014).
150. Wenzel, S. *et al.* Interphase formation and degradation of charge transfer kinetics between a lithium metal anode and highly crystalline $\text{Li}_7\text{P}_3\text{S}_{11}$ solid electrolyte. *Solid State Ionics* **286**, 24–33 (2016).

151. Mizuno, F., Hayashi, A., Tadanaga, K. & Tatsumisago, M. High lithium ion conducting glass-ceramics in the system $\text{Li}_2\text{S}-\text{P}_2\text{S}_5$. *Solid State Ionics* **177**, 2721–2725 (2006).
152. Nose, M., Kato, A., Sakuda, A., Hayashi, A. & Tatsumisago, M. Evaluation of mechanical properties of $\text{Na}_2\text{S}-\text{P}_2\text{S}_5$ sulfide glass electrolytes. *J. Mater. Chem. A* **3**, 22061–22065 (2015).
153. Shiotani, S., Ohara, K., Tsukasaki, H., Mori, S. & Kanno, R. Pair distribution function analysis of sulfide glassy electrolytes for all-solid-state batteries: Understanding the improvement of ionic conductivity under annealing condition. *Sci. Rep.* **7**, 6972 (2017).
154. Sakuda, A., Hayashi, A. & Tatsumisago, M. Sulfide solid electrolyte with favorable mechanical property for all-solid-state lithium battery. *Sci. Rep.* **3**, 2–6 (2013).
155. Dunn, B., Schwarz, B. B., Thomas, J. O. & Morgan, P. E. D. Preparation and structure of Li-Stabilized Na^+ β "-Alumina single crystals. *Solid State Ionics* **28–30**, 301–305 (1988).
156. Wenzel, S. *et al.* Interfacial Reactivity Benchmarking of the Sodium Ion Conductors Na_3PS_4 and Sodium β -Alumina for Protected Sodium Metal Anodes and Sodium All-Solid-State Batteries. *ACS Appl. Mater. Interfaces* **8**, 28216–28224 (2016).
157. Hayashi, A., Noi, K., Sakuda, A. & Tatsumisago, M. Superionic glass-ceramic electrolytes for room-temperature rechargeable sodium batteries. *Nat. Commun.* **3**, 856 (2012).
158. Duchardt, M., Ruschewitz, U., Adams, S., Dehnen, S. & Roling, B. Vacancy-Controlled Na^+ Superion Conduction in $\text{Na}_{11}\text{Sn}_2\text{P}_2\text{S}_{12}$. *Angew. Chemie Int. Ed.* 1351–1355 (2017). doi:10.1002/anie.201712769
159. Wang, H. *et al.* An Air-Stable Na_3SbS_4 Superionic Conductor Prepared by a Rapid and Economic Synthetic Procedure. *Angew. Chemie - Int. Ed.* **55**, 8551–8555 (2016).
160. Chu, I.-H. *et al.* Room-Temperature All-solid-state Rechargeable Sodium-ion Batteries with a Cl-doped Na_3PS_4 Superionic Conductor. *Sci. Rep.* **6**, 33733 (2016).
161. Zhang, L. *et al.* Na_3PSe_4 : A Novel Chalcogenide Solid Electrolyte with High Ionic Conductivity. *Adv. Energy Mater.* **5**, 1501294 (2015).
162. Hayashi, A. *et al.* A sodium-ion sulfide solid electrolyte with unprecedented conductivity at room temperature. *Nat. Commun.* **10**, 5266 (2019).
163. Tian, Y. *et al.* Compatibility issues between electrodes and electrolytes in solid-state batteries. *Energy Environ. Sci.* **10**, 1150–1166 (2017).
164. *Solid state electrochemistry.* (Cambridge University Press, 1995).
165. Iwasaki, R. *et al.* Weak Anisotropic Lithium-Ion Conductivity in Single Crystals of $\text{Li}_{10}\text{GeP}_2\text{S}_{12}$. *Chem. Mater.* **31**, 3694–3699 (2019).
166. Kuhn, A., Köhler, J. & Lotsch, B. V. Single-crystal X-ray structure analysis of the superionic conductor $\text{Li}_{10}\text{GeP}_2\text{S}_{12}$. *Phys. Chem. Chem. Phys.* **15**, 11620 (2013).
167. Weber, D. A. *et al.* Structural Insights and 3D Diffusion Pathways within the Lithium Superionic Conductor $\text{Li}_{10}\text{GeP}_2\text{S}_{12}$. *Chem. Mater.* **28**, 5905–5915 (2016).
168. Liang, X. *et al.* In-Channel and In-Plane Li Ion Diffusions in the Superionic Conductor $\text{Li}_{10}\text{GeP}_2\text{S}_{12}$ Probed by Solid-State NMR. *Chem. Mater.* **27**, 5503–5510 (2015).
169. Adams, S. & Prasada Rao, R. Structural requirements for fast lithium ion migration in $\text{Li}_{10}\text{GeP}_2\text{S}_{12}$. *J. Mater. Chem.* **22**, 7687 (2012).
170. Mo, Y., Ong, S. P. & Ceder, G. First Principles Study of the $\text{Li}_{10}\text{GeP}_2\text{S}_{12}$ Lithium Super Ionic Conductor Material. *Chem. Mater.* **24**, 15–17 (2012).

171. Phani Dathar, G. K., Balachandran, J., Kent, P. R. C., Rondinone, A. J. & Ganesh, P. Li-ion site disorder driven superionic conductivity in solid electrolytes: a first-principles investigation of β -Li₃PS₄. *J. Mater. Chem. A* **5**, 1153–1159 (2017).
172. Ong, S. P. *et al.* Phase stability, electrochemical stability and ionic conductivity of the Li_{10+x}MP₂X₁₂ (M = Ge, Si, Sn, Al or P, and X = O, S or Se) family of superionic conductors. *Energy Environ. Sci.* **12**, 148–156 (2012).
173. Garcia, A., Torres-Trevino, G. & West, A. R. New lithium ion conductors based on the γ -LiAlO₂ structure. *Solid State Ionics* **40–41**, 13–17 (1990).
174. Chen, Y., Rangasamy, E., Liang, C. & An, K. Origin of High Li⁺ Conduction in Doped Li₇La₃Zr₂O₁₂ Garnets. *Chem. Mater.* **27**, 5491–5494 (2015).
175. Larraz, G., Orera, A. & Sanjuán, M. L. Cubic phases of garnet-type Li₇La₃Zr₂O₁₂: the role of hydration. *J. Mater. Chem. A* **1**, 11419 (2013).
176. Wu, J.-F. *et al.* Gallium-Doped Li₇La₃Zr₂O₁₂ Garnet-Type Electrolytes with High Lithium-Ion Conductivity. *ACS Appl. Mater. Interfaces* **9**, 1542–1552 (2017).
177. Liu, Z. *et al.* Anomalous High Ionic Conductivity of Nanoporous β -Li₃PS₄. *J. Am. Chem. Soc.* **135**, 975–978 (2013).
178. Ahn, B. T. & Huggins, R. A. Synthesis and lithium conductivities of Li₂Si₃S₃ and Li₄Si₄S₄. *Mater. Res. Bull.* **24**, 889–897 (1989).
179. Wang, Y. *et al.* Design principles for solid-state lithium superionic conductors. *Nat. Mater.* **14**, 1026–1031 (2015).
180. He, X., Zhu, Y. & Mo, Y. Origin of fast ion diffusion in super-ionic conductors. *Nat. Commun.* **8**, 15893 (2017).
181. Zhu, Y., He, X. & Mo, Y. Origin of Outstanding Stability in the Lithium Solid Electrolyte Materials: Insights from Thermodynamic Analyses Based on First-Principles Calculations. *ACS Appl. Mater. Interfaces* **7**, 23685–23693 (2015).
182. Park, K. H. *et al.* Design Strategies, Practical Considerations, and New Solution Processes of Sulfide Solid Electrolytes for All-Solid-State Batteries. *Adv. Energy Mater.* **8**, 1800035 (2018).
183. Schwöbel, A., Hausbrand, R. & Jaegermann, W. Interface reactions between LiPON and lithium studied by in-situ X-ray photoemission. *Solid State Ionics* **273**, 51–54 (2015).
184. Lepley, N. D., Holzwarth, N. A. W. & Du, Y. A. Structures, Li⁺ mobilities, and interfacial properties of solid electrolytes Li₃PS₄ and Li₃PO₄ from first principles. *Phys. Rev. B - Condens. Matter Mater. Phys.* **88**, (2013).
185. Wenzel, S. *et al.* Direct Observation of the Interfacial Instability of the Fast Ionic Conductor Li₁₀GeP₂S₁₂ at the Lithium Metal Anode. *Chem. Mater.* **28**, 2400–2407 (2016).
186. Han, F., Zhu, Y., He, X., Mo, Y. & Wang, C. Electrochemical Stability of Li₁₀GeP₂S₁₂ and Li₇La₃Zr₂O₁₂ Solid Electrolytes. *Adv. Energy Mater.* **6**, 1501590 (2016).
187. Han, F., Gao, T., Zhu, Y., Gaskell, K. J. & Wang, C. A battery made from a single material. *Adv. Mater.* **27**, 3473–3483 (2015).
188. Chen, C. H. & Amine, K. Ionic conductivity, lithium insertion and extraction of lanthanum lithium titanate. *Solid State Ionics* **144**, 51–57 (2001).
189. Wenzel, S., Leichtweiss, T., Krüger, D., Sann, J. & Janek, J. Interphase formation on lithium solid electrolytes - An in situ approach to study interfacial reactions by photoelectron

- spectroscopy. *Solid State Ionics* **278**, 98–105 (2015).
190. Hartmann, P. *et al.* Degradation of NASICON-type materials in contact with lithium metal: Formation of mixed conducting interphases (MCI) on solid electrolytes. *J. Phys. Chem. C* **117**, 21064–21074 (2013).
 191. Feng, J. K., Lu, L. & Lai, M. O. Lithium storage capability of lithium ion conductor $\text{Li}_{1.5}\text{Al}_{0.5}\text{Ge}_{1.5}(\text{PO}_4)_3$. *J. Alloys Compd.* **501**, 255–258 (2010).
 192. Alpen, U. v., Bell, M. F., Wichelhaus, W., Cheung, K. Y. & Dudley, G. J. Ionic conductivity of $\text{Li}_{14}\text{Zn}(\text{GeO}_4)_4$ (Lisicon). *Electrochim. Acta* **23**, 1395–1397 (1978).
 193. Zhang, W. *et al.* Interfacial Processes and Influence of Composite Cathode Microstructure Controlling the Performance of All-Solid-State Lithium Batteries. *ACS Appl. Mater. Interfaces* **9**, 17835–17845 (2017).
 194. Kato, Y. *et al.* High-power all-solid-state batteries using sulfide superionic conductors. *Nat. Energy* **1**, 16030 (2016).
 195. Cheng, L. *et al.* Effect of Surface Microstructure on Electrochemical Performance of Garnet Solid Electrolytes. *ACS Appl. Mater. Interfaces* **7**, 2073–2081 (2015).
 196. Xu, B. *et al.* Li_3PO_4 -added garnet-type $\text{Li}_{6.5}\text{La}_3\text{Zr}_{1.5}\text{Ta}_{0.5}\text{O}_{12}$ for Li-dendrite suppression. *J. Power Sources* **354**, 68–73 (2017).
 197. Han, F. *et al.* High electronic conductivity as the origin of lithium dendrite formation within solid electrolytes. *Nat. Energy* **4**, 187–196 (2019).
 198. Koerver, R. *et al.* Capacity Fade in Solid-State Batteries: Interphase Formation and Chemomechanical Processes in Nickel-Rich Layered Oxide Cathodes and Lithium Thiophosphate Solid Electrolytes. *Chem. Mater.* **29**, 5574–5582 (2017).
 199. Yubuchi, S. *et al.* Preparation of high lithium-ion conducting $\text{Li}_6\text{PS}_5\text{Cl}$ solid electrolyte from ethanol solution for all-solid-state lithium batteries. *J. Power Sources* **293**, 941–945 (2015).
 200. Ito, S. *et al.* A rocking chair type all-solid-state lithium ion battery adopting Li_2O – ZrO_2 coated $\text{LiNi}_{0.8}\text{Co}_{0.15}\text{Al}_{0.05}\text{O}_2$ and a sulfide based electrolyte. *J. Power Sources* **248**, 943–950 (2014).
 201. Machida, N., Kashiwagi, J., Naito, M. & Shigematsu, T. Electrochemical properties of all-solid-state batteries with ZrO_2 -coated $\text{LiNi}_{1/3}\text{Mn}_{1/3}\text{Co}_{1/3}\text{O}_2$ as cathode materials. *Solid State Ionics* **225**, 354–358 (2012).
 202. Ohta, N. *et al.* LiNbO_3 -coated LiCoO_2 as cathode material for all solid-state lithium secondary batteries. *Electrochem. commun.* **9**, 1486–1490 (2007).
 203. Chen, C. & Guo, X. Space Charge Layer Effect in Solid State Ion Conductors and Lithium Batteries: Principle and Perspective. *Acta Chim. Slov.* **63**, 489–495 (2016).
 204. Fingerle, M., Buchheit, R., Sicolo, S., Albe, K. & Hausbrand, R. Reaction and Space Charge Layer Formation at the LiCoO_2 – LiPON Interface: Insights on Defect Formation and Ion Energy Level Alignment by a Combined Surface Science–Simulation Approach. *Chem. Mater.* **29**, 7675–7685 (2017).
 205. Gittleson, F. S. & El Gabaly, F. Non-Faradaic Li^+ Migration and Chemical Coordination across Solid-State Battery Interfaces. *Nano Lett.* **17**, 6974–6982 (2017).
 206. Liu, T. *et al.* Non-successive degradation in bulk-type all-solid-state lithium battery with rigid interfacial contact. *Electrochem. commun.* **79**, 1–4 (2017).

207. Ji, L. N. *et al.* Subsolidus phase relations of the ZnO-Li₂O-P₂O₅ system. *J. Alloys Compd.* **486**, 352–356 (2009).
208. Boultif, A. & Louer, D. Indexing of powder diffraction patterns for low-symmetry lattices by the successive dichotomy method. *J. Appl. Cryst.* **24**, 987–993 (1991).
209. Favre-Nicolin, V. & Černý, R. FOX, ‘free objects for crystallography’: A modular approach to ab initio structure determination from powder diffraction. *J. Appl. Crystallogr.* **35**, 734–743 (2002).
210. Sandomirskii, P. A., Simonov, M. A. & Belov, N. V. Crystal structure of the mixed lithium zinc orthophosphate Li₄Zn[PO₄]₂. *Dokl. Akad. Nauk SSSR* **228**, 344 (1976).
211. Torres-Treviño, G. & West, A. R. Compound Formation, Crystal Chemistry, and Phase Equilibria in the System Li₃PO₄-Zn₃(PO₄). **66**, 56–66 (1986).
212. Torres-Treviño, G. & West, A. R. Thermodynamic, kinetic, and conductivity studies of an order-disorder transition in Li₄Zn(PO₄)₂. *J. Solid State Chem.* **71**, 380–383 (1987).
213. Jensen, T. R., Hazell, R. G., Christensen, A. N. & Hanson, J. C. Hydrothermal Synthesis of Lithium Zinc Phosphates: Structural Investigation of Twinned α-Li₄Zn(PO₄)₂ and a High Temperature Polymorph β-Li₄Zn(PO₄)₂. *J. Solid State Chem.* **351**, 341–351 (2002).
214. Anantharamulu, N. *et al.* A wide-ranging review on Nasicon type materials. *J. Mater. Sci.* **46**, 2821–2837 (2011).
215. Lander, L. *et al.* Synthesis and Electrochemical Performance of the Orthorhombic Li₂Fe(SO₄)₂ Polymorph for Li-Ion Batteries. *Chem. Mater.* **26**, 4178–4189 (2014).
216. Irvine, J. T. S., Sinclair, D. C. & West, A. R. Electroceramics: Characterization by Impedance Spectroscopy. *Adv. Mater.* **2**, 132–138 (1990).
217. Gopi Krishna Phani Dathar, Janakiraman Balachandran, a Paul R. C. Kent, ab Adam J. Rondinonea and P. Ganesh*Gopi Krishna Phani Dathar, ‡a Janakiraman Balachandran, a Paul R. C. Kent, ab A. J. R. and P. G. Li-ion site disorder driven superionic conductivity in solid electrolytes- A first-principles investigation of β-Li₃PS₄,. *J. Mater. Chem. A* **5**, 1153–1159 (2017).
218. Jacquet, Q. *et al.* The Li₃RuyNb_{1-y}O₄ (0 ≤ y ≤ 1) System: Structural Diversity and Li Insertion and Extraction Capabilities. *Chem. Mater.* **29**, 5331–5343 (2017).
219. Imashuku, S. *et al.* Improvement of Grain-Boundary Conductivity of Trivalent Cation-Doped Barium Zirconate Sintered at 1600°C by Co-doping Scandium and Yttrium. *J. Electrochem. Soc.* **155**, B581 (2008).
220. Avila-Paredes, H. J., Choi, K., Chen, C.-T. & Kim, S. Dopant-concentration dependence of grain-boundary conductivity in ceria: A space-charge analysis. *J. Mater. Chem.* **19**, 4837 (2009).
221. Thokchom, J. S. & Kumar, B. The effects of crystallization parameters on the ionic conductivity of a lithium aluminum germanium phosphate glass–ceramic. *J. Power Sources* **195**, 2870–2876 (2010).
222. Mariappan, C. R., Yada, C., Rosciano, F. & Roling, B. Correlation between micro-structural properties and ionic conductivity of Li_{1.5}Al_{0.5}Ge_{1.5}(PO₄)₃ ceramics. *J. Power Sources* **196**, 6456–6464 (2011).
223. IRVINE, J. & WEST, A. Solid electrolytes based on Na₃PO₄:M₂⁺ (M=Mg, Zn, Ca, Sr). *Solid State Ionics* **37**, 73–78 (1989).

224. Jansen, M. Volume Effect or Paddle-Wheel Mechanism—Fast Alkali-Metal Ionic Conduction in Solids with Rotationally Disordered Complex Anions. *Angew. Chemie Int. Ed. English* **30**, 1547–1558 (1991).
225. Zhang, Z., Roy, P., Li, H., Avdeev, M. & Nazar, L. F. Coupled Cation-Anion Dynamics Enhances Cation Mobility in Room Temperature Superionic Solid-State Electrolytes. *J. Am. Chem. Soc.* jacs.9b09343 (2019). doi:10.1021/jacs.9b09343
226. Wilmer, D. *et al.* Anion reorientation in Na₃PO₄. *Phys. B Condens. Matter* **241–243**, 338–340 (1997).
227. H, H., E, L. & M, J. Na-Ion conduction in the solid solutions of Na₃PO₄/Na₂SO₄ and Na₃AlF₆/Na₂SO₄. *Solid State Ionics* **28–30**, 159–162 (1988).
228. Ghule, A., Baskaran, N., Murugan, R. & Chang, H. Phase transformation studies of Na₃PO₄ by thermo-Raman and conductivity measurements. *Solid State Ionics* **161**, 291–299 (2003).
229. Milne, S. J. & West, A. R. Conductivity of Zr-doped Na₃PO₄: A new Na⁺ ion conductor. *Mater. Res. Bull.* **19**, 705–710 (1984).
230. Ghule, A., Murugan, R. & Chang, H. Thermo-Raman studies on dehydration of Na₃PO₄ · 12H₂O. *Thermochim. Acta* **371**, 127–135 (2001).
231. A, H., P, M., HARRISON, K. T. & TOFIELD, B. C. Ionic conductivity of pure and doped Na₃PO₄. *J. Solid State Chem.* **24**, 265–275 (1978).
232. Harrison, R. J., Putnis, A. & Kockelmann, W. Phase transition behaviour and equilibrium phase relations in the fast-ion conductor system Na₃PO₄-Na₂SO₄. *Phys. Chem. Chem. Phys.* **4**, 3252–3259 (2002).
233. Strauss, F. *et al.* Impact of Cathode Material Particle Size on the Capacity of Bulk-Type All-Solid-State Batteries. *ACS Energy Lett.* **3**, 992–996 (2018).
234. Xu, Z. M., Bo, S. H. & Zhu, H. LiCrS₂ and LiMnS₂ Cathodes with Extraordinary Mixed Electron-Ion Conductivities and Favorable Interfacial Compatibilities with Sulfide Electrolyte. *ACS Appl. Mater. Interfaces* **10**, 36941–36953 (2018).
235. Thackeray, M. M., Thomas, J. O. & Whittingham, M. S. Science and Applications of Mixed Conductors. *MRS Bull.* **25**, 39–46 (2000).
236. OZAWA, K. Lithium-ion rechargeable batteries with LiCoO₂ and carbon electrodes: the LiCoO₂/C system. *Solid State Ionics* **69**, 212–221 (1994).
237. Liu, Q. *et al.* Approaching the capacity limit of lithium cobalt oxide in lithium ion batteries via lanthanum and aluminium doping. *Nat. Energy* **3**, 936–943 (2018).
238. Reimers, J. N. & Dahn, J. R. Electrochemical and In Situ X-Ray Diffraction Studies of Lithium Intercalation in Li_xCoO₂. *J. Electrochem. Soc.* **139**, 2091 (1992).
239. Ohzuku, T. & Ueda, A. Solid-State Redox Reactions of LiCoO₂ (R3m) for 4 Volt Secondary Lithium Cells. *J. Electrochem. Soc.* **141**, 2972 (1994).
240. Amatucci, G. G., Tarascon, J. M. & Klein, L. C. CoO₂, The End Member of the Li_xCoO₂ Solid Solution. *J. Electrochem. Soc.* **143**, 1114 (1996).
241. Tarascon, J. M. *et al.* In Situ Structural and Electrochemical Study of Ni_{1-x}CoxO₂ Metastable Oxides Prepared by Soft Chemistry. *J. Solid State Chem.* **147**, 410–420 (1999).
242. Blandeau, L., Ouvrard, G., Calage, Y., Brec, R. & Rouxel, J. Transition-metal dichalcogenides from disintercalation processes. Crystal structure determination and Mossbauer study of Li₂FeS

- 2 and its disintercalates Li_xFeS_2 ($0.2 \leq x \leq 2$). *J. Phys. C Solid State Phys.* **20**, 4271–4281 (1987).
243. Zhang, L. *et al.* Tracking the Chemical and Structural Evolution of the TiS_2 Electrode in the Lithium-Ion Cell Using Operando X-ray Absorption Spectroscopy. *Nano Lett* **18**, 4506–4515 (2018).
244. Wu, Z. Y. *et al.* Sulfur k-edge x-ray-absorption study of the charge transfer upon lithium intercalation into titanium disulfide. *Phys. Rev. Lett.* **77**, 2101–2104 (1996).
245. Moreau, P., Ouvrard, G., Gressier, P., Ganal, P. & Rouxel, J. Electronic structures and charge transfer in lithium and mercury intercalated titanium disulfides. *J. Phys. Chem. Solids* **57**, 1117–1122 (1996).
246. Tarascon, J. M., Disalvo, F. J., Eibschutz, M., Murphy, D. W. & Waszczak, J. V. Preparation and chemical and physical properties of the new layered phases $\text{Li}_x\text{Ti}_{1-y}\text{MyS}_2$ with $M=\text{V, Cr, or Fe}$. *Phys. Rev. B* **28**, 6397–6406 (1983).
247. Rouxel, J. Anion-cation redox competition and the formation of new compounds in highly covalent systems. *Chem. - A Eur. J.* **2**, 1053–1059 (1996).
248. Rouxel, J. Some solid state chemistry with holes: Anion–cation redox competition in solids. *Curr. Sci.* **73**, 31–39 (1997).
249. Rouxel, J. & Toumoux, M. Chimie deuce with solid precursors, past and present. *Solid State Ionics* **84**, 141–149 (1996).
250. Britto, S. *et al.* Multiple Redox Modes in the Reversible Lithiation of High-Capacity, Peierls-Distorted Vanadium Sulfide. *J. Am. Chem. Soc* **137**, (2015).
251. Brec, R., Prouzet, E. & Ouvrard, G. Redox processes in the $\text{Li}_x\text{FeS}_2/\text{Li}$ electrochemical system studied through crystal, Mössbauer, and EXAFS analyses. *J. Power Sources* **26**, 325–332 (1989).
252. ONUKI, Y., INADA, R., TANUMA, S., YAMANAKA, S. & KAMIMURA, H. Electrochemical characteristics of transition-metal trichalcogenides in the secondary lithium battery. *Solid State Ionics* **11**, 195–201 (1983).
253. Murphy, D. W. & Trumbore, F. A. Metal chalcogenides as reversible electrodes in nonaqueous lithium batteries. *J. Cryst. Growth* **39**, 185–199 (1977).
254. Murphy, D. W. The Chemistry of TiS_3 and NbSe_3 Cathodes. *J. Electrochem. Soc.* **123**, 960 (1976).
255. Lindic, M. H. *et al.* XPS investigations of TiO_yS_z amorphous thin films used as positive electrode in lithium microbatteries. *Solid State Ionics* **176**, 1529–1537 (2005).
256. Matsuyama, T. *et al.* Structure analyses using X-ray photoelectron spectroscopy and X-ray absorption near edge structure for amorphous MS_3 (M: Ti, Mo) electrodes in all-solid-state lithium batteries. *J. Power Sources* **313**, 104–111 (2016).
257. Furuseth, S., Brattås, L., Kjekshus, A., Andresen, A. F. & Fischer, P. On the Crystal Structures of TiS_3 , ZrS_3 , ZrSe_3 , ZrTe_3 , HfS_3 , and HfSe_3 . *Acta Chem. Scand.* **29a**, 623–631 (1975).
258. Guilmeau, E. *et al.* ZrSe_3 -Type Variant of TiS_3 : Structure and Thermoelectric Properties. *Chem. Mater.* **26**, 5585–5591 (2014).
259. Taniguchi, K., Gu, Y., Katsura, Y., Yoshino, T. & Takagi, H. Rechargeable Mg battery cathode TiS_3 with d–p orbital hybridized electronic structures. *Appl. Phys. Express* **9**, 011801 (2016).
260. Kong, W. *et al.* Angle resolved vibrational properties of anisotropic transition metal

- trichalcogenide nanosheets. *Nanoscale* **9**, 4175–4182 (2017).
261. Island, J. O. *et al.* TiS₃ Transistors with Tailored Morphology and Electrical Properties. *Adv. Mater.* **27**, 2595–2601 (2015).
262. Island, J. O. *et al.* Electronics and optoelectronics of quasi-one dimensional layered transition metal trichalcogenides. *2D Mater.* **4**, (2017).
263. Gorlova, I. G., Pokrovskii, V. Y., Zybtev, S. G., Titov, A. N. & Timofeev, V. N. Features of the conductivity of the quasi-one-dimensional compound TiS₃. *J. Exp. Theor. Phys.* **111**, 298–303 (2010).
264. Ferrer, I. J. J., Ares, J. R. R., Clamagirand, J. M. M., Barawi, M. & Sánchez, C. Optical properties of titanium trisulfide (TiS₃) thin films. *Thin Solid Films* **535**, 398–401 (2013).
265. Mariam Barawi *et al.* Hydrogen Storage by Titanium Based Sulfides: Nanoribbons (TiS₃) and Nanoplates (TiS₂). *J. Electr. Eng.* **3**, 24–29 (2015).
266. Ferrer, I. J., Maciá, M. D., Carcelén, V., Ares, J. R. & Sánchez, C. On the photoelectrochemical properties of TiS₃ films. *Energy Procedia* **22**, 48–52 (2011).
267. Wu, K. *et al.* Unusual lattice vibration characteristics in whiskers of the pseudo-one-dimensional titanium trisulfide TiS₃. *Nat. Commun.* **7**, 12952 (2016).
268. Fleet, M. E., Harmer, S. L., Liu, X. & Nesbitt, H. W. Polarized X-ray absorption spectroscopy and XPS of TiS₃: S K- and Ti L-edge XANES and S and Ti 2p XPS. *Surf. Sci.* **584**, 133–145 (2005).
269. Xue, W. *et al.* Intercalation-conversion hybrid cathodes enabling Li–S full-cell architectures with jointly superior gravimetric and volumetric energy densities. *Nat. Energy* **4**, 374–382 (2019).
270. Zhang, R. *et al.* Lithiophilic Sites in Doped Graphene Guide Uniform Lithium Nucleation for Dendrite-Free Lithium Metal Anodes. *Angew. Chemie Int. Ed.* **56**, 7764–7768 (2017).
271. Sun, W. *et al.* Zn/MnO₂ Battery Chemistry With H⁺ and Zn²⁺ Coinsertion. *J. Am. Chem. Soc.* **139**, 9775–9778 (2017).
272. Flamaray-Mespoulie, F. Synthèse et caractérisation de sulfures de métaux de transition comme matériaux d'électrode positive à forte capacité pour microbatteries au lithium, Université de Bordeaux. (2016).
273. Endo, K., Ihara, H., Watanabe, K. & Gonda, S. XPS Study of One-Dimensional Compounds: TiS₃. *J. Solid State Chem.* **44**, 268–272 (1982).
274. Hawkins, C. G. & Whittaker-Brooks, L. Vertically oriented TiS_{2-x} nanobelt arrays as binder- and carbon-free intercalation electrodes for Li- and Na-based energy storage devices. *J. Mater. Chem. A* **6**, 21949–21960 (2018).
275. Lindic, M. H. *et al.* Electrochemical Mechanisms during Lithium Insertion into TiO[sub 0.6]S[sub 2.8] Thin Film Positive Electrode in Lithium Microbatteries. *J. Electrochem. Soc.* **152**, A141 (2005).
276. Shkvarin, A. S., Yarmoshenko, Y. M., Yablonskikh, M. V., Merentsov, A. I. & Titov, A. N. AN X-RAY SPECTROSCOPY STUDY OF THE ELECTRONIC STRUCTURE OF TiS₃. *J. Struct. Chem.* **55**, 1039–1043 (2014).
277. Farrell, S. P. *et al.* Evolution of local electronic structure in alabandite and niningerite solid solutions [(Mn,Fe)S, (Mg,Mn)S, (Mg,Fe)S] using sulfur K - and L -edge XANES spectroscopy. *Am. Mineral.* **87**, 1321–1332 (2002).

278. Assat, G., Glazier, S. L., Delacourt, C. & Tarascon, J.-M. Probing the thermal effects of voltage hysteresis in anionic redox-based lithium-rich cathodes using isothermal calorimetry. *Nat. Energy* (2019). doi:10.1038/s41560-019-0410-6
279. Xie, Y., Saubanère, M. & Doublet, M.-L. Requirements for reversible extra-capacity in Li-rich layered oxides for Li-ion batteries. *Energy Environ. Sci.* **10**, 266–274 (2017).
280. Ohta, S., Kihira, Y. & Asaoka, T. Grain Boundary Analysis of the Garnet-Like Oxides $\text{Li}_{7+x}\text{YLa}_3\text{XAXZr}_2\text{YNbYO}_{12}$ (A = Sr or Ca). *Front. Energy Res.* **4**, 1–6 (2016).
281. Li, B. *et al.* Thermodynamic Activation of Charge Transfer in Anionic Redox Process for Li-Ion Batteries. *Adv. Funct. Mater.* **28**, 1704864 (2018).
282. Sakuda, A. *et al.* A Reversible Rocksalt to Amorphous Phase Transition Involving Anion Redox. *Sci. Rep.* **8**, 15086 (2018).
283. Sakuda, A. *et al.* Rock-salt-type lithium metal sulphides as novel positive-electrode materials. *Sci. Rep.* **4**, 2–6 (2014).
284. House, R. A. *et al.* What Triggers Oxygen Loss in Oxygen Redox Cathode Materials? *Chem. Mater.* **31**, 3293–3300 (2019).
285. Poizot, P. *et al.* Nano-sized transition-metal oxides as negative-electrode materials for lithium-ion batteries. *Nature* **407**, 496–499 (2000).
286. Sathiya, M. *et al.* Origin of voltage decay in high-capacity layered oxide electrodes. *Nat. Mater.* **14**, 230–238 (2015).
287. Finklea, S. L., Cathey, L., Amma, E. L. & IUCr. Investigation of the bonding mechanism in pyrite using the Mössbauer effect and X-ray crystallography. *Acta Crystallogr. Sect. A* **32**, 529–537 (1976).
288. Chamas, M., Sougrati, M.-T., Reibel, C. & Lippens, P.-E. Quantitative Analysis of the Initial Restructuring Step of Nanostructured FeSn_2 -Based Anodes for Li-Ion Batteries. *Chem. Mater.* **25**, 2410–2420 (2013).
289. Fatseas, G. A. & Goodenough, J. B. Mössbauer ^{57}Fe spectra exhibiting “ferrous character”. *J. Solid State Chem.* **33**, 219–232 (1980).
290. Vaughan, D. J. & Ridout, M. S. Mössbauer studies of some sulphide minerals. *J. Inorg. Nucl. Chem.* **33**, 741–746 (1971).
291. Michael Bancroft, G., Kasrai, M., Fleet, M. & Stin, C. S K- and L-edge X-ray absorption spectroscopy of metal sulfides and sulfates: Applications in mineralogy and geochemistry. *Can. Mineral.* **33**, 949–960 (1995).
292. Fleet, M. E. XANES spectroscopy of sulfur in earth materials. *Can. Mineral.* **43**, 1811–1838 (2005).
293. Kowalska, J. K. *et al.* Iron L_{2,3}-Edge X-ray Absorption and X-ray Magnetic Circular Dichroism Studies of Molecular Iron Complexes with Relevance to the FeMoco and FeVco Active Sites of Nitrogenase. *Inorg. Chem.* **56**, 8147–8158 (2017).
294. Szilagyi, R. K. *et al.* Description of the Ground State Wave Functions of Ni Dithiolenes Using Sulfur K-edge X-ray Absorption Spectroscopy. *J. Am. Chem. Soc.* **125**, 9158–9169 (2003).
295. Martinez, H. *et al.* Influence of the cation nature of high sulfur content oxysulfide thin films MO_yS_z (M^{1/4}W, Ti) studied by XPS. *Appl. Surf. Sci.* **236**, 377–386 (2004).
296. Dai, K. *et al.* High Reversibility of Lattice Oxygen Redox Quantified by Direct Bulk Probes of

- Both Anionic and Cationic Redox Reactions. *Joule* **3**, 518–541 (2019).
297. Yang, W. & Devereaux, T. P. Anionic and cationic redox and interfaces in batteries: Advances from soft X-ray absorption spectroscopy to resonant inelastic scattering. *J. Power Sources* **389**, 188–197 (2018).
298. Li, N. *et al.* Unraveling the Cationic and Anionic Redox Reactions in a Conventional Layered Oxide Cathode. *ACS Energy Lett.* 2836–2842 (2019). doi:10.1021/acsenergylett.9b02147
299. Hong, J. *et al.* Metal–oxygen decoordination stabilizes anion redox in Li-rich oxides. *Nat. Mater.* **18**, 256–265 (2019).
300. Gent, W. E. *et al.* Coupling between oxygen redox and cation migration explains unusual electrochemistry in lithium-rich layered oxides. *Nat. Commun.* **8**, (2017).
301. Xu, J. *et al.* Elucidating anionic oxygen activity in lithium-rich layered oxides. *Nat. Commun.* **9**, 1–10 (2018).
302. Liu, X. *et al.* Distinct charge dynamics in battery electrodes revealed by in situ and operando soft X-ray spectroscopy. *Nat. Commun.* **4**, 1–8 (2013).
303. SAKUDA, A. *et al.* Development of Li₂TiS₃-Li₃NbS₄ by a mechanochemical process. *J. Ceram. Soc. Japan* **125**, 268–271 (2017).
304. Strehle, B. *et al.* The Role of Oxygen Release from Li- and Mn-Rich Layered Oxides during the First Cycles Investigated by On-Line Electrochemical Mass Spectrometry. *J. Electrochem. Soc.* **164**, A400–A406 (2017).
305. Assat, G., Iadecola, A., Foix, D., Dedryvere, R. & Tarascon, J. M. Direct quantification of anionic redox over long cycling of li-rich nmc via hard x-ray photoemission spectroscopy. *ACS Energy Lett.* **3**, 2721–2728 (2018).
306. Sathiya, M. *et al.* A Chemical Approach to Raise Cell Voltage and Suppress Phase Transition in O₃ Sodium Layered Oxide Electrodes. *Adv. Energy Mater.* **8**, 1–10 (2018).
307. Yan, G. *et al.* Assessment of the Electrochemical Stability of Carbonate-Based Electrolytes in Na-Ion Batteries. *J. Electrochem. Soc.* **165**, A1222–A1230 (2018).
308. Yan, G. *et al.* Higher energy and safer sodium ion batteries via an electrochemically made disordered Na₃V₂(PO₄)₂F₃ material. *Nat. Commun.* **10**, (2019).
309. Koerver, R. *et al.* Redox-active cathode interphases in solid-state batteries. *J. Mater. Chem. A* **5**, 22750–22760 (2017).
310. Maier, J. Ionic conduction in space charge regions. *Prog. Solid State Chem.* **23**, 171–263 (1995).
311. Sakuda, A., Takeuchi, T. & Kobayashi, H. Electrode morphology in all-solid-state lithium secondary batteries consisting of LiNi_{1/3}Co_{1/3}Mn_{1/3}O₂ and Li₂S-P₂S₅ solid electrolytes. *Solid State Ionics* **285**, 112–117 (2016).
312. Otoyama, M., Ito, Y., Hayashi, A. & Tatsumisago, M. Raman Spectroscopy for LiNi_{1/3}Mn_{1/3}Co_{1/3}O₂ composite positive electrodes in all-solid-state lithium batteries. *Electrochemistry* **84**, 812–814 (2016).
313. Takada, K. Progress in solid electrolytes toward realizing solid-state lithium batteries. *J. Power Sources* **394**, 74–85 (2018).
314. Tanibata, N., Matsuyama, T., Hayashi, A. & Tatsumisago, M. All-solid-state sodium batteries using amorphous TiS₃ electrode with high capacity. *J. Power Sources* **275**, 284–287 (2015).
315. Shin, B. R. *et al.* Comparative Study of TiS₂ /Li-In All-Solid-State Lithium Batteries Using

- Glass-Ceramic Li₃PS₄ and Li₁₀GeP₂S₁₂ Solid Electrolytes. *Electrochim. Acta* **146**, 395–402 (2014).
316. Trevey, J. E., Stoldt, C. R. & Lee, S.-H. High Power Nanocomposite TiS₂ Cathodes for All-Solid-State Lithium Batteries. *J. Electrochem. Soc.* **158**, A1282 (2011).
317. Tatsumisago, M., Nagao, M. & Hayashi, A. Recent development of sulfide solid electrolytes and interfacial modification for all-solid-state rechargeable lithium batteries. *J. Asian Ceram. Soc.* **1**, 17–25 (2013).
318. Xu, R., Xia, X., Wang, X., Xia, Y. & Tu, J. Tailored Li₂S–P₂S₅ glass-ceramic electrolyte by MoS₂ doping, possessing high ionic conductivity for all-solid-state lithium-sulfur batteries. *J. Mater. Chem. A* **5**, 2829–2834 (2017).
319. Doux, J.-M. *et al.* Stack Pressure Considerations for Room Temperature All-Solid-State Lithium Metal Batteries. *arXiv* (2019).
320. Zhang, W. *et al.* The Detrimental Effects of Carbon Additives in Li₁₀GeP₂S₁₂-Based Solid-State Batteries. *ACS Appl. Mater. Interfaces* **9**, 35888–35896 (2017).
321. Hakari, T. *et al.* Structural and Electronic-State Changes of a Sulfide Solid Electrolyte during the Li Deinsertion-Insertion Processes. *Chem. Mater.* **29**, 4768–4774 (2017).
322. Yoon, K., Kim, J.-J., Seong, W. M., Lee, M. H. & Kang, K. Investigation on the interface between Li₁₀GeP₂S₁₂ electrolyte and carbon conductive agents in all-solid-state lithium battery. *Sci. Rep.* **8**, 8066 (2018).
323. Kasemchainan, J. *et al.* Critical stripping current leads to dendrite formation on plating in lithium anode solid electrolyte cells. *Nat. Mater.* (2019). doi:10.1038/s41563-019-0438-9
324. Doux, J.-M. *et al.* Stack Pressure Considerations for Room Temperature All-Solid-State Lithium Metal Batteries. (2019).
325. Dietrich, C. *et al.* Lithium ion conductivity in Li₂S–P₂S₅ glasses – building units and local structure evolution during the crystallization of superionic conductors Li₃PS₄, Li₇P₃S₁₁ and Li₄P₂S₇. *J. Mater. Chem. A* **5**, 18111–18119 (2017).
326. Oh, D. Y. *et al.* Wet-Chemical Tuning of Li_{3–x}PS₄ (0 ≤ x ≤ 0.3) Enabled by Dual Solvents for All-Solid-State Lithium-Ion Batteries. *ChemSusChem* **4**, cssc.201901850 (2019).
327. Banerjee, A. *et al.* Revealing Nanoscale Solid-Solid Interfacial Phenomena for Long-Life and High-Energy All-Solid-State Batteries. *ACS Appl. Mater. Interfaces* acsami.9b13955 (2019). doi:10.1021/acsami.9b13955
328. Leube, B. T. *et al.* Lithium Transport in Li_{4.4}M_{0.4}M'_{0.6}S₄ (M = Al³⁺, Ga³⁺, and M' = Ge⁴⁺, Sn⁴⁺): Combined Crystallographic, Conductivity, Solid State NMR, and Computational Studies. *Chem. Mater.* **30**, 7183–7200 (2018).
329. Indris, S., Cabana, J., Rutt, O. J., Clarke, S. J. & Grey, C. P. Layered Oxysulfides Sr₂MnO₂Cu_{2m–0.5}S_{m+1} (m = 1, 2, and 3) as Insertion Hosts for Li Ion Batteries. *J. Am. Chem. Soc.* **128**, 13354–13355 (2006).
330. Rutt, O. J., Williams, G. R. & Clarke, S. J. Reversible lithium insertion and copper extrusion in layered oxysulfides. *Chem. Commun.* **88**, 2869 (2006).
331. Salter, E. J. T., Blandy, J. N. & Clarke, S. J. Crystal and Magnetic Structures of the Oxide Sulfides CaCoSO and BaCoSO. *Inorg. Chem.* **55**, 1697–1701 (2016).
332. Jin, S. F. *et al.* Two-dimensional magnetic correlations and partial long-range order in

- geometrically frustrated CaOFeS with triangle lattice of Fe ions. *Phys. Rev. B* **91**, 094420 (2015).
333. Hiramatsu, H. *et al.* Crystal Structures, Optoelectronic Properties, and Electronic Structures of Layered Oxychalcogenides $M\text{CuOCh}$ ($M = \text{Bi, La}$; $\text{Ch} = \text{S, Se, Te}$): Effects of Electronic Configurations of M^{3+} Ions. *Chem. Mater.* **20**, 326–334 (2008).
334. Otzsch, K., Ogino, H., Shimoyama, J. & Kishio, K. New Candidates for Superconductors; A Series of Layered Oxysulfides $(\text{Cu}_2\text{S}_2)(\text{Sr}_{n+1}\text{MnO}_{3n-1})$. *J. Low Temp. Phys.* **117**, 729–733 (1999).
335. Le Bail, A., Duroy, H. & Fourquet, J. L. Ab-initio structure determination of LiSbWO_6 by X-ray powder diffraction. *Mater. Res. Bull.* **23**, 447–452 (1988).
336. Rodríguez-Carvajal, J. *FullProf Suite; all the programs can be obtained from: <http://www.ill.eu/sites/fullprof>.*
337. Momma, K. & Izumi, F. VESTA; the program can be obtained from: <https://jp-minerals.org/vesta>.
338. Momma, K. & Izumi, F. VESTA 3 for three-dimensional visualization of crystal, volumetric and morphology data. *J. Appl. Crystallogr.* **44**, 1272–1276 (2011).
339. Adams, S. From bond valence maps to energy landscapes for mobile ions in ion-conducting solids. *Solid State Ionics* **177**, 1625–1630 (2006).
340. Tilmann, L., Matthias, Z. & Hartmut, S. *Electrochemical Storage Materials*. (De Gruyter, 2018). doi:10.1515/9783110493986
341. Shoar Abouzari, M. R., Berkemeier, F., Schmitz, G. & Wilmer, D. On the physical interpretation of constant phase elements. *Solid State Ionics* **180**, 922–927 (2009).
342. Sinclair, D. C. D.C. Characterization of Electro-materials using AC Impedance Spectroscopy. *Bol. la Soc. Esp. Ceram. y Vidr.* **65**, 55–66 (1995).
343. Fehse, M. *et al.* The Electrochemical Sodiation of FeSb_2 : New Insights from Operando ^{57}Fe Synchrotron Mössbauer and X-Ray Absorption Spectroscopy. *Batter. Supercaps* **2**, 66–73 (2019).
344. Ruckebusch, C. & Blanchet, L. Multivariate curve resolution: A review of advanced and tailored applications and challenges. *Anal. Chim. Acta* **765**, 28–36 (2013).
345. de Juan, A., Jaumot, J. & Tauler, R. Multivariate Curve Resolution (MCR). Solving the mixture analysis problem. *Anal. Methods* **6**, 4964–4976 (2014).
346. Fehse, M. *et al.* Applying chemometrics to study battery materials: Towards the comprehensive analysis of complex operando datasets. *Energy Storage Mater.* **18**, 328–337 (2019).
347. Qiao, R. *et al.* High-efficiency in situ resonant inelastic x-ray scattering (iRIXS) endstation at the Advanced Light Source. *Rev. Sci. Instrum.* **88**, (2017).
348. Shirley, D. A. High-resolution X-Ray photoemission spectrum of the valence bands of gold. *Phys. Rev. B* **5**, 4709–4714 (1972).
349. Scofield, J. H. Hartree-Slater subshell photoionization cross-sections at 1254 and 1487 eV. *J. Electron Spectros. Relat. Phenomena* **8**, 129–137 (1976).
350. AU - Wu, J. *et al.* Elemental-sensitive Detection of the Chemistry in Batteries through Soft X-ray Absorption Spectroscopy and Resonant Inelastic X-ray Scattering. *JoVE* e57415 (2018). doi:doi:10.3791/57415

